Computer Aided Assessment of CT Scans of Traumatic Brain Injury

Adnan Nabeel Abid Qureshi

COMPUTER AIDED ASSESSMENT OF CT SCANS OF TRAUMATIC BRAIN INJURY PATIENTS

by

Adnan Nabeel Abid Qureshi

A thesis submitted in partial fulfilment for
the degree of Doctor of Philosophy

in the
Institute for Research in Applicable Computing
UNIVERSITY OF BEDFORDSHIRE

2015

Contents

List of Figures v

List of Tables vii

Declaration of Authorship ix

Abstract xi

Acknowledgements xiii

Abbreviations xiv

Symbols xvi

1 Introduction 1
- 1.1 Motivation . . . 3
- 1.2 Aim and Objectives . . . 6
- 1.3 Scope and Limitations of the Research . . . 7
- 1.4 Contribution . . . 8
- 1.5 List of Publications . . . 9
  - 1.5.1 Publications in Conferences . . . 9
  - 1.5.2 Publications in Journals . . . 11
- 1.6 Thesis Organization . . . 11

2 Analysis of Medical Images 14
- 2.1 Medical Diagnosis . . . 14
- 2.2 Medical Diagnostic Imaging . . . 16
  - 2.2.1 CT Scans and Brain Protocol . . . 18

2.2.2 Head CT in Emergency Cases . . . 22
2.2.3 Noncontrast CT in Emergency Cases . . . 23
2.3 Brain Trauma CT Scans . . . 23
2.3.1 Prognosis from TBI CT . . . 25
2.4 Brain Ratios and Indices . . . 33
2.5 Inter- and Intra-Observer Variability . . . 36
2.5.1 Manual Annotation of Medical Images . . . 37
2.5.2 Perception and Contrast . . . 40
2.5.3 Inattentional Blindness . . . 41
2.5.4 Effect of Ambient Light . . . 42
2.6 Patients' Clinical and Imaging Profile . . . 43
2.6.1 Pre-injury Profile . . . 43
2.6.2 Post-injury Profile . . . 44
2.6.3 Imaging Profile and Spatial Localization . . . 45
2.7 Prognosis Model . . . 48
2.8 Summary . . . 51

3 State of the Art 53
3.1 Double Reporting . . . 54
3.2 Computer Aided Diagnosis (CAD) . . . 55
3.3 Image Segmentation and Analysis in CAD . . . 59
3.3.1 Approaches using Image Processing . . . 60
3.3.1.1 Spatially Blind Methods . . . 60
3.3.1.2 Spatially Guided Methods . . . 64
3.3.2 Approaches using Machine Learning . . . 68
3.3.2.1 Selection of Machine Learning method . . . 72
3.3.2.2 Feature Extraction and Selection . . . 73
3.3.3 Hybrid Approaches . . . 74
3.4 Evaluation of Segmentation . . . 77
3.5 Conclusion . . . 78

4 Pattern Driven, Content Aware Active Contours 80
4.1 Description of the Framework . . . 83
4.1.1 Correction of Orientation of Head in CT image . . . 83
4.1.2 Estimation of brain midline shift . . . 83
4.1.3 Feature Extraction, Selection and Classification . . . 85
4.1.3.1 Features from Clinical Profile . . . 85
4.1.3.2 Contrast Enhancement . . . 87
4.1.3.3 Classification of Features from CT Image . . . 88
4.1.4 Segmentation using Modified Active Contours . . . 90
4.1.5 Matching with CT Rating & Linear Measurements . . . 90
4.2 Summary . . . 91

5 Implementation of the PDCAAC Framework 93
5.1 Preprocessing of CT Images . . . 94

5.2 Estimation of brain midline and vote α_H . . . 95
5.3 Extraction, Selection and Classification of Features . . . 103
5.3.1 Classification using Artificial Neural Networks (ANN) . . . 103
5.3.2 Features from Clinical Profile . . . 106
5.3.3 Contrast Enhancement of Probable ROI . . . 108
5.3.4 Features from CT Images . . . 111
5.3.4.1 Feaure Extraction . . . 111
5.3.4.2 Feature Selection . . . 116
5.3.4.3 Classification of CT Image Pixels . . . 119
5.4 Segmentation using Active Contours . . . 123
5.4.1 Existing Models of Active Contours . . . 124
5.4.1.1 Geometric Active Contours . . . 124
5.4.1.2 Active Contours without Edges . . . 125
5.4.2 Limitations of Existing Models . . . 127
5.4.3 Modified Active Contour (MAC) Method . . . 132
5.4.3.1 Location vote β_H for Haematomas . . . 133
5.4.3.2 Defining Constraint Energy . . . 136
5.4.3.3 Stopping Criterion using Gradient . . . 140
5.5 Visualization of the ROI . . . 141
5.6 Measurements and Estimation of Volume . . . 143
5.7 Matching CT with Marshall et al. Rating . . . 146
5.8 Summary . . . 146

6 Results and Discussion **148**
6.1 Evaluation Measures . . . 148
6.1.1 Sensitivity, Specificity, Precision, Recall and ROC . . . 149
6.1.2 Cross-Validation . . . 151
6.1.3 Jaccard Similarity Index (JI) . . . 151
6.1.4 Intraclass Correlation Coefficient (ICC) . . . 152
6.1.5 Paired *t-test* . . . 152
6.2 Dataset . . . 153
6.3 Estimation of Brain Midline . . . 155
6.4 Classification of Clinical Data . . . 157
6.5 Pixel Classification using ANN . . . 158
6.6 Segmentation using proposed method . . . 160
6.6.1 Performance with Feedforward Network . . . 163
6.6.2 Performance with Pattern Network . . . 164
6.6.3 Performance with Cascadeforward Network . . . 166
6.6.4 Limitations of the proposed method . . . 168
6.7 Segmentation of the Regions of Interest . . . 170
6.7.1 Skull Bone as ROI . . . 170
6.7.2 Brain as ROI . . . 171
6.7.3 CSF Spaces as ROI . . . 172
6.7.4 Blood as ROI . . . 172

6.8 Estimation of Size of Haematoma . . . 173
6.8.1 Estimations of EDH . . . 177
6.8.2 Estimations of SDH . . . 179
6.9 Estimation of Brain Indices and Ratios . . . 182
6.9.1 Estimation of Cella Media Index (CMI) . . . 184
6.9.2 Estimation of Bifrontal Index . . . 185
6.9.3 Estimation of Width of Third Ventricle . . . 186
6.10 Identification of CSF Spaces as ROI . . . 187
6.11 Performance of the Junior Radiologist . . . 188
6.12 Correlation to the Marshall CT Classification . . . 190
6.13 Hardware and Software Resources . . . 191
6.14 Summary . . . 192

7 Conclusion **193**
7.1 Transferability . . . 196
7.2 Future work . . . 197

Appendix A Typical CT Study of Brain **201**

Appendix B Typical MRI Study of Brain **202**

Appendix C CT Scans of TBI Patients **203**

Appendix D Clinical and Neurological Assessment Data **210**

Appendix E CT Device and Protocol **216**
E.1 Toshiba Activion 16 . . . 216
E.2 Philips Brilliance 16 . . . 218

Bibliography **220**

List of Figures

1.1 Representation of body parts in the brain homunculus 2

2.1 Polyrepresentation of evidence for diagnosis 16
2.2 Imaging Modalities 18
2.3 CT Scanner 20
2.4 CT Scan Procedure 21
2.5 Cases seen on Brain CT 22
2.6 Haematomas, as seen on CT scans. 24
2.7 Three Slice Method 28
2.8 Marshall Classification of CT 29
2.9 Modified Marshall Classification 30
2.10 Measurements on Axial CT Scans 33
2.11 Labelled Brain MRI Slices 38
2.12 Manual annotation of ROI by radiology experts. 39
2.13 Simultaneous Contrast 41
2.14 The Invisible Gorilla 42
2.15 Brain CT image findings. 45
2.16 Probability of Mortality or Unfavourable Outcomes 51

3.1 Typical work flow of Computer Aided Diagnosis 56
3.2 Spatially blind segmentation 62
3.3 DRLSE in medical images 67
3.4 Effect of initial curve size 67

4.1 Work flow of the PDCAAC framework 82
4.2 Manual annotation of the midline 84

5.1 Estimation of tilt of head in CT Scans. 96
5.2 Detection of skull edges 97
5.3 Correction of orientation of CT Scans 99
5.4 Templates generated for Cross Correlation 101
5.5 Template matching for Septum Pellucidum 102
5.6 Architecture of ANN 103
5.7 Architecture of the ANN for classification of Clinical Phenotype . . 108
5.8 Anisotropic Contrast Enhancement 110
5.9 ROC of Radiologists' Annotation 114

5.10 ROC of individual Statistical Features, m = 3 . . . 115
5.11 ROC of individual Statistical Features, m = 5 . . . 116
5.12 ROC of individual Statistical Features, m = 7 . . . 117
5.13 ROC of Combination of Features, m = 5 . . . 118
5.14 Manual annotation of ROI by radiology experts. . . . 120
5.15 Architecture of the ANNs for classification of CT image features . . 120
5.16 Architecture of the ANNs with two hidden layers for classification of CT image features . . . 121
5.17 Pixel classification with different transfer functions in ANN . . . 122
5.18 Active contours and level sets . . . 127
5.19 Effect of initial curve size . . . 129
5.20 Segmentation results from state of the art . . . 130
5.21 Segmentation from state of the art with contrast adjustment . . . 131
5.22 Work flow of proposed method . . . 133
5.23 Constraint on the Contour . . . 139
5.24 Gradient for Edges . . . 140
5.25 Localization of ROI . . . 142
5.26 Measurements of haematoma on a single CT slice . . . 143
5.27 Output of the proposed method . . . 145

6.1 CT of TBI Cases . . . 155
6.2 Classification performance of clinical profile . . . 157
6.3 ANN pixel classification without Clinical Phenotype . . . 158
6.4 ANN pixel classification with Clinical Phenotype . . . 159
6.5 Comparison of SLIC and ANN classification . . . 160
6.6 Pixel Classification using ANN . . . 162
6.7 Performance using Feedforward Net . . . 164
6.8 Performance using Pattern Net . . . 166
6.9 Performance using Cascadeforward Net . . . 167
6.10 Demarcation of only one ROI in the case. . . . 168
6.11 Cases with gross deformity of the brain structures. . . . 169
6.12 Stripping scalp and skull . . . 170
6.13 Brain boundary demarcation . . . 171
6.14 Demarcation of ventricles . . . 172
6.15 Segmentation results from hybrid approach . . . 173
6.16 Output of the method . . . 174

C.1 CT of TBI Cases . . . 203
C.2 CT of TBI Cases . . . 204
C.3 CT of TBI Cases . . . 205
C.4 CT Scans of TBI Patients . . . 206
C.5 CT Scans of TBI Patients . . . 207
C.6 CT Scans of TBI Patients . . . 208
C.7 CT Scans of TBI Patients . . . 209

List of Tables

2.1 Glasgow Outcome Scale - Extended . . . 26
2.2 Marshall et al. CT Rating . . . 27
2.3 Rotterdam CT Classification . . . 31
2.4 Rotterdam Outcome Scale . . . 32
2.5 GCS, volume of haemorrhage and probability of mortality . . . 33
2.6 Measurements on the axial CT scans . . . 34
2.7 Indices and Ratios estimated on the axial CT scans . . . 35
2.8 Clinical features predisposing to ICH . . . 44
2.9 Clinical Profile at time of admission . . . 46
2.10 Size and location of haemorrhages and clinical presentation . . . 48
2.11 Score chart for outcome at 6 months after TBI . . . 50
2.12 Prognosis Model based on Clinical Profile . . . 51

4.1 Clinical Phenotype for classification . . . 86
4.2 Clinical phenotype classification . . . 87
4.3 64-bin histogram of 8-bit gray scale CT images in PNG format. . . . 88

5.1 Hounsfield Unit (HU) scale for CT . . . 95
5.2 Clinical phenotype classification . . . 107
5.3 Clinical features for ANN . . . 107
5.4 Features extracted from CT images . . . 113
5.5 Voting scheme for the probable location of haematoma . . . 136

6.1 Sensitivity and specificity . . . 149
6.2 The detection of midline shift . . . 157
6.3 Performance using Feedforward Net . . . 163
6.4 Performance using Pattern Net . . . 165
6.5 Performance using Cascadeforward Net . . . 167
6.6 Estimation of Haematoma Length . . . 175
6.7 Two Tail t-test on estimation of Haematoma Length . . . 175
6.8 Estimation of Haematoma Breadth . . . 176
6.9 Two Tail t-test on estimation of Haematoma Breadth . . . 176
6.10 ICC of measurements of Haematoma . . . 177
6.11 Estimation of EDH Length . . . 178
6.12 t-test on estimation of EDH Length . . . 178

6.13 Estimation of EDH Breadth 178
6.14 t-test on estimation of EDH Breadth 179
6.15 Estimation of SDH Length 180
6.16 t-test on estimation of SDH Length 180
6.17 Estimation of SDH Breadth 181
6.18 t-test on estimation of SDH Breadth 181
6.19 Linear measurements on the axial CT scans 183
6.20 Indices and Ratios estimated on the axial CT scans 184
6.21 Estimation of Cella Media Index 185
6.22 t-test on estimation of Cella Media Index 185
6.23 Estimation of Bifrontal Index 186
6.24 t-test on estimation of Bifrontal Index 186
6.25 Estimation of width of third ventricle 187
6.26 t-test on estimation of width of third ventricle 187
6.27 Identification of CSF spaces as ROI 188
6.28 Performance of the Junior Radiologist 189
6.29 Two Tail t-test on Performance of the Junior Radiologist 189
6.30 CT Classification according to Marshall et al. 191

D.1 Clinical and Neurological Assessment Data Elements 211
D.2 Patient Data 215

E.1 Acquisition of Brain CT on Toshiba Activion 16 217
E.2 Acquisition of Brain CT on Philips Brilliance 16 219

Declaration of Authorship

I declare that this thesis is my own unaided work. It is being submitted for the degree of Doctor of Philosophy at the University of Bedfordshire.

It has not been submitted before for any degree or examination in any other University.

Adnan Nabeel Abid Qureshi

Name of candidate: Signature:

Date:

The Examination Board:

Chair:	Professor Patrick Carmichael
External Examiner:	Dr. Gregory G. Slabaugh
External Examiner:	Dr. Huseyin Seker
Internal Examiner:	Dr. Mehmet Aydin

I pay my humble tribute to one of the greatest minds of all times, Nikola Tesla, by quoting him:

"What the result of these investigations will be the future will tell; but whatever they may be, and to whatever this principle may lead, I shall be sufficiently recompensed if later it will be admitted that I have contributed a share, however small, to the advancement of science."

Adnan Nabeel Abid Qureshi

UNIVERSITY OF BEDFORDSHIRE

Abstract

Institute for Research in Applicable Computing

Doctor of Philosophy

by

A. N. A. QURESHI

One of the serious public health problems is the Traumatic Brain Injury, also known as silent epidemic, affecting millions every year. Management of these patients essentially involves neuroimaging and noncontrast CT scans are the first choice amongst doctors. Significant anatomical changes identified on the neuroimages and volumetric assessment of haemorrhages and haematomas are of critical importance for assessing the patients' condition for targeted therapeutic and/or surgical interventions.

Manual demarcation and annotation by experts is still considered gold standard, however, the interpretation of neuroimages is fraught with inter-observer variability and is considered 'Achilles heel' amongst radiologists. Errors and variability can be attributed to factors such as poor perception, inaccurate deduction, incomplete knowledge or the quality of the image and only a third of doctors confidently report the findings. The applicability of computer aided dianosis in segmenting the apposite regions and giving 'second opinion' has been positively appraised to assist the radiologists, however, results of the approaches vary due to parameters of algorithms and manual intervention required from doctors and this presents a gap for automated segmentation and estimation of measurements of noncontrast brain CT scans.

The Pattern Driven, Content Aware Active Contours (PDCAAC) Framework developed in this thesis provides robust and efficient segmentation of significant anatomical landmarks, estimations of their sizes and correlation to CT rating to assist the radiologists in establishing the diagnosis and prognosis more confidently. The integration of clinical profile of the patient into image segmentation algorithms has significantly improved their performance by highlighting characteristics of the region of interest. The modified active contour method in the PDCAAC framework

achieves Jaccard Similarity Index (JI) of 0.87, which is a significant improvement over the existing methods of active contours achieving JI of 0.807 with Simple Linear Iterative Clustering and Distance Regularized Level Set Evolution. The Intraclass Correlation Coefficient of intracranial measurements is >0.97 compared with radiologists. Automatic seeding of the initial seed curve within the region of interest is incorporated into the method which is a novel approach and alleviates limitation of existing methods.

The proposed PDCAAC framework can be construed as a contribution towards research to formulate correlations between image features and clinical variables encompassing normal development, ageing, pathological and traumatic cases propitious to improve management of such patients. Establishing prognosis usually entails survival but the focus can also be extended to functional outcomes, residual disability and quality of life issues.

Acknowledgements

I would like to express my gratitude to my Director of Studies, Dr. Vitaly Schetinin, and my Second Supervisor, Dr. Dayou Li, for their help, support and guidance throughout my research. I would also like to thank Prof. Edmond Prakash, Prof. Carsten Maple and Prof. Feng Dong for their valuable suggestions and advices which have always encouraged and fortified my research endeavours. I am indebted to Dr. Xujiong Ye, University of Lincoln, for sharing her ideas and experiences and whetting my work. I also highly appreciate the training and counselling provided by the Research Graduate School.

I would also wish to thank Prof. Dr. Muhammad Amjad Shahzad, Medical Superintendent, Lahore General Hospital, Pakistan, for providing the clinical and imaging data. The support extended by Prof. Dr. Safdar Ali Malik (TI), Head of Radiology Department, Services Institute of Medical Sciences, Lahore, Pakistan, in annotating the cases and providing expert opinion is invaluable and I am deeply indebted to him for his knowledge and friendly advice.

The support and friendship of my fellow students and friends in the Institute for Research in Applicable Computing has always humbled me. My colleagues, M. Kamran Abbassi, Ghulam Mustafa, Tao Cao and Raymond Brown have been guiding and helping me throughout my research.

The privilege of presenting my work at the Medical Image Understanding and Analysis conference at Royal Holloway, supported the impetus and perseverance necessary for my research. I am grateful to the audience for their questions and comments which sifted away many of the problems. I would also express my regards to the many unknown reviewers who invested their valuable time in analysing my research papers and providing precious comments.

Abbreviations

ANN	Artificial Neural Networks
CAD	Computer Aided Diagnosis
CSF	Cerebrospinal Fluid
CT	Computed Tomography
CNN	Convolutional Neural Networks
DBN	Deep Belief Networks
DAI	Diffuse Axonal Injury
DFT	Discrete Fourier Transform
DICOM	Digital Imaging and Communications in Medicine
DWT	Discrete Wavelet Transform
DRLSE	Distance Regularized Level Set Evolution
EDH	Epidural Haematoma
GCS	Glasgow Coma Scale
GOS	Glasgow Outcome Scale
GOSE	Glasgow Outcome Scale Extended
GMDH	Group Method of Data Handling
HU	Hounsfield Unit
ICC	Intraclass Correlation Coefficient
ISS	Injury Severity Score
ICP	Intracranial Pressure
JI	Jaccard Similarity Index
LM	Levenberg-Marquardt algorithm

MRI	Magnetic Resonance Imaging
PDCAAC	Pattern Driven, Content Aware Active Contours
ROC	Receiver Operator Characteristic
ROI	Region of Interest
SAH	Subarachnoid Haemorrhage
SDH	Subdural Haematoma
SLIC	Simple Linear Iterative Clustering
TAI	Traumatic Axonal Injury
tSAH	Traumatic Subarachnoid Haemorrhage

Symbols

Ω	Region of image
Ω_0	Region of interest pixels within image
Ω_1	Non-Region of Interest pixels within image
$\int$	Integration
$\oint$	Integration around curve
$\int_\Omega$	Integration of region of image domain
τ	Boundary around region of interest
$\int_{\Omega \setminus \tau}$	Integration of region within the boundary
$\sum$	Summation
$\prod$	Product
σ	Standard deviation
κ	Curvature of the curve
∇	Gradient
$\phi(x, y)$	Level set function at pixels (x, y)
$\vec{N}$	Normal to ϕ
V	Velocity of geometric active contour
u	Image segment defined in $\Omega \rightarrow \mathcal{R}^2$
c_1	Average intensity inside region
c_2	Average intensity outside region
μ	Permissible length of curve
ν	Permissible area of curve
H	Heaviside function
α_H	Haematoma location vote from brain midline
β_H	Haematoma location vote from ANN classification

Υ	Vote from clinical phenotype
Ψ	Distance between haematoma and midline pixels
ψ	Minimum distance between haematoma and midline pixels
γ	Rectangular image window for locating bony protuberances
φ	Intensity threshold for locating bony protuberances
ϵ	Error function for ANN
$conf(Loc_{init})$	Location confidence $= \alpha_H + \beta_H$
$\mathbf{v}$	Matrix representing active contour
E	Energy for the active contour
E_{int}	Internal energy from length and curvature of contour
E_{ext}	External energy from edges and gradients
E_{con}	Constraint energy
E_{ann}	Energy regularizing shrinking of contour
E_{loc}	Energy regularizing location and number of contours
$C_{init})$	Curve representing initial contour (seed)
C_{evol}	Curve representing evolving contour
$D(C_{evol}, C_{init})$	Distance between initial and evolving contour
$\mathbf{NC}$	Feature matrix of Clinical phenotype
$\mathbf{W}$	Matrix representing input CT image
$\mathbf{G}$	Sliding window for feature extraction
$\mathbf{F}$	Feature matrix of image data
S_{ANN}	Set of pixels classified by ANN
R_{ANN}	Subset of S_{ANN} pixels based on proximity within ROI
$\mathbf{y}$	Subset of R_{ANN} pixels belonging to ROI
P_{cal}	Spatial resolution of pixels for measurements

Dedicated to the loving memory of my late father,
Prof. Dr. Abid Hussain Qureshi,
whose aphorisms of tenacity still guide me,
and to the immeasurable, unconditional and endless love
my mother, Mrs. Nasim Qureshi, has for me.
I also dedicate this work to my sister, Tania, who has
never left my side and always supports me with a
smiling face,
and to my wife, Alliya, whose love, selfless devotion and
courage has given me the strength for my quest.
This work is dedicated to the love and persuasion
constantly flowing towards me from my two angels,
Yusra and Farheen.
Without your strong faith in my abilities and
endorsement of my scholarly pursuit, this work would
not have completed.

Chapter 1

Introduction

No head injury is so trivial that it can be ignored, and none so serious that the life must be despaired of.

Hippocrates

The human brain is a marvel of nature. Consisting of a complex network of more than 100 billion neurons and consuming almost 25% of nutrition from blood, it is an amazing organ and perhaps the only one which has not yet been transplanted. Amongst the animals, the human brain is not the largest, yet it is the most highly evolved. It is capable not only of logical reasoning as well as analytical decision making but also of concurrently controlling and regulating the functions of the other organs.

The brain, with its intricate connectivity to the rest of the body, has confounded researchers, since Hippocrates, pursuing them to delve into the realms of diagnosing and then treating pathologies and injuries to this anatomical structure. Hippocrates, in his Aphorisms (Adams et al. 1849), describes its working in parts and as a whole and he says:

> *And if incision of the temple is made on the left, spasm seizes the parts on the right, while if the incision is on the right, spasm seizes the parts*

on the left.

There is extensive ongoing research into its physical, functional and cognitive characteristics, however, most of the work is in its infancy. The physiology and anatomy is quite well understood, but isolation of functionality still baffles the doctors. A injury or pathology in one part may manifest itself with localized or general somatosensory and/or motor deficit(s) ranging from slurring of speech to weakness of a limb to vegetative coma. A cortical homunculus, as shown in Fig. 1.1, is often used in medical education to represent the allocation of areas of brain cortex to different body parts both for the sensory and motor control (Gray 1948, Marieb & Hoehn 2007, Hall 2010). The relative sizes and locations of these areas vary from person to person and also change with age and diseases and, hence, its anatomy, physiology and pathophysiology for every human becomes unique.

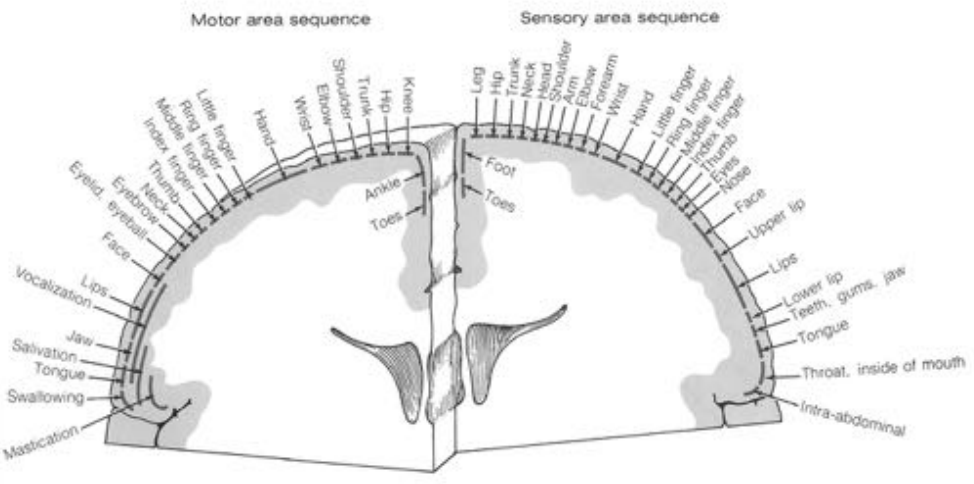

FIGURE 1.1: Representation of body parts in the brain homunculus
Representation of body parts in the brain homunculus. (Gray 1948)

This marvellous organ, however, is often affected by one of the serious public health problems: **Traumatic Brain Injury (TBI)**, blighting millions worldwide every year. Also called a 'Silent Epidemic' it affects all age groups and both genders (Goldstein 1990, Thompson et al. 2006). The incidence is much higher in

the developing countries due to frequent occurrence of assaults and road traffic accidents and higher mortality is related to less specifically available treatment (Steyerberg et al. 2008). The Brain Injury Association of America reports that the frequency of incidence of head trauma is almost three cases every minute (CDC.GOV 2014). The incidence of falls in the old and frail or those intoxicated by alcohol is a common cause of brain injuries. Shaken baby syndrome is a another cause of brain injuries in infants. Occupational hazards as in military personnel and sports related injuries as in football or rugby predispose those who are involved to sustain brain trauma. For most people the prospect of being repeatedly punched in the head and body is the stuff of nightmares, however, for boxers it is a way of life to fend off the blows (Kelly 1999, Langlois et al. 2005).

While the severity of the injury can range from mild to severe, the high mortality and morbidity rates due to TBI can be attributed to the fact that the extent of injury is often difficult to be accurately reported by doctors which makes prognosis nearly impossible to predict (Saatman et al. 2008, Robinson 1997). The patient usually arrives at the hospital intubated and sedated and the initial CT scan is the key emergency investigation for immediate surgical intervention or for invasive ICP monitoring. The accuracy of establishing clinical picture, when a TBI is suspected, within early hours of trauma can help improve patient outcomes through timely management and appropriate referral. The initial noncontrast CT carries significant prognostic value and when this information is combined with other clinical parameters, it can be helpful in prediction of long-term outcomes (Yuh et al. 2012).

1.1 Motivation

Having worked as a doctor in emergency departments, I have the first hand knowledge of the plight of the patients and the stress on the doctors. It is quite common that the duty rosters allocate junior doctors for $36-48$ hours at a stretch

due to limited number of personnel available. The physical fatigue and mental duress can affect the performance of any individual and doctors are no exception. Sleep deprivation can seriously alter cognitive processes which can lead to missed diagnoses by the same doctor who would otherwise be fully capable of giving succinct analyses and report subtle findings.

Variability in assessment of medical images, however, is a complicated phenomenon and the onus can not be put on physical and/or mental exhaustion alone. The perceptual skills, deduction and knowledge of the observers and the quality of the image being studied are some common factors that often affect the assessment reports by the radiologists and lead to possible errors (Armato III et al. 2009, McCreadie & Oliver 2009, Donald & Barnard 2012). This problem has quite justifiably been termed 'Achilles heel' amongst radiologists and it has often been reported that significantly sized abnormalities can be missed by radiologists resulting in false negative or vice versa (Quekel et al. 1999, Robinson 1997).

An ideal solution to this problem would be to have enough personnel in every hospital and emergency units so that every patient's case can be examined by more than one radiologists concurrently and a consensus would guide the treatment plan. Errors in interpretation of medical images can also be minimized by complementing the image with clinical findings to give a clue to the observer about possible features to look for (Robinson 1997, McCreadie & Oliver 2009). However, the financial costs involved in recruiting personnel limits the implementation of this utopian idea.

Computer based analyses of the neuroimages is an active area of research which can help the radiologists and neurologists ascertain the extent and progress of the lesions by giving the valuable second opinion (Krestin et al. 2012). The applicability of computer aided diagnosis (CAD) in assisting the radiologists has been extensively studied with plausible results and the potential of using CAD in mainstream radiology is quite encouraging (Jiang et al. 2001, Roos et al. 2010,

Freedman & Osicka 2006, Balleyguier et al. 2005, Shiraishi et al. 2011). Computer aided quantitative radiology and volumetry studies have been undertaken by many researchers proposing methods inspired from image processing and machine learning domains (Shi & He 2010, Kondo & Ueno 2012).

Processing medical images to increase contrast on the screen and creating a better definition of anatomy is one of several possibilities that CAD can offer to the doctors. Similarly, segmentation of image regions provides a pertinent representation highlighting relevant information for the observer and making delineation and measurements easier and more accurate. A surfeit of image processing and segmentation methods have been formulated over time handling both generic and specific requirements set by the problem domain (Vantaram & Saber 2012). However, suitability of the methods is still mostly governed by the characteristics of the application sphere and there is still no '*silver bullet*' method to satisfy all constraints and requirements.

Machine learning and artificial intelligence algorithms devised in the last few decades have demonstrated notable applicability in almost every problem domain including medicine (Shiraishi et al. 2011). These techniques mimic the working of neurons in brain and exploit their property of activation and inhibition to generate a decision. These architectures can be designed to adaptively learn while being supervised or unsupervised based on the availability of training data and optimize the relationship between inputs and outputs (Kononenko 2001). The tenable integration of such methods in CAD is a significant indicator of the achievable performance that they offer and numerous methods have been proposed in literature which can be applied for analyses of medical image (Jiang et al. 2010, Shi & He 2010, Kondo & Ueno 2012).

With availability of such technological advancements, it seems resourcefully feasible to integrate CAD into the clinical environment and address the imminent need to reduce the errors and omissions made by human observers (van Ginneken et al.

2011). However, it is imperative that the integration of such system in clinical setting be seamless and should not engage the doctors in manually setting the parameters or demarcating the probable pathology or trauma. The output from an efficient and robust CAD can presumably be used as proxy for a second human observer and support the decision making process of the radiologist. The final deciding authority still lies with the radiologist and the deployment of CAD should not be inferred as a total replacement of the deductive skills of humans.

1.2 Aim and Objectives

The aim of this research is to develop a computer aided traumatic brain injury assessment and classification system which will enable the physicians and (neuro)radiologists to efficiently interpret the neuroimages and establish diagnoses and prognoses with more precision.

This research identifies the following objectives:

1. Assessment of the existing methods and techniques for segmentation of anatomical regions and examining their strengths and weaknesses within the context of TBI cases.

2. Development of a framework for aumatically segmenting anatomical structures and estimating their measurements on noncontrast CT images with maximum approximation of the experts' intuition. Further, correlate these measurements to clinical models and frameworks to estimate ratios and indices of the brain.

3. Investigation of using the clinical and neurological assessments of patients as features to identify probable pathology or trauma and then development of a method to classify these features.

4. Development of a method to extract relevant intensity based and statistical features for classification from the medical images by adjusting the contrast levels based on suspected pathology or trauma.

5. Development of a method for automatic seeding of initial curves in active contours using votes from salient clinical profile data and image features.

6. Development of a modified active contour based level set segmentation method which is regularized by constraints from imaging and clinical features.

7. Development of an automated classification system for neurologists and radiologists for rating TBI cases and establishing prognoses in these patients.

1.3 Scope and Limitations of the Research

The methods to be developed are limited to noncontrast CT scans of the patients acquired at the time of admission to the emergency departments or trauma clinics. It is often a question that MRI can provide better resolution and segmentation results then why is CT preferred. The proposed research is for reducing the inter-observer variability in the emergency departments and CT is the modality of choice to study both the skull bone as well as the soft intracranial structures within early hours of trauma. MRI takes longer scanning time, does not provide good visualization of bones and can not be performed on patients who may have metal implants or intubated.

Similarly, contrast enhanced radiography requires assessment of renal functions of the patient to ensure that the contrast medium will not have any adverse effects. The processing time for these renal function tests can cause delay of the imaging procedure and patients' condition can deteriorate during this time. Therefore, the methods have been evaluated only on initial, noncontrast enhanced CT studies.

The research uses cross-sectional CT studies on patients of both genders and all age groups. The objective is to delineate the relevant anatomical structures and provide their measurements. The research does not compare the preoperative and postoperative images from the same patient and, hence, no longitudinal data are used in experiments.

The research does not assess the accuracy or significance of the established trauma classification models or rating systems being used in clinical settings. This work is only limited to the segmentation of pertinent structures which can be used by radiologists to more precisely use the established classification models and rating systems.

1.4 Contribution

- The Pattern Driven, Content Aware Active Contours (PDCAAC) framework is developed to be used in a clinical environment and assist the radiologist by giving various segmentations and estimations of measurements as second opinion in TBI cases. This framework can considerably reduce the radiologists' workload and also the inter-observer variability.

- Modified Active Contour algorithm for segmentation of brain CT scans is the main component of the PDCAAC in which the features from clinical profile of the patient and CT image data are used for segmentation of desired ROI. This approach of integrating clinical and neurological assessments into processing of medical images following the principle of polyrepresentation is a novel contribution.

- The automatic seeding of the initial curve in active contour method using the votes from clinical phenotype and CT image data features is a novel contribution. This approach circumvents the manual fixing of initial seed by the users in existing state of the art methods.

- The proposed regularization of evolution of the active contour using energies from pixel classification through ANN, location vote and distance constraint is a salient contribution. This approach minimizes the problems of creeping of active contour into surrounding regions or undersegmentation.

- The PDCAAC framework can be used for intracranial measurements in routine clinical practice for assessment of neuropsychiatric disorders, geriatric problems, drug induced changes and other structural disorders and pathologies. There is no automated system available to segment the brain CT scans and estimate the various brain indices and ratios which makes this work a novel contribution.

- Semi-automated classification of brain CT in TBI patients according to Marshall CT Scheme is achieved. Using the PDCAAC Framework, the salient CT features are classified according to the established CT rating schemes and prognosis models which can guide the doctors to adopt more target therapeutic regimen for TBI patients.

1.5 List of Publications

Following is a list of peer-reviewed research articles that have either been published or accepted for publication to date, and which have contributed to the work in this thesis.

1.5.1 Publications in Conferences

1. Qureshi, A. N. & Schetinin, V. (2013). Helping clinicians to read brain scans. Poster presented at *University of Bedfordshire Research Conference 2013*, Bedfordshire, UK.

The contribution included introducing the concept, reviewing related work, designing the experiments and presenting results.

2. Qureshi, A. N. & Schetinin, V. (2014). Computer-aided segmentation and estimation of indices in brain CT scans. *Medical Image Understanding and Analysis 2014*, City University London, 161-166.
   The contribution included introducing the concept and highlighting clinical importance, reviewing related work, designing the experiments and presenting results.

3. Soltaninejad, M., Lambrou, T., Qureshi, A., Allinson, N. & Ye, X. (2014). A hybrid method for haemorrhage segmentation in trauma brain CT. *Medical Image Understanding and Analysis 2014*, City University London, 99-104.
   My contribution included highlighting clinical importance, reviewing literature related to active contours and preparation of CT image data for experiments.

4. Qureshi, A. N. (2014). Segmentation and estimation of indices in brain CT scans using neural networks and level sets. *Advances in Computer Vision 2014*, KOC University, Turkey.

5. Qureshi, A. N. (2014). A framework for segmentation and estimation of intracranial measurements in CT scans. *7th Cairo International Biomedical Engineering Conference (CIBEC 2014) sponsored by the IEEE-EMBS*, Egypt, 129-132.

6. Qureshi, A. N. (2014). A hybrid approach for estimation of volume of haematomas in brain CT scans. *2014 International Conference on Artificial Intelligence*, Barcelona, Spain.

7. Qureshi, A. N. (2014). Segmentation and estimation of indices in brain CT scans using neural networks and level sets. *IEEE Symposium Series on Computational Intelligence (IEEE SSCI 2014)*, Florida, USA.

8. Qureshi, A. N. (2014). A framework for semi-automated classification of CT scans in traumatic brain injury patients. *Second International Conference on Advances in Computing, Communication and Information Technology - CCIT 2014*, Birmingham, UK.

9. Qureshi, A. N. (2014). Iterative Segmentation Algorithm for Segmentation of Traumatic Brain Injury CT Scans. *International Conference on Artificial Intelligence and Pattern Recognition (AIPR2014)*, Malaysia.

1.5.2 Publications in Journals

1. Maple, C., Prakash, E., Huang, W., & Qureshi, A. N. (2014). Taxonomy of optimisation techniques and applications. *International Journal of Computer Applications in Technology*, 49(3), 251-262.
   My contribution included introducing the concept, reviewing related work, proposing the taxonomy of optimisation techniques and highlighting research contributions from University of Bedfordshire.

2. Qureshi, A. N. (2014). Estimation of volume of haematomas in CT scans using level sets and artificial neural networks. *International Journal of Artificial Intelligence & Applications*, 1 - 8.

1.6 Thesis Organization

The overall significance of medical imaging in assessment and management of traumatic brain injury patients is presented in Chapter 2. The description of imaging modalities used in hospitals, process of the scanning procedure and acquisition of images and key assessments performed by the radiologists are discussed with special emphasis on traumatic brain injury cases. An overview of the classification and rating schemes used in emergency department to establish

the diagnosis and prognosis of patients from CT images is also presented. This chapter entails the systematic processes used by radiologists to assess clinical and neurological findings and interpret brain CT scans. This knowledge lays the foundations of a robust and efficient CAD system which can approximate the experts' intuition in demarcating the regions of interest.

Chapter 3 presents a literature review of the state of the art techniques being used in computer-aided diagnosis systems to determine their strengths and weaknesses in segmentation of brain CT scans. This does not cover every possible technique and the discussion concentrates only on salient image segmentation methods and machine learning algorithms which are relevant to this thesis and are likely to be useful in achieving the objectives.

The Pattern Driven, Content Aware Active Contours (PDAAC) framework is presented in Chapter 4 which is the main tool for achieving the research aim. A systematic description of the proposed method in assessment of CT scans in traumatic brain injury patients is presented which can provide 'second opinion' to the radiologists and reduce inter-observer and intra-observer variability.

The PDAAC framework is implemented by applying the concept of spatially guided segmentation using geometric active contours. The discussion in Chapter 5 includes integration of clinical and neurological assessment of the patients and their use in predicting the suspected abnormality. The extraction and selection of features from the CT image and the conceptual and design details of the modified active contour method are also presented which elaborate the steps taken to achieve the objectives of this research.

Chapter 6 presents the results of experiments implementing the proposed method on noncontrast CT studies. The comparative analyses of the performance of the proposed method and state of the art approaches are also presented and discussed. The chapter includes discussion of applying the proposed framework for segmentation and estimation of measurements of clinically relevant ROI. Different

evaluation measures to statistically signify performance of the proposed method in approximating experts' intuition are also presented.

The thesis is concluded in Chapter 7 which presents an overview of the problem domain as well as discussion of how the identified problems have been addressed in this research. The transferability of the proposed method to other imaging modalities and anatomical structures as well as further work which can stem out of this research are also presented.

Chapter 2

Analysis of Medical Images

The fact that your patient gets well does not prove that your diagnosis was correct.

Samuel J. Meltzer

2.1 Medical Diagnosis

Medical diagnosis is a complex cognitive task. It requires both logical reasoning and pattern matching by the doctor while assessing the patient. A pathology or trauma can be represented in patients' expression called symptoms, through signs elicited by the doctor and through invasive and non-invasive laboratory procedures. The underlying principle is to correlate these representation and find the common, most evident 'cognitive overlap' which identifies the pertinent diagnosis based on a developed clinical model. Experienced clinicians group the findings into meaningful clusters based on the representations, called differential diagnosis, and refine it further by incorporating new information as it becomes available. This addition of new information leads to adjustment of relative likelihood of the ailments, ruling out of certain possibilities and consequently, establishment of the final diagnosis (Richardson et al. 2008).

While the patient is presenting the symptoms to the doctor, there is a possibility that the actual state and severity which is being experienced by him is not conveyed due to lack of words which can express or portray the most elusive picture and context. This loss of information is called 'cognitive freefall' and in order to bridge the gap between what is felt and what is causing it, multiple evidences are required. The process of establishing diagnosis can then be considered analogous to the concept of 'ploy representation', also known as multi-evidence, in the domain of information retrieval (Ingwersen 1996, Larsen et al. 2006). The concept entails that multiple representations of an information object make the evidence stronger. The representations could be coming from distinct cognitive actors (cognitively different) or from same actor but for distinct purpose (functionally different) (Larsen et al. 2006). The hypothesis covers a broad perspective and, hence, the actor could be any entity like a human being, a machine, or an algorithm. In medical context, representation of the patients' complaints (symptoms), signs (elicited by the doctor), lab findings and diagnosis models can give useful insight to the establishment of provisional and differential diagnoses. In certain cases, the established models of diseases have additional use to classify the patients into groups and/or decide the therapeutic or surgical interventions which could be required.

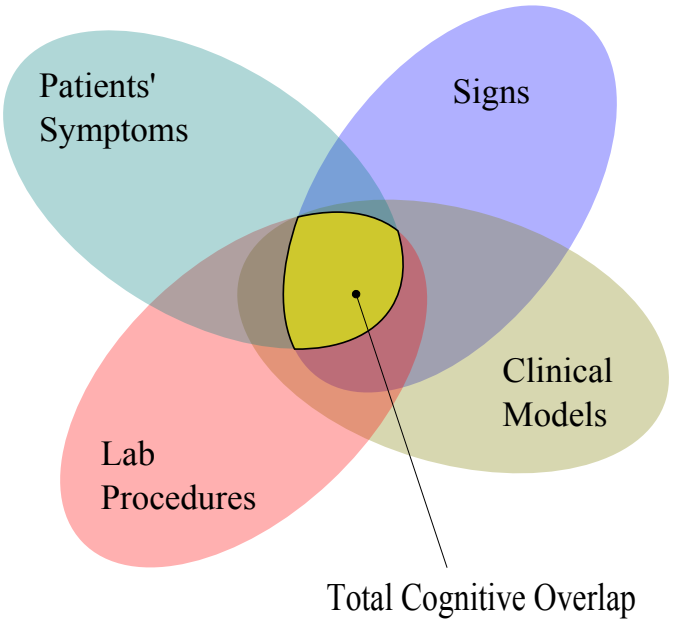

FIGURE 2.1: Principle of Polyrepresentation in context of Medical Diagnosis. The area labelled Total Cognitive Overlap' represents the diagnostic features of a pathology common amongst the different representation. This area signifies the diagnosis.

In context of clinical methods, a pathology (or trauma) can be represented by the patient (symptoms), the doctor (signs and clinical assessment) and invasive and non-invasive laboratory procedures. Hence, all constitute an evidence regarding the patient's condition and underlying ailment. The availability of such cognitively and functionally different evidence pointing to the common ailment constitute the cognitive overlap which could possibly help to diagnoses and plan treatment. A weak overlap suggests provisional diagnoses which is further refined as more findings and information are added, thus, maximizing the certainty of inference towards a more apposite final diagnosis as depicted in Fig. 2.1 and labelled 'Total Cognitive Overlap'.

2.2 Medical Diagnostic Imaging

Laboratory procedures are a key component in establishing the diagnosis by the doctor. Invasive procedures involve any surgical or exploratory activity in which

the body is pierced by a device, instrument, or by manual digitation. While these methods have their accepted significance, non-invasive procedures tend to be more patient friendly requiring very little or no piercing of the body whilst allowing the observer to get the information sought. An important field of non-invasive investigation is medical imaging which presents the information about a specific physiological structure, *in-situ*, in the form of an image as shown in Fig. 2.2. It can be defined as technique, process and art of creating visual representations of the internal structures of the human body for clinical assessment.

Medical imaging relies on the predefined characteristic properties of biological tissue being imaged (Wolbarst & Cook 1999). An energy source is used to obtain information about the object placed between it and the image capturing medium which then displays the penetration and absorption in the form of an image. In some modalities, radiation such as optical light, X-ray, gamma-ray, RF or acoustic waves, are focused to pass through the object tissue or organ to provide information about its characteristic property. For example, in X-Ray and CT, the tissue density make certain structures appear lighter than others. The lighter structures have higher radio-density, absorb more radiation and are also called hyperdense. The darker structures allow more radiation to pass through and , hence, appear lighter or hypodense. In Magnetic Resonance Imaging (MRI) imaging, the water content and local magnetic properties of a particular area of the body are measured when placed in a strong magnetic field. Tissues with more water content appear dark (T1 MRI) while tissues with relatively less water appear lighter. In nuclear medicine, Positron Emission Tomography (PET) measure the gamma-ray emission from the body injected with radioactive material while single photon emission computed tomography (SPECT) uses gamma-rays and is able to provide true 3D information. Ultrasonography works by using reflected echoes of high frequency sound waves from different internal organs. The enhancement of ultrasonography on the principle of Doppler effect allows the doctor to assess real-time movements of organs within the body or flow of blood in vessels (Wolbarst & Cook 1999).

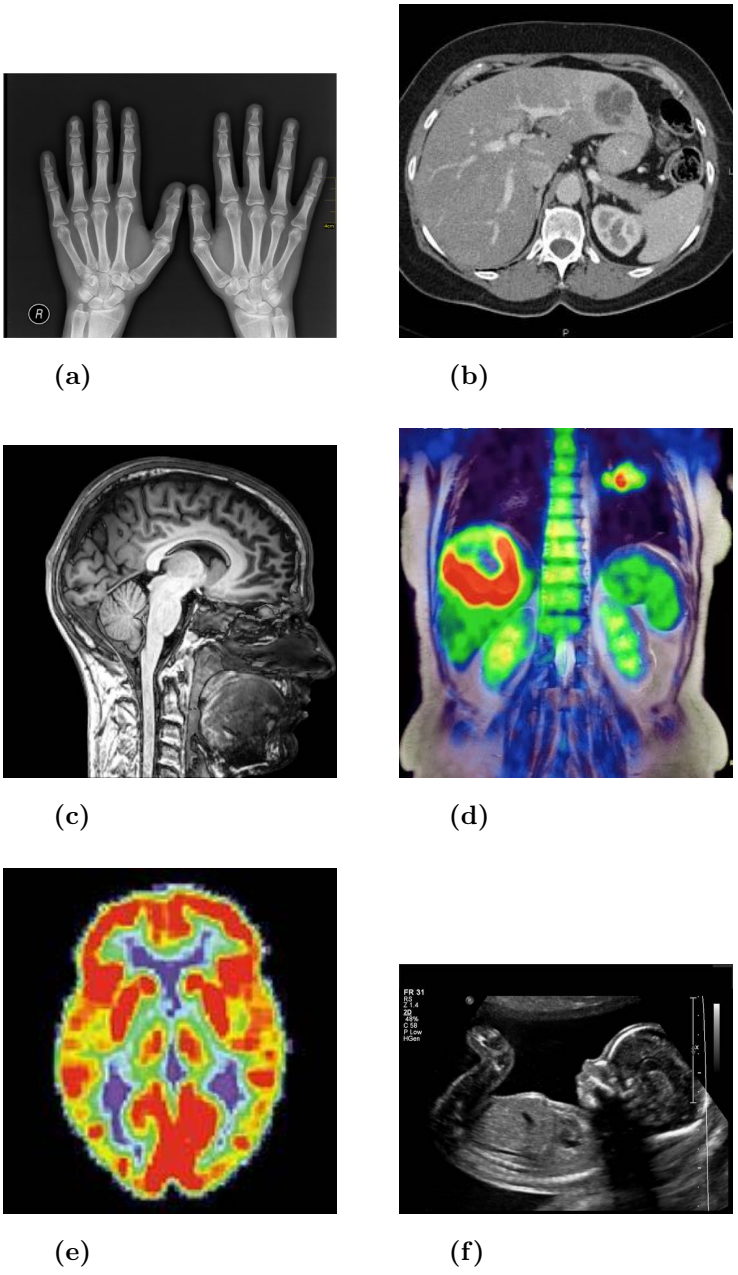

(a) **(b)**

(c) **(d)**

(e) **(f)**

FIGURE 2.2: Different Modalites used in Medical Imaging. Image (a) is the X-Ray of hands, (b) is a CT of abdomen showing viscera. Image (c) is an MRI of the head and neck. Images (d) and (e) are the PET scan of abdomen and SPECT of brain respectively. Image (f) is the ultrasound of a human baby in mother's womb. (Radiopaedia.org 2014)

2.2.1 CT Scans and Brain Protocol

Computed tomography (CT or CAT scan) is one of the noninvasive diagnostic modalities using a combination of X-rays and computer based reconstruction to

produce horizontal, or axial, images (often called slices) of the object or interest. The radiation is generated by an external ionized source and the beam of radiation is transmitted through human body and recorded on the other end by the scintillator. Absorption or attenuation to X-ray radiation beam is represented by different shades (levels) of gray to provide information about variations in the tissue density. The information can be visualized in 2D in X-ray scans or 3D in the CT images (Dhawan 2011, Wolbarst & Cook 1999).

In simple X-ray scans, the beam of energy is aimed at the body part being studied and a film plate or digital sensor behind the body part captures the variations of the energy beam after it passes through skin, bone, muscle, and other tissue. A standard X-ray does provide substantial and clinically pertinent information, however, a lot of spatial detail about internal organs and viscera is not obtained because body part touching the film behaves different than the part facing the x-ray tube. Hence, the doctor should suggest Antero-Posterior (AP) or Postero-Anterior (PA) while requesting the scan.

In computed tomography, the X-ray beam source circles around the body (Fig. 2.3). The patient lies on a bed that slowly moves through the gantry during the procedure. The x-ray tube rotates around the patient, emitting narrow beams of x-rays through the body. This produces multiple images from different viewpoints of the same organ or structure. The X-ray information is captured by a scintillator and sent to a computer that reconstructs the views captured during 360° rotations into slices using inverse Radon transformation and displays it in a two-dimensional (2D) form on a monitor. One 360° rotation is used to produce one slice so the scanner's bed moves according to the protocol being used when multiple slices are required as depicted in Fig. 2.4. The scout x-ray guides the technician about setting the boundaries of areas to be scanned. The slice thickness determines the spatial resolution in the $z - axis$ and is usually set in millimetres (Wolbarst & Cook 1999).

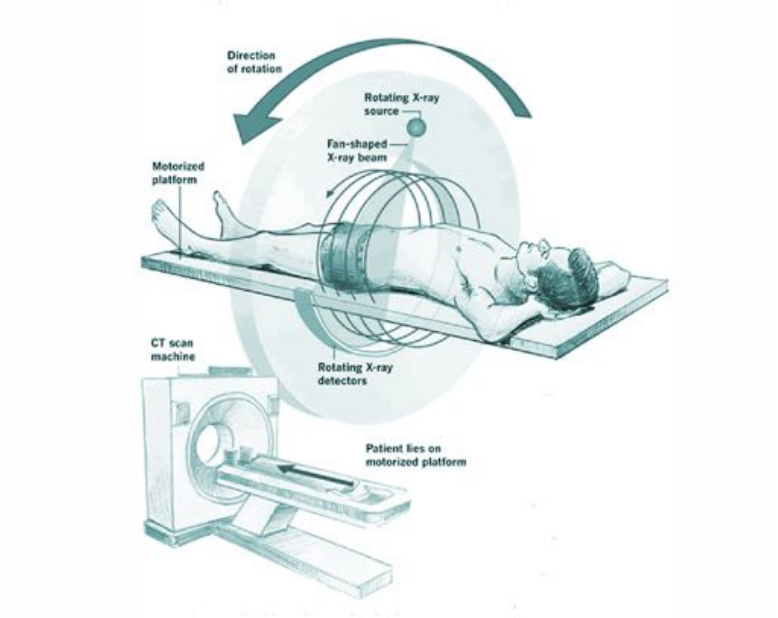

FIGURE 2.3: Structure of a CT Scanner (Cyberphysics.co.uk 2014)

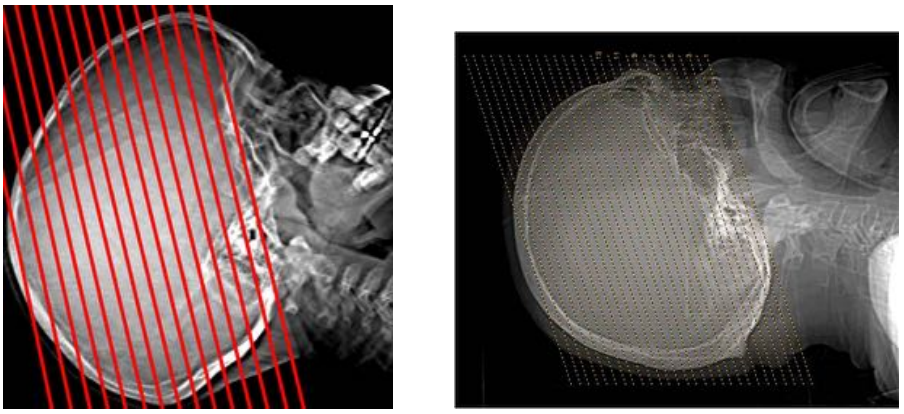

(a) **(b)**

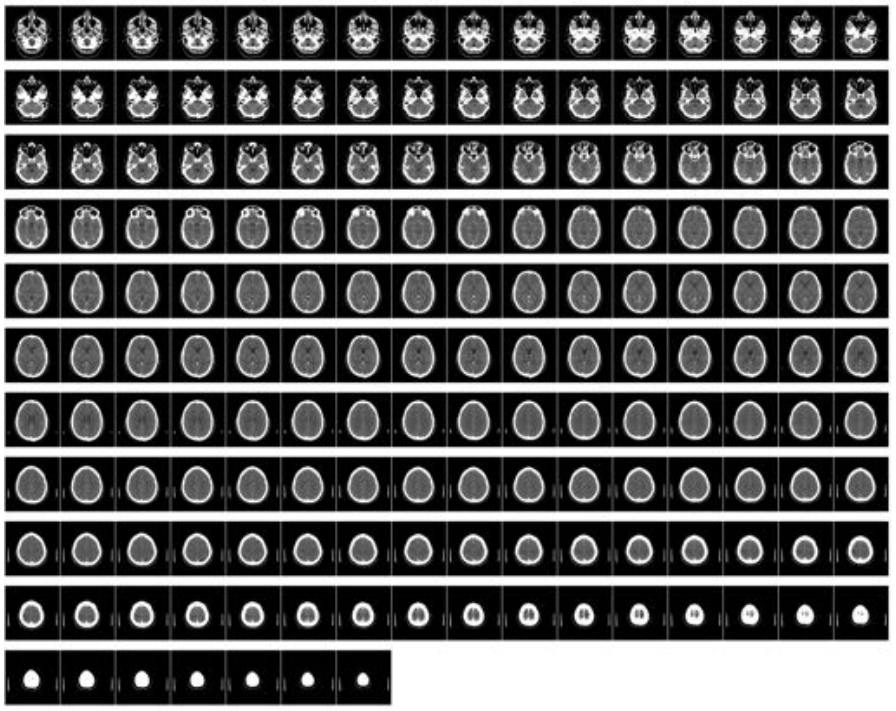

(c)

FIGURE 2.4: Typical CT scan procedure for brain. Images (a) and (b) represent the X-Ray scout images of the head that is to be scanned. The scout serves as a guide for the technologist indicating where to start and stop scanning (University of Virginia 2014, University of Wisconsin 2014). Image (c) is the typical CT study of brain performed for assessment.

The protocol of CT scanning describes all the device settings and parameters to be used during the scan and determines data collection, patient positioning and contrast administration. The quality and dose of CT is predetermined based on the prescribed protocol appropriate to the specified diagnostic task. There is no

'best' protocol for use in all cases and most diagnostic centres set up their own protocols (Wolbarst & Cook 1999). An example of protocols adopted for CT scans used in this thesis are listed in Appendix E. All CT images are acquired in the axial/transverse plane, like slicing a loaf of bread, as shown in Fig. 2.4 and individual slices, as given in Fig. 2.5, are examined by the doctors.

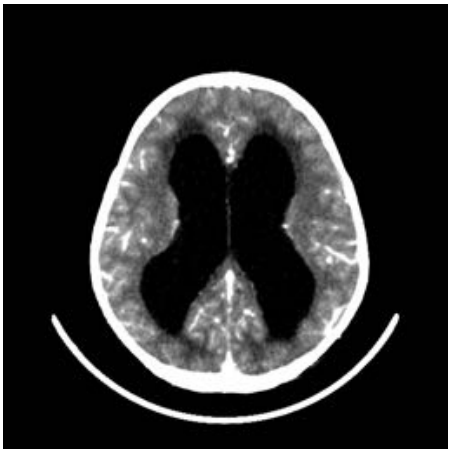

(a) Hydrocephalus

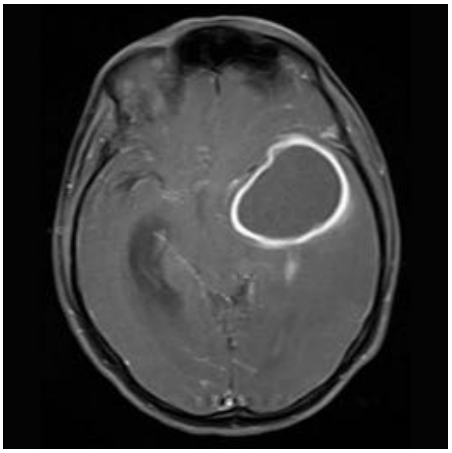

(b) Abscess

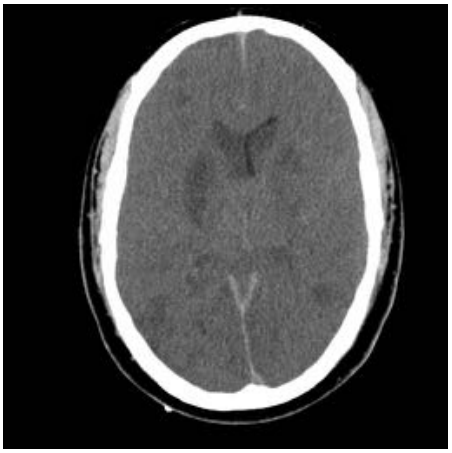

(c) Oedema

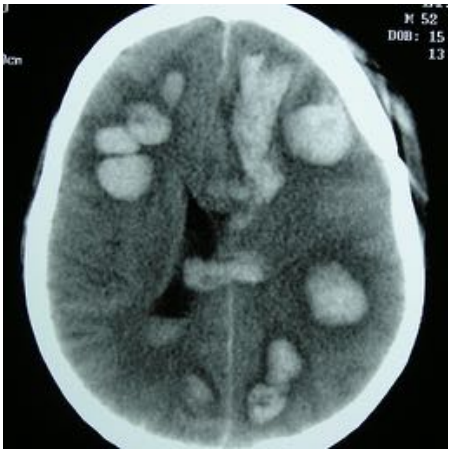

(d) Diffuse Axonal Injury

FIGURE 2.5: Cases seen on Brain CT

2.2.2 Head CT in Emergency Cases

Although the spatial resolution of MRI is far superior than that of the CT, there are certain advantages that make the CT first choice amongst doctors in the emergence departments. For instance, CT scan procedure takes less time than MRI, making

it the study of choice in cases of trauma and other acute neurological emergencies. The motion artefacts due to patients' movement are better handled by CT due to the shorter scanning time. Claustrophobic patients may not feel comfortable inside the MRI machine and also the very obese patients can be a problem. The presentation of bones is much detailed on a CT as is the detection of calcifications and metal foreign bodies. Most importantly, CT can be performed at no risk to the patient with metal implants, such as cardiac pacemakers, ferromagnetic vascular clips, nerve stimulators and can also be performed on the bed side or on patient on life-support systems. Also CT scanning has a widespread availability and costs less than MRI (Davis 2007, Wolbarst & Cook 1999).

2.2.3 Noncontrast CT in Emergency Cases

Contrast media are usually injected prior to x-ray or CT procedures to enhance specific tissues under investigation (Norton et al. 1978). Contrast enhancement can make the visualization much better however adverse side-effects such as nausea and vomiting, anaphylaxis and renal failure pose a serious risk. Gadolinium based contrast media have been reported to produce Nephrogenic Systemic Fibrosis in some cases while iodine based contrast media have the potential to cause a condition known as Contrast Induced Nephropathy in patients with reduced kidney function (Barrett & Parfrey 2006). It is not advised to perform contrast enhanced CT before a report on the renal functions is available which can take a couple of hours to obtain. Hence, the emergency clinical approach usually requests noncontrast CT studies within early hours of admission.

2.3 Brain Trauma CT Scans

One of the serious public health problems worldwide is the Traumatic Brain Injury (TBI). According to recent statistical data, nearly 1.7 million cases are reported in

the USA and 1 million in UK every year (Patient.Co.UK 2012). While the severity of the injury can range from mild to severe, the high mortality and morbidity rates due to TBI can be attributed to the fact that the extent of injury is often difficult to be accurately reported by doctors making prognosis nearly impossible to predict (Beers et al. 2003, Saatman et al. 2008, Robinson 1997). Management of TBI cases essentially involves suggesting neuroimaging and noncontrast CT scans are the first choice amongst doctors over other modalities (X-Ray, MRI, PET, SPECT etc.) due to widespread availability and the less time taken to perform the scan (Davis 2007). The noncontrast CT presents the EDH as biconvex, lenticular shaped hyperdense area while the SDH appears crescent shaped hyperdense areas inside the skull in TBI as shown in Fig. 2.6.

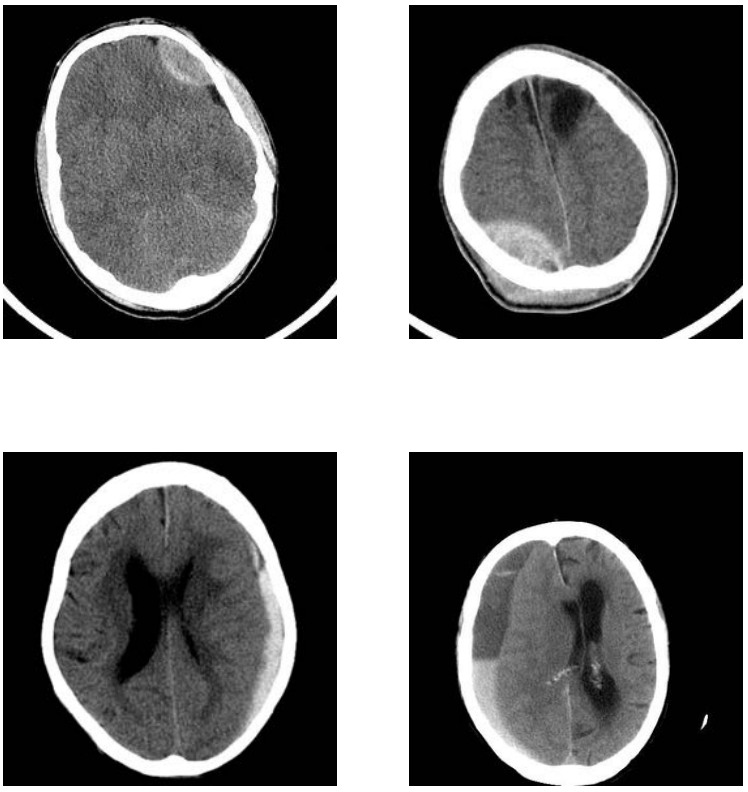

FIGURE 2.6: Intracranial haematomas, as seen on noncontrast brain CT scans. Images in top row show the lenticular presentation of EDH. Images in the bottom row present the crescent shaped SDH.

The emergency clinical approach includes neurophysiological examination and assessment of the severity of the trauma using established scales like Injury Severity Score (ISS), Glasgow Coma Scale (GCS) and JFK Coma Recovery Scale etc. combined with CT classification schemes such as Marshall and Rotterdam to help establish diagnosis, prognosis, mortality, morbidity and hospitalization time after trauma (Pohlman & BjerkeHS 2007, d'Anesthésie et de Réanimation) 2012, Patient.Co.UK 2012).

2.3.1 Prognosis from TBI CT

The importance of medical imaging as one of the biomarkers for diagnosis and prognosis of traumatic brain injuries is well established (Li, Li, Feng & Pan 2010). Neuroimaging is not indicated in all patients with head trauma due to the time and costs involved and many criteria have been developed to assess the indication (Lee & Newberg 2005, IG et al. 2005). These criteria are not completely foolproof and even in the absence of neurological and clinical signs and symptoms, neuroimages can be useful especially within the first 24 hours after injury (Baraff et al. 2010). While assessment of extremely small intracranial damage might not be possible with the CT, coarse findings like *Blood, Cisterns, Brain, Ventricles* and *Bone* can provide valuable and vital information for timely management (Perron 2008). The calculated volume of haemorrhage and GCS score are strongly correlated to mortality at 1 month (Broderick et al. 1993). An early and accurate assessment of prognosis is critical for deciding methods of treatment and outcomes e.g., GOS classifies patients into 8 categories as shown in Table 2.1 which are more sensitive to change in mild to moderate TBI (Lingsma et al. 2010, Vespa 2014). Only about one third of doctors confidently give accurate assessment which impacts the management and outcomes of patients (Perel et al. 2007).

TABLE 2.1: Glasgow Outcome Scale - Extended Nell et al. (2000)

Score	**Description**	**Label**
1	Death	D
2	Vegetative State	VS
3	Lower Severe Disability	SD-
4	Upper Severe Disability	SD+
5	Lower Moderate Disability	MD-
6	Upper Moderate Disability	MD+
7	Lower Good Recovery	GR-
8	Upper Good Recovery	GR+

Initial brain CT assessment of patients with suspected injury or trauma is a systematic approach. The radiologist has to visually locate and then measure the sizes of abnormal findings which are manifested by the injury. The reporting commonly focuses on:

- Left-right symmetry along midline
- Location of anatomical structures and bleeds
- Size estimations of normal and abnormal structures
- Ventricular blood
- Hydrocephalus

Assessment of the severity of trauma by consulting CT classification schemes such as one proposed by Marshall et al. (Table 2.2) is then performed to help establish

diagnosis, prognosis, mortality, morbidity and hospitalization time after trauma (Marshall et al. 1991).

TABLE 2.2: Marshall et al. CT Rating. Descriptive categories of abnormalities seen on CT scans (Marshall et al. 1991)

Rating	**Level**	**Description**
I	Diffuse injury I	No visible intracranial pathological changes seen
II	Diffuse injury II	Cisterns are present with midline shift $0-5mm$ and/or lesion densities present
III	Diffuse injury III	Cisterns compressed or absent with midline shift $0-5mm$, no high or mixed density lesion $> 25cm^3$
IV	Diffuse injury IV	Midline shift $> 5mm$, no high or mixed density lesion $> 25cm^3$
V	Evacuated mass lesion	Any lesion surgically evacuated
VI	Non-evacuated mass	High or mixed density lesion $> 25cm^3$, not surgically evacuated

The patient usually arrives at the hospital intubated and sedated and the initial CT scan is the key clinical feature for immediate surgical intervention or for invasive ICP monitoring. In acute neuroimaging, the three key slices succinctly observed are the brainstem, basal ganglia and level of lateral ventricles as shown in Fig. 2.7 for inspecting normal sizes and positions of ventricles and visibility of the sulci along with grey-white matter distinction (Smirniotopoulos 2012, Haacke et al. 2010).

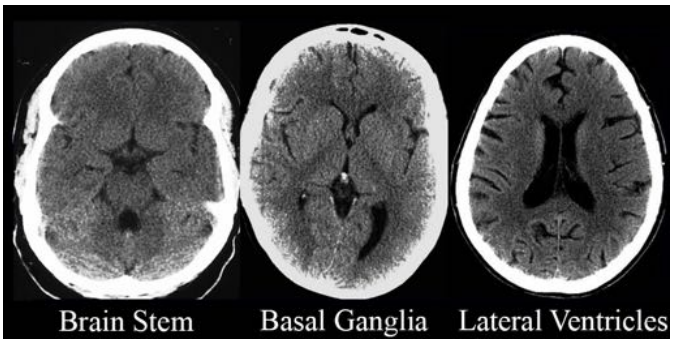

(a)

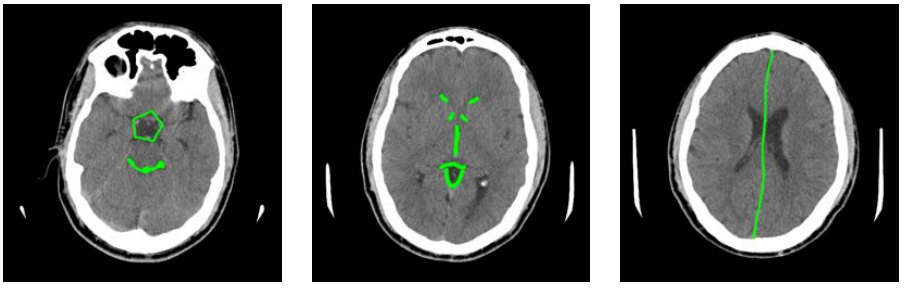

(b) **(c)** **(d)**

FIGURE 2.7: Three Slice Method for Acute Neuroimaging Assessment (Smirniotopoulos 2012). In image (a) left slice is examined for suprasellar cistern and fourth ventricle, the middle slice shows two frontal horns, third ventricle and quadrigeminal cistern and the slice on right presents lateral ventricles and the brain midline. Images (b), (c) and (d) are manually annotated by expert.

The accuracy of establishing clinical picture, when a TBI is suspected, within early hours of trauma can help improve patient outcomes through timely management and appropriate referral. The initial noncontrast CT carries significant prognostic value and combined with other clinical parameters, can be helpful in prediction of long-term outcomes (Yuh et al. 2012).

Prognostic models developed on clinical data of patients can be a useful aide in deciding therapeutic interventions (Murray et al. 1993). One of the systems for head injury prognosis, CRASH, has been modelled after one of the largest clinical trials using variables such as country of origin, age, GCS, pupil reaction, extra-cranial injury and information from CT scans (Perel et al. 2007). The CT scans are assessed for presence of petechial haemorrhages, obliteration of the third ventricle or basal cisterns, subarachnoid bleeding, midline shift and non-evacuated

haematoma. The model is an effort to predict death at 14 days and for death or severe disability six months after traumatic brain injury.

Maas et al. have added several CT features to the Marshall classification system in order to improve the outcome prediction (Maas et al. 2005). The original Marshall system classifies patients into six groups (figure 2.8) based on morphological abnormalities seen on the CT scans.

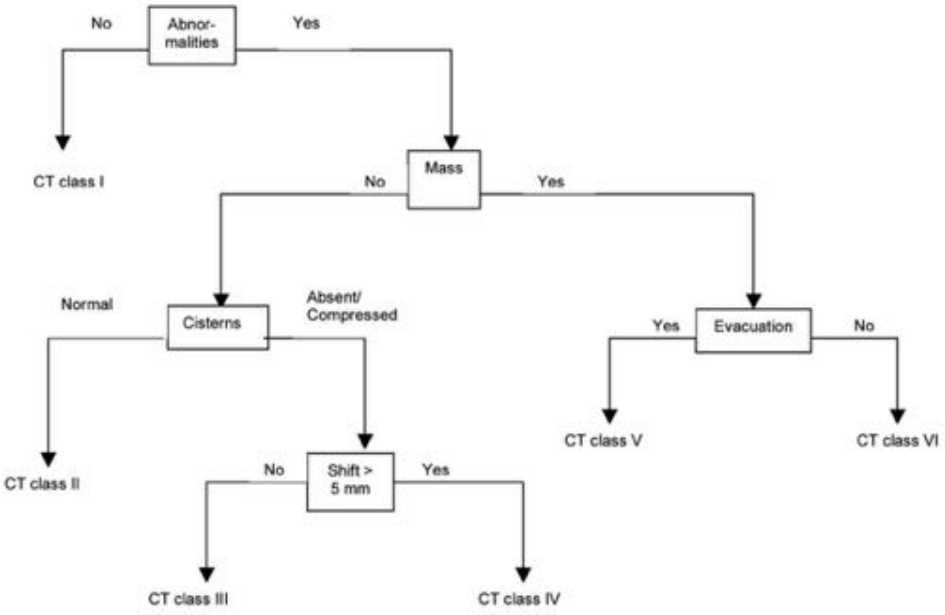

FIGURE 2.8: Marshall Classification of CT (Marshall et al. 1991)

The approach adopted by Maas et al. suggests midline shift, basal cisterns, intraventricular blood and traumatic subarachnoid haemorrhage as significant predictors of mortality and improved results are obtained by partitioning the prediction tree (Fig. 2.9) on the appearance of basal cisterns and midline shift.

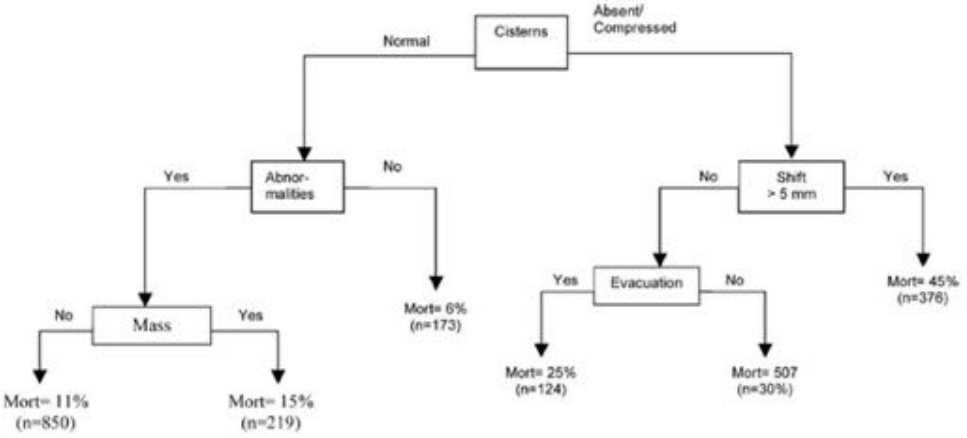

FIGURE 2.9: Maas et al. modified Marshall Classification with mortality (Maas et al. 2005)

TABLE 2.3: Scoring scheme for Rotterdam CT Classification (Maas et al. 2005)

Factor	**Score**
Basal Cisterns	
Normal	0
Compressed	1
Absent	2
Midline Shift:	
None or $\leq 5mm$ 0	
$> 5mm$	1
Epidural mass lesion:	
Present	0
Absent	1
Intraventricular blood or tSAH	
Absent	0
Present	1
Sum score	+1

TABLE 2.4: Rotterdam Outcome Scale correlating score from Table 2.3 to the probability of mortality at 6 months (Maas et al. 2005).

Score	**Mortality at 6 months**
1	0%
2	7%
3	16%
4	26%
5	53%
6	61%

Several other models have been proposed to establish prognosis of patients with traumatic brain injuries incorporating different anatomical and physiological scales (Schreiber et al. 2002, Signorini et al. 1999, Maas et al. 2005, Lesko et al. 2010, Timmons et al. 2011). However, most of the studies do not include pre-injury characteristics and further research is needed to ascertain relationships between CT findings and prediction of outcomes by including more common factors such as age and gender (MTBI 2004, Ragan et al. 2009, Chrastina et al. 2013). The existing classification systems like Marshall and Rotterdam (Table 2.3 and 2.4) do not differentiate between haemorrhage volume which is a strong marker of injury severity (Chieregato et al. 2005, Maas et al. 2005). The calculated volume of haemorrhage and GCS score are strongly correlated to mortality at 1 month (Broderick et al. 1993). The probability in correlation to these is given in table 2.5. Hence, it will be useful to conduct retrospective analyses of CT scans from brain trauma patients and research the application of this factor into clinical practice.

TABLE 2.5: GCS, volume of haemorrhage and probability of mortality at 1 month after injury (Broderick et al. 1993).

Clinical findings	**Mortality at 1 month**
GCS < 9, volume > 90ml	90%
GCS ≥ 9, volume < 30ml	17%

2.4 Brain Ratios and Indices

Quantitative assessment of neuro-images to report structural abnormalities is an effective approach to reveal structural changes in conditions such as Alzheimer's disease (AD), Schizophrenia, Huntington's disease, hydrocephalus and many other neurological and psychiatric disorders (Gyldensted & Kosteljanetz 1976, Wilk et al. 2011, Zhang et al. 2008, González-Reimers & Santolaria-Fernández 2011, Barker-Collo et al. 2012). Linear measurements of anatomical landmarks in brain (Fig. 2.10) are routinely performed to give indices and ratios (Keats & Sistrom 2001) which are clinically significant and comparison with control populations can be done to assess the condition.

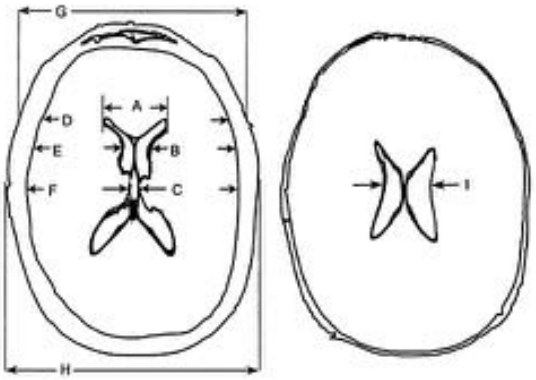

(a)

FIGURE 2.10: Measurements performed by doctors on Axial CT Scans (Keats & Sistrom 2001)

TABLE 2.6: Measurements on the axial CT scans (Keats & Sistrom 2001). Labels correspond to Fig. 2.10.

Label	Description
A	maximum frontal horn diameter
B	minimum width of the lateral ventricles at the heads of the caudate nuclei
C	maximum width of the 3rd ventricle
D	inner skull diameter at the level of the frontal horns
E	inner skull diameter at the level of the caudate nuclei
F	maximum inner skull diameter
G	outer skull diameter at the frontal horns
H	maximum outer skull diameter
I	minimum width of the lateral ventricles separated by the septum (cella media)

TABLE 2.7: Indices and Ratios estimated on the axial CT scans (Keats & Sistrom 2001)

Indices	Calculation
Evan's Ratio (ER)	A/F
Bifrontal Index (BFI)	A/D
Bicaudate Index (BCI)	B/E
Cella Media Index (CMI)	H/I
Frontal Horn Index (FHI)	G/A
Ventricular index (VI)	B/A
Huckman number (HN)	A+B
3rd ventricle width (V3)	C

Doctors typically perform measurements on the axial CT scans as shown in Fig. 2.10 and their descriptions are given in table 2.6. The brain indices and ratios calculated from these measurements are given in table 2.7. Wilk et al. (2011) have identified reference values for indices of intercerebral spaces showing that these normative values change in a non-uniform manner with age. Zhang et al. (2008) have shown that AD cases show cortical atrophy, widening of the ventricles and significant loss of brain mass . Atrophy of the hippocampal formation by using temporal horn volume and temporal horn index has been studied by Giesel et al. and shown to be significant marker of AD (Giesel et al. 2006). CT indices of raised intracranial pressure in mild and severe traumatic brain injuries ascertains the relevance of these in assessing injury severity (Barker-Collo et al. 2012). The comparison of these indices in normal cases and patients can help neuroradiologists, clinicians and researchers establish correlations between measurements and extent of the disease process or trauma (González-Reimers & Santolaria-Fernández 2011, Ragan et al. 2009). The significance of estimation of brain indices is well established, however,

to our knowledge, there is no automated system for performing measurements and calculation of these from CT scans.

2.5 Inter- and Intra-Observer Variability

The accuracy of establishing clinical picture, when a TBI is suspected, within early hours of trauma can help improve patient outcomes through timely management and appropriate referral. The initial noncontrast CT carries significant prognostic value and combined with other clinical parameters, can be helpful in prediction of long-term outcomes for the patient (Yuh et al. 2012).

The process of interpreting the medical images, however, is not foolproof and the practitioners with less developed skills can often overlook the significant findings leading to misdiagnosis. Postmortem studies show that up to 20% of fatal illness can be misdiagnosed (Leonhardt 2006). This poses a question that whether junior doctors, who are less adept, should be in the emergency departments or not. A study conducted to investigate performance of junior doctors in accident and emergency (A&E) to diagnose significant x-ray reported that only 32% of junior doctors correctly diagnosed the illness. The average performance of the senior doctors was 80% (McLauchlan et al. 1997). A study by Brandt et al. on blind interpretation of paediatric CT reported that a radiologist with 12 years experience had an accuracy of 75% when reporting significant abnormalities while a junior radiologist with only 3 years experience, had accuracy of 48% when compared with a consultant radiologist (Brandt et al. 2007). Interpretation of cranial CT by emergence specialists also showed misinterpretation in 14.8% cases out of which 41.1% were of potential or acute consequences (Arendts et al. 2003). Conditions requiring immediate assessment and management can not be postponed until the more experienced staff is available and interestingly, most traumas happen on the weekend when only the junior staff is there (Saposnik et al. 2007). A radiologist studying and reporting more than 20 CT cases per day can make twice

the errors which can be avoided with 'second opinion' augmented with the findings during clinical assessment of the patient (McCreadie & Oliver 2009, Robinson 1997). Errors in interpretation of medical images do not necessarily stipulate incompetence because multiple factors such as perceptual errors, lack of experience and quality of the image being assessed (Lev et al. 1999).

2.5.1 Manual Annotation of Medical Images

Manual measurements of regions of interest by expert radiologists are still considered 'gold standard' (Giesel et al. 2006). Figure 2.11 shows labelling of a brain MRI scans and Fig. 2.12 presents demarcation of haematomas in CT of TBI cases by radiology experts which become the training set for automatic segmentation algorithms. However, assessment of neuroimages is fraught with variability and can lead to misdiagnosis and poor outcomes and it is imperative to address the discrepancies to prevent any grave consequences (Lev et al. 1999).

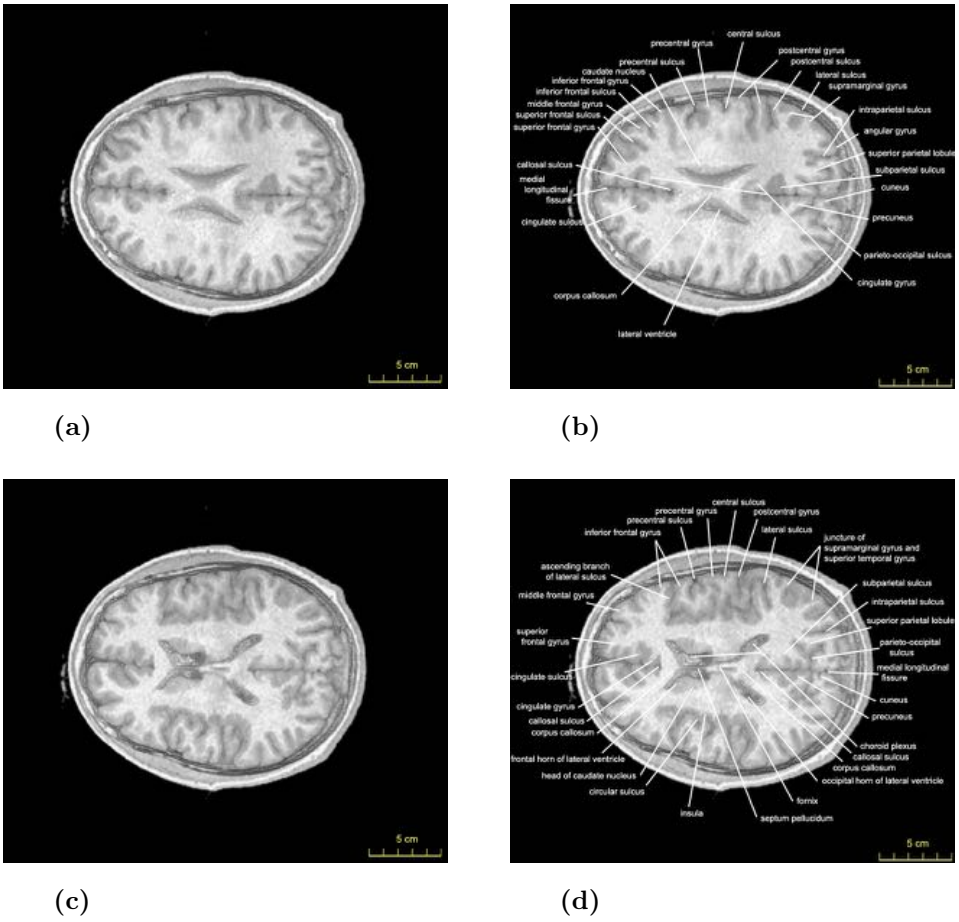

FIGURE 2.11: Labelled Brain MRI Slices described as reference for radiologists (Michigan State University 2014).

In the field of diagnostic medical imaging, accuracy of interpretation by the radiologists plays a vital role. The assessment and extent of the pathology (or trauma) is an important factor for ascertaining the prognosis and medical intervention required. Depending upon the perceptual skills, deduction and knowledge of the observers, the interpretation results are fraught with variability and this problem is considered 'Achilles heel' amongst radiologists (Robinson 1997). It has been observed that lesions of up to 16mm size can be missed by radiologists (Quekel et al. 1999) resulting in false negative or vice versa. Difficulty in distinguishing lacunar infarcts and enlarged Virchow-Robin spaces is another common reason for ambiguity. The disagreement between observers can be as high as 20% and this results in up to 75% errors in cancer diagnosis and up to 40% of

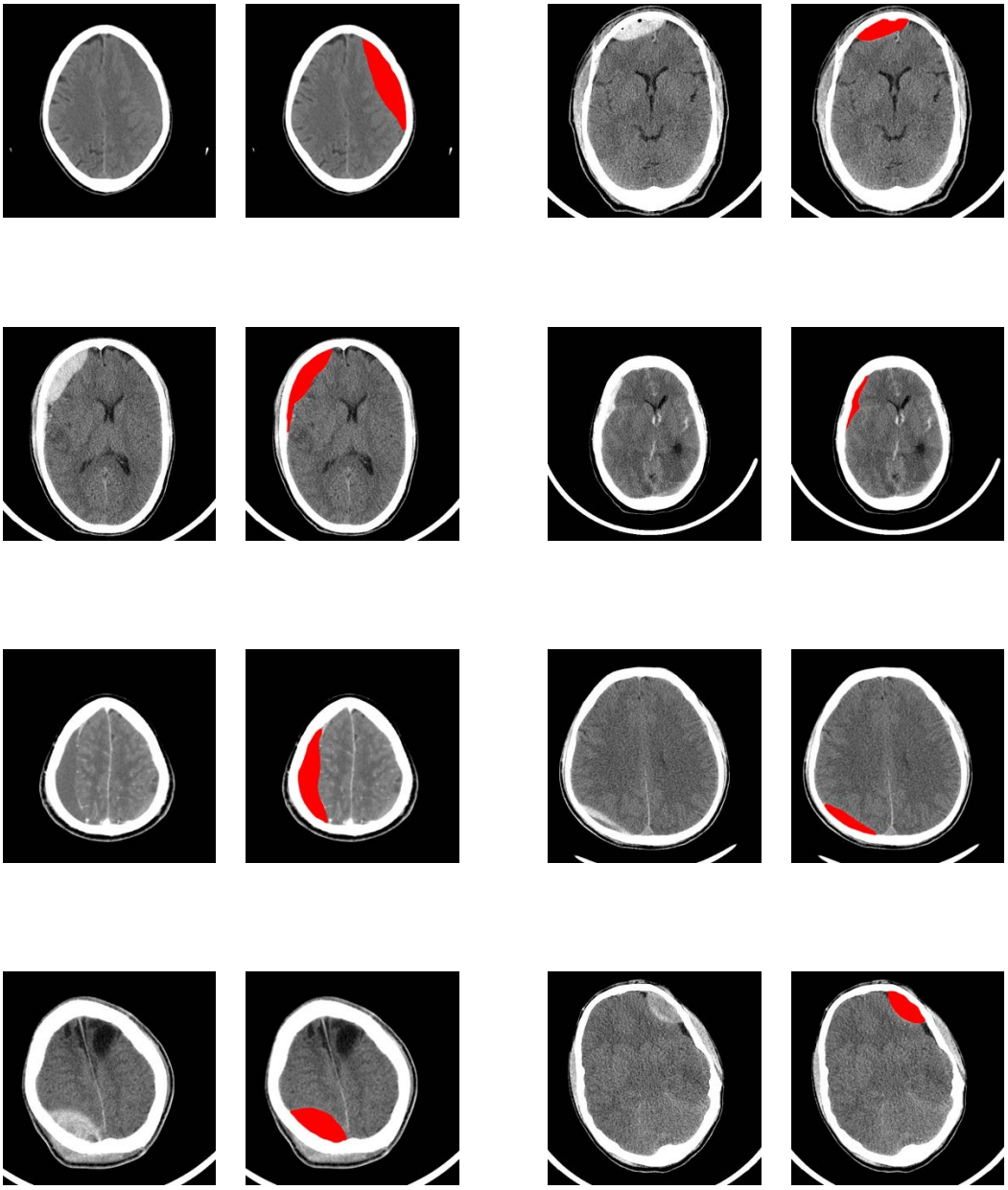

FIGURE 2.12: Manual annotation of ROI by radiology experts. Images in first and third columns are the brain CT scans from TBI patients. Images in the second and fourth columns show the respective haematomas highlighted by the experts.

deaths caused by missed diagnosis (Lev et al. 1999, Fitzgerald 2001, Stevens et al. 2008, Fisher 2000). Other studies have also identified observer variability due to poor image interpretation and perceptual errors (McCreadie & Oliver 2009, Donald & Barnard 2012, Arendts et al. 2003, Levin & Rao 2004, Brandt et al. 2007).

2.5.2 Perception and Contrast

The acuity of human vision is strongly affected by the contrast of the scene being looked at. It has been observed that the sensitivity of human vision is more towards contrast rather than absolute luminance (Chaudhuri 2011) and the contrast threshold required to perceive the scene properly is a function of the spatial frequency of the detail in the scene (Campbell & Robson 1968). The contrast sensitivity, which is reciprocal of the contrast threshold, reaches maximum at 20 years age and then gradually reduces (Richards 1977, Sia et al. 2012, Hashemi et al. 2012). At this age it is most sensitive to 2-5 cycles per degree and decreases at both sides (Campbell & Robson 1968). Contrast sensitivity is a measure of the ability to discern between luminance of different levels in a static image. Another characteristic of human vision is the simultaneous contrast in which colours (shades) of two regions can affect the perceived contrast as shown in Fig. 2.13. The central grey bar in Fig. 2.13a and the grey square in Fig. 2.13b have same uniform intensity, however, they appear different depending upon the influence of the their neighbourhood.

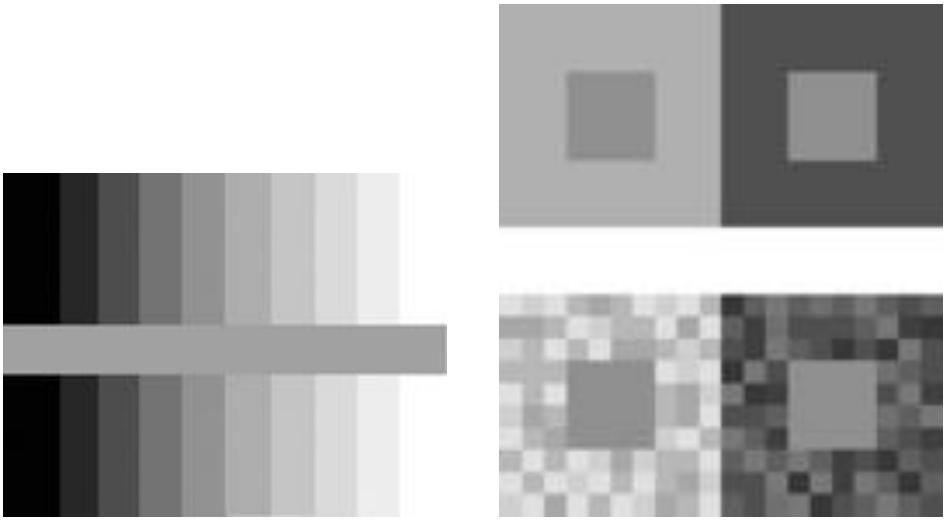

(a) **(b)**

FIGURE 2.13: Simultaneous Contrast. The grey horizontal bar in the centre of image (a) has same intensity level throughout. However, it appears lighter to darker due to the shade surrounding it from left to right. Image (b) shows same phenomenon with the solid grey square within different neighbourhoods.

2.5.3 Inattentional Blindness

Psychological lack of attention while performing a task can result in missing obvious information and this is known as inattentional blindness. This phenomenon is not associated with any defects or deficits in the vision of the observer. If people are engaged in a different cognitive task, they often miss the presence of an unexpected yet visibly salient feature. Demonstrations of inattentional blindness have typically involved naive observers engaged in an unfamiliar task, however, experts who have spent years in visually detecting small abnormalities in specific types of images, can also fall prey to this psychological phenomenon. In a study, 24 radiologists were asked to perform a familiar lung-nodule detection task on thoracic CT. Image of a gorilla (Fig. 2.14), larger than the average size of a nodule, was intentionally inserted in the last case that was presented. Interestingly, 20 out of the 24 radiologists participating in the study did not notice the gorilla. Eye tracking of the experts while they were observing the CT showed that the majority of observers did look

directly at the location of the inserted gorilla but still missed to point it out (Drew et al. 2013).

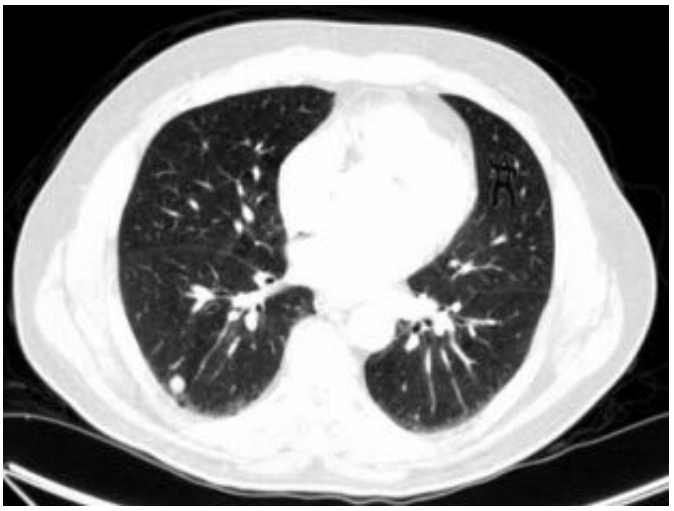

(a)

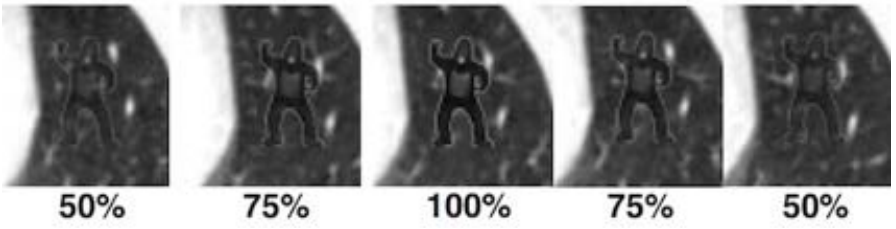

(b)

FIGURE 2.14: The Invisible Gorilla. Image of a gorilla, 48 times the size of the average nodule, was inserted in the lung CT as shown in (a). Different opacity levels were applied to the gorilla with respect to the original CT as shown in (b). The gorilla was missed by 80% of the radiologists (Drew et al. 2013).

2.5.4 Effect of Ambient Light

The perception of the observer can be affected by the ambient light in the diagnostic room and is degraded by increased room illumination for detecting low contrast features (Brennan et al. 2007, Chawla & Samei 2007, Pollard et al. 2008, Rill et al. 1999, Kimme-Smith et al. 1997). The lighting conditions in hospitals sometimes are not adequate for viewing medical images and can result in diagnostic inaccuracies (Blackshaw et al. 2003). It is seen that human vision is affected both by the contrast

of the image as well as the ambient light levels. Hence, it can be construed that the interpretation of medical images by the experts and novice is also affected by these two factors. Adjustment of contrast in CT scans can improve perception, however, instead of global, it will give better results if contrast of distinct structures is adjusted independent of others.

2.6 Patients' Clinical and Imaging Profile

2.6.1 Pre-injury Profile

Factors such as age, gender, genetics (APOE), psychosocial factors, education, recurrent head trauma and substance abuse etc. have also been studied and researchers have established their correlation to outcomes (Evans et al. 1992, Hukkelhoven et al. 2005, Maas et al. 2005). The factors noted in past medical history and previous neuroimaging studies can be useful in alerting the clinician about potential predisposition to haemorrhages. For example, based on the factors given in table 2.8, patients can be classified into intracerebral haemorrhages risk-groups (Qureshi et al. 2001).

TABLE 2.8: Clinical findings which may hint towards incidence of intracerebral haemorrhages (Qureshi et al. 2001).

Clinical Feature
Diastolic $> 95mmHg$
Systolic $> 160mmHg$
Cholesterol $< 160mg/dl$
Alcohol and tobacco use
$\epsilon 2$ and $\epsilon 4$ alleles of APOE gene
Amyloid angiopathy
Repeating haemorrhage within 1hr and 20hrs
Oedema usually persists for 5 days (up to 2 weeks)
Cerebral ischaemia due to mechanical compression

2.6.2 Post-injury Profile

The clinical and neurological assessment of the patient at the time of admission provides information such as gender, age, cause of injury, neurological assessment, vital signs and presenting symptoms (McCluskey 1990, Shah & Kelly 2003) as listed in Table 2.9. The features are assessed by the doctor and findings are reported for further management.

The brain CT characteristics play an important role in establishing the diagnosis and provide valuable information to the doctors. Fig. 2.15 depicts CT scans of two cases highlighting the typical presentation of haematomas as hyperdense regions and infarctions as hypodense regions.

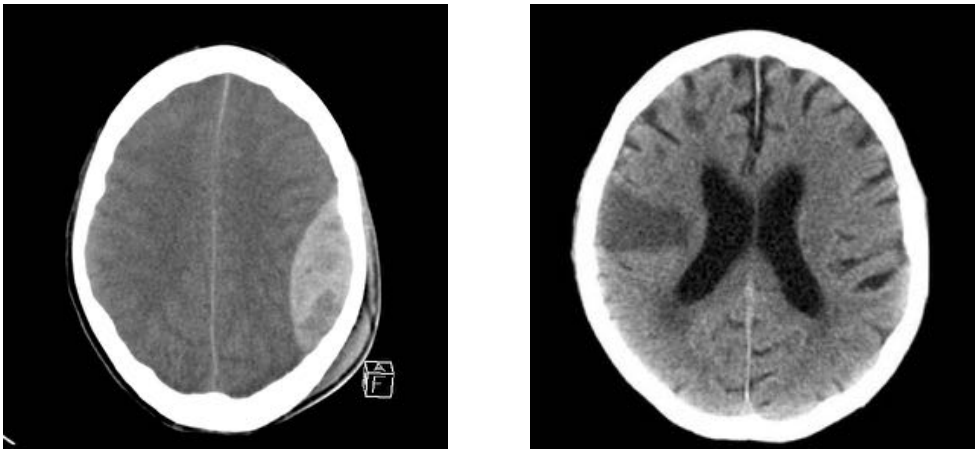

(a) **(b)**

FIGURE 2.15: Brain CT image findings. Image (a) is the typical hyperdense presentation of a haematoma on CT. Image (b) is a case of ischaemic infarction presented as a hypodense region.

Subdural haematomas (SDH) appear from shearing of the dural veins often due to blunt trauma. They are observed in all age groups but aetiology may vary and most patients (65-80%) present with conscious state severely depressed. Repeated traumas are often the cause and sub-acute SDH are presented with active and old bleeds. Extradural or epidural haematomas (EDH) are mostly observed with younger patients who have sustained head injury (sports of accident) and present ongoing and severe headache as an important symptom. The might be no loss of consciousness at the time of injury, however, later after injury gradual loss of consciousness is observed. In case of transient loss of consciousness at the time of injury, these patient exhibit what is know as 'lucid period' after which their condition deteriorates quickly.

2.6.3 Imaging Profile and Spatial Localization

Haematomas as seen in Fig. 2.6 are spatially bound by the skull on one side. Subdural haematomas (SDH) often result due to blunt trauma and the shearing of the dural veins. They present the familiar concave or crescent shape, 85% are

TABLE 2.9: Clinical Profile of patient at time of admission (McCluskey 1990, Shah & Kelly 2003).

Feature	**Findings**
Gender	Male
	Female
Age	Years
Cause of injury	Unknown
	Road traffic accident
	Fall
	Assault
Loss of consciousness	Yes/No
Vomit	None
	number of episodes
ENT Bleed	Yes/No
Fits	Yes/No
Dizziness	Yes/No
Headache	Yes/No
Weakness	None
	Left
	Right
	Generalized
Slurred speech	Yes/No
Hypertension	Yes/No
GCS at admission	Value
Pupil response	Normal reactivity
	Left Fixed normal size
	Left Fixed dilated
	Right Fixed normal size
	Right Fixed dilated
	Bilateral fixed dilated
Temperature	Value
Pulse rate	Value
Respiratory rate	Value
Blood pressure	Systolic Value
	Diastolic Value

usually unilateral and may cross suture lines but are limited by dural reflections, such as the falx cerebri, tentorium, and falx cerebelli. Common sites for subdural hematomas are fronto-parietal convexities and the middle cranial fossa. The appearance of SDHs on CT varies with clot age and organization.

Epidural hematomas (EDH) most often do not cross suture lines because the dura mater is tightly adherent to the calvarium at these locations and restricts extension of the haematoma and appear unilateral in more than 95% of cases (Qureshi et al. 2001). The source of bleeding is typically from a torn meningeal artery and EDH classically presents a biconvex or lenticular disc shape, usually with an associated fracture of the skull.

- $90-95\%$ EDH are supratentorial
  - temporoparietal - 60%
  - frontal - 20%
  - parieto-occipital - 20%
- $5-10\%$ EDH are located infratentorially in posterior fossa

Subarachnoid haemorrhages (SAH) present as star shaped hyperdensitites within cisterns. The hypertensive interparenchymal haemorrhages (IPH) are observed in basal ganglia (50%), thalamus (15%) or pons (10-15%) in cases. Signs and symptoms observed in relation to size and location of haemorrhage are given in table 2.10.

TABLE 2.10: Size and location of haemorrhages and clinical presentation (Qureshi et al. 2001).

Size and location	**Clinical presentation**
Large size	LOC, ↑ ICP, pressure and compression effect on thalamic and brain stem reticular activating system
Small size	↓ Central Benzodiazepine receptor binding, in small deep lesions.
Supratentorial	Putamen, caudate and thalamus affected → contra-lateral sensory motor deficit due to internal capsule involvement.
Infratentorial	Abnormalities of gaze, cranial nerve abnormalities, contra-lateral motor deficit.
Cerebellum	Ataxia, nystagmus, dysmetria.
Diaschisis	Aphasia, neglect, gaze deviation, hemianopia.

2.7 Prognosis Model

The information gathered from the clinical and imaging profile of the patient is used by the doctors to ascertain the diagnosis, plan treatment and most importantly, establish the prognosis. Prediction of prognosis is a clinically critical task for the doctors, patients and carers of the patients. Steyerberg et al. (2008) have attempted to develop prognostic models based on these data to predict the outcome for the patient at the time of admission to the hospital. The authors performed analysis of prospectively collected data of more than 8,500 patients with severe or moderate TBI and presented a model with a strong discriminative ability and area under curve (AUC) of 0.80 through external validation.

Steyerberg et al. (2008) have suggested a scoring chart based on the clinical and image characteristics which is given in Table 2.11 representing the extended model. The image characteristics include Marshall et al. Classifications I - VI as well as features such as presence or absence of EDH, tSAH, hypoxia and hypotension. A logistic regression model is then proposed by Steyerberg et al. (2008) using linear predictors (LP) calculated from the score. The coefficients of mortality with reference to the respective clinical or imaging factors are given in Table 2.12. The probabilities of mortality and 6 months outcome are calculated using $1/(1+e^{LP})$ and the values of LP are estimated as Equation 2.1 and Equation 2.2 respectively. The Fig. 2.16 depicts the probabilities with reference to the extended model score.

$$LP_{extended} = -2.98 + 0.256 \times (\text{sum score core} + \text{subscore CT}) \tag{2.1}$$

$$LP_{extended} = -2.10 + 0.276 \times (\text{sum score core} + \text{subscore CT}) \tag{2.2}$$

TABLE 2.11: Score chart for outcome at 6 months after TBI (Steyerberg et al. 2008).

Attribute	**Score**
Age:	
$\leq$ 30 years	0
30 - 39	1
40-49	2
50-59	3
60-69	4
70+	5
Motor score:	
None / Extension	6
Abnormal flexion	4
Normal flexion	2
Localizes / obeys	0
Untestable / missing	3
Pupil reactivity:	
Both reactive	0
One reactive	2
None reactive	4
Marshall CT Class:	
I	-2
II	0
III or IV	2
V or VI	2
tSAH: Yes	2
No	0
EDH:	
Yes	-2
No	0
Hypoxia:	
Yes or suspected	1
No	0
Hypotension:	
Yes or suspected	2
No	0

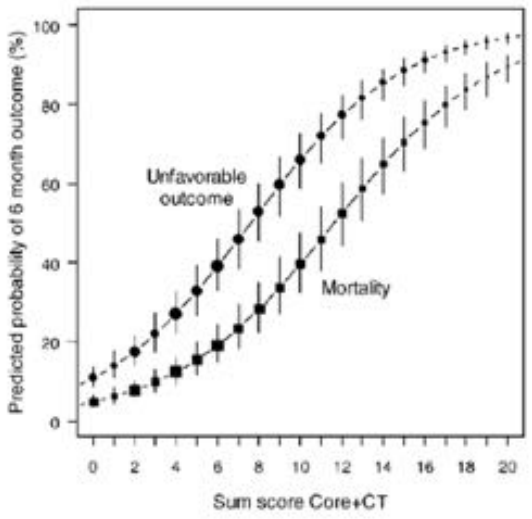

FIGURE 2.16: Probability of Mortality or Unfavourable Outcomes (Steyerberg et al. 2008)

TABLE 2.12: Prognosis Model based on Clinical and Imaging Profile of the Patient (Steyerberg et al. 2008).

Factor	**Coefficient for Mortality**
Intercept	-3.787
Age	0.032
Pupil reactivity:	
One reactive	0.334
None reactive	0.970
Marshall CT Class:	
I	-0.298
III or IV	0.774
V or VI	0.651
tSAH	0.606
EDH	-0.379
Hypoxia: yes or suspected	0.237
Hypotension: yes or suspected	0.667

2.8 Summary

Medical image analysis and understanding has been recognized as one of the hallmarks of clinical practice since the invention of X-Rays. The requirement of

medical imaging is indicated in all pathological and traumatic cases where the anatomical structures and viscera are not directly visible to the naked eye and their assessment in a non-invasive manner is required. While the research in developing and enhancing instruments and machines for scanning the body is advancing, the CT scan holds its value as the first choice amongst emergency radiologists due to low cost of scanning, widespread availability, ability to discern hard and soft tissue in the same image and less susceptibility to motion artefacts. Also it can be carried out on patients who are intubated due to trauma and the noncontrast CT requires no special preparations. There are quite a few established models of classification of CT scans of such patients available to be followed in clinical environments. These guide the radiologists to identify distinct image features and correlate these to the patients' outcome.

However, the inter-observer and intra-observer variability is frequently observed in emergency assessment of cranial CT scans which can affect the diagnosis, management and prognosis of the patient. Factors such as physical and mental fatigue, less experience, perception and judgemental errors and quality of the image can mislead a radiologist to ascertain the diagnosis. Even a minor head injury can sometimes prove fatal and, hence, it becomes imperative to give second opinion in such TBI cases to minimize possibilities of misdiagnosis to improve the treatment and management of the patient and subsequently, his quality of life.

Chapter 3

State of the Art

Let the future tell the truth and evaluate each one according to his work and accomplishments. The present is theirs, the future, for which I really worked, is mine.

Nikola Tesla

In the field of diagnostic medical imaging, timing and accuracy of interpretation by the radiologists plays a vital role for patients' management within the 'golden hour'. The localization, assessment, measurement and extent of the pathology or trauma is an important factor for ascertaining the prognosis and accordingly deciding the intervention required. It has been observed that the initial interpretation by emergency radiologists often disagrees with that of the more experienced owing to flaws in methodology (Levin & Rao 2004, Stevens et al. 2008). McCreadie et al. have presented their findings in which 256 radiology errors were identified in 222 patients; 88% were due to poor image interpretation 3% were technical and 9% were due to poor communication, and majority of these arose during reporting of CT (McCreadie & Oliver 2009). These errors were identified in retrospect and could have possibly been avoided while the patient was being treated if a second opinion was available. An important point to realize is that clinical consequence with regards to misinterpretation of radiological investigations bear far more importance

than just the adverse patient outcome. They also affect patients' satisfaction, administrative, financial and medicolegal dimensions (Arendts et al. 2003).

3.1 Double Reporting

Owing to the vital information gained through medical imaging, the volume of scans performed has surmounted enormously. Robinson reported in 1997 that a typical study can include 60-70 images to be interpreted by the radiologist (Robinson 1997). This number, however, has tremendously increased because of the advances in technology and directly increases the workload of radiologists resulting in overlooking of the abnormalities due to interpretation errors and physical tiredness. Donald et al. have endeavoured ot find common patterns in 558 diagnostic errors and have reported that 80% were perceptual and 20% was due to poor interpretation and radiographs and CT were the more common modality in these cases (Donald & Barnard 2012). A radiologist studying and reporting more than 20 CT cases per day can make twice the errors which can be avoided with some form of double reporting (Fisher 2000, McCreadie & Oliver 2009). Lesions of up to 16mm in size can be missed which could pose serious consequences (Quekel et al. 1999). This discrepancy amongst radiologists can be life-threatening for the patient and in case of non-availability of a senior and more experienced consultant, grave consequences can be difficult to avoid. Errors in interpretation could be influenced by the observers' intuition because novice and junior doctors mostly use knowledge-based interpretations while the rules acquired through experience and skills guide the experts (Lev et al. 1999).

The problem of misinterpretation by a single doctor can be minimized by double reporting and second opinion which have been implemented at some medical centres (Arendts et al. 2003). Goddard et al. have reported that the variance of $2 - 20\%$ in clinically significant, major errors can be reduced by introducing double reporting (Goddard et al. 2001). Considering the identification of errors

when cases were studies retrospectively as reported by McCreadie et al., it can be construed that there can be significant reduction in diagnostic variability with two or more opinions if resources permit (McCreadie & Oliver 2009). However, the cost effectiveness of employing more radiologists with expert skills can be a concern for the management.

A cost effective approach in such circumstances can be double reporting and second opinion generated through computer-aided diagnosis (CAD) (Doi 2014). These systems offer opportunities of improving performance, minimizing misinterpretations and increasing speed of the diagnostic process in clinical settings (Krestin et al. 2012, van Ginneken et al. 2011). However, it is imperative that the integration of such systems in clinical environment should be seamless in order to realize the opportunities and that these systems should require minimal intervention by the users for operation. Use of CAD in radiology mainly focuses on the identification and measurement of pathological and traumatic changes detected through pertinent segmentation of the region of interest (van Ginneken et al. 2011). Review of relevant literature highlights the existing state of the art methods and approaches proposed for use in mainstream CAD and these are discussed in the next section.

3.2 Computer Aided Diagnosis (CAD)

The research and development of CAD can be historically traced back to 1960's but plausible implementation can be accredited to Kurt Rossman Laboratories, Chicago, USA (Doi 2007, van Ginneken et al. 2011). Research, since then, has come a long way and various methods and approaches have been proposed (Jiang et al. 2001, Giger et al. 2008). Fundamentally, for the assessment of medical images, the strategy of development of CAD focuses on the processes involved while images are studied by radiologists. The identifications of patterns of how they demarcate lesions, how they differentiate between benign and malignant and why they misdiagnose at times, can be the bases for development of computer

algorithms to mimic the behaviour of the experts (Doi 2007). Automatic analyses of the neuroimages is an active area of research which can help the radiologists and neurologists ascertain the extent and progress of the lesions (Krestin et al. 2012). While the recent advances have shown success in assisting the radiologists, a CAD system replacing an expert still seems like a far fetched premonition amongst medical practitioners (van Ginneken et al. 2011).

The present day medical imaging modalities yield a great deal and depth of information often surpassing the levels which can be perceived by the human eye. The high spatial resolution of images gives tenable representation of conspicuous anatomical structures but their identification and demarcation depends upon the skills of the observer. In this situation, CAD can provide an admissible visualization of the image features and support the assessment by the doctor (van Ginneken et al. 2011). The CAD, under this premise, can give a second opinion to the doctors enabling them to reconsider any subtleties that may have been overlooked in the initial observation. Robust and efficient CAD can, therefore, provide invaluable support in the medical imaging practice and reduce the inter-observer and intra-observer variability (Freedman & Osicka 2006, van Ginneken et al. 2011).

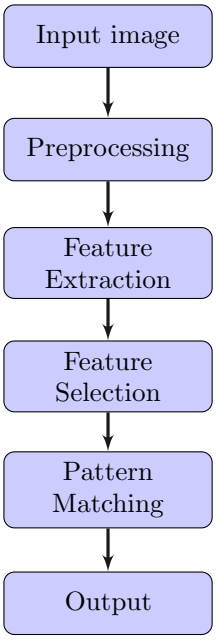

FIGURE 3.1: Typical work flow of Computer Aided Diagnosis

CAD is fundamentally based on highly complex pattern recognition and the workflow of a typical CAD application is depicted in Fig. 3.1. The image is input to the system which performs the necessary preprocessing to remove artefacts, minimize noise and adjust contrast inhomogeneities. The preprocessing could also involve adjusting the bit-depth and/or the spatial resolution to better suite the algorithm to be applied later. The next step is to extract features that form the basis of comparing and contrasting with the predefined parameters to ascertain match or exclusion. Common image features include, but are not limited to, intensity based statistical features such as mean, mode, histogram, entropy and variance etc. and more complex texture based features such as local binary patterns, Fourier transform and shape descriptors (Guyon & Elisseeff 2003, Guyon et al. 2008). The performance of CAD is highly dependent on the extraction and selection of specific features. It is observed and discussed in our experiments that same set of features may not give plausible results in all anatomical regions presented on the brain CT.

The next step is pattern matching which compares the selected features with a predetermined set to classify them into appropriate categories. Depending upon the intended use of the CAD application e.g., segmentation of a region of interest, the categories would be formed to correctly classify features that appear within the region of interest and exclude those which do not. This step differs during the training and testing phases because during training, the patterns have to be learnt and added to the set which involves learning from manual annotations, called the labelled data, provided by experts for supervised learning. During testing, the algorithm assigns classes to the extracted features according to the patterns learned earlier and demarcate the image pixels into specific regions.

The applicability of CAD in assisting the doctors has been extensively studied in many areas of medicine and surgery. A plethora of methods and algorithms have been proposed which encourage and support the potential of using CAD in mainstream radiology (Barnhill & Zhang 1998, Armato III et al. 2007, Giger

et al. 2008, Armato III et al. 2009, Bogoni et al. 2014, van Ginneken et al. 2011). The work undertaken by Jiang et al. compared the variability in deciding biopsy or follow-up with and without a computer aid in assessment of mammograms amongst 10 radiologists (Jiang et al. 2001). The CAD supported the decision by classifying whether the microcalcification lesion was due to malignancy or not and it reduced two thirds of the substantial disagreements amongst the radiologists. The performance improvement of radiologists from 53% to 69% with CAD resulting in a greater prevalence of true positives of lung nodules $\geq 3mm$ was reported by Roos et al. (2010). Freedman and Osicka have validated the premise that CAD usage can reduce both inter-observer and intra-observer variability in radiology (Freedman & Osicka 2006).

Evaluation of the impact of CAD on the ability of a junior and senior radiologist to detect breast cancers on mammograms has been conducted by Balleyguier et al. (2005) and demonstrates an increase in sensitivity from 61.9% to 84.6% for the junior doctor and from 76.9% to 84.6% for the senior. The CAD also detected three cancer cases what were missed by the junior radiologist. Another useful application of CAD using artificial neural networks is temporal subtraction in longitudinal studies, where unchanged structures are suppressed during the detection, hence, highlighting only the changes (Shiraishi et al. 2011). Computer aided quantitative radiology and volumetry studies of the anatomical structures such as liver (Suzuki et al. 2011), lungs (Bendtsen et al. 2011, Oda et al. 2010), breast lesions (Athanasiou et al. 2010), oncology (Jaffe et al. 2010) and brain (Bardera et al. 2009, Liao et al. 2010, Zaki et al. 2010, Gholipour et al. 2011, Liu et al. 2014) have been proposed by researchers. In order to appraise the applicability of CAD in radiology for segmentation and measurements of ROI, the methods of medical image segmentation utilizing image processing, machine learning and hybrid approaches are examined next.

3.3 Image Segmentation and Analysis in CAD

In development of computer aided techniques, one of the foremost requirements is the segmentation of the image based on given parameters of the region of interest (Sharma & Aggarwal 2010). The decomposition of the medical image into regions of interest then depends upon the results of segmentation. The analysis of size, location and shape etc. of a region can be plausibly performed only when identified segments closely approximate the corresponding regions of interest and normal anatomical structures. To obtain a pertinent representation of image information, segmentation is, hence, the most important step.

Most of the image processing applications designed for CAD provide tools for segmentation but their usage either requires manual interaction (called seeding) or adjustment of a long list of parameters, which may seem like a daunting task for the radiologists or doctors. When performing a task requires too many steps, the frustration of users is justified because most of the time, they discover a mistake was made earlier the process has to start all over again (Shneiderman & Plaisant 2005). Overlooking some parameters can lead to variability in results and in clinical environment, this can impede the workflow of the radiologists when different combinations of parameters can results in significantly different segmentation results. The inconsistency in algorithm's output can lead to uncertainty of the results which can no more be considered admissible as second opinion. The integration of CAD should be seamless and provide robust results in the work environment in order to persuade radiologists to use it (van Ginneken et al. 2011).

Due to the low spatial resolution and noisy images formed in CT scans, it is sometimes difficult to apply general edge detection algorithms to delineate the region of interest and get conclusive results. Medical images and specifically noncontrast brain CT scans differ from general images. The distinct locations of anatomical regions, intensity inhomogeneities, blurred region boundaries and

structural changes from trauma or pathology, hence, demand modification of the image processing techniques which would, otherwise, give satisfactory results with general images.

In recent years, a surfeit of image segmentation approaches have been proposed. Vantaram & Saber (2012) have elaborated the methods into categories based on characteristics such as image type based on colour information, whether any human interaction is involved, number of features, and spatial information. Their work is quite useful to get an overview of the existing techniques and know the fields of application being served by these methods. The authors also provide results of these algorithms on general images to present a visualization of their segmentation (Vantaram & Saber 2012).

The results from segmentation approaches vary according to the image domain where they are applied. Extraction of the foreground from the background can be based on intensity differences, texture and /or colour, however, the applicability across domains is still a challenge. Segmentation of medical images, for instance, requires refining these because the methods applicable in segmentation of objects in general can often fail to do well when applied to medical images (Bankman 2008). Based on this premise, researchers often combine approaches and techniques, which are intrinsically different, to propose hybrid approaches expecting to achieve more robust results (Chan 2007, Prakash et al. 2012, Bhadauria et al. 2013, Soltaninejad et al. 2014). This amalgamation often yields better performance by harnessing the strengths and minimising the weaknesses of multiple distinct algorithms.

3.3.1 Approaches using Image Processing

3.3.1.1 Spatially Blind Methods

Segmentation algorithms that are spatially blind, usually cluster the pixels intensities to generate regions of interest. The feature space in these algorithms is limited

to the grey-level intensity and usually no information of the location of the pixels in relation to the region of interest is taken into account (Bankman 2008). This is, however, not useful in medical images because a region of interest can have dissimilarity of pixel intensity, inhomogeneity of background contribution and noise which can result in disjoint quasi-homogeneous regions (Tao et al. 2007).

These methods rely on the global characteristics of the image ignoring the spatial information. Image features such as colour or texture are mostly used to generate well separated clusters, however, the edges and boundaries within the image are not well preserved because regions of overlapping feature spaces can merge into similar clusters. Vrooman et al. (2007) have proposed brain tissus segmentation using k-nn which can demarcate white matter, gray matter and CSF spaces in multi-spectral brain scans. This approach is supported with the formulation of a non-rigid tissue probability atlas which demarcates the white matter, gray matter and CSF spaces. The approach is robust in segmenting the normal structures of the brain, however, the performance on TBI cases is not discussed.

The approach proposed by Lauric & Frisken (2007) examines Bayesian classification, Fuzzy c-Means and Expectation Maximization to segment skull, brain matter and CSF spaces. It is observed that successive executions of clustering analysis can get different results due to these overlaps as shown in Fig. 3.2 which is Bayesian classification. As it has been discussed earlier, these methods can segment relatively fixed anatomical structures and do not produce plausible results with pathological or trauma cases. Hu et al. (2006) propose segmentation of the brain CT using Fuzzy C-means, however, their approach does not segment abnormal regions and only segments gray and white matter in two cases. Venu & Anuradha (2013) propose Fuzzy C-maens with spatial information for medical image segmentation.

In histogram matching, the image is divided into foreground and background based on bimodal (or multimodal) histograms. It is a simple method but gives less acceptable results in noisy images. Chawla et al. (2009) have proposed a

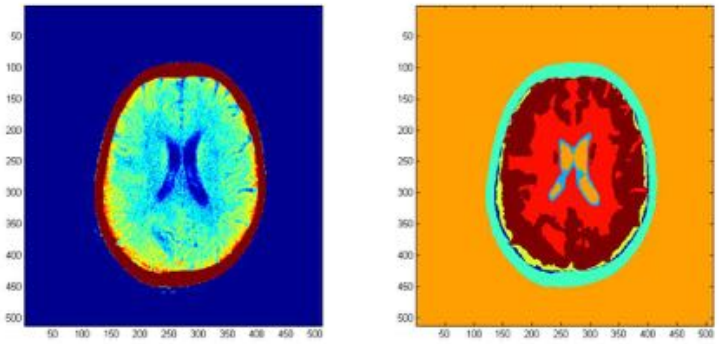

FIGURE 3.2: Spatially blind segmentation using Bayesian clustering. The clusters identified represent air, skull, grey and white matter and the CSF spaces. However, the results on the same input image vary in successive executions of the algorithm due to centres identified in clustering analysis.

method which compares histograms of the two hemispheres of the brain to detect haemorrhagic strokes. The method, evaluated on a dataset of 15 patients, classifies them into normal or stroke cases and further classification into acute or chronic strokes is achieved through wavelet decomposition and comparing the energy distribution of the histograms. Chawla et al. (2009) further propose that spatial information and heuristics can be incorporated into the method to improve the results. Their approach is useful to classify the images, however, it does not segment the images to demarcate the ROI which is required for the assessment of haematomas in TBI cases. In the methods proposed by Chan et al. (2009), the image is segmented either with or without using a reference histogram. The local histograms of different regions show similarities based on Wasserstein distances which can be used to group them into partitions for segmentation.

The method proposed by Zhang et al. (2013), adaptive thresholding and case based reasoning is used to detect intracranial haemorrhagic strokes in brain CT. They propose adaptive thresholding based on local contrast which is represented by local intensity standard deviation within the images. Using windows of varying sizes, adaptive thresholding generates binarized images. Segmentation performed on the binarized image is used to identify connected regions which are then compared with the stored cases for classification as haemorrhage cases. Zhang et al. (2013)

have reported a segmentation accuracy of 0.95 during evaluation on 426 CT cases of suspected stroke patients.

A method of automatic detection of intracranial haemorrhage using intensity thresholding is proposed by Maduskar & Acharyya (2009). They propose that a range of intensity values representing bleed regions is estimated from a representative seed point which is manually demarcated. The image is converted into a binary representation using intensity threshold and the analysis of connected components is used to keep only the region where initial seed point was fixed. The method has been evaluated on 11 CT studies and 96% accuracy of classification of haemorrhage slices has been reported.

Automatic segmentation of brain haemorrhage is proposed by Shahangian & Pourghassem (2013). They propose method on 8-bit JPG images in which any pixels with intensities that are above 225 and below 100 are set to zero to remove skull and CSF spaces. Then the image intensity distribution is pruned with a threshold which can separate haemorrhagic region from the brain tissue. This results in a binary image with the haemorrhage represented as a white region. Features of this region, such as the geometric measures, contrast, gray level co-occurance matrix, correlation and homogeniety, are classified using k-nn and multilayer neural network to classify cases into ICH, EDH or SDH.

Detection of the deformed midline in brain CT scans has been proposed by Liao et al. (2006). They use the difference of intensity levels on brain hemispheres on the CT image to generate a one dimensional reflective symmetry map. The sum of these intensity differences across 48 pixels at each side represents the deformed midline at the global minimum. The method has been evaluated on 81 cases and plausible results are reported in 71.6% cases where the difference between manual and automated demarcation was less than 1mm. The method proposed by Liu et al. (2014) detects and quantifies the midline shift of brain using an anatomical marker model. The anatomical landmarks such as the bony protuberances and ventricles

are detected using intensity levels and the landmarks are joined to represent the deformed line.

A lot of user interaction and time from the user are required in methods such graph-cuts and mean-shift where the image pixels are modelled into weighted graphs which can be partitioned into disjoint subsets (Shi & Malik 2000, Vicente et al. 2008). The segmentation of corpus callosum in brain scans is proposed by Freedman & Zhang (2005) using graph cuts. However, it requires users to manually identify regions and if large volumes of images have to be segmented, then these methods become less usable in clinical settings.

Techniques such as simple linear iterative clustering (SLIC), adapt K-means approach and cluster pixels into superpixels (Achanta et al. 2012). The input image is divided into small user-defined sections, which are the initial superpixels, and then the centres of these are used for computing the mean of clusters. Iterations update the regions and the location of centres. Based on the distance of the pixels from the cluster centre, a label is assigned and the process is repeated until the error between successive cluster centres falls below the defined threshold (Achanta et al. 2010). The algorithm, however, intrinsically depends upon the selected size of the initial superpixels which needs to be changed based on the size of the region of interest (Soltaninejad et al. 2014).

3.3.1.2 Spatially Guided Methods

The neighbourhood information can influence the labelling of the pixels which can result in better segmentation, supplanting the spatially blind methods, because these take into account the spatial characteristics of medical images (Chuang et al. 2006*a*). Considering the importance of edge information, as well as the need to preserve the spatial relationship between the pixels, spatially guided techniques such as region growing and merging, graph cuts, Markov random fields, active

contours and level sets have been proposed (Vantaram & Saber 2012, Osher & Sethian 1988, Leventon et al. 2000, Karasev et al. 2013).

In region growing and merging, the region surrounding a manual seed point is iteratively grown to include pixels with similar characteristics and spatial proximity (Tremeau & Borel 1997). The method depends upon the seed points, noise in the image and threshold of the pixel intensities to merge and final result may not conform well to the object boundaries in medical images. Bardera et al. (2009) have proposed semi-automated segmentation of haematoma using region growing. The user is required to fix the initial seed point and the threshold interval values are experimentally obtained from damaged regions of different patients. They have evaluated the method on 18 cases and report 0.80 matching ratio and improved time efficiency of 4 minutes compared to the 10 minutes required for manual segmentation

Markov Random Field Models are similar to Bayesian models and have been widely applied to segmentation of noisy images. These models combine contextual constraints into the prior probability in a quantitative way to reach the optimal solution. However, an intrinsic drawback in most of these techniques is the extreme computational requirements (Suri et al. 2002). Graph-cuts, similarly, require a lot of interaction from the user.

Low level segmentation, template matching and using prior information from MRI templates to locate different anatomical structures has been suggested by Chen et al. (2009). The template slices are enlarged through morphological dilation to accommodate for variations in locations but no information is provided about cases in which there is gross deformity of the anatomical structures. The MRI templates are usually derived from normal subjects and their mapping to severe pathological or traumatic cases can lead to inaccurate results. Giesel et al. have used watershed transform to interactively segment the lateral ventricles by manually specifying landmarks on T1 weighted MRI images to overcome the assumptions of optimal

scale to be used in watershed transform (Giesel et al. 2006). MRI images have a better delineation of white-matter, grey-matter and CSF as compared to CT images.

The application of active contour and level sets methods for segmentation of the images has gained popularity owing to the fact that these deformable models can better adapt to the topological shapes and contours of the objects of interest (Caselles et al. 1993, 1997, Chan & Vese 2001, Osher & Sethian 1988). The approach of segmenting an object bounded by a closed curve has resulted in their plausible applicability for segmentation of neuroimages (Yezzi Jr et al. 1997, Vese & Chan 2002, Wang et al. 2009, Dubrovina & Kimmel 2012). The underlying principle of active contours is to deform a spline driven by a piecewise smooth function using a combination of internal and external energies around the region of interest to achieve the required segmentation. The methods proposed can deform the curve either on the basis of energy minimization, as with snakes model, or implicitly as a level set function, as in geometric active contours (Prakash et al. 2012). The application of snakes and level sets methods for segmentation of the medical images has gained significant popularity in the recent years such as segmentation of neuroimages (Yezzi Jr et al. 1997, Vese & Chan 2002, Wang et al. 2009, Liao et al. 2010, Dubrovina & Kimmel 2012, Soltaninejad et al. 2014).

The 'snakes' models tend to minimize image energy but suffer from problems such as local minima and often overlook minute features in the image. The segmentation using geometric active contours either relies on the gradient based edges within the image or description of the regions. Medical images, such as brain CT, mostly present regions of interest without hard, distinct edges and active contours not relying on gradient edges can produce better results of segmentation. The implementation by Chan-Vese, based on minimizing Mumford-Shah functional, is considered state of the art when the edges are not used to differentiate between the ROI and non-ROI (Chan & Vese 2001). To keep the contour smooth, it is

necessary to re-initialize the level set which can be computationally expensive and may produce undesirable results (Gomes & Faugeras 2002).

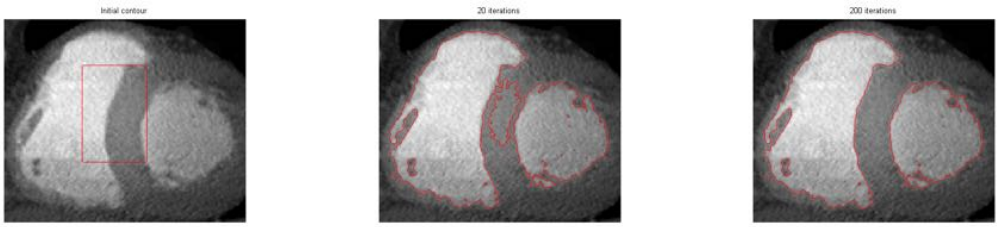

(a) Initial Contour **(b)** 20 Iterations **(c)** 200 Iterations

FIGURE 3.3: Evolving Contours in medical images using DRLSE approach (Li, Xu, Gui & Fox 2010).

To avoid the costs of the re-initialization problem, Li et al. proposed a distance regularized level set (DRLSE) which enforces a signed distance function in the evolution of the curve (Li, Xu, Gui & Fox 2010). The segmentation results depend upon the difference of the average intensities within and outside the region of interest as shown in Fig. 3.3.

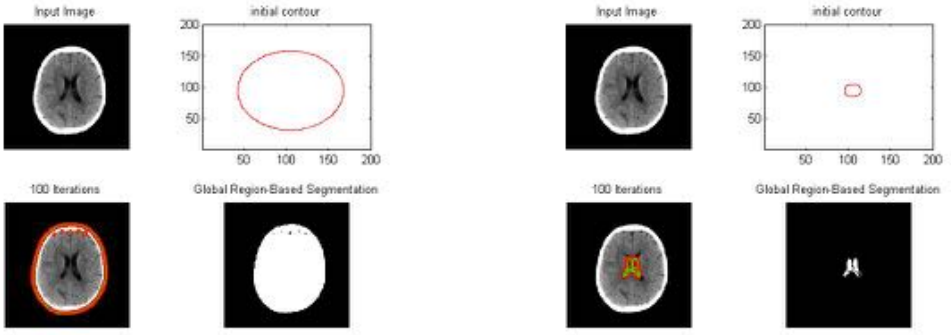

(a) **(b)**

FIGURE 3.4: Effect of initial curve size on the final segmentation results using Chan-Vese model of active contours.

The method proposed by Liao et al. (2010) uses multiresolution binary level sets. The candidate haematoma voxels are identified using adaptive thresholds and connectivity and subsequently, binary level set algorithm is applied to segment the ROI. They report correlation coefficient of 0.97 in 15 cases used in evaluation.

However, in segmentation of distinct anatomical structures from brain CT scans, placement of the initial seed curve still poses a constraint on the evolution of the curve and has to be performed manually by the user else it gives less satisfactory results as shown in Fig. 3.4. Image 3.4a is initialized with a large curve which adheres to the skull boundary. Image 3.4b is initialized with a small curve which only segments the ventricles in the given slice. These methods are further discussed in Chapter 5 as the proposed method is built upon the foundations of active contours.

3.3.2 Approaches using Machine Learning

The extensive and tenable integration of machine learning in medical problems can be attributed to the fact that these systems can adaptively learn and optimize the relationship between inputs and outputs (Yegnanarayana 2009, Kononenko 2001, Shi & He 2010, Schetinin & Schult 2005, Kondo & Ueno 2012, Schetinin & Schult 2006). Numerous methods have been proposed in literature which can be applied to medical image analysis (Ma et al. 2010, Jiang et al. 2010, Shiraishi et al. 2011). A CAD system based on machine learning would be considered useful if it is robust in dealing with missing and noisy data and its performance is comparable to the human expert. Based on the principles of biological neurons and synapses, these methods employ different architectures (networks) of artificial neurons to mimic the supervised and unsupervised learning processes in human brain (Bishop et al. 2006).

Artificial neural networks (ANN) such as feedforward network can be used to fit a finite input-output mapping problem and, hence, can be employed for medical applications (Kononenko 2001, Haykin 2004). The architecture of feed-forward networks is unidirectional and backpropagation is mostly used to update the network (Heaton 2008). There can be multiple layers in the network e.g., Multi-Layer Perceptron which are useful in nonlinear separability problems. In feedback

networks, the communication is bidirectional and the network changes its state continuously until it is stable. This architecture introduces loops to propagate values back and forth within the network while maintaining stable equilibrium with varying inputs (Heaton 2008, Nakano 2012, Yegnanarayana 2009). Medical images e.g., CT scans, usually have inhomogeneity of background and noise. The recognition of ROI in 2-D images of the solar filaments with similar intensity characteristics has been proposed utilizing ANN and the technique has given plausible results (Zharkova & Schetinin 2005). In addition, ANN's can be trained using a few representative images which have been manually annotated and labelled by human experts in order to learn to recognize the ROI. The training process of ANN can suffer from the occurrence of local minima if the weights are not initialized properly (Wessels & Barnard 1992, Thimm & Fiesler 1997). This also influences the speed of convergence and generalization performance (Fernandez-Redondo & Hernandez-Espinosa 2000). The proposed approaches for initialization rely on defining an optimal distribution and range for the weights either empirically or based on characteristics of the neurons (Thimm & Fiesler 1997).

Shi & He have elaborated the use of ANN in medical image processing highlighting their efficiency and weaknesses (Shi & He 2010). In their review, they report that for image segmentation and recognition, feedforward network is the most commonly used architecture. Compared with the performance of Maximum Likelihood Classifier, feedforward network exhibits better noise tolerance and less sensitivity to the selection of the training set. However, the convergence can be slow and a priori learning parameters are required to achieve the results.

The use of ANN to explore relationships in complex clinical situations, such as closed head trauma, has been proposed by Sinha et al. (2001). They have evaluated the predictive ability of an ANN on CT studies of a cohort of 351 patients with head injury. The training of ANN was performed using clinical, demographic and CT imaging data of 382 patients (retrospective) with head injury. Validation of

the ANN on 351 patients (prospective) showed that the prediction from ANN was more sensitive (82.2%) than the prediction from doctor (62.2%).

The use of ANN in medical decision support systems for TBI patients has been elaborated by Li et al. (2000). The clinical profile of 9480 patients containing data about type of injury, Glasgow Coma Scale and episodes of fits etc. was used to train the ANN. Validation was performed on another 3160 patients and area under ROC for the neural network was reported to be 0.897 which supported the feasibility of using ANN for TBI decision support systems. The methods proposed by Balasooriya & Perera (2012) and Ramana et al. (2009) employ ANN to detect haemorrhagic regions on the brain CT of TBI patients. Al-Ayyoub et al. (2013) has proposed an approach to detect and classify haemorrhages on brain CT scans and results on 37 haematoma cases show 92% classification accuracy.

Prediction of mortality and functional outcome after intracerebral haemorrhage using ANN has been proposed by Lukić et al. (2012). They have evaluated their method on 411 patients based on initial clinical parameters and the ANN based prediction of outcome has been correctly classified in 93.55% of patients.

Applicability of complex-valued artificial neural networks combined with wavelet transforms for segmentation of chest CT scans has been suggested by Ceylan et al. (Ceylan et al. 2010). In a two stage approach, they propose that the feature extraction is performed in the first stage using complex valued wavelet transform at four levels of decomposition and the second stage uses complex valued artificial back-propagation neural network for classification. The output in the form of a real and an imaginary part and comparison of performance is only discussed with discrete wavelet transform.

Support vector machines (SVM) have been in limelight for a long time for linear classification problems. The algorithm's goal is to construct a hyperplane that gives maximum separation between the two classes by mapping the input non-linearly into a higher dimension feature space (Cortes & Vapnik 1995). Chaplot et al.

have proposed using SVM to classify brain MRI as either normal or abnormal and the results are shown to be better than self-organizing maps (Chaplot et al. 2006). The input images are decomposed using discrete wavelet transformation with Daubechies-4 wavelets to overcome the problems of Haar wavelets for smooth signals and it constitutes the feature vectors. Daubechies-4 wavelets can be computationally expensive to compute and their proposed approach achieved 94% accuracy with 52 images. Zhang et al. addressed the same problem and proposed PCA for extracting features and back propagation neural networks for classification and their approach on 66 images gave 100% classification accuracy (Zhang et al. 2011). However, although the SVM approach is deemed effective in learning tasks, the computational cost is relatively high (Yang et al. 2009). Also, the choice of kernel and complexity of the algorithm pose problems in applicability (Burges 1998, Hussain et al. 2011). The number of support vectors typically increases linearly with the number of samples, which results in an increased classification time during testing (Yang et al. 2009).

The use of random forests to detect cerebral contusions in TBI cases has been proposed by Rao et al. (2014). They propose training a random forest using image features and the ground-truth labels to achieve segmentation of cerebral contusions. The evaluation of the method shows a mean DICE overlap of 0.60 on 23 MRI scans of TBI patients. Prediction of depression following TBI has been proposed by Kennedy et al. (2005) using random forests. The classification rate achieved on 78 patients was 83% using the features from the depression scale of Neurobehavioral Functioning Inventory.

The Group Method of Data Handling (GMDH) has been applied in a multitude of medical problems and researches such as Kondo et al. have demonstrated the applicability of the technique in image segmentation and diagnosis (Kondo 1998, Kondo & Ueno 2012). In their method, they have introduced a knowledge base for organizing the network architecture. They extract statistical features such as mean, standard deviation, variance and pixel location from the image

and integrate medical, physical and image processing knowledge as rules into the GMDH architecture. Kondo et al. in their various contributions, have implemented GMDH in the cases of liver cancer, lung nodules, blood vessels and brain (Kondo & Ueno 2007, 2012). In recognition of lungs in x-ray images, Kondo et al. have demonstrated that GMDH can adapt itself and demarcate the boundaries of air filled lungs on x-ray images (Kondo et al. 1999). However, no comparison results with other techniques, which could be applied to the same problem, are given in their work.

The researchers Lo et al. (1995) have applied convolutional neural networks for pattern recognition in medical images and for the detection of lung nodules. The proposed approach designed the model with one input layer and four levels with two layers of simple-cell and complex-cell in each. The 32×32 pixels image block representing suspected ROI and proposed for convolution calculation has been assumed similar to the information perception by the retina without evidence from literature, however, the experiments are run with 16×16 pixels image blocks. The technique has been applied to detect only the T1NxMx tumours based on the TNM classification in 25 of the total 55 chest radiographs and they reported that the performance could not be compared to 68% sensitivity of the radiologist due to small sample size (Lo et al. 1995).

3.3.2.1 Selection of Machine Learning method

The review of literature highlights several approaches for the classification of medical data for use in CAD. The choice of selecting a single machine learning method is a 'silver bullet' problem for use in all domains of clinical applications. However, the generalization ability of neural networks in terms of mean square error is better than the SVM albeit slower convergence (Moavenian & Khorrami 2010). The comparison of SVM and ANN for differential diagnosis of benign and malignant breast tumours shows nearly identical performance through area

under ROC curve evaluation (Moavenian & Khorrami 2010). The choice of SVM kernel is a critical consideration which can influence the classifier's results (Hussain et al. 2011, Zanaty 2012) and selecting different kernel functions may result in different performances (Zanaty 2012). The classification task in the experiments is performed using the ANN, however, further investigation other classification methods such as SVM, Random Forests and Case Based Reasoning has been noted as an extension of the work in future endeavours.

The machine learning algorithms discussed above require pertinent features extracted from the data to perform classification (Blum & Langley 1997). The concepts of feature extraction and selection are presented in the next section to elaborate the working of machine learning approaches.

3.3.2.2 Feature Extraction and Selection

The intelligence in the pattern recognition systems depends upon the features extracted during the processing of the image (Nixon 2008). Feature extraction techniques reduce dimensionality (Hinton & Salakhutdinov 2006) of the data so that it can be processed more effectively. Incomplete or erroneous features can adversely affect the performance which is expected to be robust and invariant to transformations and distortions. Blum and Langley comprehensively review the problem of feature selection in machine learning (Blum & Langley 1997). The authors define 'relevance' of features based on the target, sample and incremental usefulness. According to them, a relevant feature should appear in all samples being used and a differentiation of samples based on this feature should be possible. Similarly, tweaking the value of this feature should allow classification result to change for the given sample.

In grey scale medical images like CT, however, feature selection is a challenge because a single feature can not fulfil the definition of 'relevance'. If only the intensity of pixels is selected, then an 8-bit image with pixel values from 0-255 can

have as many as 256 classes if each intensity level is considered a distinct class, or as little as 2 if only the pure black and white intensities are considered. Cranial CT is usually assessed for bone, blood, brain parenchyma, cerebrospinal fluid and air. However, distinct grouping of pixels into these five categories is not plausible owing to the noise and overlapping shades.

Intensity based statistical features such as mean, mode, histogram, and variance combined with pixel location have been used by Kondo et al. for segmentation of medical images (Kondo & Ueno 2012). Image segmentation using information entropy have been proposed by Barbieri et al. (Barbieri et al. 2011). Entropy is a measure to quantify information necessary to specify an object within the image. More complex texture based features such as local binary patterns, Fourier transforms, and shape descriptors have also been suggested in literature (Guyon & Elisseeff 2003, Guyon et al. 2008, Ceylan et al. 2010).

Extraction of features can consider global or local image characteristics (Nixon 2008). The local neighbourhood information can strongly influence the 'relevance' of the feature and, hence, it is common to use a sliding window operation to transform the input image into a feature vector. Just as a man is known by the company he keeps, a pixel can be classified based on the neighbourhood it appears in. The concept of a square sliding window suggests using an even number neighbourhood in both the vertical and horizontal directions (which would include the diagonals also), so that the final window is odd sized in both directions with the central pixels being the current pixel under consideration (Gonzalez & Woods 2002, Nixon 2008).

3.3.3 Hybrid Approaches

Researchers have further expanded the possibilities by combining different methods of segmentation and feature extraction to get better results than using the methods alone. The idea is to create more stable results that are less sensitive to parameter

changes and the combinations are applicable across multiple images. Several hybrid methods have been proposed to segment regions in brain CT images. Bhadauria et al. (2013) proposed combination of Fuzzy C-Means clustering and region-based active contour to segment the haemorrhage region . They used clustering to find an initial mask and then propagate it to the haemorrhage boundaries using region-based active contour.

The approach suggested by Lee et al. (2008) uses k-means and EM clustering to segment the head CT images into abnormal regions, CSF spaces and brain matter. To improve the contrast of the gray levels in the brain CT, they apply contrast stretching based on histogram analysis. The skull bone is removed by applying intensity thresholding and then setting the pixels of skull and background to zero. The regions of brain are segmented by first classifying the pixels using k-means clustering and then binarising the results. Extraction of features such as area, mean, standard deviation, eccentricity and orientation is then used to classify the regions into normal or abnormal. For demarcation of CSF spaces and brain matter, Lee et al. (2008) propose EM clustering. The precision of >98% is reported based on evaluation of the method on 2 images each from 28 patients.

Turaga et al. propose enhancement of the graph cut based segmentation methods using convolutional neural networks (Turaga et al. 2010). However, a salient feature in the electron-microscopy images in their data set is the delineation of cell boundaries which can also be demarcated using gradient based edge detection algorithms. Turaga et al. (2010) report that the proposed method achieves better segmentation performance than graph cuts and normalized cuts by significant reduction in the number of splits.

An automatic procedure based on modified distance regularized level set (DRLSE) has been proposed by Prakash et al. (2012) to segment haemorrhage in brain CT images . Their method first creates a general intensity mask defined by a set of DRLSE parameters to localize the region rapidly. Then the region boundaries

are identified in another level-set step by choosing the parameters so that more accurate boundaries are detected. This method is sensitive to initial threshold values and results in leakages in boundaries in which the normal brain tissue and trauma have very close intensity values. Furthermore, global threshold values are different for individual cases, and the user should predetermine them.

An improvement of the DRLSE based segmentation was proposed by Soltaninejad et al. (2014). In that method, the pixels are first classified using SLIC and then the results are fed into the DRLSE algorithm to delineate the final segmentation. The proposed method has been implemented on brain trauma CT scans and plausible results show improvement from the DRLSE algorithm. However, the performance of SLIC is highly dependant on the selection of parameters of the algorithm, like the number of superpixels (Achanta et al. 2012).

The hybrid method proposed by Tao detects haemorrhage regions based on top-hat transformation and left-right asymmetry (Chan 2007). The preprocessing involves intensity thresholding and morphological erosion to remove regions which do not constitute the region of interest. Since the intensity values for haemorrhages overlaps with the normal tissues, it causes difficulties for segmentation task. Also the proposed method for rotating the head, in case it was tilted during the scan procedure, assumes the lateral ventricles to be identical bilaterally and this is compared with iterative rotations. This, however, can not promise plausible results because of variations in the sizes of lateral ventricles in normal subject and more importantly, in the case where TBI can cause one or both lateral ventricles to disappear due to mass effect or oedema. In such cases, this approach fails to find features to correct the orientation of the head.

The integration of shape information in level set based segmentation has been proposed by many researchers, however, most of these approaches do not allow for translation, rotation and scaling of prior shapes and also require placing the initial seed points of the shape priors exactly inside the desired objects (Cremers,

Kohlberger & Schnörr 2003, Rousson & Paragios 2002, Cremers et al. 2002, Chan & Zhu 2005, Cheng et al. 2008, Khalifa et al. 2010). This leads to limited real-world applicability of these methods as the anatomical structures can vary in sizes and shapes. The number of shape priors used in these methods is also a limitation and the resulting segmentation often fails to converge if the shape differences between the stored prior and object of interest are too high (Cremers, Kohlberger & Schnörr 2003). This limitation can be addressed if a baseline shape prior is extracted from the atlas and morphological deformations in abnormal cases is extracted during training (Pan et al. 2009). Cheng et al. proposed a method for segmentation of liver MRI by manually seeding a point and then calculating a feature image (Cheng et al. 2008). A labelling function is then used to designate region of interest for initial results. The shape prior is calculated using Mean Shift on contour points of manually labelled images and cubic spline curves form final contour. Cheng et al. (2008) further proposed to match the shape models to the initial segmentation results using distance maps to overcome the shortcomings (translation, rotation and scaling) in method used by Cremers, Sochen & Schnörr (2003).

In medical images, the distribution of intensity values in one anatomical structure may overlap those of another structure, hence, defeating the intensity based techniques of segmentation. Similarly, techniques using low level features are effective upto a certain point but retrieving an entire geometric structure is beyond their capabilities. In such limiting situations, active contours and level sets offer a fundamentally robust and more plausible solution.

3.4 Evaluation of Segmentation

An important factor to be considered during the development of image segmentation algorithms is the accuracy of the results they produce. The researchers in literature have evaluated their methods using the Jaccard Index and Dice's coefficient. These statistical validation metrics signify the performance of both the proposed

algorithms and their reproducibility with reference to manual segmentations. The spatial overlap is used as the criterion to assess accuracy of automated segmentation results. Their significance is highlighted by (Zou et al. 2004, Shattuck et al. 2009). Similarly, Student's t-test is often used to compare the measurements of segmentation results between algorithms and experts (Evans et al. 2004, Chuang et al. 2006*b*). The null hypothesis in these cases states that there is no statistically significant difference between the paired measurements coming from different observers and it is either accepted or rejected based on the results of the test. Other evaluations such as sensitivity, specificity, recall and precision and f-measure have also been suggested in literature for evaluating solutions related to medical domain (Mould 1989). An assessment of the consistency and variability amongst observers in estimating measurements of same objects can also be evaluated using the Intraclass Correlation Coefficient (Koch 1982).

3.5 Conclusion

The significance and importance of 'second opinions' in assessment of neuroimages is an accepted fact which can reduce the incidence of inter-observer variability. The double reporting can assist the clinicians to more succinctly identify the cause and effect of the trauma and follow more targeted therapeutic regimen. However, due to the costs involved, number of personnel in the emergency departments is often limited which increases the pressure and workload on the doctors on duty. In such cases, an automated, computer-aided system can be an effective and cost-efficient way to fill the gap and provide information which can support the radiologists' assessment.

The applicability of CAD in clinical and research environments has shown plausible results and literature review presents a number of methods, algorithms and techniques in image processing and machine learning which endeavour to mimic the cognitive behaviour of the experts in identifying features manifested by the

trauma or pathological conditions in neuroimages. The important steps involve segmenting and localising the normal and abnormal structures and then estimating their linear measurements and volumes as presented on the cranial CT scans.

One of the foremost requirements for CAD systems is the robustness and efficiency in approximating the experts' intuition. The notion of an automated system is based on the belief that these do not require any manual intervention by the user. However, the *modus operandi* of most of the suggested techniques require the user to manually specify the region of interest and its surroundings which is a time consuming task and less feasible for clinical and emergency applications. Also, the state of the art approaches do not use the clinical profile of the patient at the time of admission which can give significant information about the suspected trauma or pathology.

It can, therefore, be construed that this gap in the performance and ease of use of such medical image segmentation approaches necessitates positing a comprehensive and systematic framework harnessing the strengths and minimizing weaknesses of the existing systems. The proposed framework, presented in the next chapter, can incorporate the findings of clinical and neurological assessment of the patient at the time of admission into classification of the neuroimage features which would then be used for segmentation of the ROI. The requirement to manually specify the initial seed by users for segmentation can be circumvented through automatic identification of probable ROI from the clinical and image features. Another important clinical requirement is to classify brain trauma CT according to radiology schemes such as the Marshall CT classification to ascertain prognosis (section 2.3.1). This functionality can be fulfilled by incorporating matching of descriptive features of the radiology scheme into the proposed framework.

Chapter 4

Pattern Driven, Content Aware Active Contours

The eyes do not see what the mind does not know.

Anonymous

Assessment of the brain CT involves scrutiny of *Blood, Cisterns, Brain, Ventricles* and *Bone* which provide valuable and vital information for establishing the diagnosis and targeted management of the patient (Perron 2008). The systematic comparison of the findings with normal ranges and features guide the radiologist to deduce the salient features and determine the severity of the injury as discussed in section 2.3.1. Even in the absence of trauma, brain CT scans are useful in estimation of intracranial measurements which are routinely performed to evaluate outcomes of clinical and surgical interventions, note geriatric changes, identify deleterious effects of drugs and reveal structural changes in conditions such as Alzheimer's disease (AD), Schizophrenia, Huntington's disease, hydrocephalus and many other neurological and psychiatric disorders (Wilk et al. 2011, Zhang et al. 2008, González-Reimers & Santolaria-Fernández 2011, Barker-Collo et al. 2012).

The radiologist examining neuroimages has to deal with all such cases and requires a support of decision or second opinion in such situations. Hence, it is indispensable that a CAD system capable of a multi-faceted role is available to assist the radiologist. It has been observed in the review of relevant literature that existing state of the art CAD systems require manual identification, called seeding, of the ROI by radiologist and then the segmentation algorithm executes to demarcate the ROI. This manual intervention is time consuming and the results of segmentation can be less satisfactory if the seeding was not accurate.

To fill the gap, a comprehensive framework for segmentation and estimations of intracranial measurements simulating the systematic approach of radiologists is presented. The Pattern Driven, Content Aware Active Contours (PDCAAC) framework encapsulates the segmentation and linear measurement algorithms to segment the brain CT scan and provide estimations of brain ratios and indices in non-trauma cases; and in trauma cases, classify the CT according to the Marshall et al. CT Rating by also segmenting and estimating volume of intracranial haematomas. The PDCAAC is designed to be driven by the clinical profile of the patient as well as the image features identified on the noncontrast brain CT scans. The probable ROI is automatically identified using the clinical phenotype and image pixel classification with artificial neural networks and is used as the initial seeding point for the subsequent segmentation of ROI using active contours.

The radiology experts provide the training data and ground truth consisting of manually annotated images of TBI cases, the salient clinical presentations at the time of admission and the prognosis models used in routine emergency practice in hospitals. These descriptions follow the principle of polyrepresentation (Fig. 2.1), as discussed in chapter 2, and guide the doctors in clinical settings to establish the diagnosis based on the total cognitive overlap. The PDCAAC framework endeavours to achieve the same using clinical phenotype of the patient, respective CT image data and clinical models. The framework is depicted in Fig. 4.1.

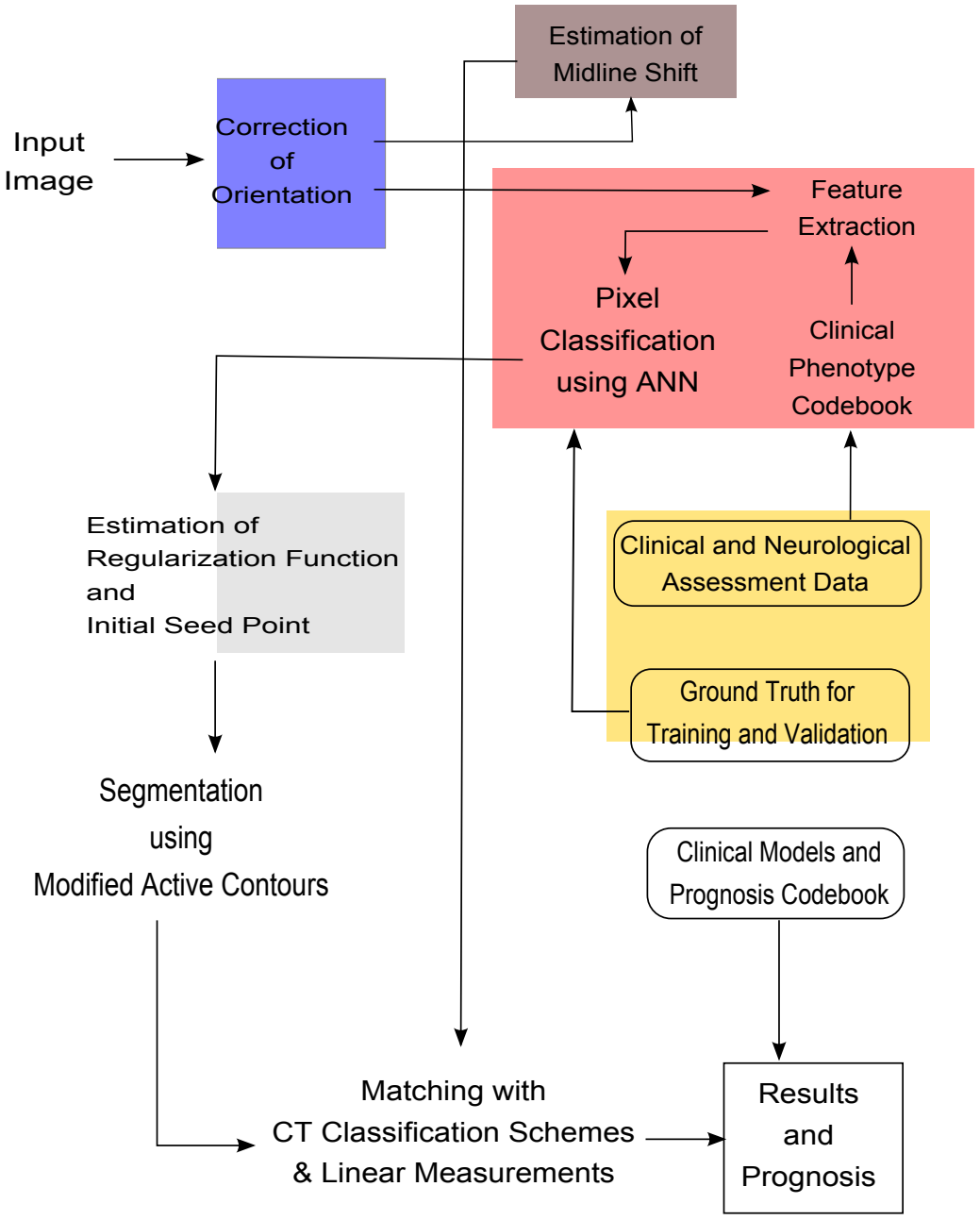

FIGURE 4.1: Work flow of the proposed PDCAAC framework. The preprocessing steps are shown in blue rectangle. The data obtained from clinical perspective and radiology experts is shown in yellow rectangle. The step for estimation of midline shift, feature extraction and pixel classification with ANN are in red rectangle. The estimation of regularization function and location of initial seed curve are within grey rectangle and these are used by the modified active contour method in green rectangle. The matching of segmentation results and measurement estimates with the CT classification scheme are in orange rectangle. The final output are the segmented ROI and prognosis.

4.1 Description of the Framework

4.1.1 Correction of Orientation of Head in CT image

The brain CT scan is the most frequently used modality in emergency radiology. During the scan procedure, it is quite commonly observed that the head of the patient is tilted to either left or right side and the nose is not pointing directly upwards which is the natural head position (Cevidanes et al. 2009). While this presentation does not have any effect on the diagnosis, it can, however, affect the computer based algorithms which have to identify the brain midline (Chan 2007), perform linear measurements on brain structures such as the ventricles and haematomas. Therefore, an important step in the proposed framework is to analyse the CT image to assess if any realigning of the patient's head is required.

4.1.2 Estimation of brain midline shift

Midline in the brain is an important reference point for assessing the severity of injuries and pathological conditions and a shift $> 5mm$ requires emergency treatment (Li, Li, Feng & Pan 2010, Maas et al. 2005). It is an anatomical imaginary line formed by the falx cerebri and passes through the septum pellucidum. In normal cases, this midline would present symmetrical hemispheres of the brain as shown in Fig. 4.2a and 4.2b. However, in traumatic cases such as EDH, this landmark is shifted laterally due to the pressure exerted by the haematoma as shown in Fig. 4.2c and 4.2d.

The significance of identifying the brain midline shift is also evident from the Marshall et al. (1991) CT classification scheme given in table 2.2 which categorises patients with midline shift $> 5mm$ as belonging to classes IV - VI. The identification of the anterior and posterior attachments of the falx cerebri at bony protuberances

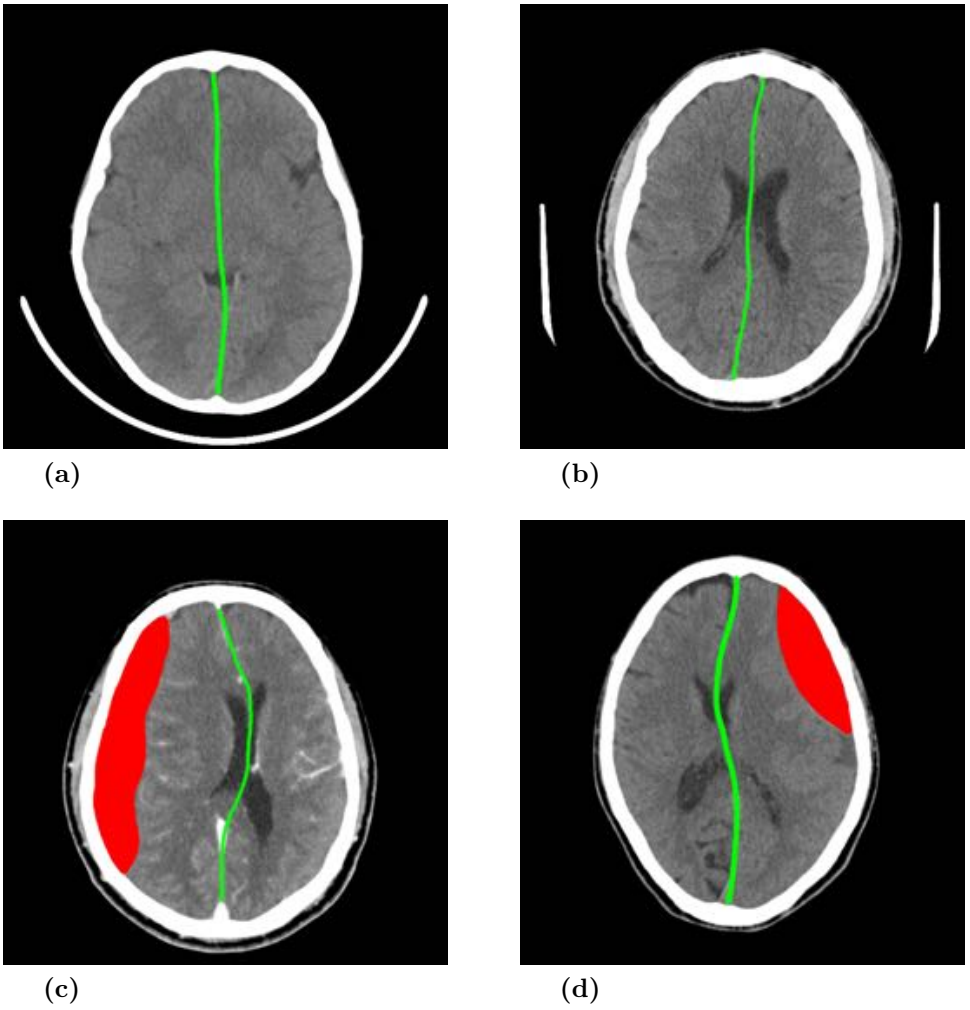

FIGURE 4.2: Manual annotation of the midline (green) on brain CT scans. Images (a) and (b) shows the midline with no shift. Image (c) has haematoma on the right side and the midline is shifted towards left (of patient) on the CT. Image (d) has haematoma on the left side and the midline is shifted towards right of the patient.

and the septum pellucidum can allow demarcation of the midline shift. Liu et al. (2014) propose that locating the anatomical landmarks, such as the CSF filled ventricles and falx attachments, can be used as markers for the midline. Other approaches such as bilateral brain symmetry, ventricle shape matching and identification of anatomical landmarks have also been suggested (Liao et al. 2006, Liu et al. 2014). For automated demarcation of midline, the proposed framework identifies the bony protuberances of the skull and septum pellucidum in the brain CT scans.

4.1.3 Feature Extraction, Selection and Classification

4.1.3.1 Features from Clinical Profile

The clinical and neurological assessment of the patient performed at the time of admission to the hospital guide the doctors to provisionally establish the underlying pathology or trauma (Perel et al. 2007, MTBI 2004). This clinical profile of the patients reports findings listed in table 2.9 and forms the cognitive representation of the patients' symptoms and signs. This representation can allow the doctors to provisionally differentiate between causes such as strokes and haemorrhages, however, further representations from the lab procedures and clinical models are necessary to reach the final diagnosis. When further investigations, such as noncontrast CT, are performed, the doctors refer to the clinical profile to look for specific image features to establish the total cognitive overlap which entails the diagnosis.

The proposed framework incorporates the clinical profile of the patient to differentiate between ischaemic stroke, EDH, acute SDH and chronic SDH. The findings from the standard clinical and neurological assessment of the patient (McCluskey 1990, Shah & Kelly 2003) are assigned numeric values, as given in table 4.1, so that these can be used with the artificial neural network. This creates the clinical phenotype which is a representation of the suspected trauma or pathology. The clinical phenotype, thus, identifies the probable content of the image representation enabling the subsequent segmentation method to be automatically aware of the characteristics of ROI.

The clinical phenotype is fed to an artificial neural network with one hidden layer and four neurons in the output layer. The neurons in the output layer correspond to the suspected abnormality as given in table 4.2. As the PDCAAC framework requires differentiation between the hyperdense or hypodense presentation of the pathologies or trauma, the classification results are combined on the basis of

TABLE 4.1: Clinical Phenotype of the patient in the proposed framework.

Feature	**Finding**	**Assigned Value**
Gender	Male	0
	Female	1
Age	Years	Value
Cause of injury	Unknown	0
	Road traffic accident	1
	Fall	2
	Assault	3
Loss of consciousness	Yes/No	Boolean
Vomit	None	0
	number of episodes	Value
ENT Bleed	Yes/No	Boolean
Fits	Yes/No	Boolean
Dizziness	Yes/No	Boolean
Headache	Yes/No	Boolean
Weakness	None	0
	Left	1
	Right	2
	Generalized	3
Slurred speech	Yes/No	Boolean
Hypertension	Yes/No	Boolean
GCS at admission		Value
Pupil response	Normal reactivity	0
	Left Fixed normal size	1
	Left Fixed dilated	2
	Right Fixed normal size	3
	Right Fixed dilated	4
	Bilateral fixed dilated	5
Temperature		Value
Pulse rate		Value
Respiratory rate		Value
Blood pressure		Systolic Value
		Diastolic Value

TABLE 4.2: Classification of the clinical phenotype.

Suspected pathology	Appearance on CT	Binary Target Pattern
EDH	Hyperdense	0001
Acute SDH	Hyperdense	0010
Chronic SDH	Hypodense	0100
Stroke	Hypodense	1000

radiodensity. Hence, the classification results 0001 and 0010 represent hyperdense regions while 0100 and 1000 represent hypodense. The classification result is then used in the next step to adjust contrast of the CT scan.

4.1.3.2 Contrast Enhancement

The typical presentation of acute intracranial haemorrhages on noncontrast brain CT is hyperdense which makes them appear lighter than the surrounding brain tissue. The ischaemic strokes are hypodense which means that they appear darker than the adjacent tissue. However, due to characteristics of the imaging modality and age of the trauma, the appearance may not be adequately demarcated for the doctor to delineate them confidently (Perel et al. 2007). The gray level of the CT image can be enhanced using analysis of the histogram (Lee et al. 2008).

The PDCAAC framework proposes that the contrast of the CT image can be selectively enhanced according to the suspected pathology or trauma. This can be achieved by considering intensities of the normal and abnormal anatomical structures in the brain CT (Dhawan 2011, Wolbarst & Cook 1999, Lee et al. 2008). The table 4.3 contains the intensity ranges of these structures observed by using 64-bin histogram of the 8-bit grayscale images from neuroimaging atlas (Radiopaedia.org 2014, Michigan State University 2014).

The classification result from the clinical phenotype suggests the probable trauma or pathology whose typical presentation is given in table 4.3. The intensity of the probable ROI can then be adjusted in relation to the surrounding structures.

TABLE 4.3: 64-bin histogram of 8-bit gray scale CT images in PNG format.

Feature	**Intensity Range**
Bone	59-64
White Matter	29-39
Gray Matter	16-22
Ventricles	3-13
Air	1-2
Infarct (ischaemic)	10-17
Haematoma (hyperdense)	32-50

For example, if acute haemorrhage is suspected from clinical phenotype, then the probable ROI will have hyperdense appearance and image pixels in bins 32-50 will be representing it. Decreasing the intensity of pixels in bins < 32 will then enhance contrast between the ROI and its surrounding.

4.1.3.3 Classification of Features from CT Image

The appearance of distinct anatomical structures on CT scans is based on their respective radiodensities presented as different intensity levels of greyscale pixels (Wolbarst & Cook 1999) and these characteristics are identified by the radiologists to demarcate the normal and abnormal findings (Perron 2008). However, there can be considerable overlap in the intensity levels of different structures which can lead to misinterpretation (Arendts et al. 2003). Similarly, while using the existing segmentation methods where manual seeding of ROI is required, incorrect placement of the seed point can result in poor segmentation results. Hence, it is proposed that a hybrid approach is necessary to locate the probable ROI which is subsequently used for segmentation (Bhadauria et al. 2013, Soltaninejad et al. 2014).

In order to estimate the initial seeding point, the PDCAAC framework can identify anatomical structures such as the skull bone, CSF spaces and intracranial haematomas. The clinical phenotype identifies the probable ROI, e.g., haematoma,

and its contrast is accordingly adjusted. The intensity values of pixels from the CT image are then assembled into features which can be classified using artificial neural networks (Nixon 2008). The features arithmetic mean, median, variance, standard deviation, Shannon's entropy and discrete Fourier transform are extracted so that they represent the characteristics of an $m \times m, m = \{3, 5, 7\}$ neighbourhood of a particular pixel. In addition, the pixels intensity values and their spatial information of the are also used as features. The receiver operator characteristics (ROC) curves of the extracted features are used as the criteria for their selection in classifying anatomical regions such as bone, CSF spaces and haematomas.

The ground truth for training and validation of the artificial neural network is provided by radiology experts in the form of manually annotated CT images. The radiologists have demarcated the haematomas in the TBI cases and provide their measurements on axial CT slices for volume estimation. The normal cases have been annotated by the radiologists to highlight the skull and CSF spaces to be used for estimating the brain indices and ratios.

The CT image features are classified using artificial neural network in the PDCAAC framework. The framework uses feedforward back-propagation type neural networks which are trained to approximate the manual annotations of the radiologists. The image features for skull, CSF spaces and haematomas are classified by three separate artificial neural networks which have been trained and cross-validated to classify desired ROI. The classified pixels are pruned for spurious and disjoint regions which are not part of the ROI and this result is forwarded to the active contours as the initial seeding point. Hence, there is no requirement for the doctor to manually provide the initial seed. Furthermore, the classified pixels are also used to impose constraint on evolution of the active contour.

4.1.4 Segmentation using Modified Active Contours

The initial noncontrast CT scan can provide a pertinent representation of the anatomical abnormality whether due to pathology or trauma (Li, Li, Feng & Pan 2010). This representation alone can be useful to establish diagnosis if the clinical phenotype representation is non-suggestive (Baraff et al. 2010). However, when used in conjunction with the other clinical representations, the final diagnosis can be formulated more accurately.

The PDCAAC framework is designed to segment the desired ROI by active contours as these can better adapt to the topological shapes of the ROI in medical images (Chan & Vese 2001, Prakash et al. 2012). The limitation of existing methods of active contours which require manual seeding of the curve is circumvented by the PDCAAC framework which uses a hybrid approach to automatically identify and provide the location of the probable ROI. The image pixels classified in the previous step also constrain evolution of the curve so that it does not creep out into the surrounding skull or brain tissue, or collapse to creep inside the ROI. This approach minimizes the problems of segmentation by existing models shown in Fig. 3.4. Hence, the proposed modified active contour approach is significantly efficient that the existing methods.

4.1.5 Matching with CT Rating & Linear Measurements

The brain CT scans of TBI patients have to be classified according to schemes such as the Marshall CT rating (Marshall et al. 1991). The ratings from I - VI represent extent of the trauma and clinical prognosis models use these to predict the outcome of the TBI patient (Maas et al. 2005).

The PDCACC framework can segment the desired ROI and also perform linear measurements of the segmented ROI. These measurements are necessary not only

for the estimation of brain indices and ratios (Keats & Sistrom 2001) but also for estimation of volume of haematomas and quantification of brain midline shift in TBI patients. The framework then uses measurements from detection of midline shift and the segmentation of CSF spaces and haematomas to classify the TBI patient according to the Marshall CT rating scheme. The presence or absence of the ventricles and cisterns identifies the CT as rating II or III and the detection of midline shift classifies them as rating IV and above. The detection of haematoma and estimation of the volume are used to classify the CT as rating V or VI.

4.2 Summary

While the research efforts to correlate image features to clinical outcomes are imperative for differential diagnosis, prognostic assessment, pre-surgical mapping and treatment planning in patients, these endeavours are fettered by the time and effort required to manually report clinical findings. Linear measurements of brain are a traditional tool to assess anatomy, trauma, pathologies and age related atrophy and there have been considerable improvements in clinical approaches since the advent of CT imaging. Management of TBI patients, for instance, essentially involves assessment and classification of noncontrast Computed Tomography (CT) scans according to Marshal CT Scheme and then use the classification to predict mortality. Manual demarcation of ROI by expert radiologists is still considered gold standard, however, providing second opinion to the doctors through CAD can help reduce the workload and inter-observer variability.

The PDCAAC Framework presented in this chapter systematically segments the brain CT scan into pertinent ROI and presents the estimated measurements of these regions to the user. The framework is an endeavour to assist in estimating various indices and ratios on brain CT which are routinely performed in the clinical environment to assess anatomical abnormalities in different illnesses and intoxications. The framework also identifies epidural and subdural haematomas

on the CT scans in TBI cases and classifies them according to the Marshall et al. CT rating for prediction of mortality. Hence, the framework can comprehensively analyse the brain CT scan and generate results which can be efficiently used as second opinion for the radiologists. The implementation details of the framework are discussed in the next chapter.

Chapter 5

Implementation of the PDCAAC Framework

It has always been my habit to hide none of my methods, either from my friend Watson or from any one who might take an intelligent interest in them.

Sherlock Holmes

The importance of integrating CAD in clinical and research settings to assist the doctors has been significantly emphasized by researchers (Freedman & Osicka 2006, Krestin et al. 2012). It has been observed that applicability of CAD in radiology can provide valuable second opinion to the junior doctors to minimize possibilities of misinterpretation (Balleyguier et al. 2005). However, it is imperative that the development of CAD applications should focus on minimizing manual intervention (and seeding) by the radiologist in order to reduce their workload and that the results should be plausible and clinically admissible (van Ginneken et al. 2011).

The PDCAAC framework proposed in chapter 4 has been designed to address these considerations in an efficient and robust manner by entailing an automated approach to segment and estimate measurements of normal and abnormal regions

in noncontrast brain CT scans. The hallmark of the framework is a modified active contour method which incorporates classification of patients' clinical data and CT images to achieve automatic seeding and regularization. This content aware approach relies on the principle of polyrepresentation to integrate the clinical phenotype and image features to identify probable ROI and subsequently segment it for visualization by the doctor. The implementation details of the components of PDCAAC framework are presented in this chapter.

5.1 Preprocessing of CT Images

The intensity of CT is expressed in Hounsfield Unit (HU) scale in which the radiodensity of water is defined as zero while that of air is defined as $1000HU$ (Hounsfield 1980). For other structures with linear attenuation coefficient μ_x, the HU value is given by:

$$HU = \frac{\mu_x - \mu_{water}}{\mu_{water}} \times 1000 \tag{5.1}$$

where μ_{water} is the linear attenuation coefficients of water. The viewing window is set up according to the structure being considered and the HU of common anatomical structures viewed on CT are given in Table 5.1. The viewing settings require the window width (W), which describes the range of Hounsfield units displayed, and the window level (L) which is the HU at the centre of the window width.

The CT scans are visualized by setting the minimum and maximum HU intensities to be displayed. These settings create a window with a width(W) and length(L) parameters for properly displaying characteristics of the ROI. To visualize the brain, the 'brain window' is used which is set in DicomWorks software (Puech et al. 2007) as $[L : 40, W = 80]$, and the same setting is used to convert the DICOM images to 8-bit PNG format for manual annotation by experts. The 64-bin histogram of the converted files is given in Table 4.3 and used subsequently in the experiments.

TABLE 5.1: Hounsfield Unit (HU) scale for CT

Region of Interest	**HU**
Bone	+700 (cancellous bone) to +3000 (dense bone)
White Matter	+20 to +30
Gray Matter	+37 to +45
Ventricles (CSF)	+15
Air	-1000

The 64-bit histogram separates the intensities consistently with minimum overlap which is not achieved by using 8-bin histograms.

5.2 Estimation of brain midline and vote α_H

TBI patients often present with midline shift due to the haematoma and the extent of the shift is a strong clinical marker as shown in Fig. 4.2. Estimation of midline shift in the proposed approach can be useful in seeding the initial contour for segmentation of the ROI in hyposense haematomas because the direction of the shift towards left or right indicates presence of haematoma on the opposite side.

This approach is more robust in detecting the ideal midline as compared to the method proposed by Chan (2007) which estimates the left right symmetry of the brain and relies on the sizes of the lateral ventricles . The lateral ventricles can get effaced due to mass effect of haematomas in those cases, their size can considerably vary. A simpler approach could be to gradually rotate the slice with patient's nose until the distance between tip of nose and the top of image is minimized.

The detection of nose in the head CT has been proposed by Chawla et al. (2009). The CT scan slice containing nose of the patient is selected as reference and using morphological dilation with 'disc' structuring element and grey level thresholding, the skull is extracted and subjected to 'Canny' edge detection as shown in Fig. 5.1.

!h

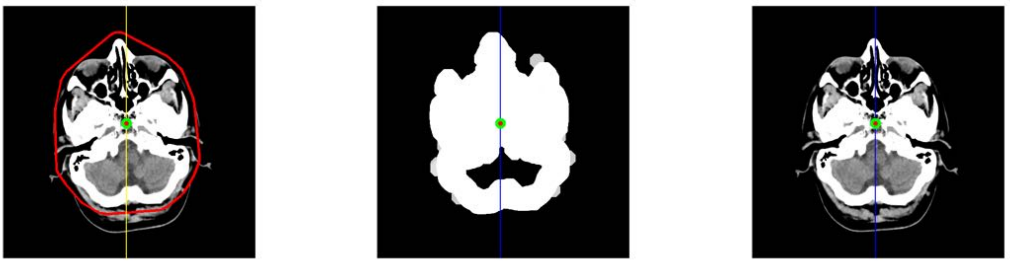

(a) **(b)** **(c)**

FIGURE 5.1: Estimation of tilt of head in CT Scans. Image (a) shows rotation of the head during CT scan procedure with reference line passing through centroid. Image (b) is the result of morphological dilation and gives estimation of tilt (θ_1) towards right of patient. Image (c) is the rotated CT.

The dilation of X by Y is defined as:

$$X \oplus Y = \bigcup X_y \tag{5.2}$$

The region properties give the convex hull enclosing the skull and the orientation of the major axis of the edge θ_1 with respect to the ideal midline passing through the centroid. Then the skull boundaries are extracted ((Fig. 5.2d)) using Canny edge detection with standard deviation $\sigma > 2.8$ for the Gaussian filter and sensitivity = [0.2 0.5] for the higher and lower thresholds, respectively, in the experiments relative to the value of the gradient magnitude of the image. These parameter values for the Canny algorithm have been empirically estimated to suppress noise and spurious edges which are otherwise detected within the brain parenchyma when $\sigma < 2.8$ is used as shown in (Fig. 5.2b). The threshold = [ ] makes the algorithm automatically choose the sensitivity threshold values which can give unexpected results.

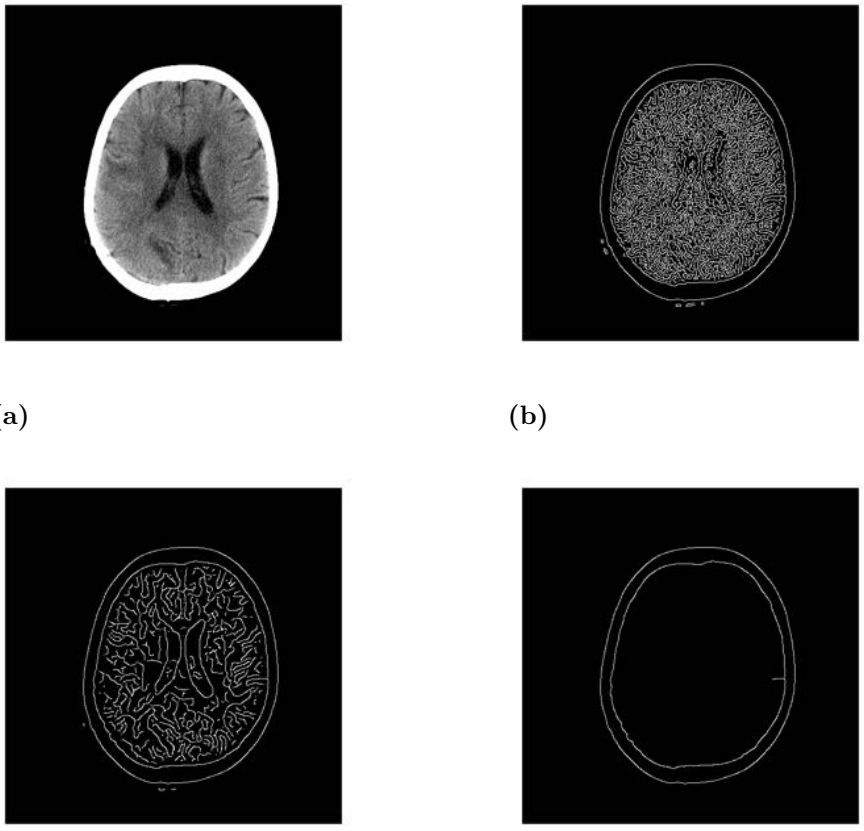

(a) **(b)**

(c) **(d)**

FIGURE 5.2: Detection of skull edges using Canny edge detector. Image (a) is the input and (b) is edge detection using Canny with $\sigma < 2.8$ and no threshold values and these show spurious edges in parenchyma. The image (c) is generated with $\sigma = 3$ for the Gaussian filter and no threshold values in Canny and image (d) shows Canny edge detection with $\sigma = 3$ and threshold = [0.2 0.5].

In cases where the axial CT slice containing nose is not available, another approach is designed to correct the orientation and demarcate the ideal midline. A boundary B wrapping the skull and its $Centroid_B$ and $Extents_B$ are identified. The skull boundaries are extracted as discussed above. The properties of identified connected regions are then measured to give centroid of the skull ellipse which should lie on an ideal midline. Using the top and bottom values of the $Extents_B$, a vertical midline is drawn from the calculated mid point. Also a sub-image S_A is created from the $Extents_B$. The pixels of skull bone with intensity I (as given in table 4.3) are traced using threshold φ in left and right directions within the window γ in

the top location of sub-image S_A as condition and the deepest white pixels (for the anterior location) are marked. The curve of the protuberance of skull bone is then modelled as a function of location of x and the number of white pixels y at x. Then the peak $\Delta y(x_i)$ where function is maximized within the range $x = 1 \ldots X_{mid}$ and $X_{mid} = \lfloor width(\gamma)/2 \rfloor$ is determined.

$$P_w(x, y) \mid I_{x,y} > \varphi, \ \forall (x, y) \in \gamma \tag{5.3}$$

$$\Delta y(x_i) = \sum_{j=1}^{h} P_w(x_i, y_j), \quad h = height_\gamma, \quad 1 \leq i \leq X_{mid} \tag{5.4}$$

$$Loc_{x_i}^L = arg\,\max_x \{\Delta y\}, \quad 1 \leq i \leq X_{mid} \tag{5.5}$$

Where $Loc_{x_i}^L$ is the location of the deepest white pixel in the left half of the sub image. The same process is repeated with $X_{mid} \leq i \leq X_{max}$ where X_{max} is the $width_\gamma$ of the sub image γ to calculate $Loc_{x_i}^R$. The orientation is calculated using the bony protuberance of the inner skull table at the anterior and taking $arctan$ of the $x_{shift} = X_{mid} - Loc_x$ with reference to the centroid calculated in the previous step. The $Loc_x = Max(Loc_{x_i}^L, Loc_{x_i}^R)$ of the two locations is taken to find whether the improper orientation is towards left or right so that the rotation in the next step could be done clockwise or counter-clockwise with reference to the top of the bounding rectangle's extents (T) estimated at the start. The $arctan$ is used to find the angle x° when $tan(x)$ is known. The adjustment using the rotation function is performed to achieve the most suitable orientation using θ from Eq. 5.6 in degrees as sown in Fig. 5.3.

$$\theta^\circ = \arctan \frac{x_{shift}}{|T - Centroid|} \tag{5.6}$$

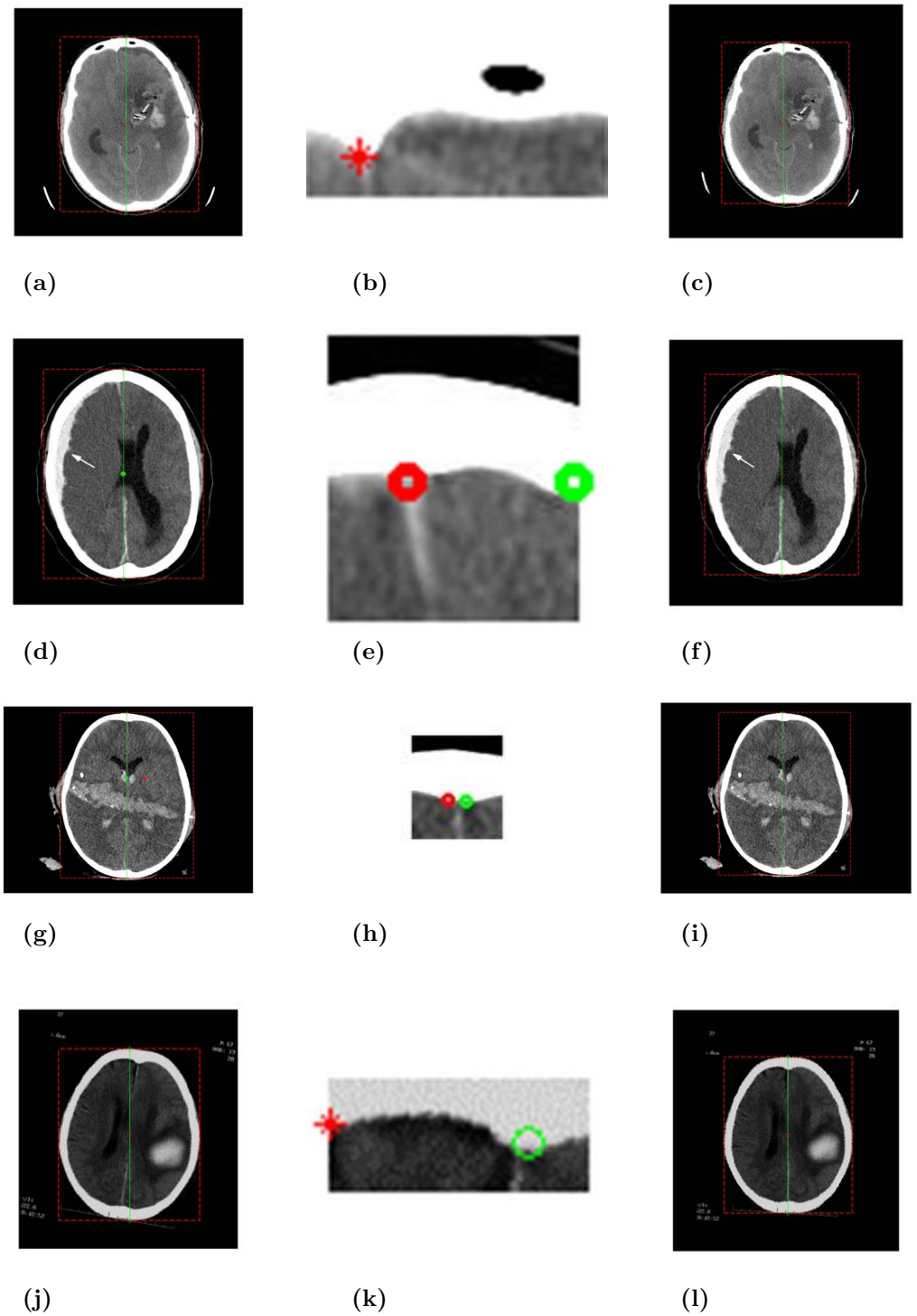

FIGURE 5.3: Correction of orientation of CT Scans. Input images in left column (a, d, g, j) show tilted head of the patient during scan process. The anterior bony protuberance is identified in middle column (images b, e, h, k) and the respective image is rotated accordingly as shown in right column (images c, f, i, l). The input image in bottom row has been manually rotated to evaluate efficiency and sensitivity of the algorithm.

To estimate the brain midline shift, the centroid indicating centre of the skull is used to draw a vertical line. Then, using cross correlation and sum of squared difference (SSD) for template matching, the septum pellucidum is identified and used as a vote for locating the midline (Fig. 5.5). A set of 32 templates, 32×32 pixel size is generated from the images at the level of lateral ventricles as given in Fig. 5.4. The locations in the training set from both CT machines are annotated by experts to define square regions of $11 - 15mm$ which form the guidelines in extraction of templates. The 32×32 pixel size represents a square region of $11 - 15mm$ based on the spatial resolution of the CT machine as suggested by the radiology experts. The regions are selected from both the normal and abnormal cases and are pruned to create the final set on the basis of the sensitivity of the templates in cross correlation results.

The normalised cross-correlation (NCC) of a template, $t(x, y)$ with a subimage $f(x, y)$ can be calculated as given in equation (5.7).

$$NCC = \frac{1}{n} \sum_{x,y} \frac{(f(x, y) - \bar{f})(t(x, y) - \bar{t})}{\sigma_f \sigma_t} \tag{5.7}$$

Where n is the number of pixels, $\bar{f}$ and σ_f are the average and standard deviation of f respectively and $\bar{t}$ and σ_t are the average and standard deviation of t respectively. The templates are matched with the input image and the location which is identified by maximum correspondence in sum of squared distance (SSD) is noted. The matches should be in $> 50\%$ of templates, and the common location is selected as probable location of septum pellucidum and, hence, the midline, and labelled as D in relation to the ideal midline.

Identifying the midline shift is an important clinical feature and a shift $> 5mm$ requires emergency treatment. Similarly, the appearance of haematoma changes with time and at some point between 3 and 21 days, it can become isodense to the adjacent cortex, making identification potentially tricky. In such cases, visualising

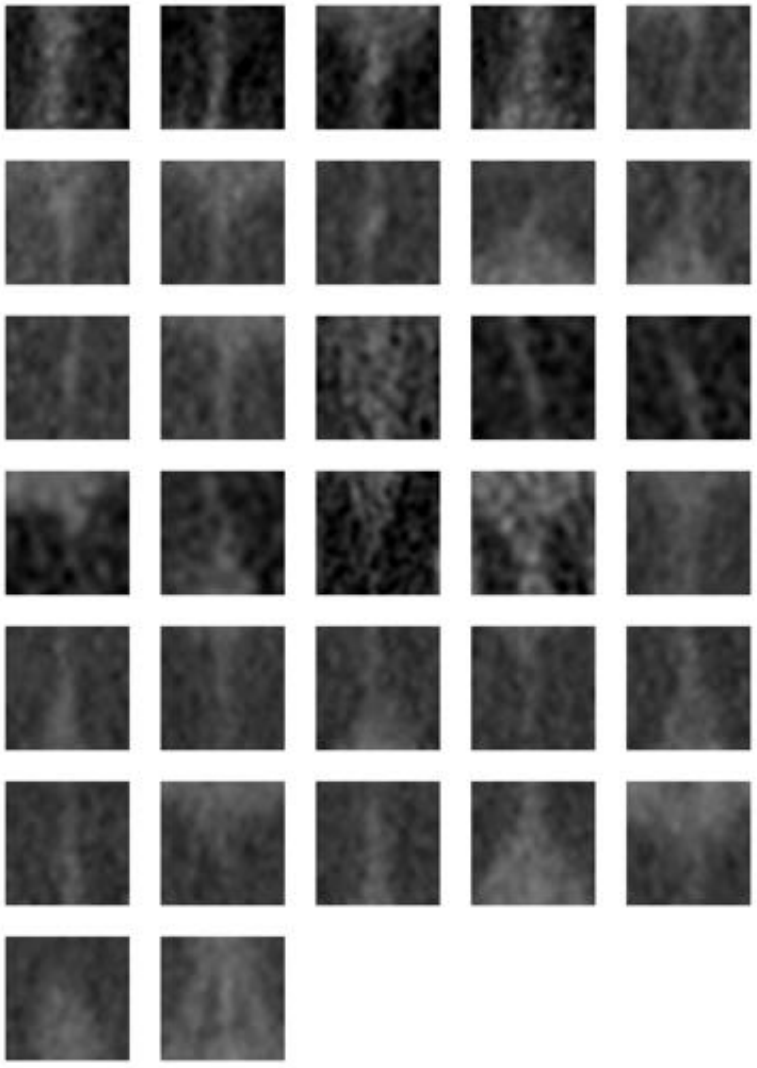

FIGURE 5.4: The set of 32 templates for matching and identification of location of the Septum Pellucidum. These represent the probable location of the septum pellucidum at the level of the lateral ventricles.

a number of indirect signs such as mass effect, sulcal distortion and midline shift are significantly important, life-saving indicators. Direction of the midline shift D is estimated and a sign function assigns a weight to direction vote α_H:

$$\alpha_H = sign(D) \tag{5.8}$$

Keeping in mind that the midline shift towards right corresponds to presence of haematoma on the left, and vice versa, the value of direction vote α_H is assigned

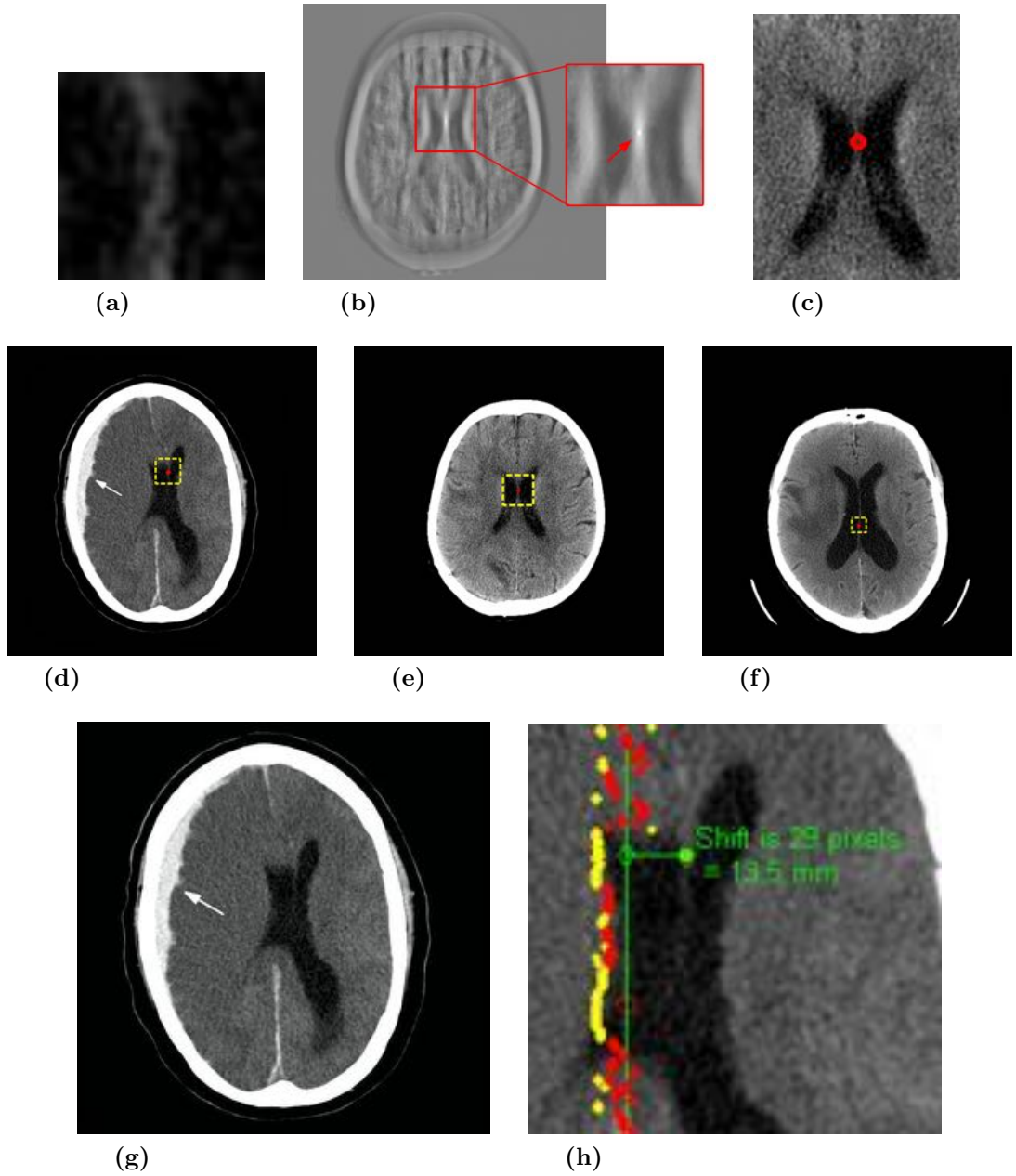

FIGURE 5.5: Template matching for Septum Pellucidum. Image (a) is one of the templates of the septum pellucidum region. Image (b) shows the identified location of septum pellucidum with red arrow in inset and the (c) is the demarcation on input image. Image (d) (e) (f) show results of template matching in locating the septum pellucidum. Image (g) is a case with haematoma and (h) shows the estimation of midline shift (13.5mm towards left of patient) in the respective case by the algorithm.

one of the following values:

$$\alpha_H(D) = \begin{cases} -1, & \text{haematoma on left} \\ 1, & \text{haematoma on right} \\ 0, & \text{no significant shift} \end{cases} \tag{5.9}$$

5.3 Extraction, Selection and Classification of Features

5.3.1 Classification using Artificial Neural Networks (ANN)

The fundamental architecture of an ANN consists of artificial neurons arranged in an input layer, hidden layer(s) and an output layer (Bishop et al. 2006, Yegnanarayana 2009, Heaton 2008). A simple perceptron model of ANN is depicted in Fig. 5.6.

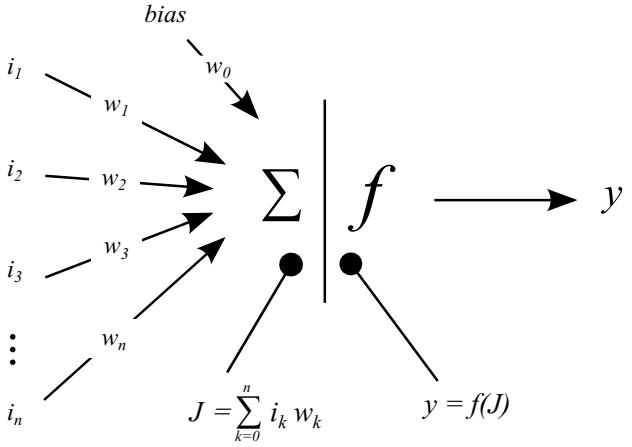

FIGURE 5.6: Fundamental architecture of ANN. The inputs $i_1 \ldots i_n$ are multiplied with respective weights $w1 \ldots w_n$. The bias is multiplied with w_0 and the weighted sum, J, is passed to a transfer function f which gives the classification result $y = \{0, 1\}$.

The neurons $i_1 \ldots i_n$ in Fig. 5.6 get their values from the input data and these are multiplied with the weights $w1 \ldots w_n$. The i_0 input is the bias = 1 which is multiplied with w_0. The multiplication results are added together to give the

weighted sum $J = \sum_{k=0}^{n} i_k w_k$. This weighted sum is given to a transfer function $f(J)$ which gives the output while satisfying the following:

$$f(input) = \begin{cases} 1, & \text{if } input \cdot weight + bias > 0 \\ 0, & \text{otherwise} \end{cases} \tag{5.10}$$

Hence, the learning in these systems is basically the value of weight(s) which would give the correct prediction at the output and the supervised learning process iteratively adjusts the weight(s) during a number of epochs until the goal of minimizing the difference between the output and ground truth (target) is achieved (Bishop et al. 2006, Bankman 2008, Shi & He 2010). An epoch is the measure of how many times the input vectors are used to update the weights until the error between output and target converges to the desired minimum. The ANN is trained with the aim to minimize an error function ϵ for a given number of training epochs. The error is calculated as mean squared error (MSE) as given in Eq. 5.11 with n samples, Y_O outputs and Y_T targets.

$$\epsilon = \frac{1}{n} \sum_{i=1}^{n} (Y_O - Y_T)^2 \tag{5.11}$$

In backpropagation type ANN, the error is propagated back to optimize error with respect to weights in the respective layer. The optimization uses function, such as Levenberg-Marquardt (LM), to calculate the gradient of the error with respect to all the weights and attempts to minimize the error by adjusting the weights accordingly (Bishop et al. 2006, Yegnanarayana 2009). The LM backpropagation function is a most common first-choice for supervised algorithms as it achieves fast and stable convergence (Yu & Wilamowski 2011, Lourakis 2005).

The design of ANN is inspired by the biological neurons. However, the activation or inhibition in biological neurons is discrete 0,1 whereas in an ANN, the classification results (or weighted sums) are presented as continuous numbers. In order to mimic

the biological system, a transfer function is used in ANN which produces discrete results from the continuous input (Duch & Jankowski 1999, Heaton 2008). The pure linear and saturating linear transfer functions are implemented as:

$$purelin(n) = n \tag{5.12}$$

$$satlin(n) = \begin{cases} 0, & n \leq 0 \\ n, & 0 \leq n \leq 1 \\ 1, & 1 \leq n \end{cases} \tag{5.13}$$

The hyperbolic tangent sigmoid transfer function is useful when speed is more important than the exact shape of the function (Duch & Jankowski 1999). The sigmoid transfer functions are calculated as given in Eq. 5.14 and 5.15.

$$tansig(n) = \frac{2}{(1 + \exp(-2 \times n))} - 1 \tag{5.14}$$

$$logsig(n) = \frac{1}{(1 + \exp(-n))} \tag{5.15}$$

The estimation of initial weights can influence the convergence of the neural network as discussed in section 3.3.2. The suggestion by Nguyen & Widrow (1990) is to initialize the weights in random direction based on the characteristics of the input vector (Rojas 2013). Fernandez-Redondo & Hernandez-Espinosa (2000) has suggested estimation of initial weights based on the learning rate in backpropagation and the number of inputs. The weights are, therefore, initialized with random values between -1 and 1 during training. The performance is cross-validated until a stable mean of error is achieved.

The number of neurons in the input layer is equal to the number of features in the training data. The size of hidden layer is usually set between the sizes of

the input and output layers, however, the optimal size can be estimated using incremental pruning of ANN (Castellano et al. 1997, Heaton 2008). In this process, an ANN is trained to achieve an acceptable error rate within a specified number of epochs while iteratively increasing the size of the hidden layer. The process is stopped when the performance of ANN does not improve by a singe percentage point (Heaton 2008). This approach has been used to determine the optimal ANN configuration for classification of clinical profile and also CT image features.

5.3.2 Features from Clinical Profile

The clinical profile of the patient at the time of admission is assigned numeric values as listed in table 4.1 in order to create the clinical phenotype discussed in section 4.1.3.1. The features in clinical phenotype are classified to provide a vote Υ differentiating between the haematoma (based on injury, loss of consciousness, vomiting and ENT bleed etc.) or ischaemic infarct (characterized by facial weakness, arm weakness, dizziness, blurred vision or speech problems etc.).

The features in the clinical phenotype indicate the suspected pathology or trauma as given in table 5.3. Past medical history can be enquired to differentiate between quick and slow onset of symptoms called FAST (Face, Arm, Speech, Time to call), disturbance of vision, ataxia or weakness. These features help establish differential diagnosis by the doctors when the patient arrives in the emergency department (Shah & Kelly 2003). The clinical phenotype, hence, is used in the PDCAAC framework to classify the patient characteristics and generate the vote Υ. The table 4.2 enlists the suspected clinical abnormalities EDH, acute SDH, chronic SDH and ischaemic stroke which are used as targets for the classification. The presentation of EDH and acute SDH on brain CT is hyperdense while the chronic SDH and ischaemic strokes appear hypodense. Hence, the classification of clinical phenotype is used in the PDCAAC to generate vote Υ so that it differentiates between hyper- or hypodense pathologies as given in table 5.2.

TABLE 5.2: Classification of the clinical phenotype for vote Υ.

Suspected pathology	CT Appearance	Vote Υ
EDH & Acute SDH	Hyperdense	$\Upsilon = 0$
Chronic SDH & Stroke	Hypodense	$\Upsilon = 1$

TABLE 5.3: Clinical features for training the ANN. These are the presenting complaints at the time of admission to the emergency department (McCluskey 1990, Shah & Kelly 2003).

Presenting Complaint	Suspected due to
History of trauma	EDH or Ac. SDH
History of trivial trauma (or forgotten)	EDH or Ch. SDH
Loss of Consciousness	EDH
Vomiting	EDH or SDH
GCS score below normal	EDH or SDH
Hypertension	Stroke or Ch. SDH
Age	
(younger)	EDH
(older)	SDH
Unequal Pupils	EDH
Sluggish pupils	SDH
Quick onset of following symptoms *	Stroke
FAST (Face, Arm, Speech, Time to call)	
Disturbance of Vision	
Ataxia	
Weakness	
Development of above symptoms over weeks	Ch. SDH

** Can not be assessed if patient is unconsciousness.*

For example, if there is a young patient, with history of traffic accident, loss of consciousness and unequal pupils, the probability of EDH is higher. The CT presentation of the pathologies has characteristic appearance based on radio-density and time interval during injury and CT scan where blood's presentation shifts from hyperdense in immediate scan to hypodense in scans delayed for several days. This reason results in Acute SDH appearing hyperdense while Chronic SDH could appear mixed density or hypodense.

To generate a vote from the clinical phenotype, a feedforward backpropagation ANN with one hidden layer with 10 neurons and an output layer with 4 neurons is

used as shown in Fig. 5.7. The size of hidden layer is determined by incremental pruning by using 1 - 20 neurons as limits. The training function used in ANN is Levenberg-Marquardt, performance goal is set to 0, maximum number of epochs allowed is 1000, damping factor $\mu = 0.001$ and minimum gradient is $1e^{-7}$. The decrease and increase ratios of μ are 0.1 and 10 respectively.

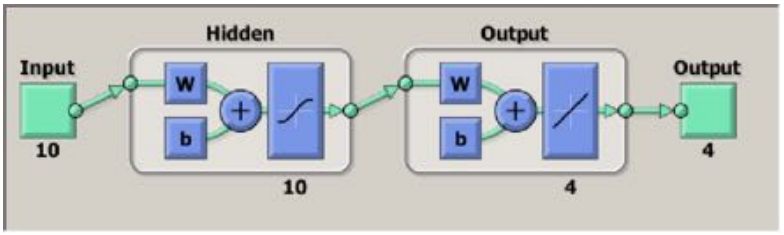

FIGURE 5.7: Architecture of the ANN for classification of Clinical Phenotype

The clinical features listed table 5.3 are selected from data of the patients given in Appendix D.2 to constitute the training matrix **NC**. The target for supervised training is defined from the diagnosis column from Appendix D.2 and is represented in the form of binary representations as given in Table 4.2. The output layer of the ANN gives the decision about probability of EDH, Acute SDH, Chronic SDH or Ischaemic Stroke. The decision vector is then converted to an index, i.e., 1, 2, 3 or 4 which represents the respective pathology. The decisions 1 and 2 are considered vote $\Upsilon = 0$ and the decisions 3 and 4 are $\Upsilon = 1$.

5.3.3 Contrast Enhancement of Probable ROI

The result of classification by ANN from the clinical phenotype generates probability of the underlying pathology which is presented as a vote Υ. The value of the vote is then used to enhance the contrast of the input image as a preprocessing step to highlight the probable regions of interest.

For example, if EDH is suspected ($\Upsilon = 0$), then the contrast of the image has to be adjusted so that the hyperdense regions become more conspicuous as compared to the surrounding parenchyma. Local contrast enhancement in brain images has

been proposed by Zhang et al. (2013) to highlight the probable ROI. Using the image characteristics from Tables 5.1 and 4.3, the histogram bins corresponding to the ROI provide the intensity ranges to select the relevant pixels and increase or decrease their discrete values to make them more discernible as shown in Fig. 5.8.

For example, the haematoma as ROI is represented within the bins 32-50 in a 64 bin histogram of the 8-bit image depending upon the radio-density of the blood at the time of scan. The corresponding pixel intensity range is selected and the values are uniformly increased by 20% which lightens the ROI and it is better distinguished from the surrounding parenchyma and bone (Fig. 5.8b and 5.8d) as intensity of the grey matter is concurrently lowered by 20%. In case of haematomas, 20% increase in brightness is empirically estimated to be the upper limit to maintain separation from the skull bone. An example of adjusting contrast in ischaemic strokes (Fig. 5.8e) is given Fig. 5.8f in which the pixels from bins 10-17 are darkened by 20% to highlight them.

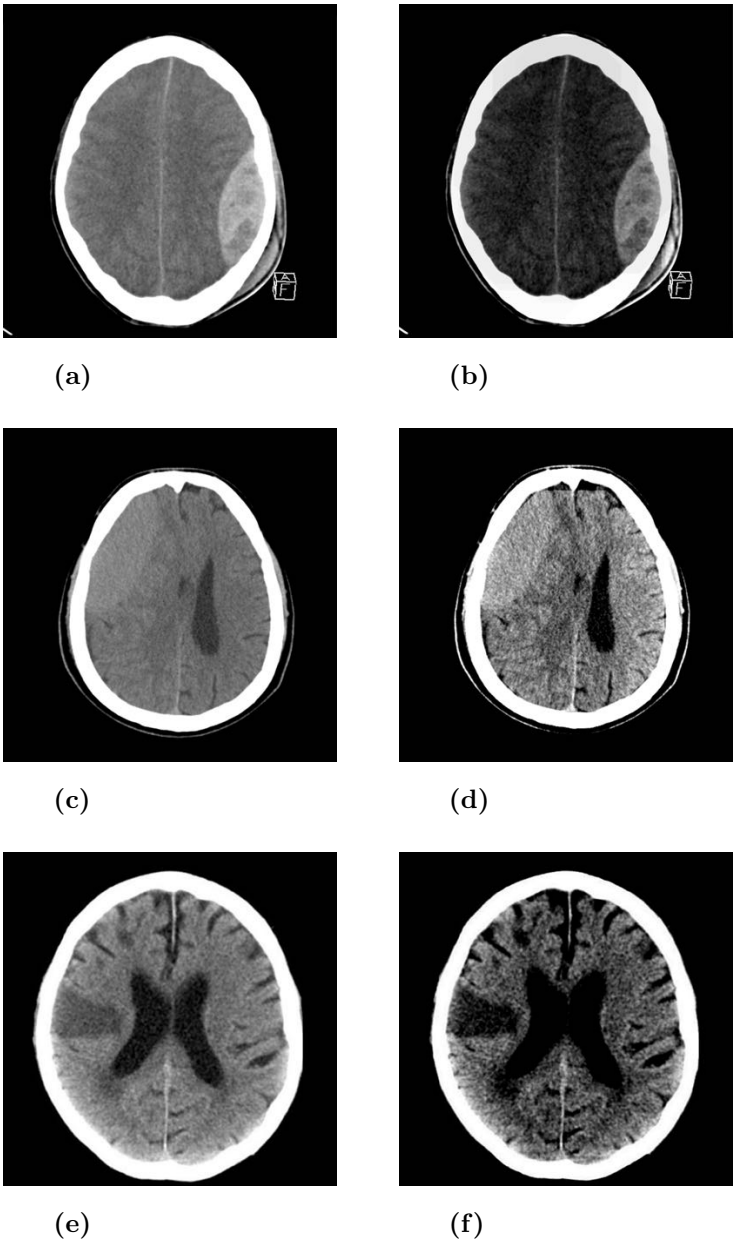

(a) **(b)**

(c) **(d)**

(e) **(f)**

FIGURE 5.8: Anisotropic Contrast Enhancement. The contrast is enhanced on the basis of suspected pathology classified by from the clinical profile. Images (a) , (c) and (e) are the input images and images (b) , (d) and (f) are obtained by anisotropic contrast adjustment.

5.3.4 Features from CT Images

5.3.4.1 Feaure Extraction

The performance of supervised learning of pattern recognition systems depends upon the features extracted during the process. Feature extraction techniques reduce dimensionality of the data so that it can be processed more effectively. An input image is represented as an $(c \times r)$ matrix $\mathbf{W} = \{w_{ij}\}, i = 1 \ldots c, j = 1 \ldots r$, whose pixels can either belong to a region of interest class Ω_0 or to a non region Ω_1. A aquare window $\mathbf{G}$, which is a $(m \times m)$ matrix containing the central pixel w_{ij} and $n-1$ nearest pixels, where $n = m^2$, is slid through the image $\mathbf{W}$. The sliding window transforms the image $\mathbf{W}$ into an $n \times s$ matrix $\mathbf{F}$ where $s = (c - m + 1)(r - m + 1)$ and the central element of a column vector, hence, represents the pixel w_{ij} of the input image.

Selection of the appropriate image features directly affects the performance of the ANN to classify pixels. In literature many features have been suggested based on the characteristics of a local neighbourhood (Guyon et al. 2008). The different features listed in Table 5.4 have been evaluated in experiments. These features have been highlighted in methods proposed by Kondo & Ueno (2012) and Lee et al. (2008) for the segmentation of medical images. Features such as the Daubechies-4 wavelets have been used in segmentation methods, however, these are computationally expensive to computer (Chaplot et al. 2006).

Arithmetic mean of a $m \times m$ neighbourhood of pixels is calculated as:

$$\text{Arithmetic mean} = \mu = \frac{1}{K} \sum_{i=1}^{K} p_i \tag{5.16}$$

Where $K = m \times m$ and p is the intensity of the pixel at location i. The median is calculated by reshaping the $m \times m$ neighbourhood into a column C by concatenating transpose of its rows, sorting the column and selecting the middle value. With

odd values of m, the middle value in the column is the central pixel in the $m \times m$ neighbourhood so it can directly be selected as well.

The geometric mean of a set $C = \{v_1, v_2, \ldots, v_n\}, n = m^2$, is calculated as:

$$\text{Geometric mean} = \left(\prod_{i=1}^{n} v_i\right)^{1/n} = \sqrt[n]{v_1 v_2 \ldots v_n} \tag{5.17}$$

The standard deviation σ of discrete pixel intensities within the $m \times m$ neighbourhood is calculated using the column C and mean μ described earlier:

$$\sigma = \sqrt{\frac{[(v_1 - \mu)^2 + (v_2 - \mu)^2 + \ldots + (v_n - \mu)^2]}{n}} \tag{5.18}$$

Variance σ^2 of discrete pixel intensities within the $m \times m$ neighbourhood is square of the standard deviation.

$$\sigma^2 = \frac{[(v_1 - \mu)^2 + (v_2 - \mu)^2 + \ldots + (v_n - \mu)^2]}{n} \tag{5.19}$$

The Shannon's entropy, H, of discrete pixel intensities within the $m \times m$ neighbourhood is the average amount of information contained within the neighbourhood. It is calculated using the column $C = \{v_1, v_2, \ldots, v_n\}, n = m^2$, probability P and logarithm of probability with base b as:

$$H = -\sum_{i} P(v_i)\ log_b P(v_i) \tag{5.20}$$

The Discrete Fourier Transform (DFT) decomposes the spatial domain image $f(x, y)$ into sine and cosine components in the frequency domain as a set of values (u, v) which are equally spaced. For the image representing the $m \times m$ neighbourhood with pixels in (x, y), the 2-D DFT is calculated as:

$$F(u,v) = \frac{1}{m^2} \sum_{x=0}^{m-1} \sum_{y=0}^{m-1} f(x,y) e^{-2\pi i(\frac{xu}{m} + \frac{yv}{m})} \tag{5.21}$$

To use as a feature with ANN, only the real part of results from DFT is used.

TABLE 5.4: List of features extracted from the CT images to be used in developing the ANN for classification.

Features
Discrete Pixel values from $m \times m$ neighbourhood
Arithmetic Mean of $m \times m$ neighbourhood
Median of $m \times m$ neighbourhood
Variance of $m \times m$ neighbourhood
Standard Deviation of $m \times m$ neighbourhood
Shanon's Entropy of $m \times m$ neighbourhood
Discrete Fourier Transform of $m \times m$ neighbourhood

Although each of the approaches discussed above have their pros and cons, they need to be evaluated on the bases of their usefulness in classification by the ANN. To ascertain the predictability of the individual features, their performance of sensitivity and false positive rate is modelled to give the receiver operator characteristic (ROC) curve. It is understood that the performance of any feature should be better than the diagonal representing mere chance, hence, this becomes a selection criterion for the features to be included in the feature vectors for the ANN. To establish the standard for acceptance, the ROC of the radiologists' performance are given in the Fig. 5.9. The annotations from the 1^{st} radiology expert are considered a benchmark and the 2^{nd} radiologists performance is quite close to the benchmark as shown in Fig. 5.9a. The junior radiologist with less than 2 years of experience in emergency radiology has a higher rate of reporting false

positives and in some cases, the major findings are missed. The performance of the junior radiologist is shown in Fig. 5.9b for comparison.

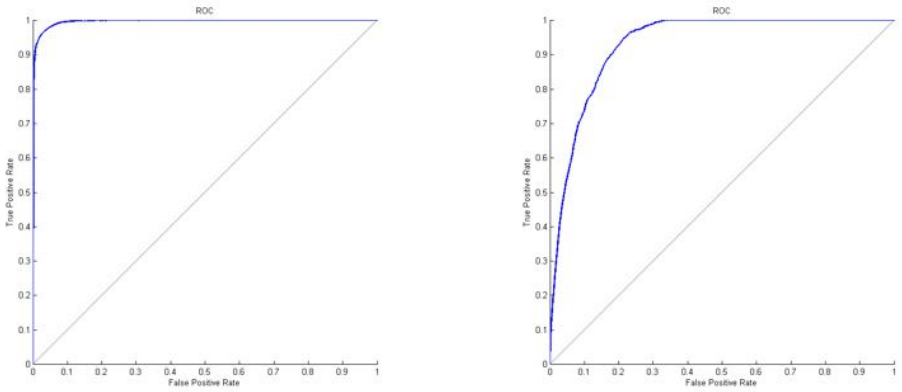

(a) **(b)**

FIGURE 5.9: The Receiver Operator Characteristics of 2^{nd} Radiology Expert (a) and Junior Radiologist (b). The annotations by 1^{st} Expert are used as baseline standard.

The ROC curves of these features are evaluated at varying neighbourhood sizes of $3 \times 3, 5 \times 5$ *and* 7×7 pixels surrounding the central pixel within the image. The results from the 3×3 neighbourhood show that the feature 'mean' of the neighbourhood shows a subpar performance as compared to others. One way of improving the poor performance of a feature is to invert it, however, the overall performance would still be lower than what is expected from the ANN.

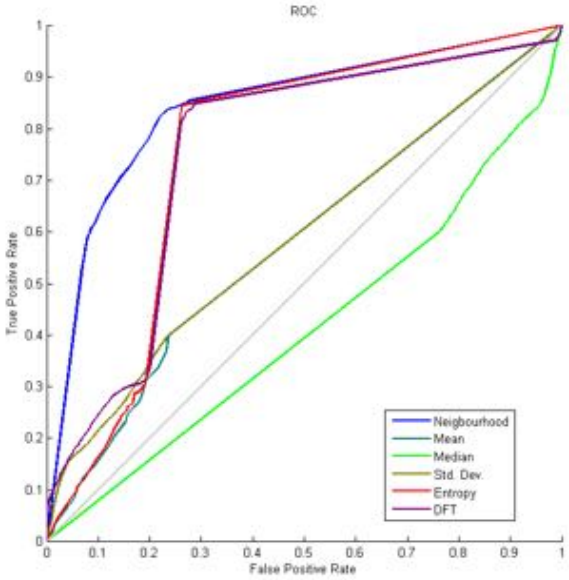

FIGURE 5.10: The Receiver Operator Characteristics of $m \times m$ neighbourhood, statistical features and DFT extracted from the CT images and used for training ANN. The value of $m = 3$.

In case of the 5×5 neighbourhood, the results are better than the previously discussed case, however, it is still not the optimal performance when considering the performance of the experts as depicted in Fig. 5.9. The features extracted from 7×7 neighbourhood show poorer results than the 5×5 neighbourhood in general.

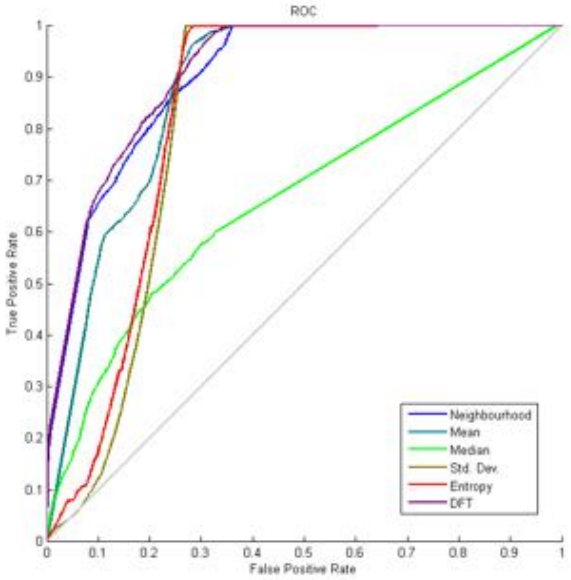

FIGURE 5.11: The Receiver Operator Characteristics of $m \times m$ neighbourhood, statistical features and DFT extracted from the CT images and used for training ANN. The value of $m = 5$.

5.3.4.2 Feature Selection

In order to test if the performance of weak predictors could be boosted, they are also evaluated in several combinations. The combinations are not exhaustive, however, they generally give improved performance than the individual features. The results in Fig. 5.13 present the ROC curves of different combinations tried during experiments with 5×5 neighbourhood. It is observed that the performance is significantly improved than previous results with weak features. The ROC of the combinations **neighbourhood + mean + DFT** (Fig. 5.13a) and **mean + standard deviation + entropy** (Fig. 5.13b) are quite similar with the latter giving slightly better results with lower false positive rate. Another consideration is the length of the feature vector which is also smaller when the latter combination is used because the 5×5 neighbourhood and DFT results in the first combination make it considerably longer.

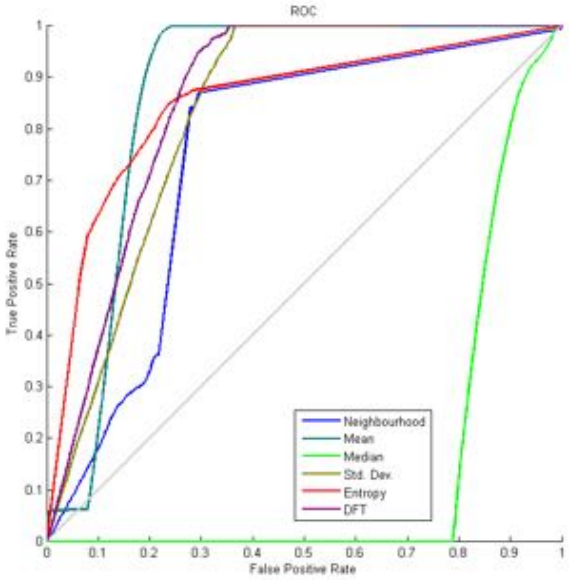

FIGURE 5.12: The Receiver Operator Characteristics of $m \times m$ neighbourhood, statistical features and DFT extracted from the CT images and used for training ANN. The value of $m = 7$.

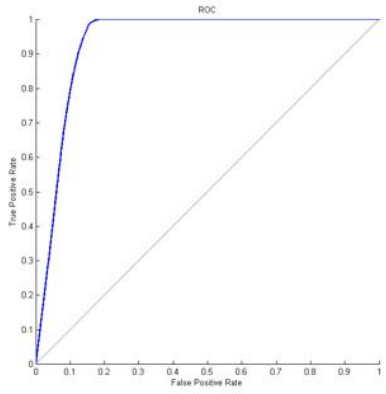

(a) Neighbourhood, Mean and DFT

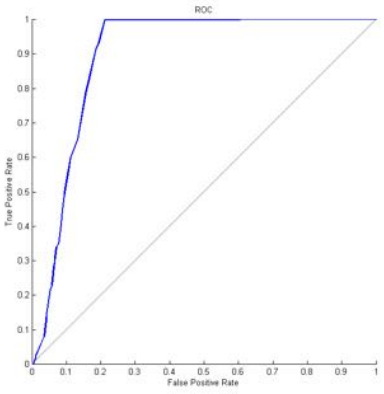

(b) Std. Dev. and Entropy

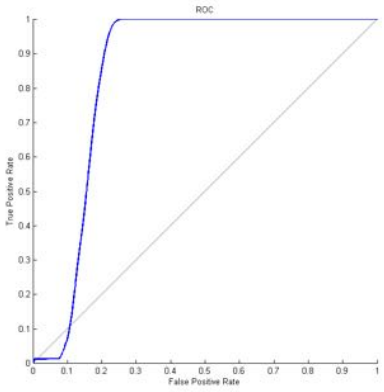

(c) Neighbourhood, Mean and Std. Dev.

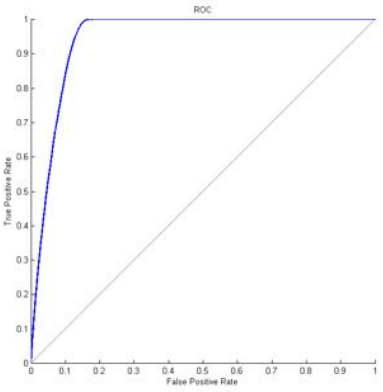

(d) Mean, Std. Dev. and Entropy

FIGURE 5.13: The Receiver Operator Characteristics of combination of the $m \times m$ neighbourhood, statistical features and DFT. The value of $m = 5$.

Based on the above considerations, a sliding window with $m = 5$ was used to extract intensity and texture features of the skull, brain parenchyma and the ROI etc. For the classification of haemorrhage pixels, the statistical features Mean, Standard deviation and Shannon's Entropy are extracted and constitute the feature vectors in **F**. For the skull bone and CSF spaces, the smoothness of the neighbourhood was significant and resulted in a higher ROC performance by the DFT. Also, these ROI have specific anatomical locations. Therefore, the DFT and pixel location are also added the feature vectors in **F** to be used for skull bone and cisterns and

ventricles. The architecture of the ANN used for classification of image features is discussed next.

5.3.4.3 Classification of CT Image Pixels

The features extracted from the brain CT scans represent the characteristics of the pixels as well as of their neighbourhoods. The PDCAAC framework is designed to identify intracranial haematomas, ventricles and cisterns and the skull bone on the axial CT images as ROI. The feature extraction and selection process has identified that the Mean, Standard deviation and Shannon's Entropy should constitute the feature vectors in $\mathbf{F}$. For the ventricles, cisterns and bone as ROI, the feature vectors include Mean, Standard deviation, Shannon's Entropy, DFT and location of pixel within the image.

The training data consists of brain CT images whose pixels are manually labelled and assigned either to ROI or non-ROI. The Fig. 5.14 presents two examples each of the haematomas, ventricles and cisterns and skull demarcated in red colour as ROI by radiology experts. In the experiments, the class Ω_0 is used to represent ROI pixels and Ω_1 represents non-ROI pixels. The features, discussed above, are extracted from the training data so that their classification using ANN could be performed.

The experiments were conducted using two architectures of ANN: Feedforward backpropagation and the Cascadeforward backpropagation. The cascadeforward networks have a connection from the input layer to every successive layer (Nakano 2012). The ANN have been used to classify the pixels because these require a few representative images to be used as training samples (Zharkova & Schetinin 2005). The Fig. 5.15 shows the feedforward and cascadeforward ANN with one hidden layer. Their input neurons are fed with the features extracted using 5×5 windows. The hidden layer consists of 10 neurons which is determined by incremental pruning and varying the size from 1 - 25 neurons. The training function

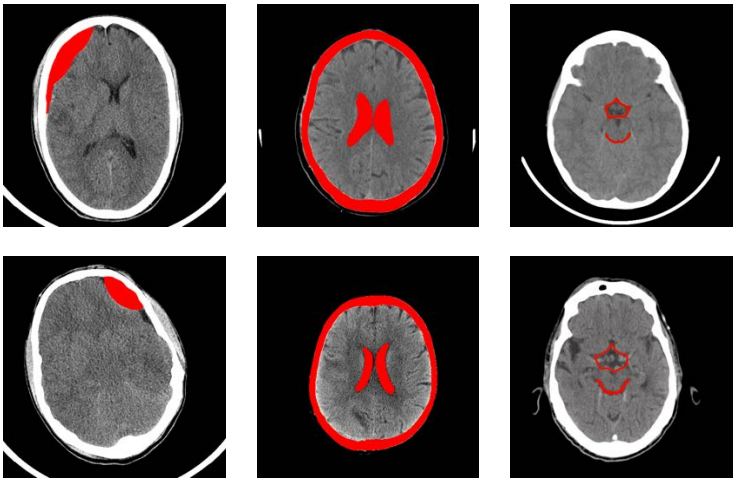

FIGURE 5.14: Manual annotation of ROI by radiology experts. Images in left column represent the annotation of haematoma. The middle column represents annotation of ventricles and skull. The right column shows the supracellar and quadrigeminal cisterns annotated by the experts.

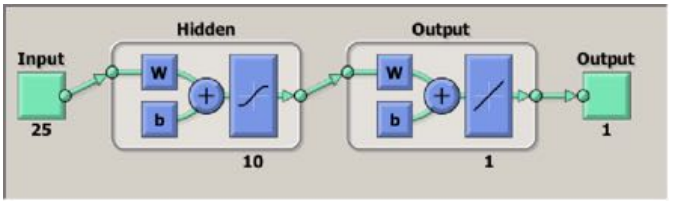

(a) Feedforward backpropagation

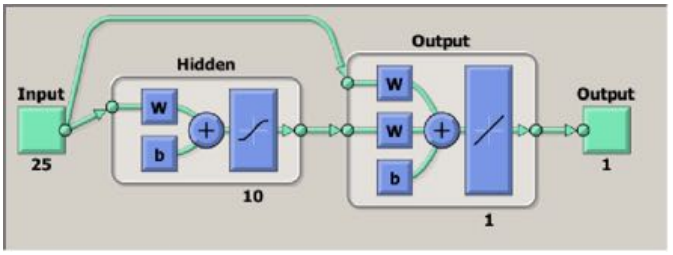

(b) Cascadeforward backpropagation

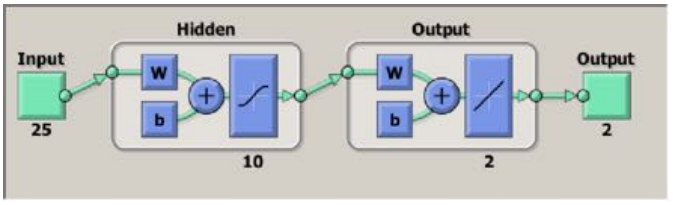

(c) Feedforward backpropagation with 2 neurons in output

FIGURE 5.15: Architecture of the ANNs for classification of CT image features

used is Levenberg-Marquardt and there is one output layer which classifies the features into Ω_0 or Ω_1. The performance goal is set to 0 and the maximum number

of epochs allowed is 1000. The value of damping factor μ is initialized at 0.001 and minimum gradient is $1e^{-7}$. The decrease and increase ratios of μ are 0.1 and 10 respectively.

The feedforward backpropagation ANN was also implemented by defining the classification target as binary patterns (01 and 10) so that the output layer had two neurons. In this scenario, the output layer has one node per class label (Heaton 2008, pp. 145-146). This architecture is referred to as *Pattern Net* in this thesis for differentiation from feedforward network with one output neuron. The experiments with the ANN architectures were further performed using two hidden layers with 4 neurons each in these (determined through incremental pruning) as shown in Fig. 5.16. The number of hidden layers were incrementally evaluated from 1 - 3, however, no significant performance improvement was observed with >2 hidden layers.

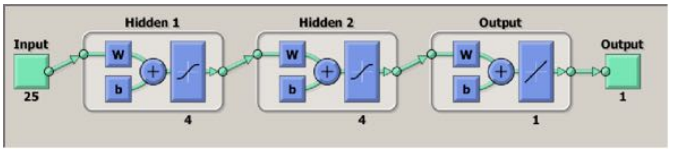

(a) Feedforward backpropagation

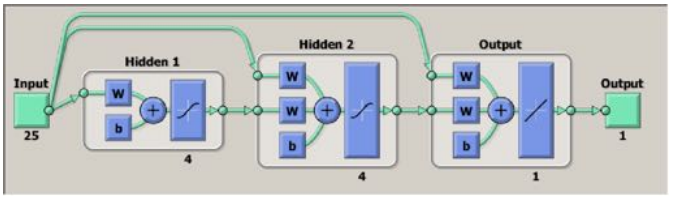

(b) Cascadeforward backpropagation

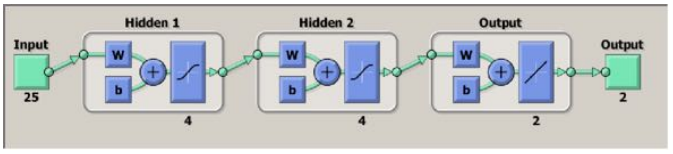

(c) Feedforward backpropagation with 2 neurons in output

FIGURE 5.16: Architecture of the ANNs with two hidden layers for classification of CT image features

In the experiments, pure linear, saturated linear and the hyperbolic tangent sigmoid functions produced better differentiation than the log sigmoid functions and a

case of haematoma is depicted in Fig. 5.17. For further experiments, pure linear function was used as transfer function.

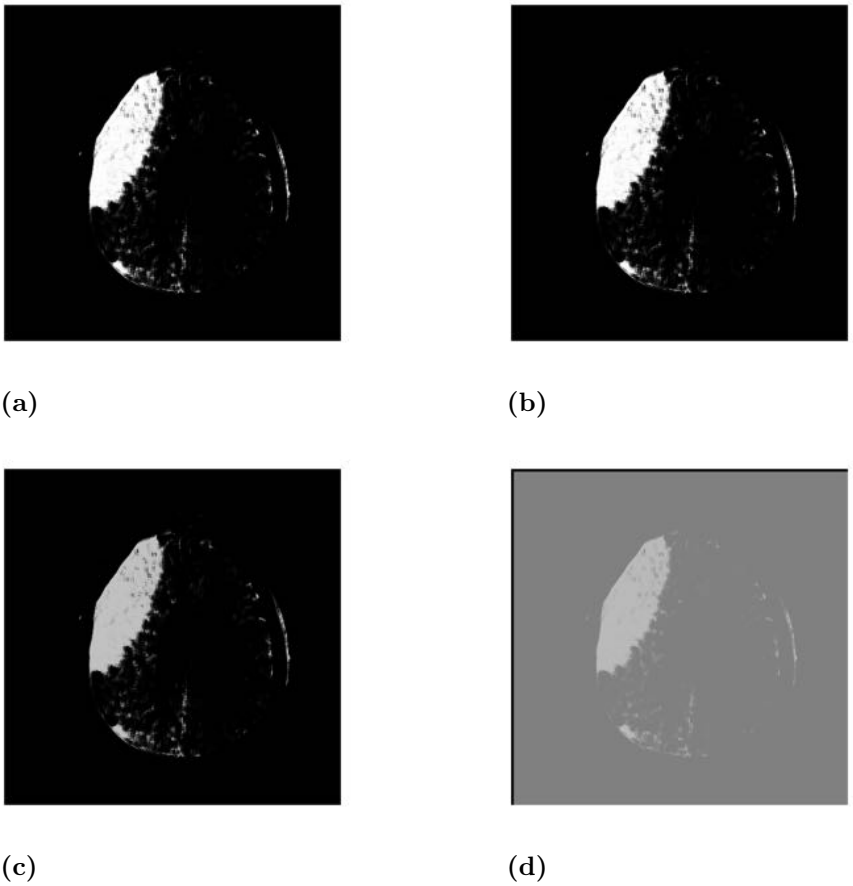

(a) **(b)**

(c) **(d)**

FIGURE 5.17: Pixel classification with different transfer functions in ANN. Images (a), (b) and (c) represent the pure linear, saturated linear and hyperbolic tangent sigmoid functions respectively, and show better differentiation of the pixels. Image (d) is the output with log sigmoid function and the differentiation between ROI and non-ROI is not very distinct.

The training and validation of classification algorithms is usually performed by partitioning the available data into a training set and a testing set. However, considering a relatively small dataset for developing CAD, a single partition poses the possibility of over-fitting and, hence, cross-validation is suggested (Bogoni et al. 2014, Arlot et al. 2010). The patient CT image data is, therefore, divided into 10 subsets of randomly selected cases and during one iteration of training, one subset is retained for testing while the algorithm is trained on the remaining subsets. This achieves a 10-fold cross-validation for the use of ANN in classification of CT image

features. The performance results of the 10 iterations are averaged to give the overall performance of the classification algorithm.

5.4 Segmentation using Active Contours

The underlying principle of active contours is to deform a boundary around the region of interest to segment it from the surrounding regions. The general parametric active contours are not able to handle the topological changes efficiently and, hence, integration of level sets within active contours has been suggested. The evolution of contours is controlled by partial differential equations which can be derived from the related evolution equation of the active contours.

The traditional approach of the active contours is based on minimizing the energies defined in Mumford-Shah's functional for segmenting the image into regions which have some form of coherence in them resulting in smoothed image and a set of curves betwixt the smooth regions. In the original Mumford-Shah approach, the segmented image is modelled as a piecewise smooth function u in the image domain Ω. The curve τ is evolved iteratively under the constraints of distance between the input image I and u, smoothness of u within the region bounded by τ and the length of the curve τ regularized by a scalar ν, as given in Equation 5.22.

$$\inf_{u,\tau} \{F^{MS}(u,\tau) = \int_{\Omega} |I-u|^2 dxdy + \mu \int_{\Omega\setminus\tau} |\nabla u|^2 dxdy + \nu|\tau|\} \tag{5.22}$$

The model penalizes for large differences between the input and the segmented image as well as for the number and lengths of the curves in the segmented image. The energies in this model refer to internal, external and constraint energies. The functional is minimized until the effect of these energies is minimum. The internal energy is dependent on the length and curvature of the contour, the external energy

is contributed by the edges and gradients in the image and the constraint energy is a user defined constraint added to the equation.

Many variations and extensions of the same have been proposed in literature and implementation of active contours have been presented both as geometric curves and active contours without edges (Osher & Sethian 1988, Osher & Fedkiw 2001, Chan & Vese 2001, Sapiro 2006) and these are examined next.

5.4.1 Existing Models of Active Contours

5.4.1.1 Geometric Active Contours

These contours are based on curve evolution and level sets representing the curves in terms of points on the curve and not the parametrizations (Osher & Sethian 1988). The points on the curve have to satisfy the condition:

$$C = \{(x, y) |\ \phi(x, y) = 0\} \tag{5.23}$$

The function ϕ is defined to based on the distance from the curve and it is positive inside, negative outside and 0 on the curve as shown in Fig. 5.18a.

$$\phi(x, y) = \begin{cases} < 0, & \text{outside the curve} \\ > 0, & \text{inside the curve} \\ 0, & \text{on the curve.} \end{cases} \tag{5.24}$$

All the points (x, y) satisfying the condition create a set called the level set of the given curve. The normal of the ϕ is defined as:

$$Normal \quad \vec{N} = -\frac{\nabla\phi}{|\nabla\phi|} \tag{5.25}$$

And the curvature of the curve represented by ϕ is calculated as:

$$Curvature \quad \kappa = div(\frac{\nabla\phi}{|\nabla\phi|}) \tag{5.26}$$

Using the method proposed by Osher & Sethian (1988), the evolution of the curve C over time t which governed by the velocity V can be considered analogous to the evolution of ϕ with respect to time as given in the following equation:

$$\frac{dC}{dt} = V\vec{N} \Longleftrightarrow \frac{d\phi}{dt} = V|\nabla\phi| \tag{5.27}$$

In curvature flow, where κ is curvature of the segment, the time varying ϕ when $V = \kappa$ is calculated as:

$$\phi(t) = \kappa|\nabla\phi| \tag{5.28}$$

5.4.1.2 Active Contours without Edges

Chan and Vese in their seminal paper proposed a method which ignores the step of finding the edge map in the image (Chan & Vese 2001). The authors proposed segmentation by minimizing the following energy functional considering the average intensities inside (c_1) and outside (c_2) the region of interest.

$$\begin{aligned} E_{cv}(c_1, c_2, C) =& \lambda_1 \int_{inside(C)} \{(u - c_1)^2 \, dxdy + \\ & \lambda_2 \int_{outside(C)} (u - c_2)^2 \, dxdy, \quad (x, y) \in \Omega \end{aligned} \tag{5.29}$$

where $u : \Omega \rightarrow \mathcal{R}^2$ is image defined on Ω. In relation to the level set function, the calculation is defined as:

$$\begin{cases} < 0, & \text{outside the curve C} \\ > 0, & \text{inside the curve C} \\ 0, & \text{on the curve C.} \end{cases} \tag{5.30}$$

And the equation can be represented with level set function ϕ as:

$$\begin{aligned} E_{cv}(c_1, c_2, \phi) = \int_{\Omega} \{ & (u - c_1)^2 H(\phi) + \\ & (u - c_2)^2 (1 - H(\phi)) + \\ & \mu |\nabla H(\phi)| + \nu H(\phi) \} dx dy \end{aligned} \tag{5.31}$$

where $u : \Omega \rightarrow \mathcal{R}^2$ is image defined on Ω, c_1 and c_2 are the average intensities, H is the Heaviside function, $\mu > 0$ determines the permissible length of boundaries and ν set the penalty for the area inside the boundaries. The evolution of the curve is depicted in Fig. 5.18a and effect of varying the penalty for μ is shown in Fig. 5.18b and 5.18c. The effect of permissible curve length on the segmentation of ventricles is shown in Fig. 5.18d and 5.18e.

The method by Chan & Vese (2001) can handle the topological changes better than the traditional active contours which rely on gradient based edges due to the implicit representation of the curve with a level set function. An assumption in the Chan-Vese model is statistical homogeneity of the pixel intensities inside and outside the region of interest which is useful in two-phase images and may not give satisfactory results when used in segmentation of medical images where multiple intensity based regions are presented.

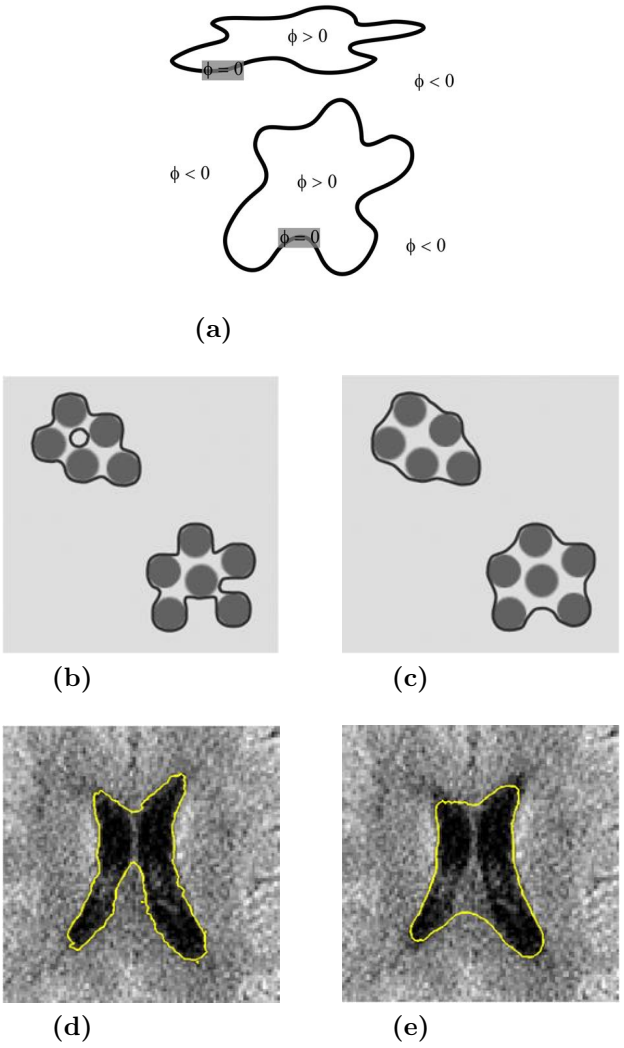

FIGURE 5.18: Active contours and level sets. Image (a) illustrates the relation of the function ϕ to the region of interest. On the boundaries, $\phi = 0$. Images (b) and (c) show the effect of curve length penalty determined by setting μ. The contour in (b) is penalized less ($\mu = 0.3$) for the curve length, hence, it moves deeper between the dots. Image (c) is observed when larger penalty ($\mu = 0.6$) is set in the algorithm. Images (d) and (e) depict the same effect, respectively, while segmenting the ventricles.

5.4.2 Limitations of Existing Models

The methods of active contours discussed above are classified amongst spatially guided techniques of segmentation. They do try to achieve finding the salient image contours but have a dependency that the initial curve needs placement inside or very close to the desired object manually by the user. This process called

seeding, is useful when the user has time to demarcate the initial curves manually on the image and then the process would continue;or, when the object is fairly well distinguished from the background and there are no other competing objects in the image which can interfere with the ROI. It can, thus, be construed that these methods are spatially blind in the beginning requiring users' interactive guidance and only then they become spatially guided.

However, in medical images like CT, the image slice may contain many anatomical structures and placing the curve in vicinity of the region of interest may not always result in segmentation of the desired region. It is quite incomprehensible for the active contour to know that a particular region has to be segmented while ignoring other regions and this results in creeping of the curve into surrounding regions as shown in Fig. 5.20d. The problem becomes more confusing when the desired ROI has less contrast than the other competing structures and the intrinsic algorithm of active contours would be pulled towards that non-ROI because of the contribution of the external energy from that region as discussed in Section 5.4 and shown in Fig. 5.19.

The results of applying contrast adjustment, discussed in section 5.3.3 and using the existing models of active contour based segmentation are given in Fig. 5.21. It is observed that the segmentation results do not improve even with the changes of contrast and the segmented ROI are not well demarcated.

Another factor to consider in context of clinical environment is that manual seeding may prove to be an additional task that the radiologist has to perform while assessing the images. It is infeasible that the radiologist would spend double the assessment time only to demarcate a boundary within the ROI. Hence, it is imperative that the active contours should automatically get seeded inside the desired anatomical structure or pathology and then slither to approximate the boundaries of that structure. A modification of the active contours method is proposed in the next section to address these considerations.

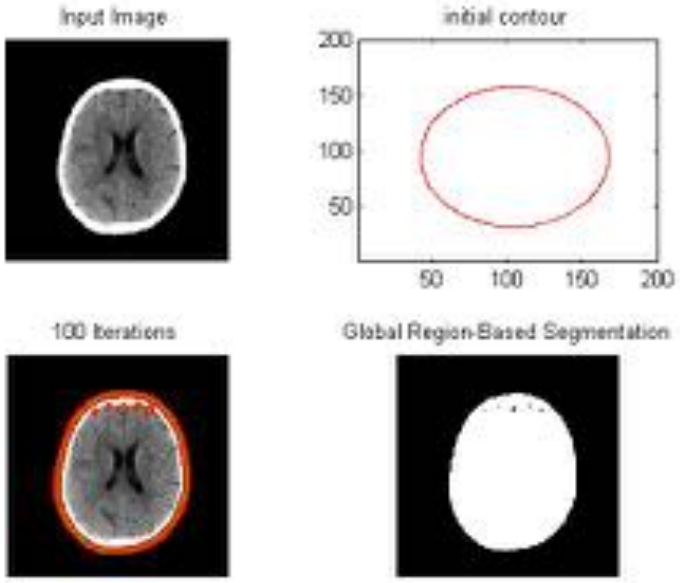

(a) Large initial contour

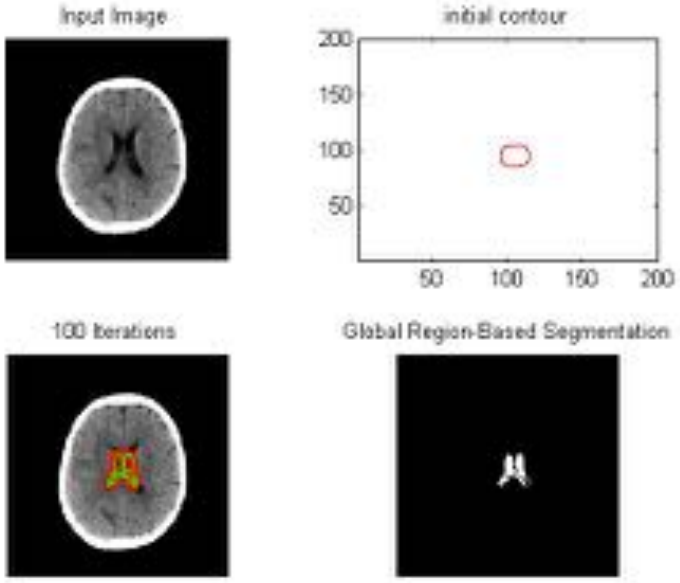

(b) Small initial contour

FIGURE 5.19: Effect of initial curve size on the final segmentation results using Chan-Vese model of active contours. Image (a) is initialized with a large curve which adheres to the skull boundary. Image (b) is initialized with a small curve which only segments the ventricles in the given slice.

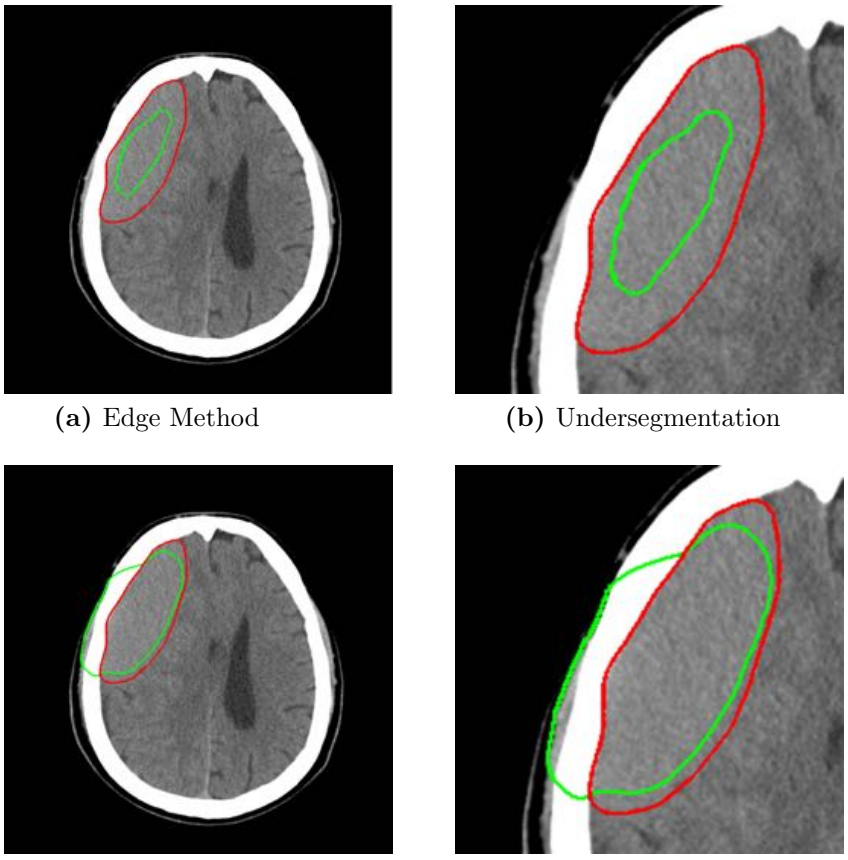

(a) Edge Method **(b)** Undersegmentation

(c) Chan-Vese **(d)** Oversegmentation

FIGURE 5.20: Segmentation results from state of the art Active Contour methods. Green curve shows the active contour while red is the manual demarcation. The initial curve is manually drawn by the user in the form of a polygon within the region of interest. Image (a), enlarged in (b) shows output with 'Edge' option. After 400 iterations, the curve evolution stops but it fails to demarcate the full ROI and results in undersegmentation. Image (b) is enlarged section of (c) which is the result of 'Chan-Vese' option with 400 iterations. It can be seen that the final curve creeps into the adjacent skull bone outside the ROI resulting in oversegmentation.

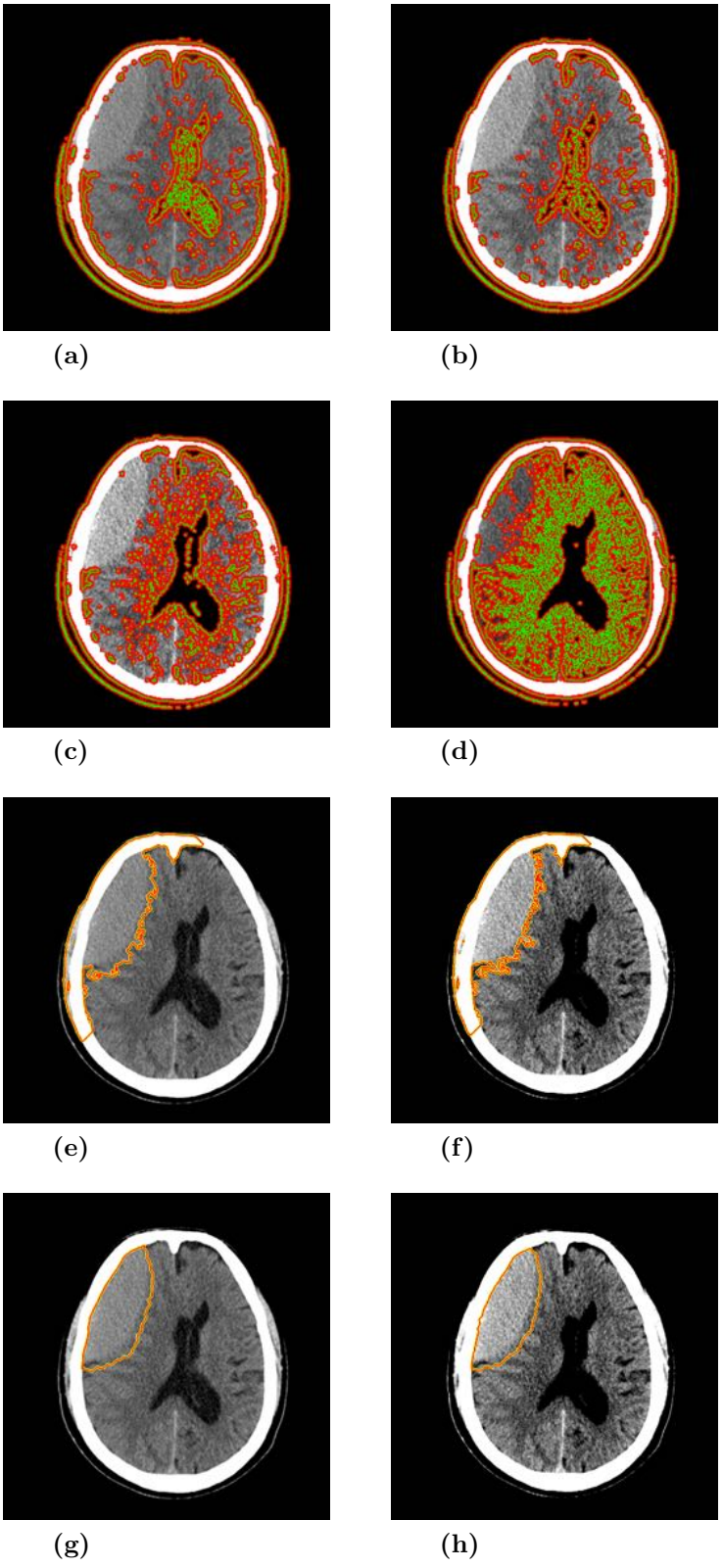

FIGURE 5.21: Segmentation results from state of the art Active Contour methods after contrast adjustment. Images (a) - (d) show segmentation output from the DRLSE algorithm. Images (e) and (f) are the results of the Chan-Vese model. Images (g) and (h) are produced with Edge model of the active contours.

5.4.3 Modified Active Contour (MAC) Method

To circumvent the problems identified in Section 5.4.2, a method utilising ANN is proposed which can both provide an initial curve within the desired ROI and also contribute as a constraint to the evolution function. The work flow is presented in Fig. 5.22. The ANN is trained to classify pixels that belong to a particular ROI within the images and then the decision output from ANN is subjected to gradient based edge detection. The disjoint regions are ignored and a closed curve is formed around the candidate ROI. This curve becomes the initial seed, provides a vote β_H in cases of haematomas and also constrains evolution of curve for the proposed modified active contour method.

The ANN in this context is supplemented by the clinical profile of the patient. This is analogous to the principle of polyrepresentation discussed in section 2.1 which states that multiple representations increase the probability of establishing the differential diagnosis. In the method described below, the clinical profile and image characteristics are combined based on the underlying medical condition. The overlap of two representations results in more efficient demarcation of the pertinent regions on the brain CT scans. This premise is also supported by the research presented by McCreadie & Oliver (2009) and Robinson (1997). The implementation details of the MAC are discussed next.

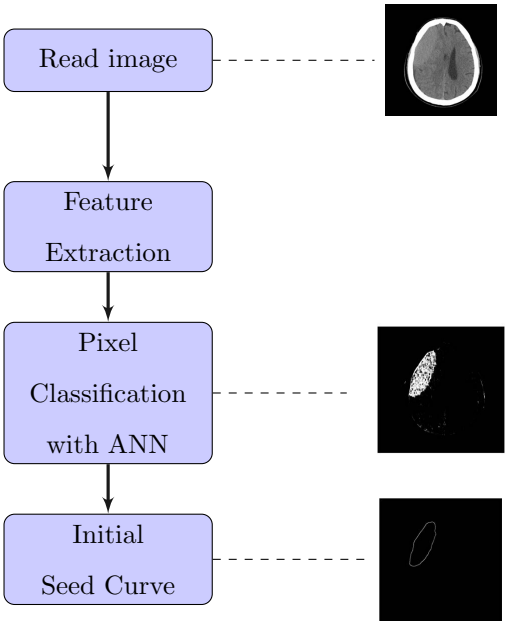

FIGURE 5.22: Work flow of proposed method for automatic seeding. The input image is read and statistical image features are extracted to constitute the feature matrix for the ANN. The output of ANN is processed with gradient based edge detector to form the initial seed curve for the active contours while ignoring disjoint, misclassified pixels.

5.4.3.1 Location vote β_H for Haematomas

The output of the ANN is a collection of pixels whose probability of belonging to an ROI is predicted by the ANN. To convert the continuous numbers into discrete decisions, the transfer function is used so that the pixels are either classified as 0,1 representing the non-region and the ROI respectively. Therefore, the resulting set S_{ANN} contains all true and false positives and negatives.

To ignore the false positives appearing as disjoint pixels, the 'watershed transform' is used to find the watershed region with maximum number of pixels. Watershed transform assumes the image analogous to a topographical relief that is flooded with water to find local minima (Meyer 1994). The relief in the image is the gradient and the algorithm segments the regions based on the difference of gradient. However, too many minima can generate spurious regions irrelevant to the problem but the transform is generally useful when the image contains a large uniform region

along with smaller disjoint regions e.g., binarized image of ROI with misclassified pixels that are distant from the ROI.

The collection of the true positives is assumed to be a larger minima than the smaller disjoint false positives. Hence, the spatial proximity of the classified pixels is used to prune the disjoint, misclassified regions and give the pixels in ROI as the set $R_{ANN} \subseteq S_{ANN}$. Therefore, in a square image of $m \times m$ dimension, the matrix $\mathbf{y}$ becomes a set of pixels, such that for every location $\{p_i, q_i\}, i = 1 \ldots m$ in $\mathbf{y}$, the specified pixel with $label = 1$ belongs to the set of pixels in the ROI and the equation below only specifies the true positives predicted by the ANN:

$$\mathbf{y} = \{p_i, q_i | (p_i, q_i) \in (R_{ANN})\}, \quad i = 1 \ldots m \tag{5.32}$$

The location of the largest watershed provides the seeding point of the initial seed for the active contour. This alleviates the problem of placement of the initial curve as discussed in section 5.4.2 and the proposed approach, hence, does not require the user to manually specify the ROI. Depending upon the underlying requirement, the radiologist can set the ROI to be the skull bone, brain parenchyma, haemorrhage and CFS spaces like cisterns or ventricles.

The ideal midline has been estimated earlier and the relation $\Psi(x)$ of a pixel from ANN output $R_{ANN}(x)$ in relation to the pixel in ideal midline $M(x)$ in the same row of image is calculated as:

$$\Psi(x) = R_{ANN}(x) - M(x) \tag{5.33}$$

On the image being observed, the possible values of $\Psi(x)$ would be:

$$\Psi(x) = \begin{cases} < 0, & x \text{ on left of midline} \\ > 0, & x \text{ on right of midline} \\ 0, & \text{otherwise} \end{cases} \tag{5.34}$$

For most of the TBI cases, the location of haematoma is usually 60% temporoparietal, 20% frontal and 20% parieto-occipital. Therefore, a correction factor ψ is used as a constraint ($|A(x) - M(x)| > \psi$) because the haematoma pixels would not be in the very close vicinity of, or on, the midline. Hence, pixels whose horizontal separation is more than ψ are considered and for the n total rows in the image, the vote β_H is estimated as given in Eq. 5.35.

$$\beta_H = \sum_{\substack{i=1 \\ |\Psi(x)_i| > \psi}}^{n} \Psi(x)_i \tag{5.35}$$

$$\beta_H = \begin{cases} < 0, & \text{haematoma on left of midline} \\ > 0, & \text{haematoma on right of midline} \\ 0, & \text{otherwise} \end{cases} \tag{5.36}$$

Direction of the midline shift D is estimated (section 5.2) and a sign function assigns a weight to direction vote α_H as given in Eq. 5.9. The output of ANN provides candidate pixels which should be within the ROI and the vote β_H is estimated as given in Eq. 5.35. The location confidence for initial curve location $conf(Loc_{init})$ is then calculated as:

$$conf(Loc_{init}) = \alpha_H + \beta_H \tag{5.37}$$

The $|conf(Loc_{init})| > 0$ indicates that there is a probable haematoma in the given case. Using the $conf(Loc_{init})$, the initial curve is placed where the voting agrees according to table 5.5. In this way, the initial curve for the active contour automatically gets seeded and provides the necessary seeding mask. It should be

noted, however, that the CT is a mirror image of the anatomy of the patient as the CT is visualized from below upwards. Hence, the presentation of haematoma on the left on CT is actually right side of the patient's brain and vice versa.

TABLE 5.5: Voting scheme for the probable location of haematoma on the CT image. The strong agreements are shown in bold. Opposite votes are considered detection errors in either of the two. A vote of 0 from both signifies absence of any haematoma detected by the approach.

α_H \ β_H	-1	0	1
-1	**Left**	left	error
0	left	none	right
1	error	right	**Right**

5.4.3.2 Defining Constraint Energy

Considering the formulation of the active contours based on Mumford-Shah functional on an image domain $\Omega \subset \Re^2$, and an image $I : \Omega \rightarrow \Re$, and the curve τ dividing the image into subregions using the fitting function u, it is defined as:

$$\inf_{u,\tau} \{F^{MS}(u,\tau) = \int_{\Omega} |I-u|^2 dxdy + \mu \int_{\Omega \setminus \tau} |\nabla u|^2 dxdy + \nu|\tau|\} \tag{5.38}$$

where $|\tau|$ is the boundary length and μ and ν are regularising weights.

The above functional has been simplified and modified to achieve higher practical applicability. The evolving contour is driven by an energy towards the salient boundary. For a set of points $\mathbf{v} = \{x_i, y_i\}, i = 1 \ldots n$ and a curve segment τ, the energy is defined as a combination of internal (E_{int}) and external (E_{ext}) energies as given below:

$$E = E_{int}(\mathbf{v}(\tau)) + E_{ext}(\mathbf{v}(\tau))d\tau \tag{5.39}$$

The internal energy (E_{int}) is dependent on the length and curvature of the contour and the external energy (E_{ext}) is contributed by the edges and gradients in the image. The external energy contributed by the strong edges such as *air - skull*, *skull - brain tissue* and *brain tissue - CSF spaces* can compel the active contour to approximate these edges and ignore the weaker edges and gradients of the ROI, e.g., haematoma. In such cases the segmentation results will adhere to strong edges as shown in Fig. 5.19. The active contour in Fig. 5.19a is initialized with a large curve which segments the CT at the air - skull boundary. The segmentation with a smaller initial curve, Fig. 5.19b, detects the strong gradient and edge between the parenchyma - ventricles and adheres to it. Though these results do not reject the usefulness of active contours and in some situations it could be necessary to segment these regions, however, these results are considered poor if haematoma is the ROI.

A constraint E_{con} is, therefore, added to the equation to steer the contours towards or away from particular features as required in the given problem space e.g., automatic seeding, spatial location and pixel classification priors. The equation then becomes:

$$E = E_{int}(\mathbf{v}(\tau)) + E_{ext}(\mathbf{v}(\tau)) + E_{con}(\mathbf{v}(\tau))d\tau \tag{5.40}$$

The problem of under-segmentation (as shown in Fig. 5.20b) is also minimized because the ROI will be at least as big as the R_{ANN} and the active contour is designed to evolve from the initial curve. The curve C_{init} bounding the R_{ANN}, hence, is used to imposes a constraint such that evolving curve C_{evol} remains at least same size or larger than C_{init}. This is defines energy E_{ann}, given in Eq. 5.41,

based on $L = C_{evol} - C_{init}$ which penalizes the algorithm if the evolving curve shrinks inwards within the bounds of the region R_{ANN}.

$$E_{ann}(\mathbf{v}(\tau)) = \begin{cases} 0, & L \geq 0 \\ -(L) & \end{cases} \tag{5.41}$$

The problem of oversegmentation due to creeping of the active contour into the surrounding regions is minimized by keeping the distance D between the evolving curve C_{evol} and the initial curve C_{init} as low as possible within the image domain Ω as depicted in Fig. 5.23. The gradient based stopping criterion, discussed in next section, stops further evolution of the active contours.

$$D(C_{evol}, C_{init}) = \oint |C_{init} - C_{evol}|^2 dxdy \tag{5.42}$$

The distance $D(C_{evol}, C_{init})$ is updated within successive iterations. This distance is depicted in Fig. 5.23 with red bidirectional arrows between the initial curve (red dots) and the evolving curve (black dashes).

The problem of active contours topologically breaking into multiple regions, as shown in Fig. 5.21a - 5.21d can supplant the requirement of segmenting one distinct haematoma as ROI. The vote $conf(Loc_{init})$ discussed in section 5.4.3.1 provides an estimate of the probable location of ROI in case of haematomas and initial seed curve and $|conf(Loc_{init})| > 0$ confirms that there is a probable ROI present in the image. A counter $J = \textbf{number of curves} - 1$ is used to maintain count of the topological breaks of the evolving curve. This counter will be zero if there is only one evolving curve and will be >0 in case there are multiple spurious disjoint curves. From the $|conf(Loc_{init})|$, a scalar K is calculated as:

$$K = \begin{cases} 0, & |conf(Loc_{init})| > 0 \\ 1, & conf(Loc_{init}) = 0 \end{cases} \tag{5.43}$$

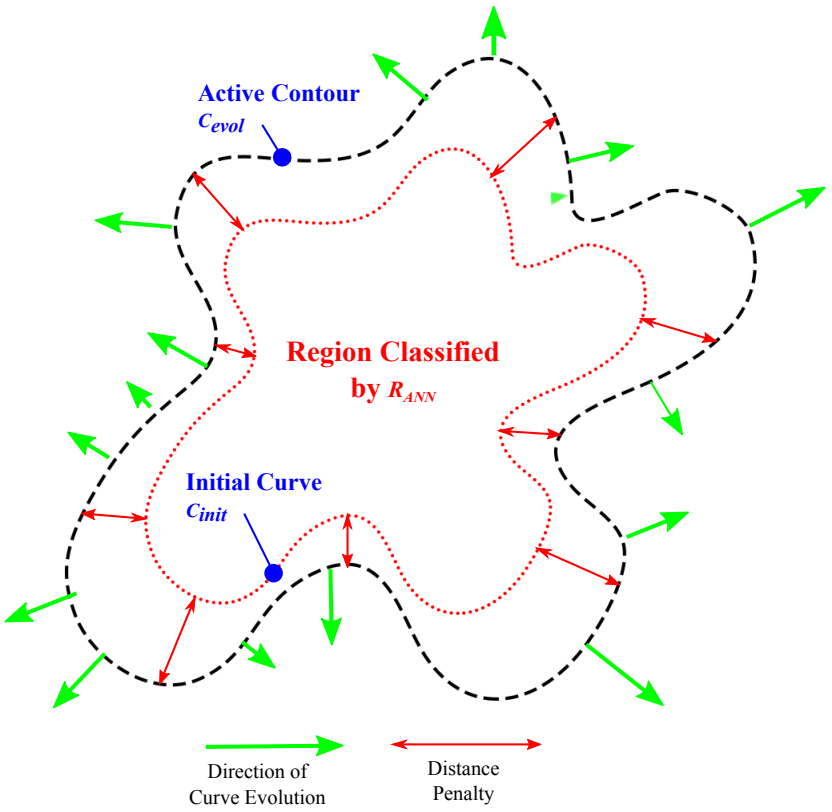

FIGURE 5.23: Distance based Constraint to regulate the evolution of the curve. The curve with red dots is the initial seed cure. The curve with black dashes is the evolving curve. The green arrows show the direction while the red arrows represent the distance between the two curves which imposes the constraint.

The constraint $E_{loc}(\mathbf{v}(\tau))$ is the defined as $E_{loc}(\mathbf{v}(\tau)) = K + J$. In the proposed approach, the $E_{con}(\mathbf{v}(\tau))$ given in Eq. 5.40 is contributed by the classification results generated by the ANN. The identified pixels E_{ann}, their spatial information E_{loc} and the distance from Eq. 5.42 are used in the formulation of Eq. 5.44 which defines the constraint energy.

$$E_{con}(\mathbf{v}(\tau)) = E_{ann}(\mathbf{v}(\tau)) + E_{loc}(\mathbf{v}(\tau)) + D(C_{evol}, C_{init}) \tag{5.44}$$

The successive evolution of the contour is constrained by minimizing the $E_{con}(\mathbf{v}(\tau))$. If the $E_{ann}(\mathbf{v}(\tau))$ or the $E_{loc}(\mathbf{v}(\tau))$ become greater than zero, the evolution of the curve is stopped. The constraint $E_{loc}(\mathbf{v}(\tau))$ is relaxed when the bilateral ventricles and cisterns have to be segmented. The distance $D(C_{evol}, C_{init})$ is updated during

the iterations until the gradient based stopping criterion is met. The combined effect of the constraints defined here attempt to minimize the weaknesses of the existing state of the art implementation of active contours that have been described in section 5.4.2.

The time complexity of the proposed approach is asymptotically bounded by the time complexity of the traditional active contours model which is $O(p^2)$ where p is the number of points on the larger dimension of the discretized curve lattice.

5.4.3.3 Stopping Criterion using Gradient

The pixels in the set R_{ANN} represent a large portion of the ROI and, hence, to estimate the average intensity of the region inside curve, a large sample is available. This average intensity can contribute to an improved gradient calculation to differentiate the regions inside and outside the curve as shown in Fig. 5.24.

The gradient term $\mu \int_{\Omega \setminus \tau} |\nabla u|^2 dxdy$ from Eq. 5.4.3.2 is dependant on the uniformity of the region specified by u. The uniformity in turn depends upon the gradient which should be minimized within the segmented region.

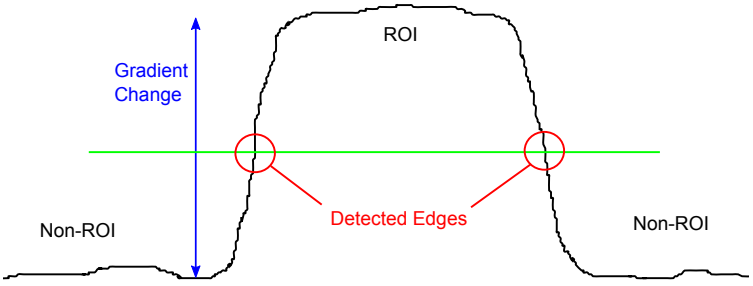

FIGURE 5.24: Edge detection using difference in gradients inside and outside the ROI.

The problem of faint and weak boundaries in medical images strongly influences the demarcation of edges. The active contours can creep out of the region of interest if the gradient difference near boundaries is small (which could be due to noise or

intensity inhomogeniety). Providing a larger initial area by the R_{ANN} minimizes this problem by making the gradient difference large between neighbouring regions.

5.5 Visualization of the ROI

The desired regions are classified by the ANN and the active contours refine the boundaries and the results are presented to the observer as shown in Fig. 6.15 and 6.16. When the results are presented, only the green coloured region of interest is displayed. The user then decides whether the results are acceptable or not.

To assist in the measurements, a reference grid is overlaid on the segmented ROI as shown in Fig. 5.25. The grid lines corresponds to the measurement calibration performed earlier during the training process on reference images. The presence of grid allows the user to estimate the sizes of the regions.

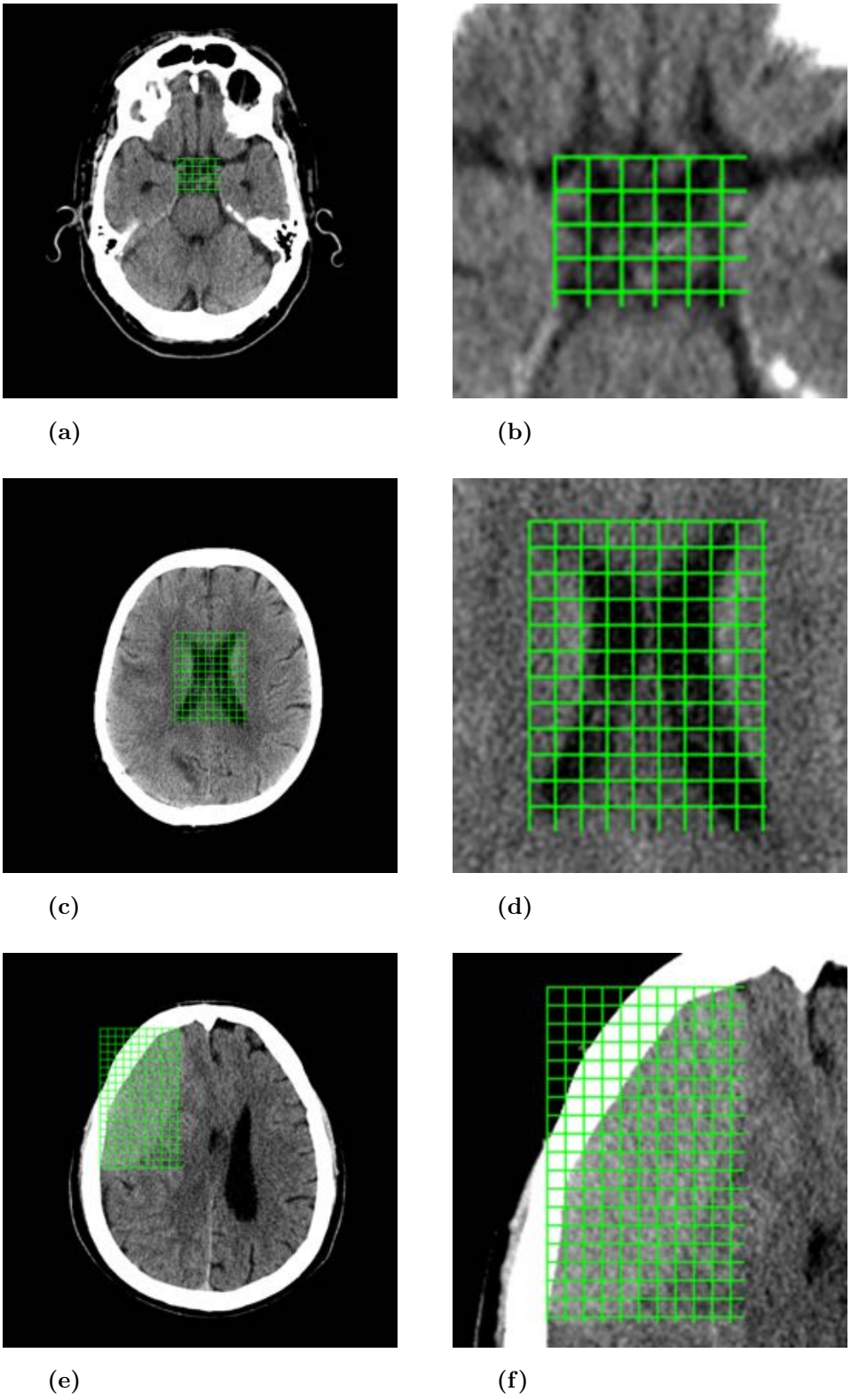

(a) **(b)**

(c) **(d)**

(e) **(f)**

FIGURE 5.25: Output of the proposed method showing identified ROI. Images (a)and (b) shows a grid overlaid on the suprasellar cistern, (c) and (d) demarcates the lateral ventricles and (e) and (f) identifies the haematoma.

5.6 Measurements and Estimation of Volume

The CT scan studies in DICOM format are viewed using 'brain window' (window width = 80, window length = 40) with image size of 512 × 512 pixels. The relevant slices from the study are selected and a reference ruler is overlaid on the images to calibrate the measurement algorithm. A radiology expert then provides the measurements in an interactive session using a simple user interface and the averages are stored as benchmarks P_{cal} for subsequent automatic measurements by the algorithm. There is an option to use Metric or Imperial units for measurements. The value of P_{cal} is also confirmed from the DICOM Header specifying the spatial resolution of the CT machine being used.

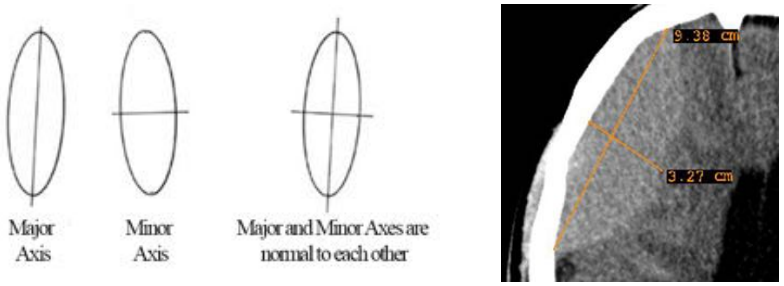

(a) **(b)**

FIGURE 5.26: Measurements of haematoma on a single CT slice. Image (a) shows the axes along which the measurements are performed. Image (a) shown manual annotation by a radiology expert.

The curves identified in previous step are modelled as contiguous image regions and are used to determine measurements such as extrema, area, orientation and axes lengths. A grid is overlaid on the ROI to show measurements (Fig. 5.25a) and the grid spacing corresponds to the calibrated pixels P_{cal} obtained earlier. The curve's 'Orientation' is a scalar representing the angle between the x-axis and the major axis of the region depicted by the yellow line in Fig. 5.25c. The green circle in Fig. 5.25c marks the point where the minor axis intersects normal to the major axis.

Rotating the curve according to the estimated orientation allows more precise measurement of the haematoma which could be required in crescent shaped subdural haematomas. The algorithm then counts the number of pixels in respective linear measurements (major and minor axes) and this is divided by P_{cal} to give the Metric or Imperial measurements of the ROI.

The haematoma in 2-D axial CT slices can be considered an ellipse and hence, the perimeter can be estimated to give permissible length of the boundary. The perimeter of an ellipse is difficult to calculate and the approximation is true to about 5% when the length of major axis is no longer than 3 times the length of the minor axis. The approximation uses the following formula :

$$Perimeter \approx 2\pi\sqrt{\frac{a^2+b^2}{2}} \tag{5.45}$$

Another approximation which can be used is:

$$Perimeter \approx \pi\left[3(a+b) - \sqrt{(3a+b)(a+3b)}\right] \tag{5.46}$$

However, Kothari et al. have proposed a simpler formula to calculate the volume V of intracerebral haematoma. The volume of ellipsoid equation given here assumes $\pi \approx 3$ for simplification and the rationale is explained by Kothari et al. (1996).

$$V = \frac{a \times b \times c}{2} \tag{5.47}$$

Where a is the largest diameter of haematoma (major axis), b the largest diameter normal to a (minor axis), and c is the approximate number of CT slices with haemorrhage multiplied by the slice thickness.

The brain CT scans used in experiments were obtained using *brain protocol* on Toshiba Activion 16, with $1mm$ slice thickness and pixel spacing of 0.468 in both

axes (x,y) in the 16-bit, 512×512 pixel DICOM images and also Philips Brilliance 16, with $5mm$ slice thickness and pixel spacing of 0.3535 in both axes (x,y). The Philips Brilliance allocates 16-bit for imaging but stores 12-bit, 512×512 pixel DICOM. The technical details of the CT machines are given in Appendix E.

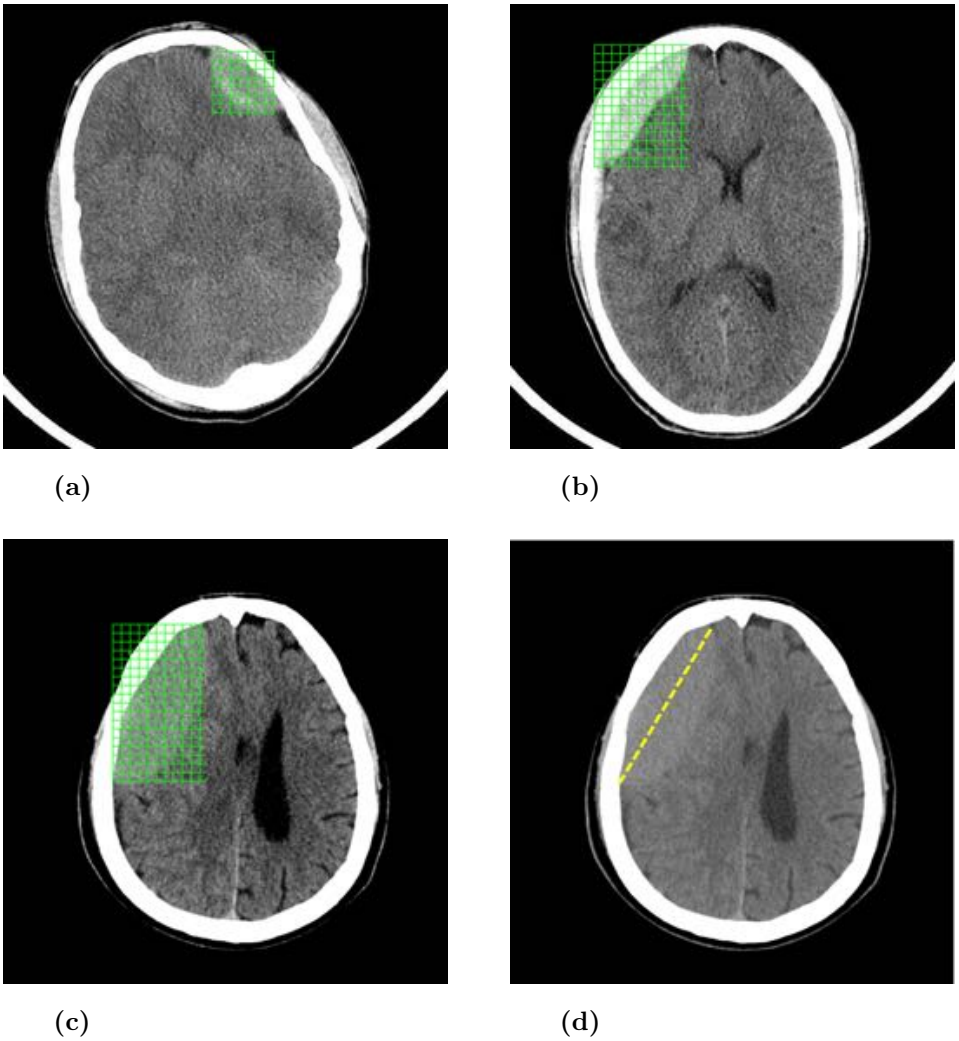

FIGURE 5.27: Output of the proposed method. Images (a) - (c) show a grid overlaid on the identified ROI to assist in estimating size. The extents of the grid correspond to the extents of the ROI. Image (d) shows the orientation of the major axis of the ROI. The yellow line is along the major axis and the green circle marks the intersection of the minor axis.

5.7 Matching CT with Marshall et al. Rating

Assessment of the severity of the trauma by consulting CT classification schemes such as one proposed by Marshall et al. (Table 2.2) is a norm in the emergency departments to establish prognosis, mortality, morbidity and hospitalization time after trauma (Marshall et al. 1991). In acute neuroimaging, the three key slices assessed are the brainstem, basal ganglia and level of lateral ventricles as shown in Fig. 2.7 for inspecting sizes and positions of cisterns and ventricles and visibility of the sulci (Smirniotopoulos 2012, Haacke et al. 2010). The haematomas can present in locations discussed in section 2.6.3 and, therefore, the relevant slices have to be processed to estimate their size and volume.

The compressed or absent cisterns are seen in Marshall et al. ratings II and III while midline shift classifies IV and above. The presence of mixed or high density lesion $> 25cm^3$ is classified as rating VI. When these characteristics are not identified, the CT would fall in rating I or normal. Since the experiments were conducted on the cross-sectional, noncontrast CT studies performed at the time of admission of within early hours of injury, none of the patients had the mass lesions removed at that time. Hence, no CT with Rating V were used in the experiments.

The estimated classification of the CT is then used either in the mortality prediction chart given in Fig. 2.9 or in Table 2.11 to calculate the score and establish prognosis after the brain trauma episode.

5.8 Summary

The integration of CAD into clinical environment, such as radiology, offers great potential in terms of improving performance, reducing errors and speeding up the diagnostic process (van Ginneken et al. 2011). The PDCAAC framework is proposed to facilitate the radiologists in a seamless manner and provide a second

opinion in the analysis of CT scans of TBI patients. The framework offers significant improvement over the existing methods by minimizing the need for manual seeding of ROI or setting of parameters of the algorithms.

The segmentation of the desired ROI in PDCAAC is achieved by a modified active contour method. Active contours and level sets methods have gained considerable noteworthiness amongst segmentation algorithms based on their capability to delineate entire geometric shapes as bounded regions. However, many of the implementations require careful placement of the initial curve within the probable ROI which is called seeding. The modified active contour method in the PDCAAC circumvents this requirement by using clinical and imaging data of the patient to predict possible location of the ROI. The framework uses ANN's for classifying the clinical phenotype of the patient and features from brain CT scans and predict the location of the ROI. The classification results from ANN also constrain evolution of the active contour to minimize undersegmentation or oversegmentation of the desired ROI.

This chapter has presented the implementation details of the PDCAAC framework. The discussion entails extraction of features from the clinical profile, contrast adjustment of the CT image, extraction and selection of features from the brain CT scans and segmentation using modified active contour method. The estimation of intracranial measurements and volumes of haematomas and matching of the CT image findings with the Marshall CT Rating have also been explained. The results of evaluation of the PDCAAC framework on patient data, including cross-sectional TBI and non-trauma cases, are presented and discussed in the next chapter.

Chapter 6

Results and Discussion

Not everything that can be counted counts, and not everything that counts can be counted.

Albert Einstein

6.1 Evaluation Measures

Statistical evaluation of the diagnostic results and their significance is emphasized in clinical practice (Mould 1989, Hosmer Jr et al. 2013). It, therefore becomes important that the performance of automated systems be evaluated and compared with the intuition and manual annotation of the experts to ascertain the applicability of CAD systems in clinical and research environments. The premise that CAD systems can give useful second opinion and decision support to the clinicians and radiologists needs ample endorsement through statistical analyses for acceptance. The method proposed in this thesis is evaluated using following statistical measures which have established reliability in assessing the data.

6.1.1 Sensitivity, Specificity, Precision, Recall and ROC

The accuracy of diagnostic features is often presented in terms of sensitivity and specificity (Reitsma et al. 2005, Sokolova et al. 2006). For evaluation, true positives (TP), true negatives (TN), false positives (FP) and the false negatives (FN) are calculated for estimating sensitivity and specificity based on Table 6.1.

TABLE 6.1: Sensitivity and specificity

	Ground Truth	
Algorithm's output	*Feature Present*	*Feature Absent*
Feature detected	True Positive	False Positive
Feature not detected	False Negative	True Negative
	Sensitivity = $\frac{\sum \text{True Positive}}{\sum \text{Feature present}}$	Specificity = $\frac{\sum \text{True Negative}}{\sum \text{Feature absent}}$

Sensitivity reflects the algorithm's ability to identify the given condition correctly and is calculated as:

$$Sensitivity = \frac{\text{TP}}{\text{TP} + \text{FN}} \tag{6.1}$$

The term sensitivity is more often used in biomedicine while in machine learning it is referred to as 'recall' (discussed below). Similarly, specificity relates to the ability to exclude a condition correctly and is calculated as:

$$Specificity = \frac{\text{TN}}{\text{TN} + \text{FP}} \tag{6.2}$$

The measure *recall* can be used to identify the ratio of pixels classified by the algorithm as belonging to the ROI to the pixels classified as belonging to the ROI by the expert. This term is commonly used in artificial intelligence and machine learning domain to assess the sensitivity of the algorithm and its calculation is same as that for *sensitivity*,

The precision would represent the ratio of properly classified pixels to the sum of pixels properly classified and misclassified

$$Precision = \frac{TP}{TP + FP} \tag{6.3}$$

The accuracy of the proposed method is measured using the following formula:

$$Accuracy = \frac{TP + TN}{TP + FP + TN + FN} \tag{6.4}$$

Another important measure is the false positive rate (FPR) which signifies the false alarms generated by the algorithm, i.e., pixels which do not belong to the ROI get classified as ROI. It is calculated as:

$$FPR = \frac{FP}{FP + TN} \tag{6.5}$$

The FPR, also known as fall-out, can also be calculated as $FPR = 1 - sensitivity$. When sensitivity is considered as a function of FPR, the resulting curve is called the Receiver Operator Characteristic (ROC), which is frequently used in evaluations of classifications systems used in health sciences and other domains (Hosmer Jr et al. 2013).

6.1.2 Cross-Validation

Algorithms dealing with prediction and classification problems are validated by splitting the sample data into training and testing subsets. The problem of overfitting of these algorithms can be circumvented by splitting the sample data several times so that one subset is used as training data while the other subset acts as *independent* testing data (Arlot et al. 2010). This method, called cross-validation, is efficient for problems where only a small number of data samples are available, for example, medical data (Ster et al. 1996).

In the k-Fold cross-validation, the whole set of patient cases D is randomly split into k subsets which are approximately equal sized ($\frac{D}{k}$). Hence, each of the learning subsets contains $D - \frac{D}{k}$ cases and the testing subset has the remaining $\frac{D}{k}$ cases. The algorithm is successively run k number of times which ensures that each case is tested once during the experiments. The k results, thus obtained, are averaged to yield a cross-validation estimate (Ster et al. 1996, Arlot et al. 2010). In the experiments in this thesis, $k = 10$ is used for 10-fold cross-validation.

6.1.3 Jaccard Similarity Index (JI)

The Jaccard Index (JI) or coefficient is used to measure similarity between experts' intuition and automated segmentation results (Zou et al. 2004, Shattuck et al. 2009). JI measures similarity between finite sets and is defined as:

$$J(M, A) = \frac{\mid M \cap A \mid}{\mid M \cup A \mid} \tag{6.6}$$

Where M is the set of pixels from manual segmentation, A is the output of the proposed algorithm and $0 \leq J(M, A) \leq 1$. JI, hence, is 0 when there is no overlap between the experts' demarcation (M) and algorithm's approximation (A) and is equal to 1 when there is perfect overlap. Consequently, values close to 1 indicate

better performance. Another measure similar to JI is Dice's coefficient and is also used to quantify the performance of the proposed method and is calculated as:

$$D = \frac{2J}{(1+J)} \tag{6.7}$$

Where J is the Jaccard index calculated earlier.

6.1.4 Intraclass Correlation Coefficient (ICC)

The intraclass correlation coefficient assesses rating reliability by comparing the variability of different ratings of the same subject (e.g., CT scan) to the total variation across all ratings and all subjects (Koch 1982). For pooled variance $\sigma^2(w)$ within subjects and variance of traits $\sigma^2(b)$, the ICC is given as:

$$ICC = \frac{\sigma^2(b)}{\sigma^2(b) + \sigma^2(w)} \tag{6.8}$$

The ICC is a descriptive statistic used for the assessment of consistency or reproducibility of quantitative measurements made by automated method and the expert radiologists measuring the same anatomical feature(s). It generally exemplifies how well the automated system's measurements matched the ground truth provided by the experts. The ICC calculation to compare the results was performed using MedCalc®software (Schoonjans et al. 1995).

6.1.5 Paired *t-test*

A *t-test* is a statistical hypothesis test following Student's t distribution if the null hypothesis is supported. If the null hypothesis suggests mean to be μ_0, then the sample mean $\bar{x}$, standard deviation s and number of observations n can be used to

calculate the one sample t -value as:

$$t = \frac{\bar{x} - \mu_0}{s/\sqrt{n}} \tag{6.9}$$

For use in estimating mean difference in experiment results where two observers give the observations e.g., algorithm and expert, then *paired t-test* is suggested to compare performance (Hsu & Lachenbruch 2008). It is calculated as:

$$t = \frac{\bar{x_1} - \bar{x_2} - \Delta}{\sqrt{\frac{s_1^2}{n_1} + \frac{s_2^2}{n_2}}} \tag{6.10}$$

where $\bar{x_1}, s_1$ and n_1 are mean, standard deviation and number of observations in algorithm's output and $\bar{x_2}, s_2$ and n_2 are mean, standard deviation and number of observations in expert's annotations. The Δ is the hypothesized difference between the means. For the training and validation in experiments reported in this thesis, $n_1 = n_2$ and the $\Delta = 0$ are used.

The *paired t-test* considers the difference between paired values in observations from the algorithm and expert, estimates the variation of values within each and produces a single number known as a *t-value*. It represents if two sets of observations are significantly different from each other resulting in the acceptance or rejection of the null hypothesis (Hsu & Lachenbruch 2008).

6.2 Dataset

The technique has been applied on corss-sectional, noncontrast CT studies from different subjects and a total of 87 TBI cases and 72 non-trauma cases were used. The total CT studies included in this research is 159. Among the 87 TBI cases, 51 cases present intracranial haematomas out of which 28 are EDH and 23 SDH.

These are all retrospect, secondary data from the archived data in the hospitals and, therefore, no direct interaction with the patients was required during collection.

On the average, the TBI cases had between 20 - 90 affected slices and, hence, the total number of axial slices examined were > 4700. The volume estimation of haemorrhages in brain CT requires using only the significant slices in which the size of ROI is at least $\geq 25\%$ of the maximum size in the respective study. Slices with size of ROI less than 25% are not counted.

The input images are DICOM (Digital Imaging and Communications in Medicine) files converted into 8-bit Portable Network Graphics (PNG) format using DicomWorks (Puech et al. 2007). Two radiology experts and a junior radiologist independently performed manual segmentations to be used for training and evaluation in the experiments. The radiologists also identified number of significant slices in each of the respective CT studies used provided for training and validation.

The subjects' personal information was anonymized and only age and gender data were retained. In the second anonymization, the clinical data and CT images were given fictitious identifiers to further minimize possibility of identification of the patient by 3-D reconstruction of facial data from images. The Fig. 6.1 shows 24 of the cases used in the experiments and the rest are included in Appendix C for reference.

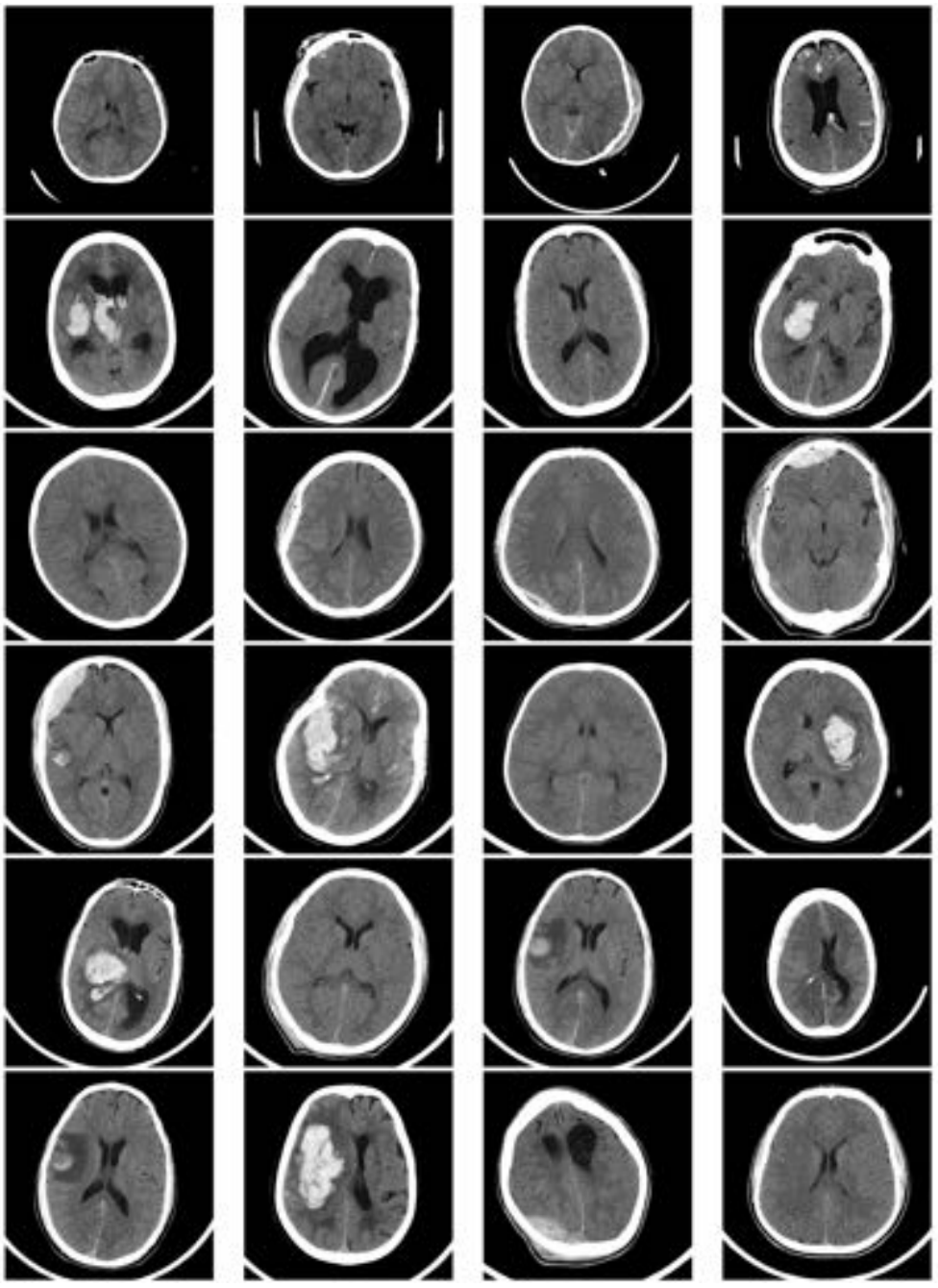

FIGURE 6.1: CT scans of the TBI Cases used in experiments.

6.3 Estimation of Brain Midline

Midline in the brain is an important reference point for assessing the severity of injuries and pathological conditions. There can be mild to moderate shift but the

resulting manifestations can be quite serious and a shift $> 5mm$ is considered a surgical emergency.

In order to asses the midline shift and brain indices and ratios, it is important that the head of the patient should be properly orientated. Out of the 159 CT studies used in experiments, the expert annotated tilted head in 122 cases. Therefore, with 122 tilted and 37 proper orientations, the algorithm classified TP = 104, FN = 18, TN = 31 and FP = 6. The sensitivity and specificity of the approach used for correction of orientation of the head are 85% and 84% respectively. The proposed method shows robust performance in detecting tilted head of the patient during the scan procedure and corrects it for proper subsequent measurements (table 6.2).

The method identifies the anterior and posterior bony protuberance of the skull as landmarks and the nose is identified in cases where the bony protuberances are not very obvious. The algorithm rotates the image accordingly so that the ideal midline would be approximately vertical. As a second step, the location of the septum pellucidum is identified to calculate the midline shift, if any, and the average performance of the proposed method is 94% and 85% in terms of sensitivity and specificity respectively.

A total of 87 cases of TBI were used in experiments and out of these, midline shift was identified in 32 cases. Hence, 55 cases had no midline shift annotated by the expert. The algorithm classified TP = 30, FN = 2, TN = 47 and FP = 8. In patients with gross shift of the midline and/or effacement of either of the ventricles due to midline shift or oedema, resulted in a slightly less accurate demarcation of the septum pellucidum and, hence, the number of FP was higher than FN.

TABLE 6.2: Performance of Proposed Method. The detection of midline shift also provides vote α_H.

CT Feature	Sensitivity	Specificity	Accuracy
Correction of Orientation	84%	85%	84.91%
Midline Shift $> 5mm$ and α_H	94%	85%	88.51%

6.4 Classification of Clinical Data

The performance of the classification of clinical phenotype is shown in Fig. 6.2. The observed performance of the classification when using a feedforward backpropagation neural network is due to the boolean nature of most of the features. The clinical feature 'age' possibly caused the less than perfect performance because the traffic accident cases in the dataset were not bounded by middle age group and some old aged patients were also hospitalized due to accidents.

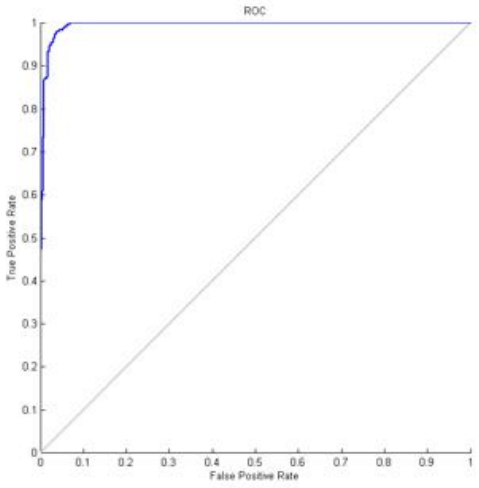

FIGURE 6.2: Performance of the classification of clinical features of the patients.

The results of classification of pixels without using the clinical phenotype votes and with using them are given in Fig. 6.3 and Fig. 6.4, respectively. It can be seen that the adjustment of the contrast using vote from classification of clinical profile

results in improved performance using the ANN. The results of detecting initial gradient based edges in the output of the ANN are given in the last columns of these figures. These edges are detected using the 'Canny' algorithm and provides the intermediate results for the active contours in the subsequent step.

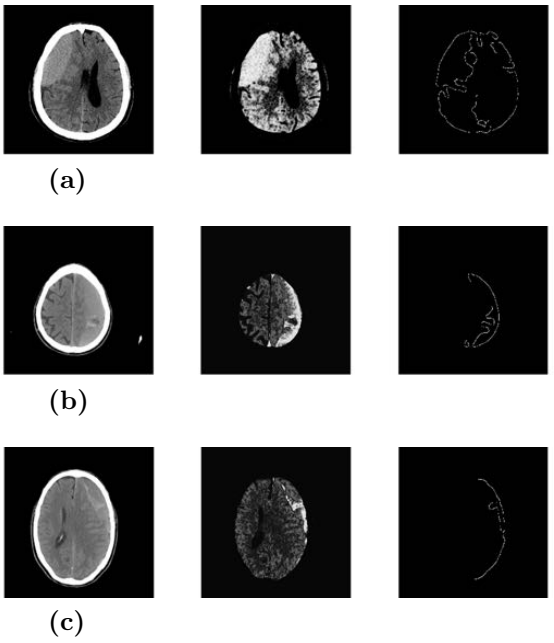

FIGURE 6.3: ANN pixel classification without Clinical Phenotype vote. The input images are in the left column, results of ANN classification in the centre column and gradient based edge detection in ANN output is in the right column.

6.5 Pixel Classification using ANN

The modified approach of combining clinical and image data was applied on TBI cases. Three architectures of ANN, name feedforward network, pattern network and cascadeforward network were separately evaluated using 10-fold cross validation on the image data. The *Pattern Network* in this thesis refers to feedforward backpropagation ANN with classification target as binary pattern and two neurons in the output layer. The experiments were run with all three architectures of ANN and using one hidden layer with 10 neurons and Levenberg-Marquardt training function for each. The maximum number of epochs was set at 1000. The number of hidden neurons was determined using incremental pruning.

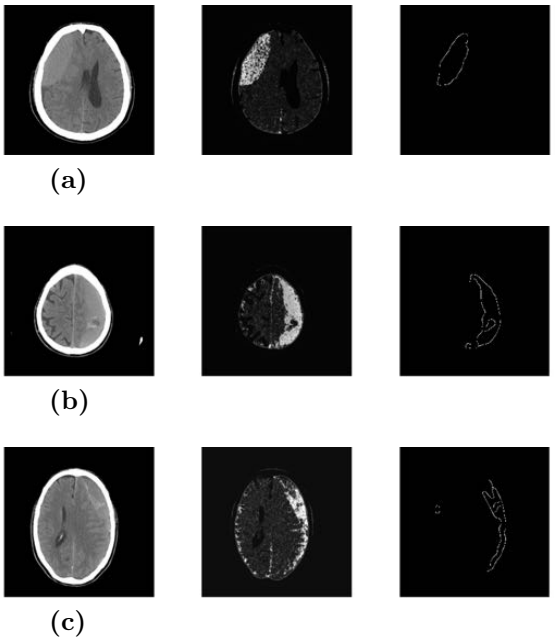

FIGURE 6.4: ANN pixel classification with Clinical Phenotype vote. The input images are in the left column, results of ANN classification in the centre column and gradient based edge detection in ANN output is in the right column.

Subsequently, the number of hidden layers was changed to two and evaluation was done using pruning with $2 - 20$ neurons in each of the hidden layers. The classification performance with 2 and 3 neurons in each of the hidden layers was <62.6% with all three architectures of ANN. An improvement to 87.2 - 88.9% was observed with 4 hidden neurons in each of the two layers in the feedforward and pattern network ANN. The cascadeforward network showed 83.3 - 85.2% classification performance. Increasing the number of neurons to 5, 10 and 20 neurons in each hidden layer in feedforward and pattern networks resulted in 87.1 - 88.0% performance and with cascadeforward network, it was 82.7 - 84.9%.

The outputs of the ANN were also evaluated using different transfer functions which are given in Fig. 5.17. The problem of detecting subtle intensity difference between the ROI and surrounding region is circumvented when the initial seeding is provided with the output of the ANN used as a mask for the active contours.

6.6 Segmentation using proposed method

The hybrid approach combining SLIC and DRLSE achieved a performance significantly better than the DRLSE method alone (Soltaninejad et al. 2014). The JI of hybrid approach was 0.807 ± 0.067 compared with the DRLSE at 0.518 ± 0.11 or active contour method 'Chan-Vese', which had an average JI of 0.5667 ± 0.2052. The results of the hybrid method are given in Fig. 6.5 in the top row. It can be seen that the SLIC identifies the probable region of interest with rather jagged edges and the jaggedness depends upon the algorithm's parameters such as the pixel resolution for the initial super pixel at 10×10. In the bottom row is Fig. 6.5, the image is processed using ANN based approach which produces much finer demarcation of the probably ROI.

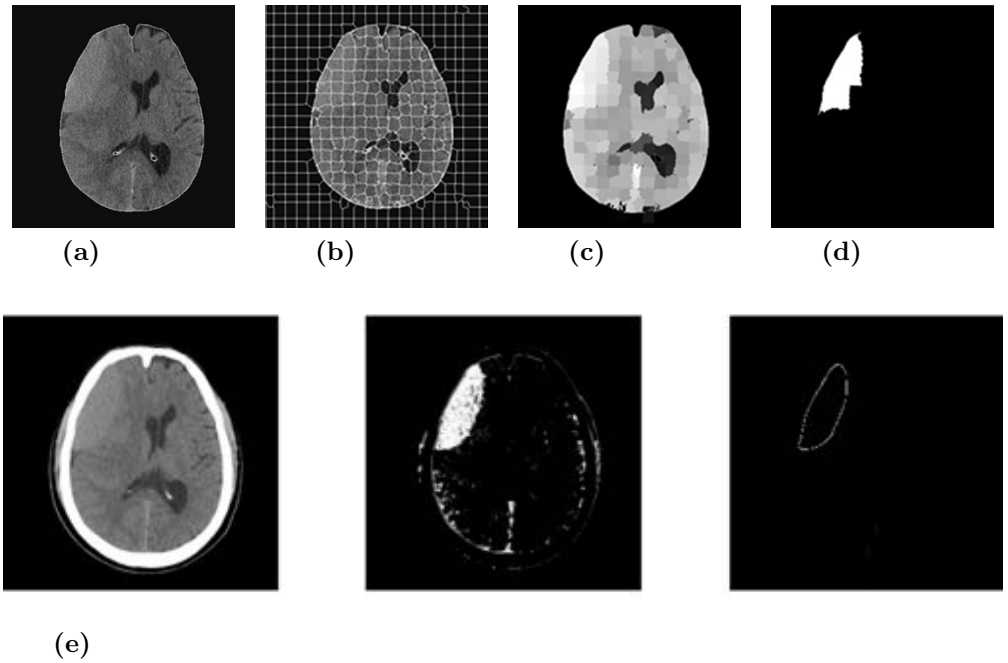

FIGURE 6.5: Comparison of the classification of pixels into probable ROI using SLIC (a)-(d) and ANN (e). It is observed that the ANN based classification results in better approximation of the haematoma as compared to the jagged results from SLIC.

Compared to the performance of active contour method, which had an average JI of 0.5667 ± 0.2052 with 'Chan-Vese' or DRLSE at 0.518 ± 0.11, the novel approach

with ANN shows JI of 0.8689 ± 0.042 when a feedforward net is used for initial classification of pixels for subsequent segmentation.

The intelligence in the pattern recognition systems depends upon the features extracted during the process and incomplete features can adversely affect the performance of the ANN. The sliding window described in section 5.3.4 was evaluated with varying sizes of 3×3, 5×5 and 7×7 neighbourhood pixels. The statistical features extracted from the image include mean, median, variance, standard deviation and entropy. Also, the local neighbourhood pixel intensities and discrete Fourier transform were also used as features to assess using ROC curves. Analyses of the ROC curves suggested using the features in combination rather than individually. The performance of the ANN to classify pixels was evaluated using these features individually and then together in combination.

The feature vector combining these along with neighbourhood pixel intensities did not significantly improve the performance, however, it took longer for the ANN to reach stable state. The optimum result was achieved with Mean, Standard Deviation and Shannon's Entropy combination (Fig. 5.13d) for extracting features and this same configuration was subsequently used in the experiments.

The use of pixel location (x, y) as a feature has been suggested in literature which can be useful if the location of the ROI is fairly fixed. However, in the case of TBI, the haematoma can appear at different locations and the only persistent characteristic is that it is bounded by skull along one edge. Hence, the use of pixel location as a feature was ignored when the ROI was haematoma and only used when anatomical structures such as ventricles had to be segmented for estimation of brain ratios and indices.

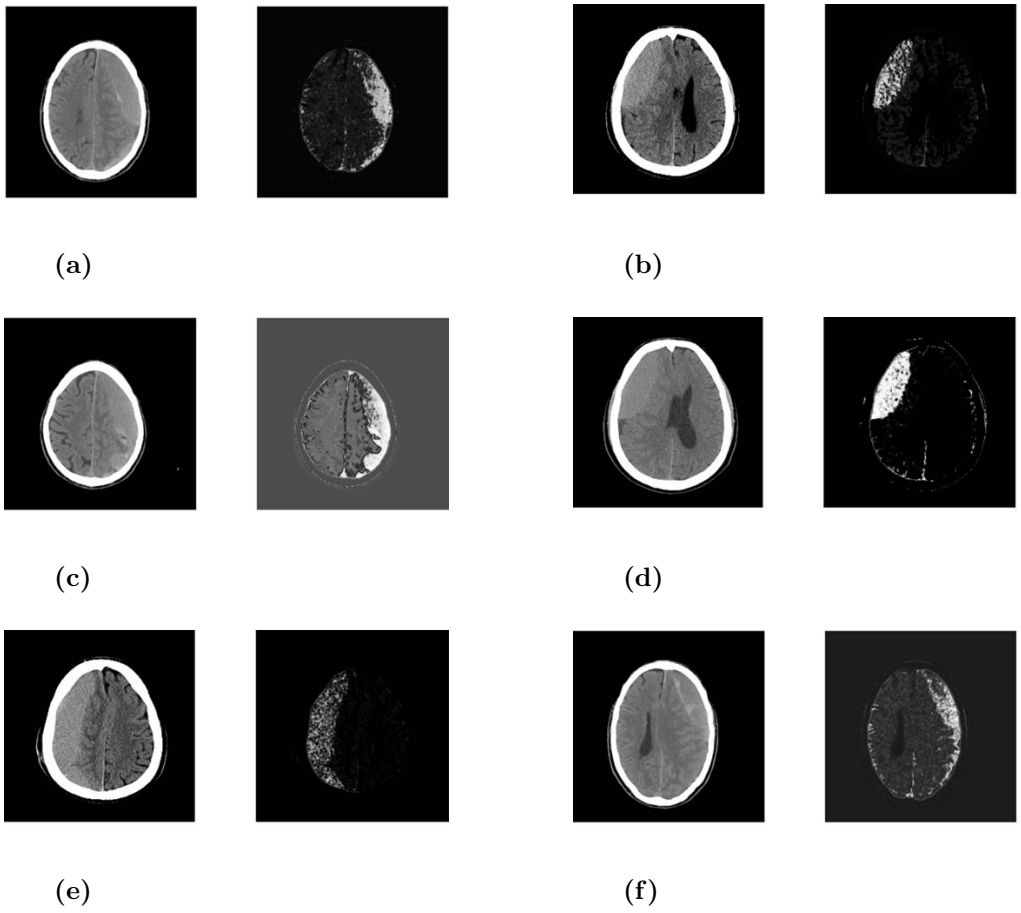

FIGURE 6.6: Classification results from different ANN configurations. Cases (a) and (b) are classified by feedforward net. Case (c) is feedforward net with DFT. Cases (d) and (e) are with pattern net. Case (f) is the output from cascade forward net.

The performance evaluation of the state of the art Chan-Vese model of active contours and the modified active contour (MAC) from the proposed work is presented in the following sections. The results of applying contrast adjustment and using these models are given in Fig. 5.21 which show that the segmentation is not improved even in changes of contrast and the ROI is not well demarcated. The results are still amiss just as observed without the contrast adjustments (Fig. 5.20) and, hence, the evaluation using Jaccard Index and Dice's Coefficients is poor.

6.6.1 Performance with Feedforward Network

The performance of the feedforward backpropagation ANN on patient data was evaluated using 10-fold cross-validation. The average pixel classification performance with one hidden layer with 10 neurons was 88.2% (from $87.4 - 88.9\%$). Incremental pruning from 5 to 20 neurons in one hidden layer did not significantly improve the performance after 10 neurons and $87.4 - 88.7\%$ classification accuracy was observed. With two hidden layers with 4 neurons each, the classification performance was $88.1 - 88.9\%$.

The evaluation of segmentation showed that JI was 0.8689 ± 0.042 with one hidden layer and 0.8687 ± 0.018 with two hidden layers when feedforward ANN was combined with MAC. These are significant improvements compared to 0.807 ± 0.067 JI with SLIC + DRLSE and Chan-Vese active contours (0.5667 ± 0.2052). The Table 6.3 and Fig. 6.7 show the performance comparisons with existing methods of segmentation.

TABLE 6.3: Performance of proposed approach using Feedforward Net. MAC is Modified Active Contour.

Method	**Jaccard Index**	**Dice's coefficient**
Active Contour (Chan-Vese)	0.5667 ± 0.2052	0.7271 ± 0.156
DRLSE	0.518 ± 0.11	0.675 ± 0.099
SLIC + DRLSE	0.807 ± 0.067	0.892 ± 0.043
Feedforward Net, 10 + MAC	0.8689 ± 0.042	0.9169 ± 0.02
Feedforward Net, 4×4 + MAC	0.8687 ± 0.018	0.9235 ± 0.016

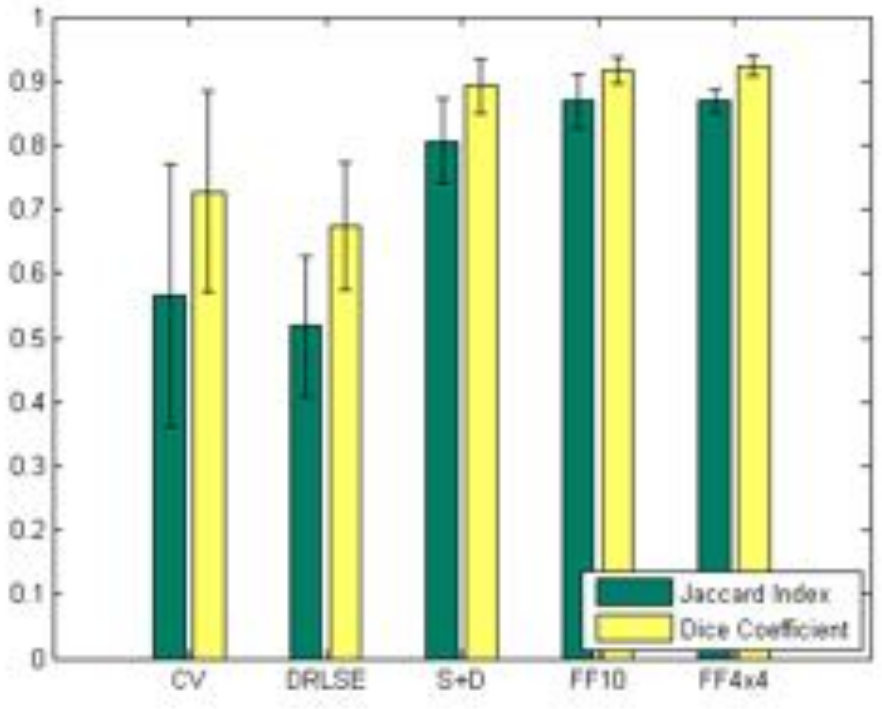

FIGURE 6.7: Performance of proposed approach using Feedforward Net. CV = Chan-Vese active contour, DRLSE = Distance Regularized Level Sets, S+D = SLIC + DRLSE, FF10 = feedforward net with one hidden layer of ten neurons + MAC and FF4x4 = feedforward net with two hidden layers with 4 neurons in each of them + MAC.

6.6.2 Performance with Pattern Network

The average performance of the pattern network was 87.6% (from $87.2 - 88.0\%$) to classify the pixels using 10-fold cross-validation using one hidden layer with 10 neurons. With 5 neurons in the hidden layer, $87.2 - 87.8\%$ performance was observed. With 10 to 20 neurons in the hidden layer, $87.1 - 88.6\%$ classification performance was seen during incremental pruning, however, the training time was significantly longer beyond 10 neurons size. The configuration of pattern net was also evaluated with two hidden layers having 4 neurons each and observed performance was $87.2 - 88.2\%$.

The JI of segmentation results using pattern network with MAC was 0.8506 ± 0.019 with one hidden layer and 0.8658 ± 0.033 with two hidden layers. The performance is very close to that of the feedforward backpropagation ANN and shows significant improvement from the Chan-Vese, DRLSE and SLIC + DRLSE as shown in Table 6.4 and Fig. 6.8.

TABLE 6.4: Performance of the proposed approach using Pattern Net. MAC is Modified Active Contour.

Method	**Jaccard Index**	**Dice's coefficient**
Active Contour (Chan-Vese)	0.5667 ± 0.2052	0.7271 ± 0.156
DRLSE	0.518 ± 0.11	0.675 ± 0.099
SLIC + DRLSE	0.807 ± 0.067	0.892 ± 0.043
Pattern Net, 10 + MAC	0.8506 ± 0.019	0.9085 ± 0.014
Pattern Net, 4×4 + MAC	0.8658 ± 0.033	0.9278 ± 0.019

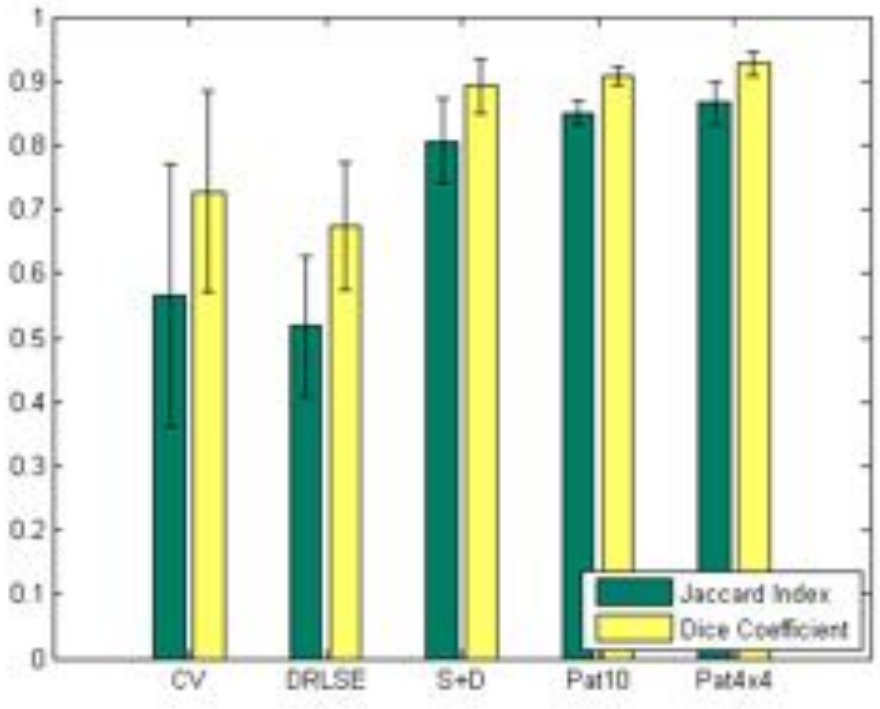

FIGURE 6.8: Performance of proposed approach using Pattern Net. CV = Chan-Vese active contour, DRLSE = Distance Regularized Level Sets, S+D = SLIC + DRLSE, Pat10 = Pattern net with one hidden layer of ten neurons + MAC and Pat4x4 = Pattern net with two hidden layers with 4 neurons in each of them + MAC.

6.6.3 Performance with Cascadeforward Network

The cascadeforward net with one hidden layer of 10 neurons showed pixel classification performance of $84.1 - 87.3\%$ (average 85.7%) during the 10-fold cross-validation. The performance was $83.3 - 86.1\%$ with 5 hidden neurons and $84.0 - 87.7\%$ with 10 to 20 hidden neurons. Hence, the size of hidden layer was set to 10 neurons for faster learning. The performance when second hidden layer was added to the network achieved classification accuracy of $83.3 - 85.2\%$ and no improvement was observed with three hidden layers.

The Table 6.5 and Fig. 6.9 depict the comparison of performance of segmentation using cascadeforward network with MAC. It can be seen that there is significant

improvement over the Chan-Vese, DRLSE and SLIC + DRLSE methods of segmentation.

TABLE 6.5: Performance of the proposed approach using Cascadeforward Net. MAC is Modified Active Contour.

Method	**Jaccard Index**	**Dice's coefficient**
Active Contour (Chan-Vese)	0.5667 ± 0.2052	0.7271 ± 0.156
DRLSE	0.518 ± 0.11	0.675 ± 0.099
SLIC + DRLSE	0.807 ± 0.067	0.892 ± 0.043
Cascadeforward Net, 10 + MAC	0.8544 ± 0.034	0.9212 ± 0.019
Cascadeforward Net, 4×4 + MAC	0.8228 ± 0.026	0.8724 ± 0.041

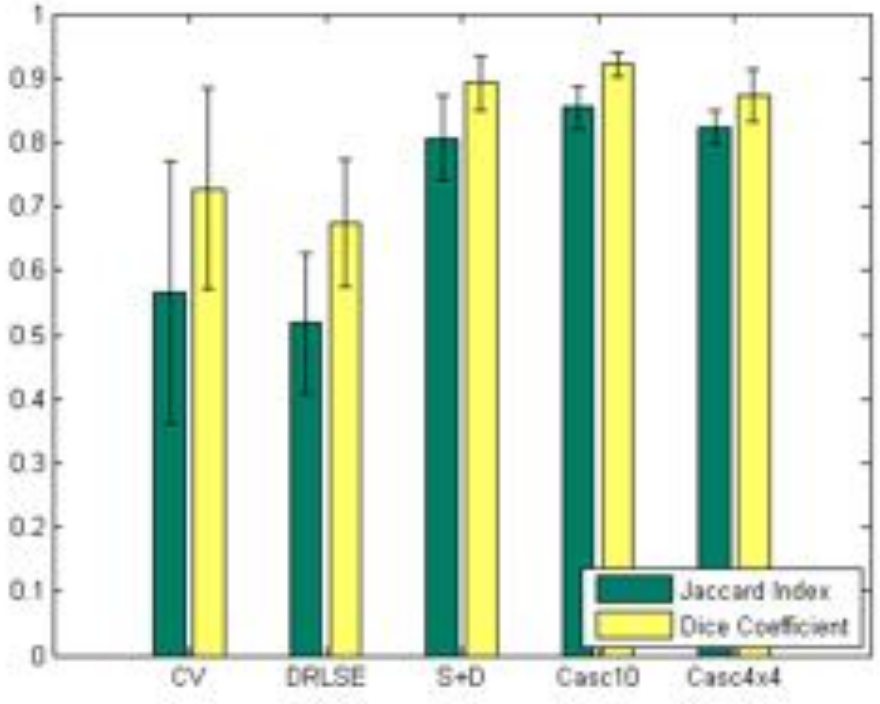

FIGURE 6.9: Performance of proposed approach using Cascadeforward Net. CV = Chan-Vese active contour, DRLSE = Distance Regularized Level Sets, S+D = SLIC + DRLSE, Casc10 = Cascadeforward net with one hidden layer of ten neurons + MAC and Casc4x4 = Cascadeforward net with two hidden layers with 4 neurons in each of them + MAC.

6.6.4 Limitations of the proposed method

The performance of the proposed method was not satisfactory in segmentation of haematoma cases where there were more than one region of interest. Fig. 6.10 depicts the two cases of haematoma where the manual annotation had specified two regions (red colour) while the proposed MAC method only identified the larger haematoma (green colour).

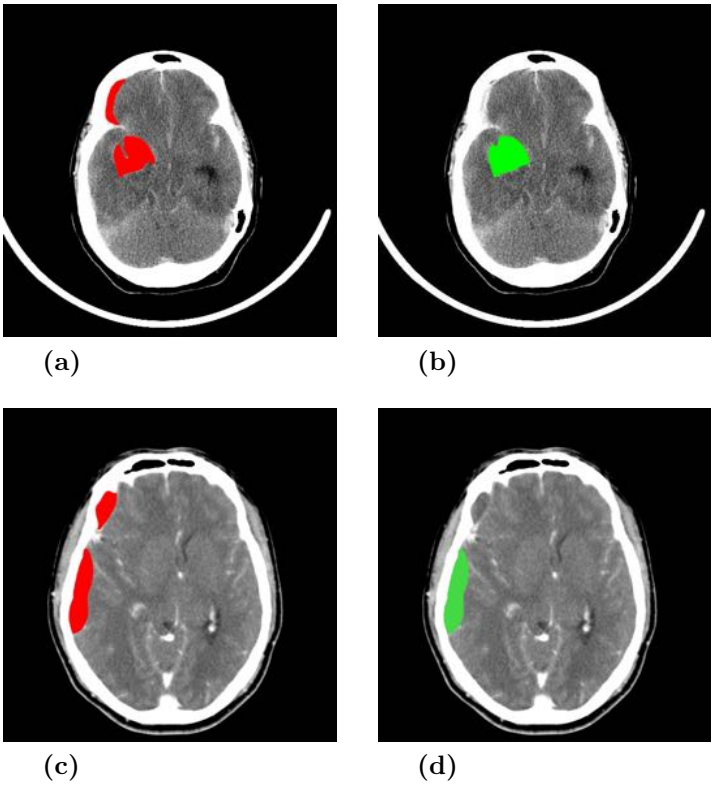

FIGURE 6.10: Demarcation of only one ROI in the case.

The above result is due to the constraint $E_{loc}(\mathbf{v}(\tau))$, discussed in section 5.4.3.2, which constrains the method to detect only one ROI. The occurrence of two or more haematomas in one case is not a frequent presentation in the emergency departments (Shah & Kelly 2003). However, the MAC can be enhanced to allow detection of multiple or bilateral haematomas by relaxing the constraint $E_{loc}(\mathbf{v}(\tau))$ when the doctor is suspecting multiple ROI.

Another limitation of the method was observed in cases where gross deformity of the brain structure due to either neoplastic metastasis, pathology or trauma was seen. The four cases are shown in Fig. 6.11 in which the proposed method could not estimate measurements and segmentation. The identification of midline was not achieved by the method in the advanced hydrocephalus case shown in Fig. 6.11a and the estimation of brain indices and ratios was incorrect with the hydrocephalus case in Fig.6.11b.

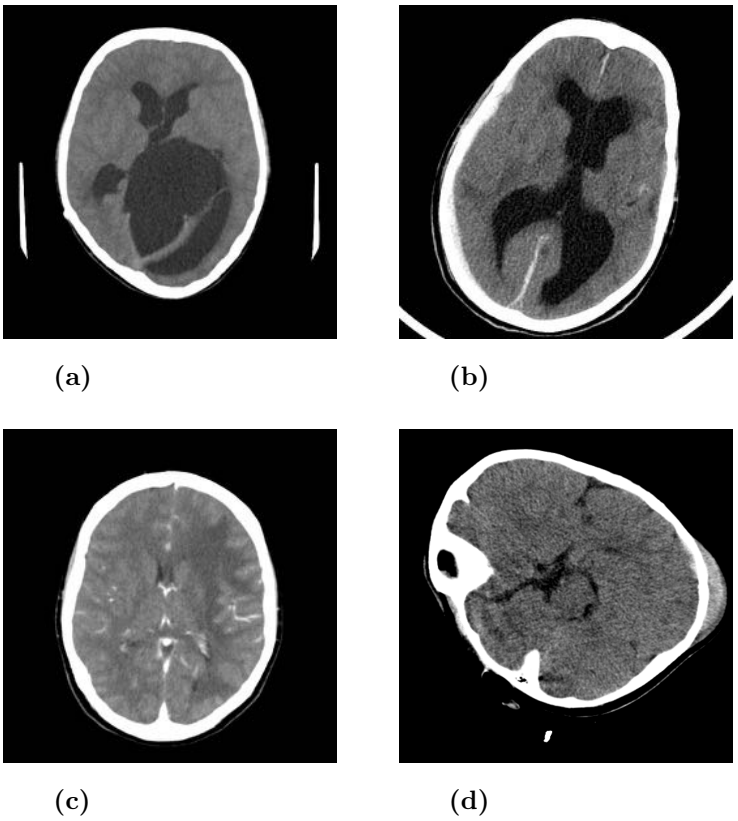

FIGURE 6.11: Cases with gross deformity of the brain structures.

The metastatic lesions due to cancer in Fig. 6.11c were classified by the algorithm as normal case. This was due to the fact that the characteristics of TBI were not present in this CT study. In the case where the skull of the patient had been compressed due to TBI as shown in Fig. 6.11d, the proposed method could not correct the orientation of the head, identify midline or estimate the linear

measurements. This was due to the absence of anatomical landmarks used by the method due to the gross deformity.

6.7 Segmentation of the Regions of Interest

6.7.1 Skull Bone as ROI

The skull pixels in the CT are identified and presented as ROI for linear measurements to be used in calculating indices and ratios as shown in Fig. 2.10. Subsequently, the classified skull pixels are used to create a mask including skull and brain tissue. The pixels outside of the mask represent scalp and soft tissue like ears. These are removed by subtracting the mask from the input image.

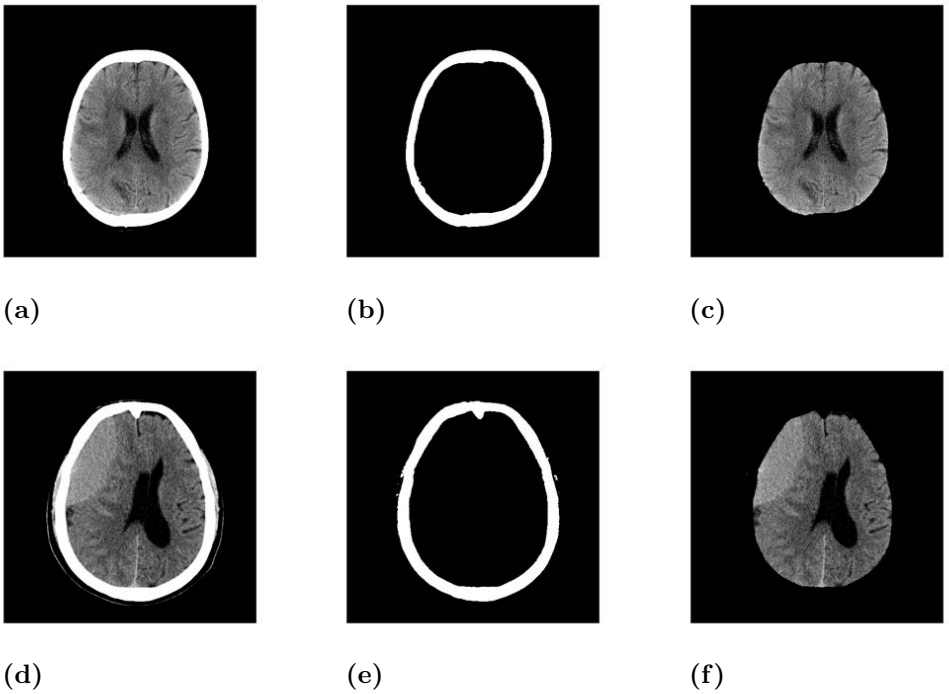

FIGURE 6.12: Stripping scalp and skull. Images in left column are the input images. The middle column shows the skull pixels detected by the algorithm and the images in right column present the extracted brain.

The skull pixels are removed in a similar way to yield only the pixels representing the brain tissue as shown in Fig. 6.12. The skull bone as ROI (Fig. 6.12b and 6.12e) is important to assess cases with depressed fractures in addition to the haemorrhages.

6.7.2 Brain as ROI

The brain tissue is extracted from the skull and scalp and any artefacts present in the image such as the head rest (Fig. 6.12c and 6.12f). The brain is then presented to the user with measurements of the length, breadth and 2-D area on the axial CT slice as shown in Fig. 6.13.

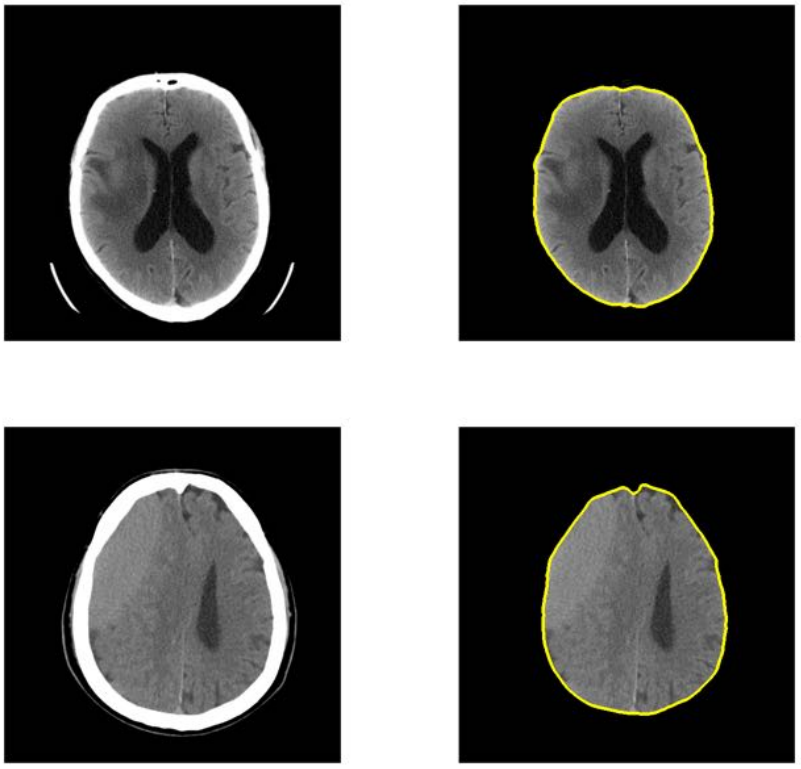

FIGURE 6.13: Brain boundary demarcation and estimation of enclosed area. The left column shows input images and right column shows results of the skull and scalp stripping to yield brain. The yellow outline in images in right column correspond to the detected brain boundary.

The whole segmented brain is assessed for right left symmetry and identification os anatomical structures from front to back. In the current approach, no demarcation

between the grey and white matter is identified, however, compressed or absent sulci delineate cerebral oedema.

6.7.3 CSF Spaces as ROI

The quadrigeminal cistern and lateral ventricles are identified on the relevant axial CT scans as shown in Fig. 5.25a and 6.14 respectively. Linear measurements based on ventricles are performed automatically for estimating various indices and ratios as given in Table 2.7. The indices and ratios are based on the labels given in Table 2.6. The demarcation of cisterns is performed to assess their appearance as present, compressed or absent in cases of oedema and mass effect.

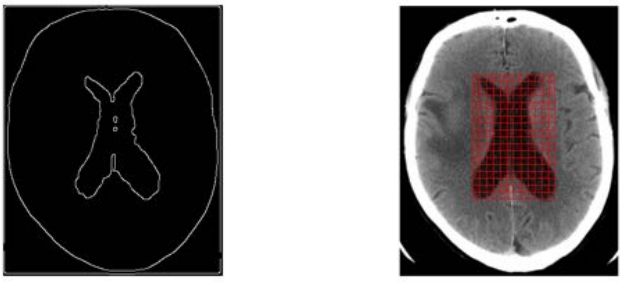

(a) **(b)**

FIGURE 6.14: Demarcation of ventricles. Image (a) shows the edges of the ventricle. Image (b) a grid overlaid on the identified ventricle ROI and the extents of the grid correspond to the extents of the ROI.

6.7.4 Blood as ROI

The presence of subdural or epidural haematomas is detected and presented with demarcated boundary as shown in Fig. 6.15. The size of haematoma can exert pressure on the brain tissue and this can lead to compression effect and shifting of the midline. The proposed algorithm can efficiently detect brain midline shift as shown in Fig 5.5c because it is a surgical emergency if the shift is $> 5mm$. Volume estimation of the haematoma is also performed which is discussed later.

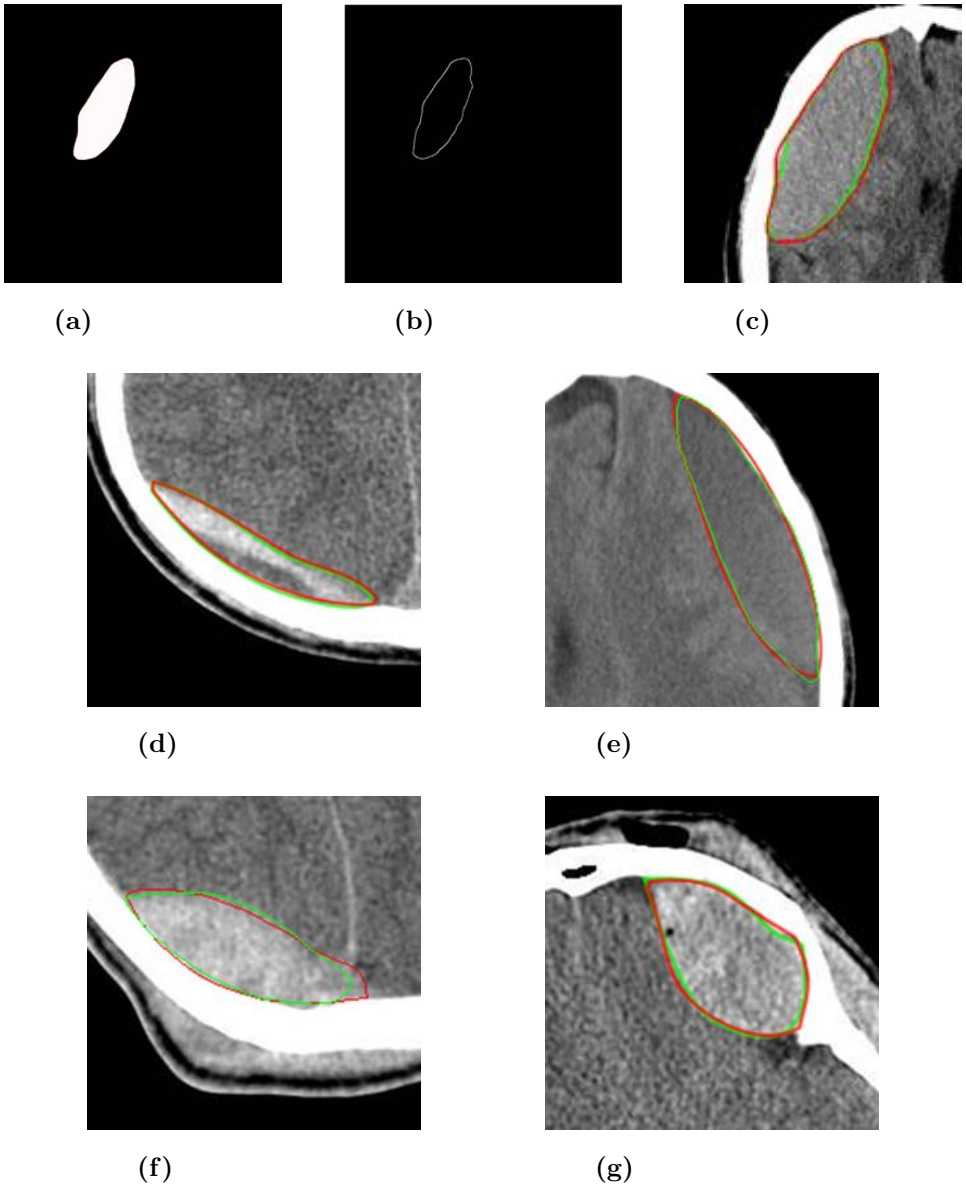

FIGURE 6.15: Segmentation results from hybrid approach. Green curve shows the active contour while red is the manual demarcation. Image (a) is the expert's demarcation of ROI. Image (b) is the result of proposed method with 400 iterations of active contour and image (b) shows the final approximation of the contour to the ROI. Images (d) - (g) show results on other cases of TBI.

6.8 Estimation of Size of Haematoma

The segmentation was initially performed using only the active contour method suggested in literature. The traditional implementation without edges, Chan-Vese,

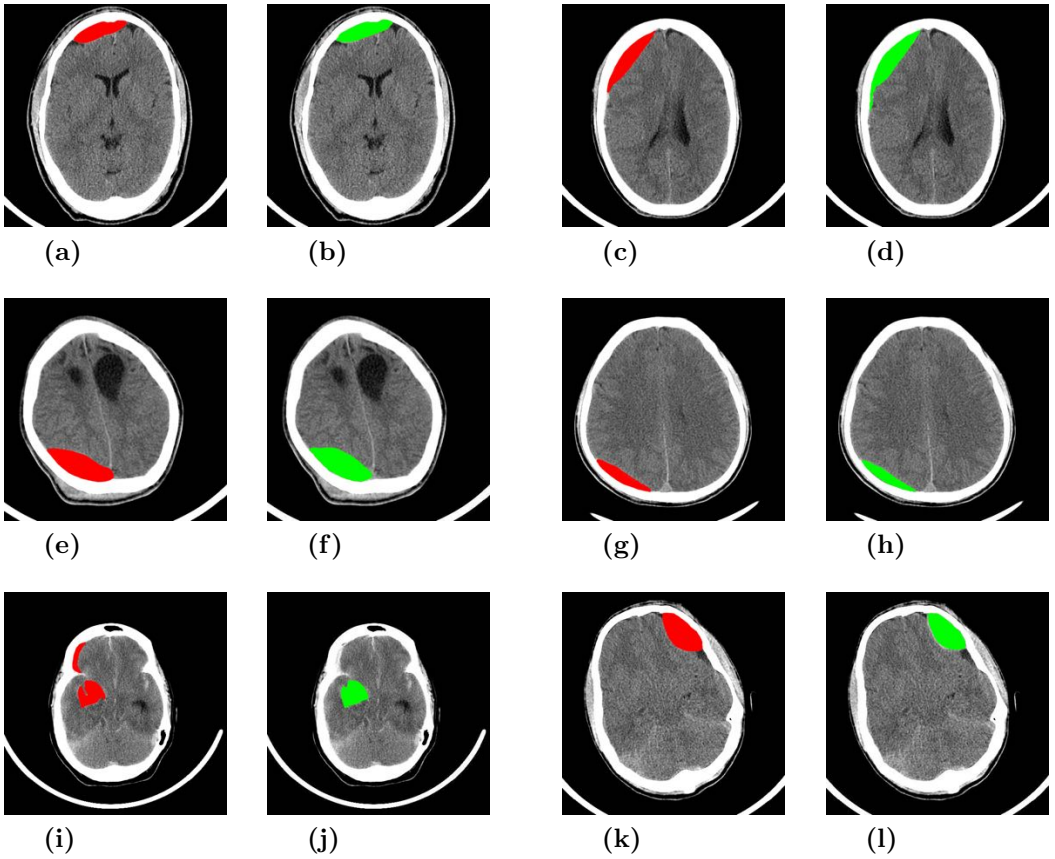

FIGURE 6.16: Output of the method on six TBI cases from the dataset. The first and third columns are the manually segmented images showing the ROI in red colour. Columns two and four are the output from the method showing results in green colour. There is good approximation of the expert's segmentation in general, however, images (i) and (j) present a case where only one region was identified by the algorithm.

which does not necessarily use gradient based edges in images, and the Edge based implementations were used for segmenting images. Both these approaches gave less than desirable results in segmenting haematoma regions in CT scans and the results are given in Fig. 5.20. The green curve shows the result of the method while the red curve is the expert's manual demarcation. It can be seen that the Chan-Vese approach which does not use gradient based edges, leaks into the adjoining skull bone, hence, falsely increasing the size of the ROI. This performance was frequently observed when the ROI was hyperdense and in case of hypodense, the curve would leak onto brain parenchyma. The performance of Edge based method was observed to be quite opposite resulting in smaller regions because of false edges

detected within the ROI. The performance was even poorer when the ROI was a mixed density lesion. The evaluation was also repeated using different number of iterations for curve evolution and Fig. 5.20 shows results with 400 iterations. Another observation was the effect of the size of the mask used as seed for the curve. The large initial seed mostly adhered to the skull boundaries ignoring the brain parenchyma while the smaller seeds were highly location specific (Fig. 5.19). When the smaller seeds were manually placed inside the possible ROI, results were observed as shown in Fig. 5.19b.

For the estimation of size of haematoma, linear measurements along the major and minor axes on the axial slice are performed as shown in Fig. 5.26.

TABLE 6.6: Estimation of Haematoma Length with different methods in brain CT Scans. The total count of cases is 51 and the degree of freedom is 50. The hypothesized difference of means is 0 suggesting that there is no difference between the expert's and the algorithms' estimations at $\alpha = 0.05$.

Groups	**Mean**	**Std. Dev.**	**Std. Err.**	**t**
Expert	7.849	2.053		
Proposed Method	7.876	1.970		
Difference	-0.027	0.336	0.047	-0.583
Chan-Vese	9.014	2.344		
Difference	-1.165	1.211	0.170	-6.866
Edge	7.179	2.607		
Difference	0.670	1.736	0.243	2.754

TABLE 6.7: Two Tail t-test on estimation of Haematoma Length with different methods.

Method	**p-value**	**t-crit**	**lower**	**upper**	**Sig.**
Chan-Vese method	9.7E-09	2.0E+00	-1.5E+00	-8.2E-01	yes
Edge method	0.008	2.009	0.181	1.158	yes
Proposed Algorithm	0.563	2.009	-0.122	0.067	no

The results of estimating the length of the major axis of the haematoma ellipse show that the state of the art Chan-Vese and Edge models have statistically significant difference in the measurements. This rejects the null hypothesis for the state of the art.

The performance of the proposed method has no significant difference from the hypothesized mean and, hence, the null hypothesis is not rejected.

TABLE 6.8: Estimation of Haematoma Breadth with different methods in brain CT Scans. The total count of cases is 51 and the degree of freedom is 50. The hypothesized difference of means is 0 suggesting that there is no difference between the expert's and the algorithms' estimations at $\alpha = 0.05$.

Groups	**Mean**	**Std. Dev.**	**Std. Err.**	**t**
Expert	3.745	1.206		
Proposed Method	3.755	1.241		
Difference	-0.010	0.259	0.036	-0.270
Chan-Vese	4.380	1.112		
Difference	-0.635	0.751	0.105	-6.039
Edge	3.341	1.213		
Difference	0.404	0.676	0.095	4.266

TABLE 6.9: Two Tail t-test on estimation of Haematoma Breadth with different methods.

Method	**p-value**	**t-crit**	**lower**	**upper**	**Sig.**
Chan-Vese method	1.9E-07	2.0E+00	-8.5E-01	-4.2E-01	yes
Edge method	8.8E-05	2.0E+00	2.1E-01	5.9E-01	yes
Proposed Algorithm	0.788	2.009	-0.083	0.063	no

The results of estimating the length of the minor axis of the haematoma ellipse show that the state of the art Chan-Vese model has statistically significant difference in the measurements. The performance of Edge model is much better and the t-test

given in Table 6.9 does not show any statistically significant difference in this case. Therefore, the null hypothesis is rejected in case of Chan-Vese only.

The performance of the proposed method has no significant difference from the hypothesized mean and, hence, the null hypothesis is not rejected in this case as well as in case of Edge model.

TABLE 6.10: Measurements on the axial CT scans. The consistency in estimating linear measurements is given as Intraclass Correlation Coefficient (ICC).

Method	**Measurement**	**ICC**
Chan-Vese method	Breadth of Haematoma	0.883
Chan-Vese method	Length of Haematoma	0.918
Edge method	Breadth of Haematoma	0.915
Edge method	Length of Haematoma	0.842
Proposed method	Breadth of Haematoma	0.989
Proposed method	Length of Haematoma	0.993

6.8.1 Estimations of EDH

Haematomas, such as EDH, are more common in road accidents and 28 TBI cases included presentation of EDH in the CT scans. The manual annotation from the expert was considered baseline and the performance of the other algorithms against that was measured.

TABLE 6.11: Estimation of EDH Length with different methods in brain CT Scans. The total count of cases is 28 and the degree of freedom is 27. The hypothesized difference of means is 0 suggesting that there is no difference between the expert's and the algorithms' estimations at $\alpha = 0.05$.

Groups	**Mean**	**Std. Dev.**	**Std. Err.**	**t**
Expert	7.811	2.163		
Proposed Method	7.854	2.061		
Difference	-0.043	0.415	0.078	-0.547
Chan-Vese	9.007	2.335		
Difference	-1.196	1.186	0.224	-5.337
Edge	7.455	2.625		
Difference	0.355	1.880	0.355	1.000

TABLE 6.12: t-test on estimation of EDH Length with different methods.

Method	**p-value**	**t-crit**	**lower**	**upper**	**Sig.**
Chan-Vese	1.23E-05	2.05E+00	-1.66E+00	-7.36E-01	yes
Edge	0.326	2.052	-0.374	1.084	**no**
Proposed	0.589	2.052	-0.204	0.118	no

TABLE 6.13: Estimation of EDH Breadth with different methods in brain CT Scans. The total count of cases is 28 and the degree of freedom is 27. The hypothesized difference of means is 0 suggesting that there is no difference between the expert's and the algorithms' estimations at $\alpha = 0.05$.

Groups	**Mean**	**Std. Dev.**	**Std. Err.**	**t**
Expert	4.214	1.273		
Proposed Method	4.257	1.298		
Difference	-0.043	0.327	0.062	-0.693
Chan-Vese	4.629	1.141		
Difference	-0.414	0.643	0.122	-3.408
Edge	4.214	1.273		
Difference	0.357	0.685	0.129	2.759

TABLE 6.14: t-test on estimation of EDH Breadth with different methods.

Method	**p-value**	**t-crit**	**lower**	**upper**	**Sig.**
Chan-Vese	0.002	2.052	-0.664	-0.165	yes
Edge	0.010	2.052	0.092	0.623	yes
Proposed	0.494	2.052	-0.170	0.084	no

The results specific to EDH identification and measurement are summarized in Tables 6.11 and 6.13 and the respective results of paired t-test are given in Tables 6.12 and 6.13.

It can be seen that the null hypothesis stating no difference in the means of measurements between expert and algorithms is rejected in case of the state of the art. The Chan-Vese model consistently creeps into the surrounding regions giving larger measurements while the Edge model mostly under-segments.

In cases where the presentation of EDH is well marked, Chan-Vese and Edge models closely match the performance of the expert. However, their performance on the whole is superseded by the proposed method which produces no statistically significant differences in measurements compared with the expert and in its case, the null hypothesis is not rejected.

6.8.2 Estimations of SDH

The SDH is observed more commonly amongst the very young or the relatively older age group and is often difficult to visually identify because of the admission of the patient in hospital and incidence of trauma may have delays of some days. In this period the blood my change into iso- or even hypo-dense. Also, in case of chronic SDH, a mixed density lesion is presented with both fresh and old blood.

This research evaluated performance of the algorithm on 23 SDH cases from the TBI patients. The manual annotation from the expert was considered baseline and the performance of the other algorithms against that was assessed.

TABLE 6.15: Estimation of SDH Length with different methods in brain CT Scans. The total count of cases is 23 and the degree of freedom is 22. The hypothesized difference of means is 0 suggesting that there is no difference between the expert's and the algorithms' estimations at $\alpha = 0.05$.

Groups	**Mean**	**Std. Dev.**	**Std. Err.**	**t**
Expert	7.896	1.959		
Proposed Method	7.904	1.899		
Difference	-0.009	0.213	0.044	-0.196
Chan-Vese	9.022	2.408		
Difference	-1.126	1.267	0.264	-4.262
Edge	6.843	2.603		
Difference	1.052	1.494	0.312	3.376

TABLE 6.16: t-test on estimation of SDH Length with different methods.

Method	**p-value**	**t-crit**	**lower**	**upper**	**Sig.**
Chan-Vese	0.0003	2.0739	-1.6740	-0.5781	yes
Edge	0.003	2.074	0.406	1.698	yes
Proposed	0.847	2.074	-0.101	0.083	no

TABLE 6.17: Estimation of SDH Breadth with different methods in brain CT Scans. The total count of cases is 23 and the degree of freedom is 22. The hypothesized difference of means is 0 suggesting that there is no difference between the expert's and the algorithms' estimations at $\alpha = 0.05$.

Groups	**Mean**	**Std. Dev.**	**Std. Err.**	**t**
Expert	3.174	0.835		
Proposed Method	3.143	0.848		
Difference	0.030	0.136	0.028	1.071
Chan-Vese	4.078	1.020		
Difference	-0.904	0.798	0.166	-5.435
Edge	2.713	0.974		
Difference	0.461	0.676	0.141	3.269

TABLE 6.18: t-test on estimation of SDH Breadth with different methods.

Method	**p-value**	**t-crit**	**lower**	**upper**	**Sig.**
Chan-Vese	1.850E-05	2.074E+00	-1.249E+00	-5.593E-01	yes
Edge	0.004	2.074	0.169	0.753	yes
Proposed	0.296	2.074	-0.029	0.089	no

The results specific to SDH identification and measurement are presented in Tables 6.15 and 6.17 and the respective results of paired t-test are given in Tables 6.16 and 6.17. It can be seen that the null hypothesis is rejected in case of the state of the art models.

Performance of the proposed method which produces no statistically significant differences in measurements compared with the expert and in its case, the null hypothesis is not rejected.

6.9 Estimation of Brain Indices and Ratios

These estimations of measurements are performed on 72 CT scans of normal and non-trauma pathological cases and compared with the manual annotation of the expert. The cases in which significant effacement of the ventricles was observed were excluded from these experiments on recommendation of the radiology expert. The Fig. 2.10 shows the landmarks for measurements and the formulae given in Table 2.7.

The Intraclass Correlation Coefficient (ICC) was calculated using MedCalc®to compare the results with experts to ascertain reliability of measurements performed by the algorithm. Linear measurements from experts and proposed algorithm show ICC range from 0.98 to 0.99 and the results are given in tables 6.19 and 6.20.

The paired t-test was performed in Microsoft^{TM}Excel using the data analysis tool. The null hypothesis was established stating that there is no difference in the performance between the algorithm and expert. Hence, $\Delta = 0$ is used in Equation 6.10, which is the hypothesized difference between the means of paired measurements. The evaluation was done with $\alpha = 0.05$.

TABLE 6.19: Measurements on the axial CT scans. The consistency in estimating linear measurements is given as Intraclass Correlation Coefficient (ICC).

Label	**Measurement**	**ICC**
A	Maximum frontal horn diameter	0.996
B	Minimum width of the lateral ventricles at the heads of the caudate nuclei	0.978
C	Maximum width of the 3rd ventricle	0.999
D	Inner skull diameter at the level of the frontal horns	0.997
E	Inner skull diameter at the level of the caudate nuclei	0.978
F	Maximum inner skull diameter	0.988
G	Outer skull diameter at the frontal horns	0.986
H	Maximum outer skull diameter	0.987
I	Minimum width of the lateral ventricles separated by the septum (cella media)	0.986

TABLE 6.20: Indices and Ratios estimated on the axial CT scans

Indices	**Calculation**	**ICC**
Evan's Ratio (ER)	A/F	0.982
Bifrontal Index (BFI)	A/D	0.995
Bicaudate Index (BCI)	B/E	0.976
Cella Media Index (CMI)	H/I	0.969
Frontal Horn Index (FHI)	G/A	0.972
Ventricular index (VI)	B/A	0.970
Huckman number (HN)	A+B	0.970
3rd ventricle width (V3)	C	0.999

6.9.1 Estimation of Cella Media Index (CMI)

The CMI is a clinically important measurement to assess the normal growth, pathological and age related atrophic changes and normally it is > 4. It is the ratio of biparietal diameter of skull to maximum external diameter of lateral ventricles at cella media (i.e central part of lateral ventricles as shown in Fig. 2.10).

The performance of the algorithm will null hypothesis stating that there is no difference between the expert's measurements and the results given by the algorithm in Tables 6.21 and 6.22, show that the null hypothesis can not be rejected.

TABLE 6.21: Estimation of Cella Media Index in brain CT Scans. The hypothesized difference of means is 0 suggesting that there is no difference between the expert's and the algorithm's estimations at $\alpha = 0.05$.

Groups	**Expert**	**Algorithm**	**Difference**
Count	72	72	72
Mean	4.770	4.788	-0.018
Std. Dev.	0.710	0.777	0.255
Std. Err.			0.030
t			-0.614
df			71

TABLE 6.22: t-test on estimation of Cella Media Index. There is no statistically significant difference in the measurements between the expert and algorithm according to the t-test.

t-test	*p-value*	*t-critical*	*lower*	*upper*	*sig*
Two Tail	0.54108	1.99394	-0.07845	0.0415	no

6.9.2 Estimation of Bifrontal Index

Atrophy of the brain is normally related to age but can be more aggressive amongst alcoholics and smokers and in such cases bifrontal index is a clinically significant measure. It is also consulted in cases with hydrocephalus and intra-ventriclar haemorrhage.

The mean of measurements from the algorithm is 0.361 and from the experts, it is 0.360 which is within the range clinically specified and established in literature. The performance of the algorithm will null hypothesis stating that difference in

means is zero is shown in Tables 6.23 and 6.24. From the results it can be inferred that the null hypothesis is not rejected.

TABLE 6.23: Estimation of Bifrontal Index in brain CT Scans. The hypothesized difference of means is 0 suggesting that there is no difference between the expert's and the algorithm's estimations at $\alpha = 0.05$.

Groups	**Expert**	**Algorithm**	**Difference**
Count	72	72	72
Mean	0.360	0.361	0.000
Std. Dev.	0.035	0.035	0.005
Std. Err.			0.001
t			-0.659
df			71

TABLE 6.24: t-test on estimation of Bifrontal Index. There is no statistically significant difference in the measurements between the expert and algorithm according to the t-test.

t-test	*p-value*	*t-critical*	*lower*	*upper*	*sig*
Two Tail	0.512	1.994	-0.002	0.001	no

6.9.3 Estimation of Width of Third Ventricle

The width of third ventricle is routinely measured in hospitals; for instance, in patients with multiple sclerosis to assess neocortical atrophy. The values range from 2.9mm in infants to up to 13mm in patients over 80 years of age.

The expert's annotations show a mean of 4.681mm while the algorithm's output has a mean of 4.696mm in linear measurement of the width of the third ventricle.

The hypothesized difference of means = 0, is thus, not rejected as shown in Tables 6.25 and 6.26 which signifies the robust performance of the algorithm.

TABLE 6.25: Estimation of width of third ventricle in brain CT Scans. The hypothesized difference of means is 0 suggesting that there is no difference between the expert's and the algorithm's estimations at $\alpha = 0.05$.

Groups	**Expert**	**Algorithm**	**Difference**
Count	72	72	72
Mean	4.681	4.696	-0.015
Std. Dev.	1.002	1.000	0.093
Std. Err.			0.011
t			-1.389
df			71

TABLE 6.26: t-test on estimation of width of third ventricle. There is no statistically significant difference in the measurements between the expert and algorithm according to the t-test.

t-test	*p-value*	*t-critical*	*lower*	*upper*	*sig*
Two Tail	0.169	1.994	-0.037	0.007	no

6.10 Identification of CSF Spaces as ROI

The identification of the cisterns showed an ICC of ≥ 0.91 which can be improved by adding shape constraint to identify supra cellar and the quadrigeminal cisterns more accurately. The third and lateral ventricles are much more precisely detected and measured.

TABLE 6.27: Identification of CSF spaces as ROI on the axial CT scans.

Region of Interest	**ICC**
Supra cellar cistern	0.91
Quadrigeminal cistern	0.97
Lateral ventricles	0.97
Intracranial haematoma	0.99

6.11 Performance of the Junior Radiologist

The junior radiologist involved in annotating the CT scans had less than 2 years experience in the emergency radiology. Therefore, his performance was slightly less accurate in identification and measurements of the salient features. However, it was not statistically significant and only 9 cases were misclassified by him out of 159. The performance in estimating brain indices and ratios was also less than the expert.

TABLE 6.28: Estimation of Haematoma size by junior radiologist in brain CT Scans. The total count of cases is 51 and the degree of freedom is 50. The hypothesized difference of means is 0 suggesting that there is no difference between the expert's, the junior radiologist's estimations and the algorithm's results at $\alpha = 0.05$.

Groups	**Mean**	**Std. Dev.**	**Std. Err.**	**t**
Breadth of the Lesion				
Expert	3.986	1.332		
Proposed Method	4.006	1.328		
Difference	-0.020	0.170	0.018	-1.074
Junior Radiologist	3.802	1.228		
Difference	0.184	0.829	0.089	2.068
Length of the Lesion				
Expert	7.989	1.911		
Proposed Method	7.990	1.799		
Difference	-0.001	0.357	0.038	-0.030
Junior Radiologist	7.906	2.276		
Difference	0.083	1.939	0.208	0.398

TABLE 6.29: Two Tail t-test on estimation of Haematoma size with different radiologist and proposed algorithm.

Method	**p-value**	**t-crit**	**lower**	**upper**	**Sig.**
Breadth of the Lesion					
Junior Radiologist	0.692	1.988	**-0.331**	**0.496**	no
Proposed Algorithm	0.286	1.988	**-0.056**	**0.017**	no
Length of the Lesion					
Junior Radiologist	0.042	1.988	**0.007**	**0.361**	**yes**
Proposed Algorithm	0.976	1.988	**-0.077**	**0.075**	**no**

The results in Tables 6.28 and 6.29 show that performance of the junior radiologist is not at par with the expert and there is disagreement between the measurements carried out on 51 cases with haematoma out of the 87 TBI cases. This is highlighted by the paired t-test results in which the length of the haematoma measurements has statistically significant discordance with the expert. The two tails in case of junior radiologists are at 0.007 and 0.361 while the algorithm shows -0.077 and 0.075.

However, the performance of the proposed algorithm is robust and the results signify that it performs better than the junior radiologist in approximating the segmentation and demarcations by the expert. There is no statistically significant difference in the results of the algorithm compared with the expert.

Also, in the measurement of the breadth of the haematoma, although the junior radiologist's results are not statistically and significantly different from the expert, the performance of the algorithm outperforms the junior radiologist as given in Table 6.29. The two tails in case of junior radiologists are -0.331 and 0.496 while the algorithm shows -0.056 and 0.017.

Hence, if the expert's opinion is considered as gold standard, then the algorithm can significantly reduce the variability in assessments by the junior radiologist by providing him the valuable 'second opinion' in absence of the senior expert.

6.12 Correlation to the Marshall CT Classification

The information gathered from the clinical and imaging profile of the patient is used by the doctors to ascertain the diagnosis, plan treatment and most importantly, establish the prognosis. Assessment of the severity of the trauma by consulting CT classification schemes such as one proposed by Marshall et al. (Table 2.2) is routinely performed to be used in trauma score chart (Table 2.11) and for establishing prognosis from the clinical model (Fig. 2.16).

The compressed or absent cisterns are seen in Marshall et al. ratings II and III while midline shift classifies IV and above. The presence of mixed or high density lesion $> 25cm^3$ is classified as rating VI. When these characteristics are not identified, the CT would fall in rating I or normal. The performance evaluation is given in Table 6.30.

Since the experiments were conducted on the cross-sectional, noncontrast CT studies performed at the time of admission of within early hours of injury, none of the patients had mass lesions removed at that time. Hence, no CT with Rating V were used in the experiments.

TABLE 6.30: Classification of the brain trauma CT according to Marshall et al. CT Rating.

Marshall CT Class	**Feature**	**ICC**
I or II	Cisterns and Ventricles	0.91 and 0.97
III or IV	Midline Shift	0.98
V or VI	Lesion $> 25cm^3$	0.99

6.13 Hardware and Software Resources

The experiments were performed using Matlab® R2013b on Mac OS X and Windows 7 platforms with Intel®Core-i7 processors and 16GB of RAM. Graphics Processing Unit (GPU) acceleration of functions was supported by nVidia GTX550Ti with 1GB memory and nVidia GTX690 with 4GB memory for Windows, and nVidia GT650M with 384 CUDA™cores and 1GB memory for Mac OS X. The Jacobian training is not supported on GPU in Matlab R2013b and in those cases, only CPU was used.

6.14 Summary

The domain of medical image analysis by the radiologists demands efficient timing and accuracy of interpretation as it plays a vital role for patients' management within the 'golden hour'. The localization, assessment, measurement and extent of the pathology or trauma is an important factor for ascertaining the prognosis and deciding the targeted therapy. However, variability in the assessments by experts and junior radiologists can significantly affect outcomes for the patients and it is imperative to minimize such discordance.

The performance of PDCAAC framework in segmentation and estimation of measurements in brain CT scans has shown plausible results with no discernible, statistically significant difference from the experts' annotations. The experiments run with different configurations of the modified active contour algorithm produce consistent and cross-validated results which outperform the state of the art in segmenting the desired regions. The decomposition of the medical image into regions of interest and otherwise is an expert task and the untrained eye can miss salient features which are critical to the diagnosis. The integration of PDCAAC framework in clinical settings can significantly reduce such errors and misses as is depicted by the results of different evaluation measures presented in this chapter.

It is also presented that the performance of the proposed method is better than the junior radiologist in approximating the 'gold standard' segmentations. Even in cases where the junior radiologist is able to identify and estimate the measurements, the performance of the algorithm is significantly closer to that of the expert. Hence, results from the proposed method can be used as 'second opinion' in the absence of the more experienced experts.

Chapter 7

Conclusion

The scientific man does not aim at an immediate result. He does not expect that his advanced ideas will be readily taken up. His work is like that of a planter – for the future. His duty is to lay the foundation for those who are to come, and point the way.

Nikola Tesla

Interpretation of the medical images by the radiologists is fraught with errors and variations which represent the weakest aspect of clinical imaging. While the research efforts to correlate image features to clinical outcomes are imperative for differential diagnosis, prognostic assessment, pre-surgical mapping and treatment planning in patients, these endeavours are fettered by the time and effort required to manually report clinical findings. Manual demarcation of ROI by expert radiologists is still considered gold standard, however, poor perception, inaccurate deduction, incomplete knowledge or the quality of the image can lead to missed diagnoses and grave consequences. The usefulness of CAD systems is established, however, this research has highlighted the gaps in the application domain and hypothesized that the inter-observer and intra-oberserver variability can be reduced by systematically following the clinical diagnosis procedures described in Chapter 2 and implementing them through image processing and artificial intelligence.

The use of image processing and machine learning techniques to help clinicians has been widely accepted with the aim to reduce inter-observer and intra-observer variability as discussed in Chapter 3. However, most of the algorithms present the users with a long list of parameters to tweak in order to get the results which can make them quite daunting and less user friendly for clinicians. Doctors and radiologists prefer simple to use interfaces and get plausible results while presenting them with complex technical jargon, Greek symbols and a plethora of adjustable arguments can be intimidating. The impetus for developing an automated medical image analysis system should be to facilitate the radiologists and reduce their workload rather than impeding them from making timely decisions of diagnoses, prognoses and management strategy.

A pertinent representation of information within neuroimages requires effective and robust segmentation as the most important image processing step. Accurate measurements and estimations can not be aptly performed if the regions of interest are not clearly demarcated which affect the diagnosis and management regimen. A surfeit of methods proposed for segmentation mostly require the user to coarsely identify the region of interest and the algorithms then endeavour to encapsulate the region. As discussed in Chapter 3, existing methods require manual fixing of the seed for segmentation and this user interaction is time consuming. Also if the initial demarcation was less accurate, the results of algorithms can go amiss. The gaps, thus identified in this chapter, are used to formulate a comprehensive framework to facilitate doctors by reducing errors, minimising misinterpretations and speeding up the diagnosis process.

The PDCAAC Framework presented in Chapter 4 is content aware, meaning that it knows what it is looking for in the neuroimages. The awareness is achieved by incorporating clinical and neurological assessment features in to the method using principles of polyrepresentation. Hence, if the region of interest is a haematoma, the algorithm will succinctly identify the hyperdense, elliptic region in the CT. If the region of interest is CFS, the algorithm can robustly ignore non-region of

interest and localize on the pertinent structures. Hence, the placement of the initial seeding curve for the active contour is totally automatic, aided by the artificial neural network, and does not require manual interaction from the radiologists. This improves the segmentation accuracy and results closely approximate the experts' intuition. The realization of objectives 1, 2 and 3 has been achieved through the proposed framework.

The implementation details of the PDCAAC framework have been presented in Chapter 5. The framework circumvents shortcomings of the state of the art methods and is an endeavour to expedite the process of neuroimage analysis by the observing radiologist. The fallibleness of the state of the art methods including placement location and size of the initial curve are efficiently solved by the proposed modified active contour method utilizing clinical profile and image features classified by ANN. Similarly, the edge detection is significantly improved by incorporating the constraint energies and ensuring the curve does not creep into the adjacent regions or under-segments which have been identified as limitations with the state of the art models. This work realizes objectives $4-6$ identified in Chapter 1.

The skull enclosing the brain saves it from a lot of external forces, however, in case of internal forces, the skull can restrict the expansion leading to raised intracranial pressure (ICP) and herniation of the brain. Skull trephination is perhaps the oldest surgical procedure with archaeological evidence to alleviate the pressure but it can also be relieved with drugs. The doctors need measurements and estimations of indices and ratios of the brain, e.g., to ascertain the ICP, which can be assessed from the brain CT. The PDCAAC Framework is capable of providing these linear measurements from noncontrast brain CT scans and achieves objective 2 enlisted in Chapter 1.

It can be seen that the proposed approach adapts well to diverse image characteristics and the performance is very close to the expert radiologists' annotation as shown by the results in Chapter 6. The limitations of the proposed method in handling less

frequent cases with gross deformation of the anatomical structures are also discussed. Is is statistically signified that the performance of the less experiences radiologist is also superseded by the proposed method and, hence, it can be construed that the proposed approach is adept for segmentation of brain CT scans in clinical and research environments. The PDCAAC framework can significantly reduce observer variability and minimize misinterpretations of brain CT scans which was set as the aim of this research.

7.1 Transferability

The proposed method gives robust and efficient segmentation and linear measurements on noncontrast brain CT scans. It is, therefore, proposed that the underlying algorithm can prove efficacious if transferred to other application domains and a few of them are listed below.

- Applicability on other body regions like thorax and abdomen can be useful in assessing the sizes of viscera in normal and abnormal cases and correlating them to established models to ascertain diagnoses. An example would be to segment the heart in chest x-ray images and indicate cases with cardiac hypertrophy.

- The proposed method can be used in assessing the size of amniotic sac to determine the rate of growth of foetuses during pregnancy. The common imaging modality of choice during pregnancy is 2-D ultrasonography and radiologists measure the lengths of the two axes of the sac to estimate its volume.

- The artificial neural network in the proposed algorithm can be trained to identify tumours both in the intracranial CT as well as other body regions. A useful application would be the segmentation of kidney tumours like

nephroblastoma which present with both hyper- and hypodense regions along with normal renal tissue.

- In longitudinal CT studies, comparisons of sizes of anatomical structures to assess effects of medical and/or surgical interventions are performed. The proposed algorithm can efficiently fulfil such requirements by analysing and estimating differences in measurements on longitudinal CT data representing pre- and post-treatment images.

7.2 Future work

This research has endeavoured to highlight the gaps in the existing computer based methodologies and clinical applications and propose a plausible solution. Automated assessment of medical images is an active area of research and there are many unexplored vistas to be investigated. The following list is not exhaustive and presents only a few research domains which can benefit from the contributions of this thesis.

- The validation of proposed method can be extended to larger datasets and longitudinal studies. The evaluation of performance on other medical imaging modalities like MRI, correlate findings related to age and gender specific observations and research to formulate correlations between image features and clinical variables encompassing normal development, ageing, pathological and traumatic cases can also be undertaken.

- The classification of clinical features and image data of TBI cases can be evaluated using techniques such as the Random Forests, Support Vector Machines and Case Based Reasoning which have been identified in the literature review. Efficient and robust results have been achieved by these approaches which necessitates their evaluation in the context of assessment of TBI cases.

- The research can also be extended to facilitate in ascertaining differences in treatment and outcome between countries and centres in comparative effectiveness research as proposed by Maas et al. (2013). Assessment of longitudinal data can help improve treatment planning and management of patients. Identification of prognostic factors and evaluation of effectiveness of drugs and/or surgical interventions requires comparison of pre- and post-treatment images which can be achieved with the proposed method.

- The approach used for identification and demarcation of CSF spaces can be modified to incorporate information of spatial location. The applicability of the enhancement will be to detect Subarachnoid Haemorrhage in CT scans. The diagnosis is suspected when hyperdense material is seen filling the subarachnoid space. The image analysis can then be classified according to the Fischer scale, based on the amount of blood, useful in predicting cerebral vasospasm (Godfrey & Singh 2009).

- Finite element modelling to correlate injury characteristics to structure-function deficit (Ruan et al. 1994, Horgan & Gilchrist 2003, Post et al. 2012). The brain tissue consists of grey and white matter with spaces filled by the cerebrospinal fluid. An injury, for example a fall, will accelerate and decelerate the distinct structures differently and the enclosed skull will restrict the movement resulting in coup and contra coup damage. A model of the brain using finite element analysis can help the clinicians predict the outcomes based on the information of the injury. The affected structures can be mapped to the functional disabilities that may follow.

- For the TBI patients, an important consideration is whether and when can they return to their regular social and professional life. The different scales, such as disability rating score (DRS) and functional independence measure (FIM), can be useful for the care givers in supporting the patient and promising return to normal pre-injury lifestyle (Brooks et al. 2013). The

proposed work can be extended to automatically correlate image features, clinical findings and neuro-psychological assessments to disability rating scores which would be useful for the clinicians, patients and carers of the patients.

- Shape matching to ascertain the structural damage due to mass effect or other abnormalities is critically important in management of the patient (Paniagua et al. 2013). Using approaches like principal component analysis, the shapes of normal and abnormal anatomical structures can be matched to atlases, controls and established models to ascertain the type, severity and progress of pathology or trauma.

- During surgery, the soft brain tissue can move due to the intervention by the surgeon or effects of gravity which can affect the accuracy of the surgical procedure. Real-time segmentation, measurement and registration for image guided surgery is an active area of research (Eggers et al. 2014). The method proposed in this thesis can be enhanced to perform real-time segmentation and registration of the acquired images along with measurements of any displacements and presented to the surgeon as a 'second opinion'.

- Development of a '**Neuroimaging Opinion Maker**' software suite for use in emergency departments of hospitals and research environment. It is an observation that fatal traumas mostly occur on weekends probably due to lifestyle, activities or mere coincidence (Haapaniemi et al. 1996, Fang et al. 2010). The incidence could be attributed to disparities in resources, expertise, and healthcare providers working during weekends (Saposnik et al. 2007). In such environments, the proposed software can support the junior radiologists in ascertaining the diagnosis leading to improved treatment and outcome for the patient.

- Development of a public dataset for TBI CT analyses. Literature review has highlighted the requirement of developing a dataset of TBI CT scans which

can be accessed and analysed by researchers interested in similar research. The are a number of brain MRI datasets, brain tumour CT datasets and PET and fMRI datasets available, however, a comprehensive and annotated brain trauma dataset is not publicly available. The FITBIR, set up by USA's Government, is an initiative but it is not yet available for public download. The CT brain trauma dataset developed by Maas et al. from the IMPACT studies only contains the text describing the CT and no image data are available (Maas et al. 2013). The data at Trauma Audit and Research Network (TARN), University of Manchester, is not available for public access. Hence, another significant contribution of this research will be to facilitate the researchers by providing them annotated images for development of methods and algorithms.

Appendix A

Typical CT Study of Brain

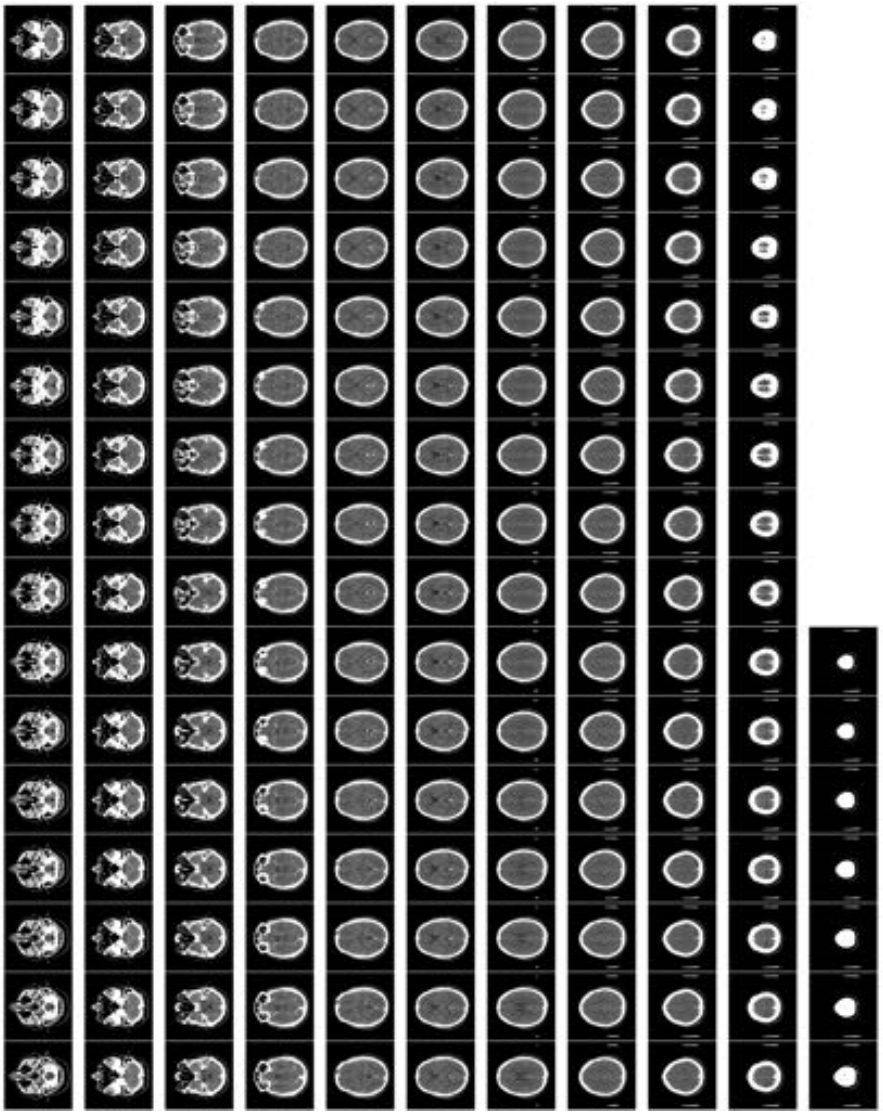

Appendix B

Typical MRI Study of Brain

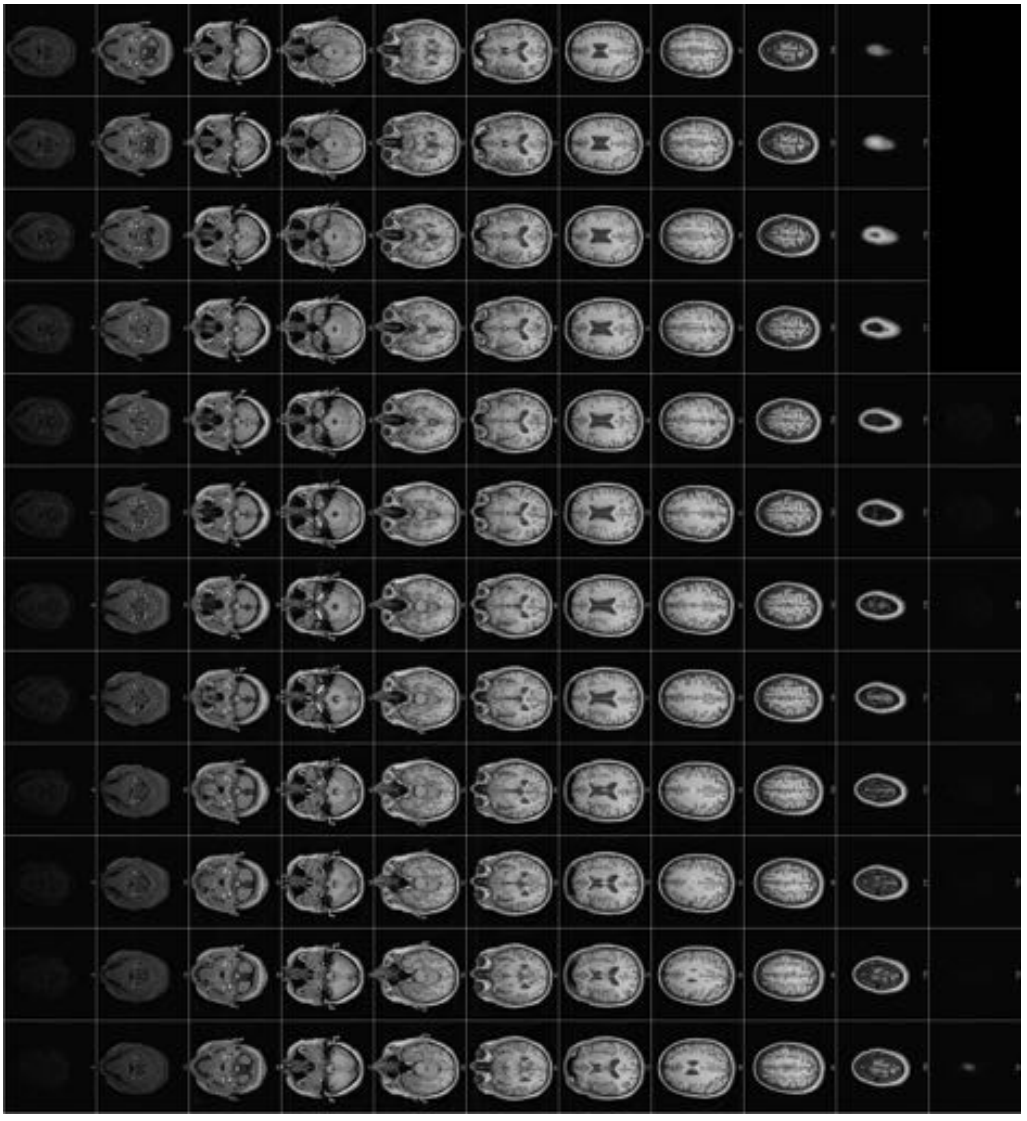

Appendix C

CT Scans of TBI Patients

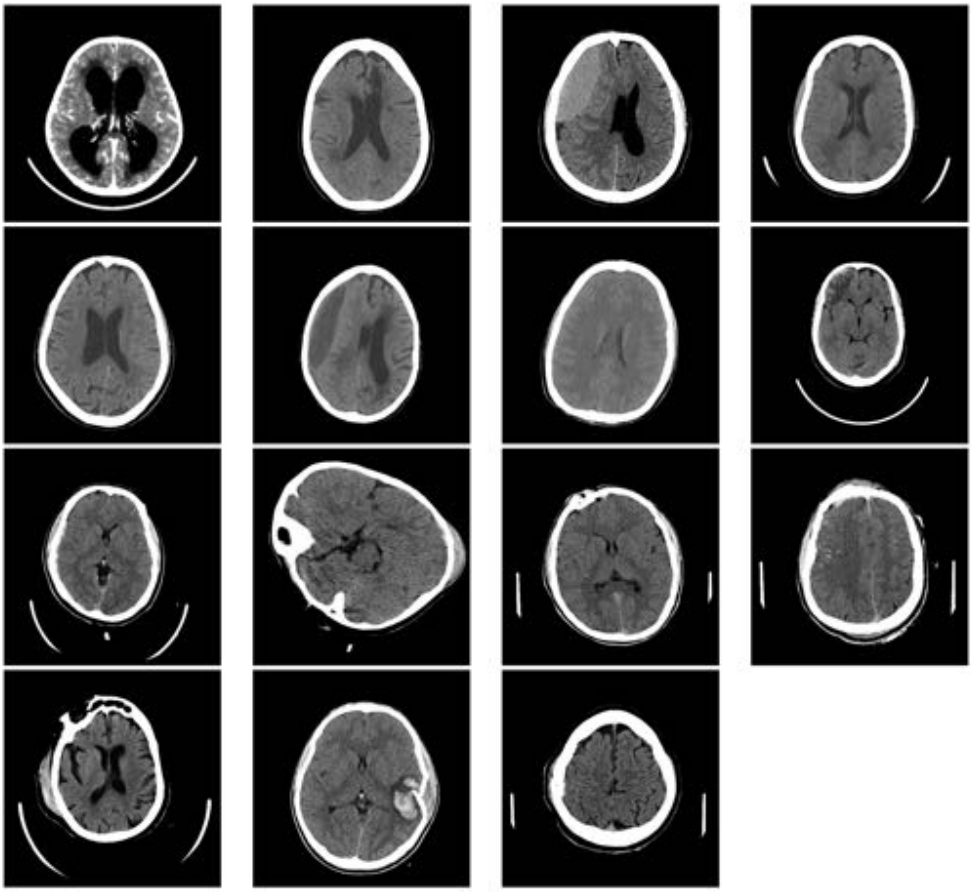

FIGURE C.1: CT scans of the TBI Cases used in experiments.

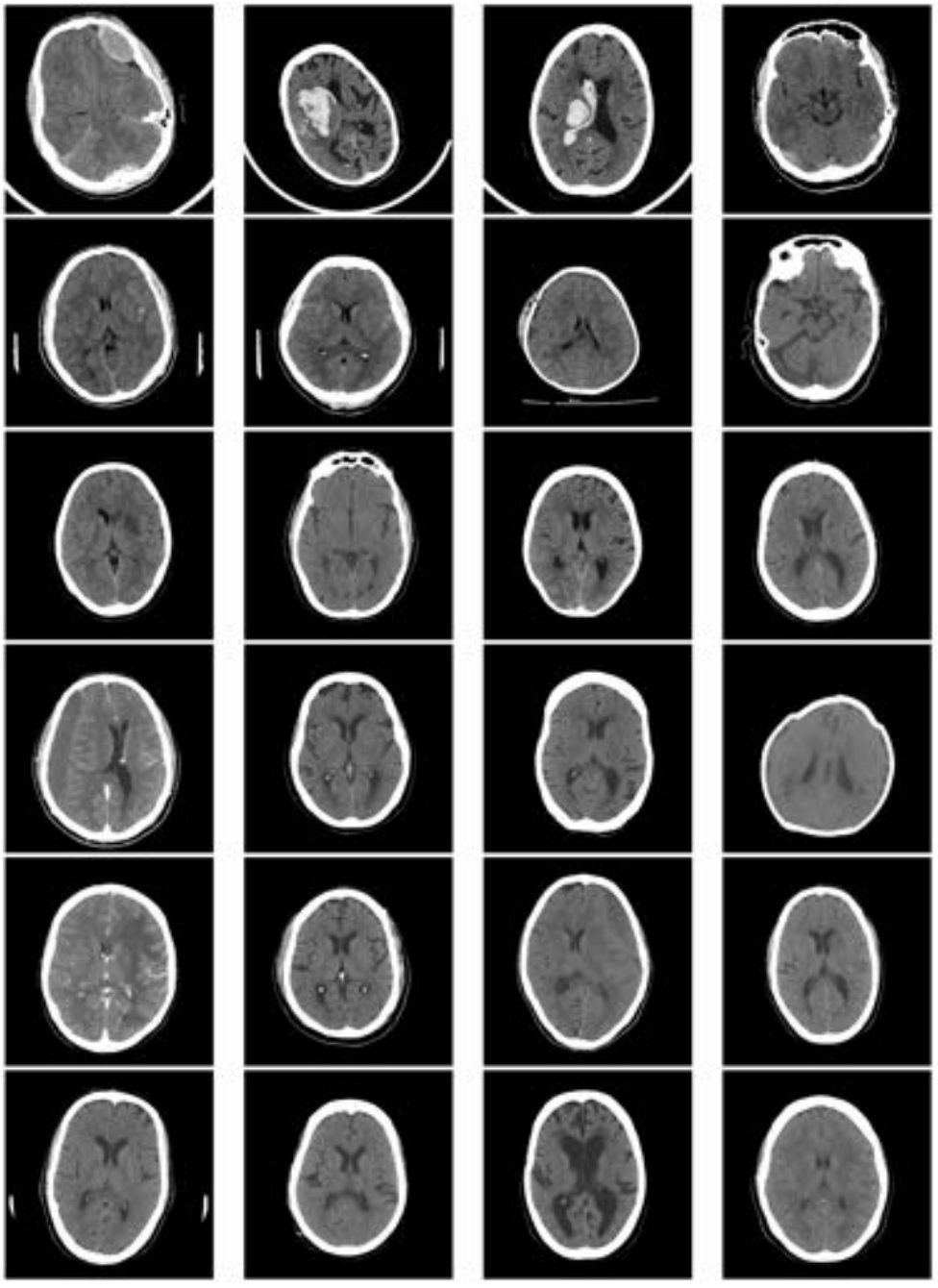

FIGURE C.2: CT scans of the TBI Cases used in experiments.

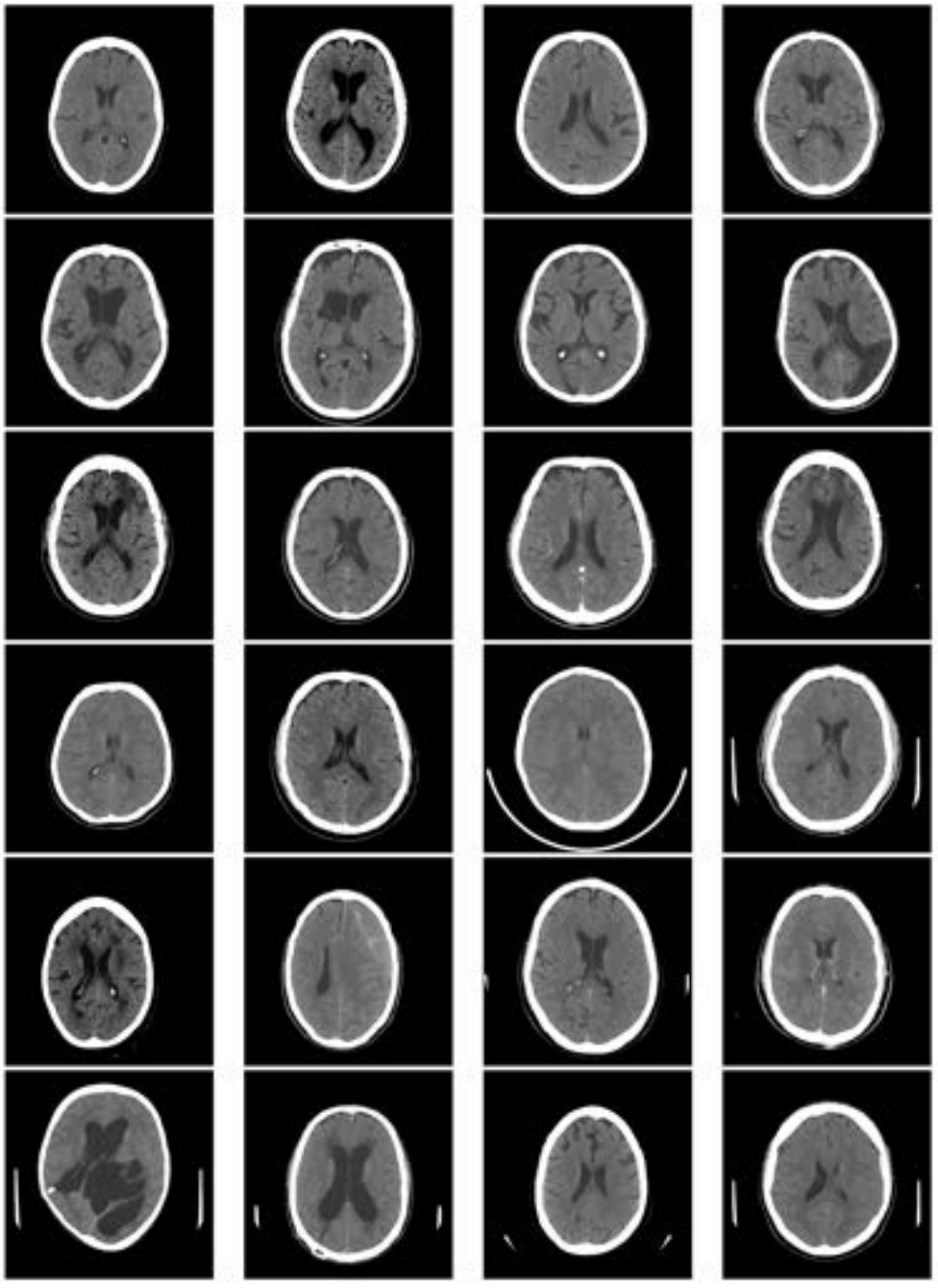

FIGURE C.3: CT scans of the TBI Cases used in experiments.

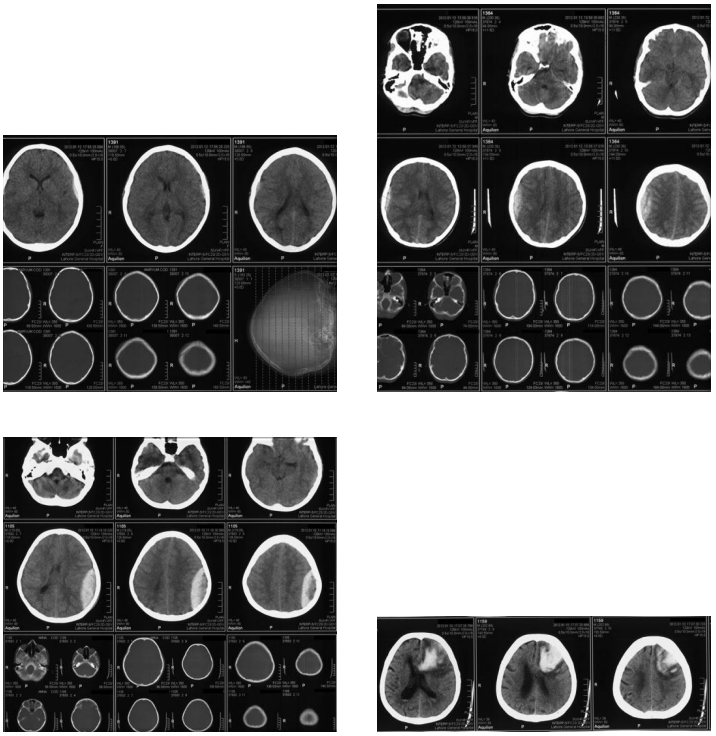

FIGURE C.4: CT scans of the TBI Patients used in experiments. Only a few cases are given to establish reference.

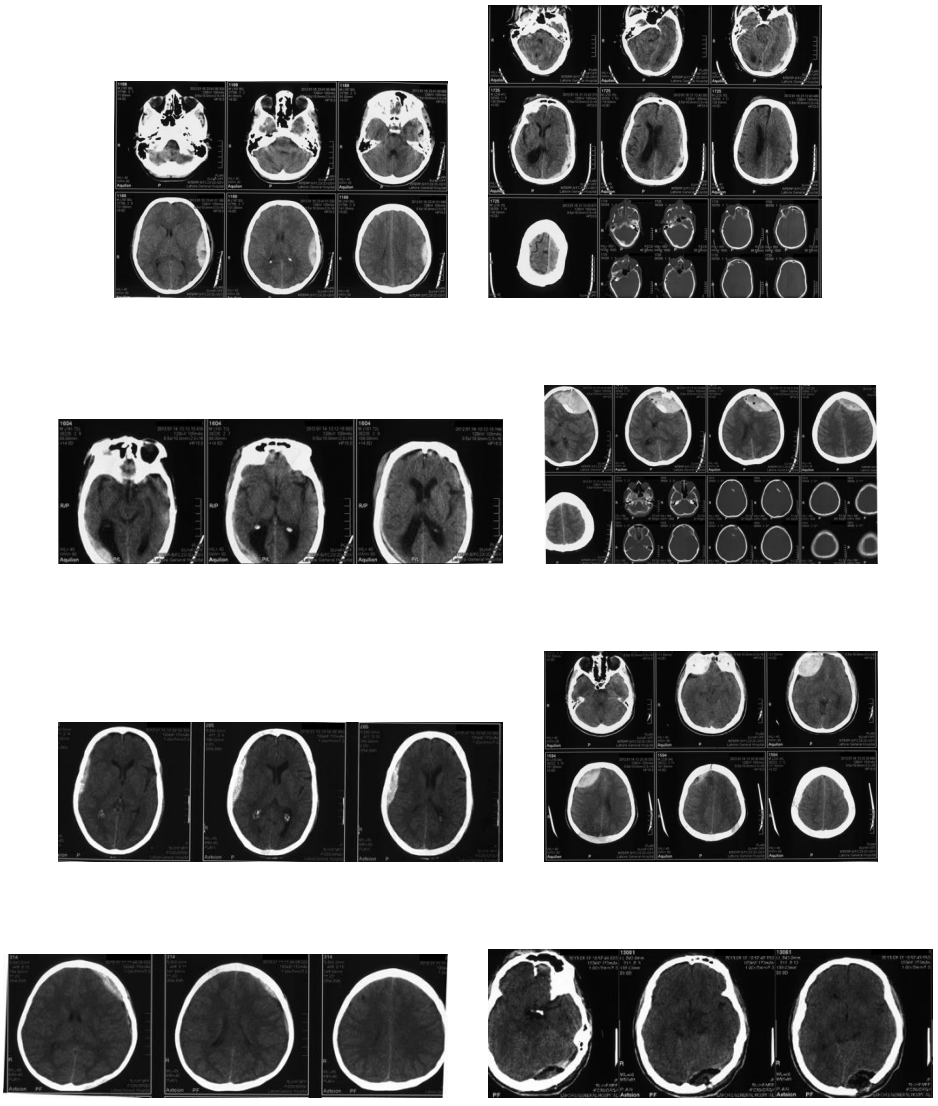

FIGURE C.5: CT scans of the TBI Patients used in experiments. Only a few cases are given to establish reference.

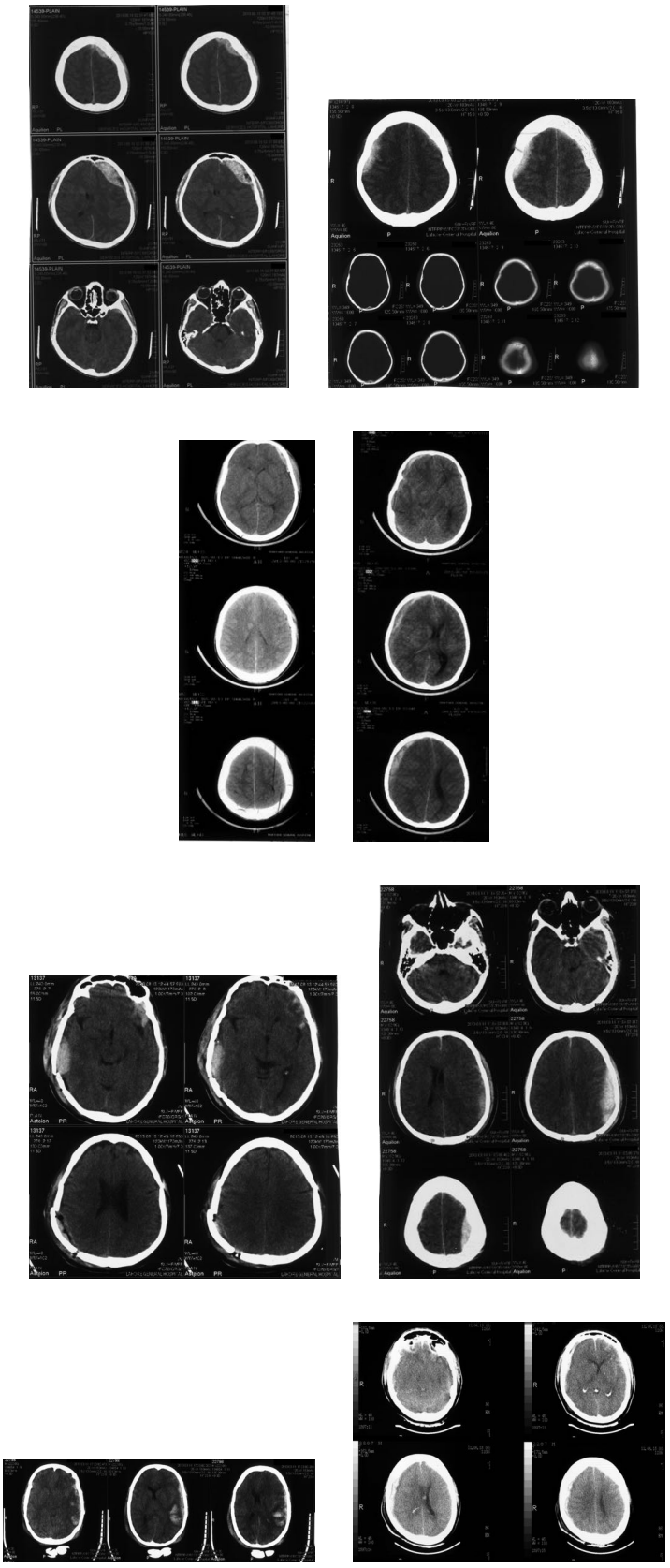

FIGURE C.6: CT scans of the TBI Patients used in experiments. Only a few cases are given to establish reference.

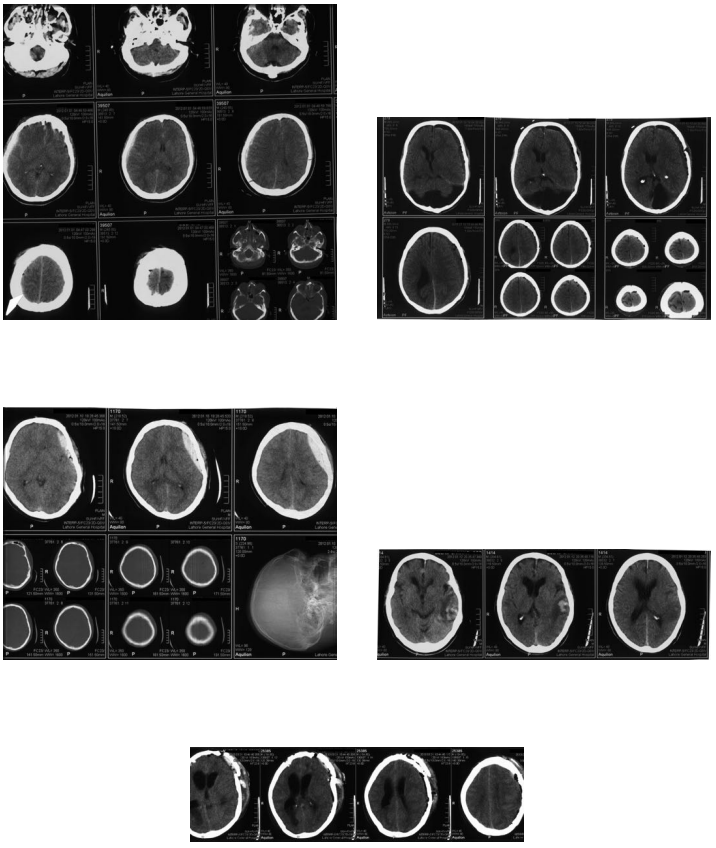

FIGURE C.7: CT scans of the TBI Patients used in experiments. Only a few cases are given to establish reference.

Appendix D

Clinical and Neurological Assessment Data

Table D.1: Description of Clinical and Neurological Assessment Data Elements

Data Element	Description
Pt. ID	Anonymous patient ID
Gender	M = Male, F = Female
Age	Age in years (or months as ##m)
Diagnosis	Differential Diagnosis
Cause	Cause of injury, 0 = unknown
LoC	Loss of consciousness after injury
Vomit	Number of vomiting episodes after injury
ENT Bleed	Bleeding from ear, nose or mouth after injury
Fits	Fits or seizures after injury
Dizziness	Dizziness after injury
Headache	Headache after injury
Weakness	History of weakness
HTN	History of Hypertension
GCS	Glasgow Coma Scale score at admission
Pupil L	Left pupil response at admission, 0 = not done
Pupil R	Right pupil response at admission, 0 = not done
Temp	Body temperature at admission
Pulse	Pulse rate at admission
Resp	Respiratory rate at admission, v = on ventilator
BP	Blood pressure at admission
Outcome	D = Dead, S = Survived
Hosp	Days spent in hospital

Pt. ID	Gender	Age	Diagnosis	Cause	LoC	Vomit	ENT Bleed	Fits	Dizziness	Headache	Weakness	HTN	GCS	Pupil L	Pupil R	Temp	Pulse	Resp	BP	Outcome	Hosp
pt_001	F	35	Edema	Fall	0	1	1	0	0	0	0	0	13	FD	FD	98	88	18	130/90	D	1
pt_002	F	48	Parieto Occipital SOL	0	0	1	0	0	0	1	Rt	0	15	FD	FD	98	80	12	130/80	D	1
pt_003	F	65	Lt Parieto Occipital Contusion, AcSDH	Fall	1	1	0	1	0	0	Rt	1	10	R	R	98	80	12	130/80	D	9
pt_004	F	65	ICH	CVA	1	0	0	0	0	0	0	1	4	0	0				140/80	D	1
pt_005	F	40	Spontaneous SAH		1	1	0	0	0	2	0	1	15	R	R	98	88	20	200/100	S	14
pt_006	F	2	Mild TBI, Edema	Fall	1	0	1	0	0	0	0	0	14	R	R	98	102	22	0	S	2
pt_007	F	20	Edema	Fall	1	0	0	0	1	0	0	0	12	R	R	98	70	0	100/70	S	4
pt_008	F	5	Frontal Contusion	Fall	1	1	1	1	0	0	0	0	10	R	R	100	106	24	0	S	17
pt_009	F	24	Rt Parietal AcSDH	RTA	1	1	1	0	0	0	0	0	10t	FD	R	98	80	20	130/50	S	20
pt_010	F	4	tSAH, IVH	Fall	1	1	0	0	0	0	0	0	7	N	N	98	108	26	0	S	3
pt_011	F	75	Lt. Fronto-temporo-parietal ch. SDH	Fall	0	0	0	0	1	1	1	1	15	N	N	98	78	20	120/80	S	4
pt_012	F	1.5	Rt. Parietal fracture	Fall	1	1	1	0	0	0	0	0	11	FD	N					S	2
pt_013	F	18	Lt. acute SDH	RTA	1	0	1	0	0	0	0	0	7	N	N	98	80	20	110/70	S	7
pt_014	F	2	Rt. F/P EDH	Fall	1	1	0	0	1	0	0	0	11	FD	FD	98	82	20	100/60	S	3
pt_015	F	38	Lt. acute SDH T/P	RTA	1	0	1	1	0	0	0	0	8	FD	N	98	65	26	120/70	D	7
pt_016	F	53	Rt. Ac. SDH	RTA	1	1	1	0	0	0	0	0	6	FD	FD	98	86	22	150/90	D	2
pt_017	F	24	Frontal SAH	RTA	1	1	0	0	0	1	0	0	13	N	N	98	82	20	100/60	D	1
pt_018	F	45	Lt. SDH	RTA	1	1	1	0	0	0	0	0	3	FD	FD	98	92	20	120/80	D	30
pt_019	F	45	Lt. Temporal EDH, Rt. Contusion	RTA	1	1	1	0	0	0	0	0	10	N	N	98	62	20	150/90	D	3
pt_020	F	45	Rt. Parietal EDH	RTA	1	1	0	0	0	0	0	1	6	N	FD	98	88	26	200/110	D	1
pt_021	F	6	Lt. Temporal EDH	Fall	1	2	0	0	0	0	0	0	15	S	S	99	100	20	130/80	S	2
pt_022	F	65	Spontaneous frontal ICH	0	0	1	0	0	0	0	0	1	9	N	N	98	68	18	140/100	S	5
pt_023	F	9	Lt. t/p EDH	Fall	1	1	0	0	1	0	0	0	15	N	N	98	94	28	130/80	S	2
pt_024	F	60	Rt. Temporal contusion	RTA	1	2	1	0	1	0	0	0	10	S	S	98	86	20	150/100	S	6
pt_025	F	8	Lt. Frontal EDH	Fall	1	1	1	0	0	0	0	0	12	N	N	89	88	20	110/70	S	5
pt_026	F	46	Rt. Ac. SDH	RTA	1	1	1	0	0	0	0	0	11	N	N	99	86	26	170/60	S	11
pt_027	F	57	Lacunar infarcts peri-ventricular	0	0	0	0	1	0	0	1	1	15	N	N	99	78	20		S	11
pt_028	F	58	Rt. Tmporal infarction	0	0	1	0	0	0	0	1	0	15	N	N	98	80	20	110/70	S	7
pt_029	F	69	Lt. cerebellar infarct	Fall	0	0	0	0	1	1	0	0	15	N	N	98	92	20		S	4
pt_030	F	2	Bifrontal infarcts	0	0	1	0	1	1	0	0	0	14	N	N	98	96	20	110/50	S	4
pt_031	F	23	Enlargement of pituitary gland	0	0	0	0	0	1	1	0	0	15	N	N	98	90	22	120/70	S	2
pt_032	F	68	Old ischaemic infarct cerebellar	0	0	1	0	0	1	0	1	1	15	N	N	98	90	22	160/70	S	3
pt_033	F	52	Bilateral cerebellar infarct	0	0	1	0	0	1	0	0	1	15	N	N	98	76	20	150/80	S	2
pt_034	F	66	Rt. Centrum semiovale infarct	0	1	0	0	0	0	0	1	0	15	N	N	98	82	18	100/70	S	4
pt_035	F	75	Lt. internal capsule infarct	0	0	1	0	0	0	1	1	1	15	N	N	98	88	22	170/90	S	3
pt_036	F	50	Bilateral basal ganglia calcifications	0	0	1	0	0	1	1	0	0	14	N	N	98	90	24	120/80	S	1
pt_037	F	50	Normal	0	0	1	0	0	0	1	1	1	15	N	N	98	94	24	160/100	S	2
pt_038	F	51	Normal	0	0	1	0	0	0	1	1	1	15	N	N	99	82	22	160/90	S	1
pt_039	F	2	Normal	Fall	0	1	0	1	0	0	0	0	15	N	N	98	88	26	110/70	S	1
pt_040	F	68	Lt. temporal infarct	0	1	0	0	0	1	1	1	0	15	N	N	98	65	20	120/70	S	1

Pt. ID	Gender	Age	Diagnosis	Cause	LoC	Vomit	ENT Bleed	Fits	Dizziness	Headache	Weakness	HTN	GCS	Pupil L	Pupil R	Temp	Pulse	Resp	BP	Outcome	Hosp
pt_041	F	53	Lt. internal capsule infarct	0	0	0	0	0	0	1	1	0	15	N	N	98	86	22	150/90	S	1
pt_042	F	50	Normal	Fall	0	1	0	0	0	0	1	1	15	N	N	98	72	18	180/80	S	2
pt_043	F	24	Normal	0	1	0	0	1	0	1	0	0	15	N	N	98	82	20	100/60	S	1
pt_044	M	13	Lt Post Parietal Contusion	Fight	0	0	0	0	1	0	0	0	13	FD	FD	98	78	18	100/80	D	1
pt_045	M	42	tSAH	RTA	1	1	1	0	0	0	0	0	6	FD	FD	98	88	22	110/70	D	1
pt_046	M	35	Lt Parietal SDH	RTA	1	1	1	0	0	0	0	0	4	FD	FD	98	92	20	160/100	D	1
pt_047	M	25	Spontaneous ICH	0	0	0	0	0	0	1	Lt	0	15	R	R	98	78	18	120/80	D	15
pt_048	M	22	Hydrocephalus, SDH	RTA	0	1	0	0	0	0	0	0	15	R	R	98	88	22	110/70	D	10
pt_049	M	1	AcSDH	Fall	1	1	1	1	0	0	0	0	10	R	FD	98	110	V	0	D	1
pt_050	M	60	C5-C6 dislocation	fall	0	0	0	0	0	0	0	0	15	R	R	98	88	20	150/90	D	5
pt_051	M	70	tSAH	Fall	0	0	0	0	0	0	0	0	10	0	0	98	86	20	150/90	D	5
pt_052	M	4	Parietal SDH	Fall	0	1	0	0	0	0	0	0	12	R	R	98	72	24	0	S	8
pt_053	M	6m	Rt Parietal EDH	Fall	2	2	0	0	0	0	0	0	13	R	R	98	124	32	0	S	8
pt_054	M	2	Rt Frontal EDH	Fall	1	1	0	1	0	0	0	0	15	R	R	104	134	38	0	S	6
pt_055	M	2.5	Normal	Fall	0	1	1	0	0	0	0	0	15	R	R	98	98	20	0	S	1
pt_056	M	30	Parietal EDH	RTA	1	0	1	0	0	0	0	0	12	R	R	98	80	18	100/80	S	4
pt_057	M	10	Edema	RTA	1	0	1	0	0	0	0	0	8	FD	FD	99	100	20	0	S	6
pt_058	M	30	Edema	Fight	1	1	1	0	0	0	0	0	8	R	R	0	0	0	0	S	1
pt_059	M	65	Posterior Parital Contusion	RTA	1	0	1	0	0	0	0	1	13	R	R	98	78	20	140/90	S	5
pt_060	M	40	Edema	Fall	1	1	1	0	0	0	0	0	11	R	R	98	80	20	100/70	S	1
pt_061	M	24	Frontal Contusion	RTA	1	0	1	0	0	0	0	0	15	R	R	98	80	20	100/80	S	2
pt_062	M	30	Edema	RTA	0	0	1	0	0	0	0	0	12	R	R	98	88	0	110/90	S	1
pt_063	M	1.5	Parital EDH	Fall	1	1	0	0	0	0	0	0	10	R	R	98	132	28	0	S	4
pt_064	M	45	SAH	RTA	0	0	0	0	0	0	0	0	15	R	R	98	88	22	130/90	S	1
pt_065	M	20	DAI	Fall	1	0	0	0	0	0	0	0	7	R	R	102	80	20	80/50	S	30
pt_066	M	18	Lt Parietal EDH	RTA	1	1	0	0	0	0	0	0	15	R	R	98	88	20	90/60	S	3
pt_067	M	26	Edema	RTA	0	1	0	0	0	0	1	0	13	R	R	98	80	20	110/60	S	3
pt_068	M	20	Lt Parietal Contusion	RTA	1	0	0	0	0	0	0	0	14	R	R	98	88	22	120/80	S	11
pt_069	M	45	Lt Temporal Contusion	RTA	1	1	1	0	0	0	0	0	12	R	R	98	80	20	100/80	S	7
pt_070	M	60	Lt Parietal Contusion	RTA	0	1	0	0	0	1	0	0	12	R	R	99	80	18	100/80	S	3
pt_071	M	17	Lt Parietal EDH	RTA	1	1	1	0	0	0	0	0	4t	R	R	99	84	22	0	S	11
pt_072	M	40	Edema	RTA	1	1	1	0	0	0	0	0	13	R	R	98	84	22	130/70	S	1
pt_073	M	40	DAI, SAH	RTA	1	0	0	0	0	0	0	0	3t	FN	FD	99	84	v	150/100	D	7
pt_074	M	10	DAI	Fall	1	0	1	0	0	0	0	0	7	N	FD	98	80	20	0	S	2
pt_075	M	25	Frontal Fracture and pneumocephaly	RTA	1	1	0	0	0	0	0	0	14	N	N	98	18	18	90/60	S	12
pt_076	M	16	Edema	RTA	1	2	1	0	0	0	0	0	9	N	N	99	88	22	120/80	S	1
pt_077	M	35	Rt. Temporal Ac SDH	Fall	1	1	0	0	0	0	0	0	13	N	N	98	82	20	130/90	S	8
pt_078	M	7	Frontal fracture and contusion	Fall	1	1	1	0	0	0	0	0	10	0	0	98	98	22		S	5
pt_079	M	25	Rt. Frontal depressed skull fracture	RTA	1	1	0	0	0	0	0	0	15	N	N	98	84	20	120/70	S	2
pt_080	M	25	Mild TBI, post ictal	RTA	1	1	0	1	0	0	0	0	10	N	N	99	88	22	120/80	S	2

Pt. ID	Gender	Age	Diagnosis	Cause	LoC	Vomit	ENT Bleed	Fits	Dizziness	Headache	Weakness	HTN	GCS	Pupil L	Pupil R	Temp	Pulse	Resp	BP	Outcome	Hosp
pt_081	M	50	SAH	Assault	1	1	1	0	0	0	0	0	3T	0	ND					D	2
pt_082	M	47	Occipital EDH, contusion	RTA	1	1	1	0	0	0	0	0	13	N	N	98	90	20	180/100	S	2
pt_083	M	23	Lt. Parieto-occipital EDH	RTA	1	1	0	0	0	0	0	0	10	N	N	98	84	20	130/90	S	3
pt_084	M	10	Rt. Parietal EDH	Fall	1	1	1	0	0	0	0	0	15	N	N	99	88	24	0	S	2
pt_085	M	25	Lt. Temporo-parietal ac SDH	Assault	1	1	1	0	0	0	0	0	11T	FD	FD	100	132	v	135/100	S	23
pt_086	M	9	SOL Postrior fossa, tuberculoma	0	0	1	0	0	1	1	0	0	15	N	N	98	102	24	115/85	S	17
pt_087	M	20	Lt. Parietal EDH	RTA	1	1	1	0	0	0	0	0	10	N	N	98	84	20	130/70	S	6
pt_088	M	9	Lt. Parietal EDH	Fall	1	1	0	0	0	0	0	0	9	N	N					S	10
pt_089	M	9	Spontaneous ICH, Thallesemia	0	0	1	0	1	0	0	1	0	15	N	N	99	78	20		S	12
pt_090	M	29	Rt. Frontal Abscess	0	1	1	0	0	0	1	0	0	15	N	N	98	80	20	120/80	S	10
pt_091	M	22	Lt. occipital EDH	RTA	1	1	0	0	0	0	0	0	12	N	N	98	80	20	120/70	S	8
pt_092	M	21	Lt. Frontal EDH	Fall	1	1	0	0	0	0	0	0	15	N	N	98	92	20		S	4
pt_093	M	32	Lt. Parietal EDH	RTA	1	1	0	0	0	0	0	0	15	N	N	98	96	20	110/50	S	4
pt_094	M	26	Rt. T/P SDH, Lt. frontal EDH	RTA	1	1	0	0	0	0	0	0	10	N	N	98	80	22	120/80	S	5
pt_095	M	50	EDH	Fall	1	1	0	0	0	0	0	0	9	ND	ND	98	86	20	120/80	S	4
pt_096	M	9	Rt. Parietal EDH	RTA	1	0	0	0	0	0	0	0	15	N	N	98	90	22	120/70	S	6
pt_097	M	18	Frontal EDH	Fall	1	1	1	0	0	0	0	0	15	N	N	98	90	22	120/70	S	3
pt_098	M	20	Lt. Oedema	RTA	1	1	0	0	0	0	0	0	12	N	N	98	88	20	120/80	S	2
pt_099	M	20	Lt. EDH, hydrocephalus	0	0	1	0	1	1	0	1	0	10	N	N	98	82	18	100/70	D	27
pt_100	M	24	Rt. Parietal EDH	RTA	1	1	1	0	0	0	0	0	12	N	N	98	90	22	120/70	S	2
pt_101	M	13	Rt. Parietal SDH	RTA	0	1	0	0	0	0	0	0	15	N	N	98	82	20	100/60	S	2
pt_102	M	18	Lt Parietal contusion, SAH	RTA	1	1	1	0	0	0	0	0	15	N	N	98	90	22	120/70	S	2
pt_103	M	60	tSAH	Fall	1	1	0	0	0	1	0	0	15	N	N	98	110	20	140/90	S	7
pt_104	M	10	Lt. Parietal EDH	Fall	1	1	0	0	0	0	0	0	15	N	N	98	90	22	120/70	S	3
pt_105	M	18	Lt. temporo-parietal EDH	Fall	1	1	1	0	0	0	0	0	14	N	N	98	90	24	120/80	S	4
pt_106	M	3	Lt. temporo-parietal EDH	Fall	0	1	0	0	0	0	0	0	15	N	N	99	84	24	160/100	S	8
pt_107	M	20	Rt. temporal EDH, Lt. parietal contusion	RTA	1	1	0	0	0	0	0	0	14	N	N	98	94	24	160/90	S	4
pt_108	M	50	Rt. T/p EDH	RTA	1	1	1	0	0	0	0	0	14	N	N	98	94	24	160/100	S	4
pt_109	M	30	Lt. Parietal EDH	RTA	0	1	0	0	0	0	0	0	12	FD	N	99	78	18	110/60	S	6
pt_110	M	5	Lt Parietal Ac SDH	Fall	1	1	0	0	0	0	0	0	15	N	N	98	110	24	120/80	S	4
pt_111	M	18	Lt. Frontal contusion	RTA	1	1	0	0	0	0	0	0	13	N	N	98	82	20	100/60	S	4
pt_112	M	12	Lt. t/p EDH	RTA	1	1	0	0	0	0	0	0	15	N	N	101	100	18	120/80	S	3
pt_113	M	11	Rt. Ac. SDH t/p	RTA	1	0	0	0	0	0	0	0	5T	FD	N	99	92	v	130/90	S	3
pt_114	M	6	Rt. Parietal contusion, SDH	Fall	1	1	0	0	0	0	0	0	15	N	N	100	110	26	140/80	S	4
pt_115	M	50	Bifrontal SDH	RTA	2	1	1	0	1	1	1	1	9	NR	NR	98	82	20	100/60	D	10
pt_116	M	70	Rt. Parietal ICH	Fall	2	2	0	0	0	0	0	0	7	N	N	98	82	v	80/50	D	2
pt_117	M	45	Rt. Parietal ICH	RTA	1	1	0	0	0	0	0	0	5	FD	FD	99	82	V	50/30	D	1
pt_118	M	25	Rt. F/P EDH	RTA	1	1	1	0	0	0	0	0	12	N	N	98	88	20	110/70	D	10
pt_119	M	50	Rt. SAH, ICH	Fall	2	0	0	0	0	0	0	1	3	FD	FD	98	72	18	180/80	D	6
pt_120	M	35	Lt. parietal EDH, Rt. Temporal contusion	RTA	1	1	1	0	0	0	0	0	5	FD	FD	100	88	20	140/70	D	1

Pt. ID	Gender	Age	Diagnosis	Cause	LoC	Vomit	ENT Bleed	Fits	Dizziness	Headache	Weakness	HTN	GCS	Pupil L	Pupil R	Temp	Pulse	Resp	BP	Outcome	Hosp
pt_121	M	22	Frontal fracture, contusion, SDH	RTA	1	1	1	0	0	0	0	0	7	FC	FD	98	84	20	160/100	D	3
pt_122	M	60	Multiple contusion	RTA	0	0	1	0	0	0	0	0	5	N	N	99	90	20	130/90	D	3
pt_123	M	27	Rt. Occipital EDH	RTA	1	1	1	0	0	0	0	0	11	S	S	99	84	20	100/70	S	4
pt_124	M	16	Lt. Temporal EDH, Rt. Contusion	RTA	1	1	0	0	0	0	0	0	15	N	N	99	84	20	110/70	S	2
pt_125	M	10	Rt. Parietal EDH	Fall	1	0	0	0	0	0	0	0	15	N	N	98	94	20	110/70	S	2
pt_126	M	35	Lt. SDH	RTA	1	1	1	1	0	0	0	0	7	FD	FD	99	84	20	165/100	S	12
pt_127	M	19	Lt. F/P EDH	RTA	0	1	0	0	0	0	0	0	12	N	N	98	88	22	130/80	S	3
pt_128	M	60	Lt. Temporal contusion	RTA	1	1	1	0	0	0	0	0	13	N	N	98	78	20	140/80	S	1
pt_129	M	48	Lt. F/P Ch SDH	0	1	1	0	0	1	1	1	0	9	N	N	100	90	20	120/80	S	4
pt_130	M	16	Lt. t/p EDH	RTA	1	1	1	0	0	0	0	0	12	N	N	99	88	20	120/80	S	1
pt_131	M	17	Frontal EDH	Machine	1	1	1	0	0	0	0	0	8	N	N	99	88	20	120/80	S	3
pt_132	M	30	Lt. Ac. SDH	RTA	1	1	0	0	0	0	0	0	11	FD	FD	98	80	20	130/90	S	3
pt_133	M	33	Rt. EDH, contusion	RTA	1	1	0	0	0	0	0	0	8	N	N	98	82	18	130/80	S	5
pt_134	M	60	Occipital EDH, contusion	Fall	1	0	0	0	0	0	0	0	14	N	N	99	84	20	140/70	S	5
pt_135	M	65	Lt. T/P/O Ac SDH	Fall	1	1	1	0	0	0	0	0	8	FD	N	99	86	20	140/70	S	3
pt_136	M	15	Frontal EDH	RTA	0	1	1	0	0	0	0	0	14	N	N	100	86	20	130/80	S	3
pt_137	M	40	Lt Ac. SDH	RTA	1	1	1	0	0	0	0	0	11	N	N	98	84	20	100/70	S	6
pt_138	M	20	Lt. Parietal EDH	RTA	1	1	1	0	0	0	0	0	10	N	N	98	84	20	130/70	S	6
pt_139	M	49	Infarction t/p	HTN	1	0	0	0	0	1	1	1	9	N	N	98	86	20	150/100	S	5
pt_140	M	65	Lt. t/p infarction	0	0	0	0	0	0	1	1	1	14	N	N	98	80	20	120/80	S	7
pt_141	M	44	Normal	0	0	0	0	0	0	1	0	0	15	N	N	98	84	24	120/70	S	1
pt_142	M	63	Anaplastic Oligodendro Glioma	0	1	0	0	0	0	1	0	1	14	N	N	98	80	22	120/80	S	15
pt_143	M	76	Normal	0	0	0	0	0	0	1	0	0	15	N	N	98	86	20	140/80	S	4
pt_144	M	65	Lt. centrum semiovale infarct	RTA	0	0	0	0	1	1	1	0	15	N	N	98	90	22	130/70	S	2
pt_145	M	70	Infarction posterior Rt. internal capsule	0	0	0	0	0	1	1	1	1	15	N	N	98	82	20	170/100	S	4
pt_146	M	72	Lt. internal capsule infarct	Fall	0	0	0	0	0	1	0	1	15	N	N	98	90	22	150/90	S	2
pt_147	M	45	Hypodensity Lt. temporal lobe	0	0	0	0	0	0	1	1	0	15	N	N	98	110	20	130/90	S	2
pt_148	M	3	Normal	Fall	0	1	0	0	0	0	0	0	15	N	N	99	84	24	140/90	S	2
pt_149	M	20	Normal	Fall	0	0	0	0	1	1	0	0	15	N	N	98	94	24	130/80	S	1
pt_150	M	30	Normal	0	0	0	0	0	1	1	0	0	15	N	N	99	78	18	100/60	S	2
pt_151	M	5	Normal	Fall	0	1	0	0	0	0	0	0	15	N	N	98	110	24	140/80	S	1
pt_152	M	18	Normal	RTA	0	0	0	0	0	0	0	0	15	N	N	98	88	26	130/80	S	1
pt_153	M	32	Normal	RTA	0	0	0	0	1	0	0	0	15	N	N	101	100	18	120/80	S	2
pt_154	M	66	Lt. centrum semiovale infarct	0	0	0	0	0	1	0	1	1	15	N	N	100	90	26	140/80	S	2
pt_155	M	70	Normal	Fall	0	0	0	0	0	1	0	1	15	N	N	98	76	20	120/70	S	2
pt_156	M	70	Lt. internal capsule infarct	Fall	0	1	0	0	0	0	1	1	15	N	N	98	82	22	130/90	S	2
pt_157	M	45	Normal	0	0	0	0	0	0	1	0	0	15	N	N	99	82	20	130/80	S	1
pt_158	M	25	Normal	Fall	0	0	0	0	1	0	0	0	15	N	N	98	88	20	110/70	S	1
pt_159	M	35	Normal	0	0	1	0	0	0	1	1	0	15	N	N	100	88	20	140/70	S	1

TABLE D.2: Patient Data of Clinical and Neurological Assessment

Appendix E

CT Device and Protocol

E.1 Toshiba Activion 16

Feature	Value
Slice thickness	1.0 mm
KVP	120
Data Collection Diameter	320.00
Protocol Name	Brain
Reconstruction Diameter [1]	240.00
Gantry/Detector tilt [1]	+6.0
Table Height [1]	+55.0
Rotation Direction	CW
X-ray tube current	220
Exposure time	220
Generator power	26
Focal Spots	1.6 \1.4
Convolution kernel	FC23
Patient position	HFS

[1] Values differ between patients

Samples per pixel	1
Photometric Interpretation	Monochrome
Rows	512
Columns	512
Pixel spacing	0.468 \0.468
Bits allocated	16
Bits stored	16
High bit	15
Window center	40
Window width	120
Rescale intercept	0
Rescale slope	1

TABLE E.1: Acquisition of Brain CT on Toshiba Activion 16

E.2 Philips Brilliance 16

Feature	Value
Slice thickness	5.0 mm
KVP	120
Data Collection Diameter	500.00
Protocol Name	Brain
Reconstruction Diameter [1]	181.00
Gantry/Detector tilt [1]	0
Table Height [1]	+141.0
Rotation Direction	CW
Exposure	300
X-ray tube current	225
Convolution kernel	UC
Patient position	HFS

Samples per pixel	1
Photometric Interpretation	Monochrome
Rows	512
Columns	512
Pixel spacing	0.3535 \0.3535
Bits allocated	16
Bits stored	12
High bit	11
Window center	40
Window width	80
Rescale intercept	-1024
Rescale slope	1

TABLE E.2: Acquisition of Brain CT on Philips Brilliance 16

Bibliography

Achanta, R., Shaji, A., Smith, K., Lucchi, A., Fua, P. & Süsstrunk, S. (2010), Slic superpixels, Technical report.

Achanta, R., Shaji, A., Smith, K., Lucchi, A., Fua, P. & Susstrunk, S. (2012), 'Slic superpixels compared to state-of-the-art superpixel methods', *Pattern Analysis and Machine Intelligence, IEEE Transactions on* 34(11), 2274–2282.

Adams, F. et al. (1849), *The genuine works of Hippocrates*, Vol. 17, Sydenham society.

Al-Ayyoub, M., Alawad, D., Al-Darabsah, K. & Aljarrah, I. (2013), 'Automatic detection and classification of brain hemorrhages', *WSEAS Transactions on Computers* 12(10), 395–405.

Arendts, G., Manovel, A. & Chai, A. (2003), 'Cranial ct interpretation by senior emergency department staff', *Australasian radiology* 47(4), 368–374.

Arlot, S., Celisse, A. et al. (2010), 'A survey of cross-validation procedures for model selection', *Statistics surveys* 4, 40–79.

Armato III, S. G., McNitt-Gray, M. F., Reeves, A. P., Meyer, C. R., McLennan, G., Aberle, D. R., Kazerooni, E. A., MacMahon, H., van Beek, E. J., Yankelevitz, D. et al. (2007), 'The lung image database consortium (lidc): an evaluation of radiologist variability in the identification of lung nodules on ct scans', *Academic radiology* 14(11), 1409.

Armato III, S. G., Roberts, R. Y., Kocherginsky, M., Aberle, D. R., Kazerooni, E. A., MacMahon, H., van Beek, E. J., Yankelevitz, D., McLennan, G., McNitt-Gray, M. F. et al. (2009), 'Assessment of radiologist performance in the detection of lung nodules: dependence on the definition of "truth"', *Academic radiology* 16(1), 28.

Athanasiou, A., Tardivon, A., Tanter, M., Sigal-Zafrani, B., Bercoff, J., Deffieux, T., Gennisson, J.-L., Fink, M. & Neuenschwander, S. (2010), 'Breast lesions: Quantitative elastography with supersonic shear imaging—preliminary results1', *Radiology* 256(1), 297–303.

Balasooriya, U. & Perera, M. (2012), Intelligent brain hemorrhage diagnosis using artificial neural networks, *in* 'Business Engineering and Industrial Applications Colloquium (BEIAC), 2012 IEEE', IEEE, pp. 128–133.

Balleyguier, C., Kinkel, K., Fermanian, J., Malan, S., Djen, G., Taourel, P. & Helenon, O. (2005), 'Computer-aided detection (cad) in mammography: Does it help the junior or the senior radiologist?', *European journal of radiology* 54(1), 90–96.

Bankman, I. (2008), *Handbook of medical image processing and analysis*, academic press.

Baraff, L. J., Byyny, R. L., Probst, M. A., Salamon, N., Linetsky, M. & Mower, W. R. (2010), 'Prevalence of Herniation and Intracranial Shift on Cranial Tomography in Patients With Subarachnoid Hemorrhage and a Normal Neurologic Examination', *Academic Emergency Medicine* 17(4), 423–428.

Barbieri, A. L., De Arruda, G., Rodrigues, F. A., Bruno, O. M. & Costa, L. d. F. (2011), 'An entropy-based approach to automatic image segmentation of satellite images', *Physica A: Statistical Mechanics and its Applications* 390(3), 512–518.

Bardera, A., Boada, I., Feixas, M., Remollo, S., Blasco, G., Silva, Y. & Pedraza, S. (2009), 'Semi-automated method for brain hematoma and edema quantification

using computed tomography', *Computerized Medical Imaging and Graphics* 33(4), 304–311.

Barker-Collo, S., Kahan, M. & Starkey, N. (2012), 'Computerised tomography indices of raised intracranial pressure and traumatic brain injury severity in a new zealand sample.', *The New Zealand medical journal* 125(1360), 92.

Barnhill, S. D. & Zhang, Z. (1998), 'Computer assisted methods for diagnosing diseases'. US Patent 5,769,074.

Barrett, B. J. & Parfrey, P. S. (2006), 'Preventing nephropathy induced by contrast medium', *New England Journal of Medicine* 354(4), 379–386.

Beers, M. H., Fletcher, A. J., Jones, T., Porter, R., Berkwits, M. & Kaplan, J. (2003), *The Merck manual of medical information*, Pocket Books.

Bendtsen, C., Kietzmann, M., Korn, R., Mozley, P., Schmidt, G. & Binnig, G. (2011), 'X-ray computed tomography: semiautomated volumetric analysis of late-stage lung tumors as a basis for response assessments', *Journal of Biomedical Imaging* 2011, 5.

Bhadauria, H., Singh, A. & Dewal, M. (2013), 'An integrated method for hemorrhage segmentation from brain ct imaging', *Computers & Electrical Engineering* 39(5), 1527–1536.

Bishop, C. M. et al. (2006), *Pattern recognition and machine learning*, Vol. 1, springer New York.

Blackshaw, G., Gostling, J., Appleton, B., Pearce, N., Thomas, G. & Lewis, W. (2003), 'Illumination of x-rays: the usual lights exposed', *Postgraduate medical journal* 79(928), 99–100.

Blum, A. L. & Langley, P. (1997), 'Selection of relevant features and examples in machine learning', *Artificial intelligence* 97(1), 245–271.

Bogoni, L., Cathier, P., Dundar, M., Jerebko, A., Lakare, S., Liang, J., Periaswamy, S., Baker, M. & Macari, M. (2014), 'Computer-aided detection (cad) for ct colonography: a tool to address a growing need', *The British Journal of Radiology* .

Brandt, A., Andronikou, S., Wieselthaler, N., Louw, B., Kilborn, T., Dekker, G., Bertelsman, J. & Dreyer, C. (2007), 'Accuracy of radiographer reporting of paediatric brain ct', *Pediatric radiology* 37(3), 291–296.

Brennan, P. C., McEntee, M., Evanoff, M., Phillips, P., O'Connor, W. T. & Manning, D. J. (2007), 'Ambient lighting: effect of illumination on soft-copy viewing of radiographs of the wrist', *American Journal of Roentgenology* 188(2), W177–W180.

Broderick, J. P., Brott, T. G., Duldner, J. E., Tomsick, T. & Huster, G. (1993), 'Volume of intracerebral hemorrhage. a powerful and easy-to-use predictor of 30-day mortality.', *Stroke* 24(7), 987–993.

Brooks, J. C., Strauss, D. J., Shavelle, R. M., Paculdo, D. R., Hammond, F. M. & Harrison-Felix, C. L. (2013), 'Long-term disability and survival in traumatic brain injury: results from the national institute on disability and rehabilitation research model systems', *Archives of physical medicine and rehabilitation* 94(11), 2203–2209.

Burges, C. J. (1998), 'A tutorial on support vector machines for pattern recognition', *Data mining and knowledge discovery* 2(2), 121–167.

Campbell, F. W. & Robson, J. (1968), 'Application of fourier analysis to the visibility of gratings', *The Journal of Physiology* 197(3), 551.

Caselles, V., Catté, F., Coll, T. & Dibos, F. (1993), 'A geometric model for active contours in image processing', *Numerische mathematik* 66(1), 1–31.

Caselles, V., Kimmel, R. & Sapiro, G. (1997), 'Geodesic active contours', *International journal of computer vision* 22(1), 61–79.

Castellano, G., Fanelli, A. M. & Pelillo, M. (1997), 'An iterative pruning algorithm for feedforward neural networks', *Neural Networks, IEEE Transactions on* 8(3), 519–531.

CDC.GOV (2014), 'Cdc - traumatic brain injury - injury center'. [Online; accessed 14-March-2014].
URL: *http://www.cdc.gov/traumaticbraininjury/*

Cevidanes, L., Oliveira, A. E., Motta, A., Phillips, C., Burke, B. & Tyndall, D. (2009), 'Head orientation in cbct-generated cephalograms', *The Angle orthodontist* 79(5), 971–977.

Ceylan, M., Ozbay, Y., Ucan, O. N. & Yildirim, E. (2010), 'A novel method for lung segmentation on chest ct images: complex-valued artificial neural network with complex wavelet transform', *Turk J Elec Eng & Comp Sci* 18(4), 613–623.

Chan, T. (2007), 'Computer aided detection of small acute intracranial hemorrhage on computer tomography of brain', *Computerized Medical Imaging and Graphics* 31(4), 285–298.

Chan, T., Esedoglu, S. & Ni, K. (2009), 'Histogram Based Segmentation Using Wasserstein Distances', *International Journal of Computer Vision* 84(1), 97–111.

Chan, T. F. & Vese, L. A. (2001), 'Active contours without edges', *Image Processing, IEEE Transactions on* 10(2), 266–277.

Chan, T. & Zhu, W. (2005), Level set based shape prior segmentation, *in* 'Computer Vision and Pattern Recognition, 2005. CVPR 2005. IEEE Computer Society Conference on', Vol. 2, IEEE, pp. 1164–1170.

Chaplot, S., Patnaik, L. & Jagannathan, N. (2006), 'Classification of magnetic resonance brain images using wavelets as input to support vector machine and neural network', *Biomedical Signal Processing and Control* 1(1), 86–92.

Chaudhuri, Z. (2011), *Postgraduate Ophthalmology*, Jaypee Brothers Medical Pub.

Chawla, A. S. & Samei, E. (2007), 'Ambient illumination revisited: A new adaptation-based approach for optimizing medical imaging reading environments', *Medical physics* 34, 81.

Chawla, M., Sharma, S., Sivaswamy, J. & Kishore, L. (2009), A method for automatic detection and classification of stroke from brain ct images, *in* 'Engineering in Medicine and Biology Society, 2009. EMBC 2009. Annual International Conference of the IEEE', IEEE, pp. 3581–3584.

Chen, Smith, Ji, Ward & Najarian (2009), 'Automated ventricular systems segmentation in brain CT images by combining low-level segmentation and high-level template matching.', *BMC medical informatics and decision making* 9(1).

Cheng, K., Gu, L., Wu, J., Li, W. & Xu, J. (2008), A novel level set based shape prior method for liver segmentation from mri images, *in* 'Medical Imaging and Augmented Reality', Springer, pp. 150–159.

Chieregato, A., Fainardi, E., Morselli-Labate, A. M., Antonelli, V., Compagnone, C., Targa, L., Kraus, J. & Servadei, F. (2005), 'Factors associated with neurological outcome and lesion progression in traumatic subarachnoid hemorrhage patients', *Neurosurgery* 56(4), 671–680.

Chrastina, J., Hrabovskỳ, D., Ríha, I., Steinerová, K. & Novák, Z. (2013), '[the effect of age, alcohol intoxication and type of brain injury on the prognosis of patients operated on for craniocerebral trauma].', *Rozhledy v chirurgii: mesicnik Ceskoslovenske chirurgicke spolecnosti* 92(3), 135–142.

Chuang, K.-S., Tzeng, H.-L., Chen, S., Wu, J. & Chen, T.-J. (2006*a*), 'Fuzzy c-means clustering with spatial information for image segmentation', *Comp. Med. Imag. and Graph.* pp. 9–15.

Chuang, K.-S., Tzeng, H.-L., Chen, S., Wu, J. & Chen, T.-J. (2006*b*), 'Fuzzy c-means clustering with spatial information for image segmentation', *computerized medical imaging and graphics* 30(1), 9–15.

Cortes, C. & Vapnik, V. (1995), 'Support-vector networks', *Machine learning* 20(3), 273–297.

Cremers, D., Kohlberger, T. & Schnörr, C. (2002), Nonlinear shape statistics in mumford—shah based segmentation, *in* 'Computer Vision—ECCV 2002', Springer, pp. 93–108.

Cremers, D., Kohlberger, T. & Schnörr, C. (2003), 'Shape statistics in kernel space for variational image segmentation', *Pattern Recognition* 36(9), 1929–1943.

Cremers, D., Sochen, N. & Schnörr, C. (2003), Towards recognition-based variational segmentation using shape priors and dynamic labeling, *in* 'Scale Space Methods in Computer Vision', Springer, pp. 388–400.

Cyberphysics.co.uk (2014), 'What is ct scanning?'.
URL: *http://www.cyberphysics.co.uk/topics/medical/CTScanner.htm*

Davis, P. (2007), 'Head Trauma', *American Journal of Neuroradiology* 28, 1619–1621.

Dhawan, A. P. (2011), *Medical image analysis*, Vol. 31, John Wiley & Sons.

Doi, K. (2007), 'Computer-aided diagnosis in medical imaging: historical review, current status and future potential', *Computerized medical imaging and graphics* 31(4-5), 198–211.

Doi, K. (2014), 'Current status and future potential of computer-aided diagnosis in medical imaging', *The British Journal of Radiology* .

Donald, J. J. & Barnard, S. A. (2012), 'Common patterns in 558 diagnostic radiology errors', *Journal of Medical Imaging and Radiation Oncology* 56(2), 173–178.

Drew, T., Võ, M. L.-H. & Wolfe, J. M. (2013), 'The invisible gorilla strikes again sustained inattentional blindness in expert observers', *Psychological science* .

Dubrovina, A. & Kimmel, R. (2012), Active contours for multi-region image segmentation with a single level set function, Technical report, Technion technical report CIS-2012-06.

Duch, W. & Jankowski, N. (1999), 'Survey of neural transfer functions', *Neural Computing Surveys* 2(1), 163–212.

d'Anesthésie et de Réanimation), S. S. F. (2012), 'Scoring systems for ICU and surgical patients', http://www.sfar.org/scores2/triss2.html. [Online; accessed 22-Mar-2012].

Eggers, G., Kress, B., Rohde, S. & Mühling, J. (2014), 'Intraoperative computed tomography and automated registration for image-guided cranial surgery'.

Evans, A., Lambrou, T., Linnery, A. & Todd-Pokroped, A. (2004), Automatic segmentation of liver using a topology adaptive snake, *in* 'International Conference on Biomedical Engineering', pp. 205–208.

Evans, R. W., Baskin, D. S. & Yatsu, F. M. (1992), *Prognosis of neurological disorders*, Oxford University Press.

Fang, J., Saposnik, G., Silver, F. L., Kapral, M. K. et al. (2010), 'Association between weekend hospital presentation and stroke fatality', *Neurology* 75(18), 1589–1596.

Fernandez-Redondo, M. & Hernandez-Espinosa, C. (2000), A comparison among weight initialization methods for multilayer feedforward networks, *in* 'Neural Networks, 2000. IJCNN 2000, Proceedings of the IEEE-INNS-ENNS International Joint Conference on', Vol. 4, pp. 543–548 vol.4.

Fisher, M. (2000), Mistakes in the management of trauma patients, *in* 'Anesthesia, Pain, Intensive Care and Emergency Medicine—APICE', Springer, pp. 449–454.

Fitzgerald, R. (2001), 'Error in radiology', *Clinical radiology* 56(12), 938–946.

Freedman, D. & Zhang, T. (2005), Interactive graph cut based segmentation with shape priors, *in* 'Computer Vision and Pattern Recognition, 2005. CVPR 2005. IEEE Computer Society Conference on', Vol. 1, IEEE, pp. 755–762.

Freedman, M. & Osicka, T. (2006), 'Reader variability: what we can learn from computer-aided detection experiments.', *Journal of the American College of Radiology: JACR* 3(6), 446.

Gholipour, A., Estroff, J. A., Barnewolt, C. E., Connolly, S. A. & Warfield, S. K. (2011), 'Fetal brain volumetry through mri volumetric reconstruction and segmentation', *International journal of computer assisted radiology and surgery* 6(3), 329–339.

Giesel, F., Hahn, H., Thomann, P., Widjaja, E., Wignall, E., von Tengg-Kobligk, H., Pantel, J., Griffiths, P., Peitgen, H., Schroder, J. et al. (2006), 'Temporal horn index and volume of medial temporal lobe atrophy using a new semiautomated method for rapid and precise assessment', *American journal of neuroradiology* 27(7), 1454–1458.

Giger, M. L., Chan, H.-P. & Boone, J. (2008), 'Anniversary paper: History and status of cad and quantitative image analysis: the role of medical physics and aapm', *Medical physics* 35, 5799.

Goddard, P., Leslie, A., Jones, A., Wakeley, C. & Kabala, J. (2001), 'Error in radiology', *The British journal of radiology* 74(886), 949–951.

Godfrey, E. & Singh, A. (2009), *Radiology: Clinical Cases Uncovered*, Vol. 33, John Wiley & Sons.

Goldstein, M. (1990), 'Traumatic brain injury: a silent epidemic', *Annals of neurology* 27(3), 327–327.

Gomes, J. & Faugeras, O. (2002), Reconciling distance functions and level sets, *in* 'Biomedical Imaging, 2002. 5th IEEE EMBS International Summer School on', IEEE, pp. 15–pp.

Gonzalez, R. C. & Woods, R. E. (2002), 'Digital image processing'.

González-Reimers, E. & Santolaria-Fernández, F. (2011), Brain atrophy in alcoholics, *in* 'Handbook of Behavior, Food and Nutrition', Springer, pp. 2993–3010.

Gray, H. (1948), *Anatomy of the human body*, Lea & Febiger.

Guyon, I. & Elisseeff, A. (2003), 'An introduction to variable and feature selection', *The Journal of Machine Learning Research* 3, 1157–1182.

Guyon, I., Gunn, S., Nikravesh, M. & Zadeh, L. A. (2008), *Feature extraction: foundations and applications*, Vol. 207, Springer.

Gyldensted, C. & Kosteljanetz, M. (1976), 'Measurements of the normal ventricular system with computer tomography of the brain. a preliminary study on 44 adults', *Neuroradiology* 10(4), 205–213.

Haacke, E. M., Duhaime, A. C., Gean, A. D., Riedy, G., Wintermark, M., Mukherjee, P., Brody, D. L., DeGraba, T., Duncan, T. D., Elovic, E. et al. (2010), 'Common data elements in radiologic imaging of traumatic brain injury', *Journal of Magnetic Resonance Imaging* 32(3), 516–543.

Haapaniemi, H., Hillbom, M. & Juvela, S. (1996), 'Weekend and holiday increase in the onset of ischemic stroke in young women', *Stroke* 27(6), 1023–1027.

Hall, J. E. (2010), *Guyton and Hall Textbook of Medical Physiology: Enhanced E-book*, Elsevier Health Sciences.

Hashemi, H., Khabazkhoob, M., Jafarzadehpur, E., Emamian, M. H., Shariati, M. & Fotouhi, A. (2012), 'Contrast sensitivity evaluation in a population-based study in shahroud, iran', *Ophthalmology* 119(3), 541–546.

Haykin, S. (2004), 'A comprehensive foundation', *Neural Networks* 2(2004).

Heaton, J. (2008), *Introduction to neural networks with Java*, Heaton Research, Inc.

Hinton, G. E. & Salakhutdinov, R. R. (2006), 'Reducing the dimensionality of data with neural networks', *Science* 313(5786), 504–507.

Horgan, T. & Gilchrist, M. D. (2003), 'The creation of three-dimensional finite element models for simulating head impact biomechanics', *International Journal of Crashworthiness* 8(4), 353–366.

Hosmer Jr, D. W., Lemeshow, S. & Sturdivant, R. X. (2013), *Applied logistic regression*, John Wiley & Sons.

Hounsfield, G. N. (1980), 'Computed medical imaging', *Journal of computer assisted tomography* 4(5), 665–674.

Hsu, H. & Lachenbruch, P. A. (2008), 'Paired t test', *Wiley Encyclopedia of Clinical Trials* .

Hu, Q., Qian, G., Aziz, A. & Nowinski, W. L. (2006), Segmentation of brain from computed tomography head images, *in* 'Engineering in Medicine and Biology Society, 2005. IEEE-EMBS 2005. 27th Annual International Conference of the', IEEE, pp. 3375–3378.

Hukkelhoven, C., Steyerberg, E., Habbema, J., Farace, E., Marmarou, A., Murray, G., Marshall, L. & Maas, A. (2005), 'Predicting outcome after traumatic brain injury: development and validation of a prognostic score based on admission characteristics', *Journal of neurotrauma* 22(10), 1025–1039.

Hussain, M., Wajid, S. K., Elzaart, A. & Berbar, M. (2011), A comparison of svm kernel functions for breast cancer detection, *in* 'Computer Graphics, Imaging and Visualization (CGIV), 2011 Eighth International Conference on', IEEE, pp. 145–150.

IG, S., CM, C., BH, R. & et al (2005), 'Comparison of the Canadian CT Head Rule and the New Orleans Criteria in patients with minor head injury', *JAMA: The Journal of the American Medical Association* 294(12), 1511–1518.

Ingwersen, P. (1996), 'Cognitive perspectives of information retrieval interaction: elements of a cognitive ir theory', *Journal of documentation* 52(1), 3–50.

Jaffe, T. A., Wickersham, N. W. & Sullivan, D. C. (2010), 'Quantitative imaging in oncology patients: part 1, radiology practice patterns at major us cancer centers', *American Journal of Roentgenology* 195(1), 101–106.

Jiang, J., Trundle, P. & Ren, J. (2010), 'Medical image analysis with artificial neural networks', *Computerized Medical Imaging and Graphics* 34(8), 617–631.

Jiang, Y., Nishikawa, R. M., Schmidt, R. A., Toledano, A. Y. & Doi, K. (2001), 'Potential of computer-aided diagnosis to reduce variability in radiologists' interpretations of mammograms depicting microcalcifications', *Radiology* 220(3), 787–794.

Karasev, P., Kolesov, I., Fritscher, K., Vela, P., Mitchell, P. & Tannenbaum, A. (2013), 'Interactive medical image segmentation using pde control of active contours', *Medical Imaging, IEEE Transactions on* 32(11), 2127–2139.

Keats, T. E. & Sistrom, C. (2001), *Atlas of radiologic measurement*, Mosby Inc.

Kelly, J. P. (1999), 'Traumatic brain injury and concussion in sports', *JAMA* 282(10), 989–991.

Kennedy, R. E., Livingston, L., Riddick, A., Marwitz, J. H., Kreutzer, J. S. & Zasler, N. D. (2005), 'Evaluation of the neurobehavioral functioning inventory as a depression screening tool after traumatic brain injury', *The Journal of head trauma rehabilitation* 20(6), 512–526.

Khalifa, F., El-Baz, A., Gimel'farb, G., Ouseph, R. & El-Ghar, M. A. (2010), Shape-appearance guided level-set deformable model for image segmentation,

in 'Pattern Recognition (ICPR), 2010 20th International Conference on', IEEE, pp. 4581–4584.

Kimme-Smith, C., Haus, A., DeBruhl, N. & Bassett, L. (1997), 'Effects of ambient light and view box luminance on the detection of calcifications in mammography.', *American Journal of Roentgenology* 168(3), 775–778.

Koch, G. G. (1982), 'Intraclass correlation coefficient', *Encyclopedia of statistical sciences* .

Kondo, T. (1998), GMDH neural network algorithm using the heuristic self-organization method and its application to the pattern identification problem, *in* 'SICE'98. Proceedings of the 37th SICE Annual Conference. International Session Papers', IEEE, pp. 1143–1148.

Kondo, T., Pandya, A. S. & Zurada, J. M. (1999), Gmdh-type neural networks and their application to the medical image recognition of the lungs, *in* 'SICE Annual, 1999. 38th Annual Conference Proceedings of the', IEEE, pp. 1181–1186.

Kondo, T. & Ueno, J. (2012), Feedback GMDH-type neural network and its application to medical image analysis of the liver cancer, *in* '42th ISCIE international symposium on stochastic systems theory and its applications', pp. 81–82.

Kondo & Ueno (2007), Medical Image Recognition of Abdominal X-ray CT Images by RBF GMDH-type Neural Network, *in* 'SICE Annual Conference'.

Kononenko, I. (2001), 'Machine learning for medical diagnosis: history, state of the art and perspective', *Artificial Intelligence in medicine* 23(1), 89–109.

Kothari, R. U., Brott, T., Broderick, J. P., Barsan, W. G., Sauerbeck, L. R., Zuccarello, M. & Khoury, J. (1996), 'The abcs of measuring intracerebral hemorrhage volumes', *Stroke* 27(8), 1304–1305.

Krestin, G., Grenier, P., Hricak, H., Jackson, V., Khong, P., Miller, J., Muellner, A., Schwaiger, M. & Thrall, J. (2012), 'Integrated diagnostics: proceedings from the 9th biennial symposium of the international society for strategic studies in radiology', *European Radiology* 22(11), 2283–2294.

Langlois, J. A., Marr, A., Mitchko, J. & Johnson, R. L. (2005), 'Tracking the silent epidemic and educating the public: CDC's traumatic brain injury-associated activities under the TBI Act of 1996 and the Children's Health Act of 2000', *The Journal of head trauma rehabilitation* 20(3), 196–204.

Larsen, B., Ingwersen, P. & Kekäläinen, J. (2006), The polyrepresentation continuum in ir, *in* 'Proceedings of the 1st international conference on Information interaction in context', ACM, pp. 88–96.

Lauric, A. & Frisken, S. (2007), 'Soft segmentation of ct brain data', *Tufts University* .

Lee, B. & Newberg, A. (2005), 'Neuroimaging in traumatic brain imaging', *NeuroRx* 2(2), 372–383.

Lee, T. H., Fauzi, M. F., Komiya, R. et al. (2008), Segmentation of ct brain images using k-means and em clustering, *in* 'Computer Graphics, Imaging and Visualisation, 2008. CGIV'08. Fifth International Conference on', IEEE, pp. 339–344.

Leonhardt, D. (2006), 'Why doctors so often get it wrong', *The New York Times* .

Lesko, M., Woodford, M., White, L., O'Brien, S., Childs, C. & Lecky, F. (2010), 'Using abbreviated injury scale (ais) codes to classify computed tomography (ct) features in the marshall system', *BMC medical research methodology* 10(1), 72.

Lev, M. H., Rhea, J. T. & Bramson, R. T. (1999), 'Avoidance of variability and error in radiology', *The Lancet* 354(9175), 272.

Leventon, M. E., Grimson, W. E. L. & Faugeras, O. (2000), Statistical shape influence in geodesic active contours, *in* 'Computer Vision and Pattern Recognition, 2000. Proceedings. IEEE Conference on', Vol. 1, IEEE, pp. 316–323.

Levin, D. C. & Rao, V. M. (2004), 'Turf wars in radiology: The quality of interpretations of imaging studies by nonradiologist physicians—a patient safety issue?', *Journal of the American College of Radiology* 1(7), 506–509.

Li, C., Xu, C., Gui, C. & Fox, M. D. (2010), 'Distance regularized level set evolution and its application to image segmentation', *Image Processing, IEEE Transactions on* 19(12), 3243–3254.

Li, J., Li, X.-Y., Feng, D.-F. & Pan, D.-C. (2010), 'Biomarkers associated with diffuse traumatic axonal injury: exploring pathogenesis, early diagnosis, and prognosis', *The Journal of Trauma and Acute Care Surgery* 69(6), 1610–1618.

Li, Y.-C., Liu, L., Chiu, W.-T. & Jian, W.-S. (2000), 'Neural network modeling for surgical decisions on traumatic brain injury patients', *International journal of medical informatics* 57(1), 1–9.

Liao, C.-C., Chiang, I.-J., XIAO, F. & WONG, J.-M. (2006), 'Tracing the deformed midline on brain ct', *Biomedical Engineering: Applications, Basis and Communications* 18(06), 305–311.

Liao, C.-C., Xiao, F., Wong, J.-M. & Chiang, I.-J. (2010), 'Computer-aided diagnosis of intracranial hematoma with brain deformation on computed tomography', *Computerized Medical Imaging and Graphics* 34(7), 563–571.

Lingsma, H. F., Roozenbeek, B., Steyerberg, E. W., Murray, G. D. & Maas, A. I. (2010), 'Early prognosis in traumatic brain injury: from prophecies to predictions', *The Lancet Neurology* 9(5), 543–554.

Liu, R., Li, S., Su, B., Tan, C. L., Leong, T.-Y., Pang, B. C., Lim, C. T. & Lee, C. K. (2014), 'Automatic detection and quantification of brain midline shift

using anatomical marker model', *Computerized Medical Imaging and Graphics* 38(1), 1–14.

Lo, S.-C., Lou, S.-L., Lin, J.-S., Freedman, M. T., Chien, M. V. & Mun, S. K. (1995), 'Artificial convolution neural network techniques and applications for lung nodule detection', *Medical Imaging, IEEE Transactions on* 14(4), 711–718.

Lourakis, M. I. (2005), 'A brief description of the levenberg-marquardt algorithm implemented by levmar', *Foundation of Research and Technology* 4, 1–6.

Lukić, S., Ćojbasić, Ž., Perić, Z., Milošević, Z., Spasić, M., Pavlović, V. & Milojević, A. (2012), 'Artificial neural networks based early clinical prediction of mortality after spontaneous intracerebral hemorrhage', *Acta Neurologica Belgica* 112(4), 375–382.

Ma, Z., Tavares, J. M. R., Jorge, R. N. & Mascarenhas, T. (2010), 'A review of algorithms for medical image segmentation and their applications to the female pelvic cavity', *Computer Methods in Biomechanics and Biomedical Engineering* 13(2), 235–246.

Maas, A. I., Hukkelhoven, C. W., Marshall, L. F. & Steyerberg, E. W. (2005), 'Prediction of outcome in traumatic brain injury with computed tomographic characteristics: a comparison between the computed tomographic classification and combinations of computed tomographic predictors', *Neurosurgery* 57(6), 1173–1182.

Maas, A. I., Murray, G. D., Roozenbeek, B., Lingsma, H. F., Butcher, I., McHugh, G. S., Weir, J., Lu, J. & Steyerberg, E. W. (2013), 'Advancing care for traumatic brain injury: findings from the impact studies and perspectives on future research', *The Lancet Neurology* 12(12), 1200–1210.

Maduskar, P. & Acharyya, M. (2009), Automatic identification of intracranial hemorrhage in non-contrast ct with large slice thickness for trauma cases,

in 'SPIE Medical Imaging', International Society for Optics and Photonics, pp. 726011–726011.

Marieb, E. N. & Hoehn, K. (2007), *Human anatomy & physiology*, Pearson Education.

Marshall, L. F., Marshall, S. B., Klauber, M. R., Clark, M. v. B., Eisenberg, H. M., Jane, J. A., Luerssen, T. G., Marmarou, A. & Foulkes, M. A. (1991), 'A new classification of head injury based on computerized tomography', *Special Supplements* 75(1S), S14–S20.

McCluskey, D. (1990), 'Hutchison's clinical methods', *The Ulster medical journal* 59(1), 99.

McCreadie, G. & Oliver, T. (2009), 'Eight ct lessons that we learned the hard way: an analysis of current patterns of radiological error and discrepancy with particular emphasis on ct', *Clinical radiology* 64(5), 491–499.

McLauchlan, C., Jones, K. & Guly, H. (1997), 'Interpretation of trauma radiographs by junior doctors in accident and emergency departments: a cause for concern?', *Journal of accident & emergency medicine* 14(5), 295–298.

Meyer, F. (1994), 'Topographic distance and watershed lines', *Signal processing* 38(1), 113–125.

Michigan State University (2014), 'Horizontal sections of the human brain'.
URL: *https://www.msu.edu/user/brains/brains/human/horizontal/montage.html*

Moavenian, M. & Khorrami, H. (2010), 'A qualitative comparison of artificial neural networks and support vector machines in ecg arrhythmias classification', *Expert Systems with Applications* 37(4), 3088–3093.

Mould, R. (1989), 'Introduction to medical statistics', *Adam Hilger, Bristol, England* .

MTBI, C. D. O. (2004), 'Methodological issues and research recommendations for mild traumatic brain injury: the who collaborating centre task force on mild traumatic brain injury', *J Rehabil Med* 43, 113–125.

Murray, L., Teasdale, G., Jennett, B., Kelly, D., Murray, G., Miller, J., Jones, P., Pickard, J., Bailey, S., Shaw, M. et al. (1993), 'Does prediction of outcome alter patient management?', *The Lancet* 341(8859), 1487–1491.

Nakano, J. S. T. (2012), 'Bio-inspired models of network, information, and computing systems'.

Nell, V., Yates, D. W. & Kruger, J. (2000), 'An extended glasgow coma scale (gcs-e) with enhanced sensitivity to mild brain injury', *Archives of physical medicine and rehabilitation* 81(5), 614–617.

Nguyen, D. & Widrow, B. (1990), Improving the learning speed of 2-layer neural networks by choosing initial values of the adaptive weights, *in* 'Neural Networks, 1990., 1990 IJCNN International Joint Conference on', pp. 21–26 vol.3.

Nixon, M. (2008), *Feature extraction & image processing*, Academic Press.

Norton, G., Kishore, P. & Lin, J. (1978), 'Ct contrast enhancement in cerebral infarction', *American Journal of Roentgenology* 131(5), 881–885.

Oda, S., Awai, K., Murao, K., Ozawa, A., Yanaga, Y., Kawanaka, K. & Yamashita, Y. (2010), 'Computer-aided volumetry of pulmonary nodules exhibiting ground-glass opacity at mdct', *American Journal of Roentgenology* 194(2), 398–406.

Osher, S. & Fedkiw, R. P. (2001), 'Level set methods: an overview and some recent results', *Journal of Computational physics* 169(2), 463–502.

Osher, S. & Sethian, J. A. (1988), 'Fronts propagating with curvature-dependent speed: algorithms based on hamilton-jacobi formulations', *Journal of computational physics* 79(1), 12–49.

Pan, Y., Birdwell, J. D. & Djouadi, S. M. (2009), 'Preferential image segmentation using trees of shapes', *Image Processing, IEEE Transactions on* 18(4), 854–866.

Paniagua, B., Emodi, O., Hill, J., Fishbaugh, J., Pimenta, L. A., Aylward, S. R., Andinet, E., Gerig, G., Gilmore, J., van Aalst, J. A. et al. (2013), 3d of brain shape and volume after cranial vault remodeling surgery for craniosynostosis correction in infants, *in* 'SPIE Medical Imaging', International Society for Optics and Photonics, pp. 86720V–86720V.

Patient.Co.UK (2012), 'Trauma Triage and Scoring', http://www.patient.co.uk/doctor/Trauma-Triage-and-Scoring-(ATLS).htm. [Online; accessed 23-Mar-2012].

Perel, P., Wasserberg, J., Ravi, R. R., Shakur, H., Edwards, P. & Roberts, I. (2007), 'Prognosis following head injury: a survey of doctors from developing and developed countries', *Journal of evaluation in clinical practice* 13(3), 464–465.

Perron, A. D. (2008), *Emergency Medicine*, Saunders, chapter How to read a head CT scan, pp. 753–63.

Pohlman, T. H. & BjerkeHS, O. P. (2007), 'Trauma scoring systems'.

Pollard, B. J., Chawla, A. S., Delong, D. M., Hashimoto, N. & Samei, E. (2008), 'Object detectability at increased ambient lighting conditions', *Medical physics* 35(2204).

Post, A., Hoshizaki, B. & Gilchrist, M. D. (2012), 'Finite element analysis of the effect of loading curve shape on brain injury predictors', *Journal of biomechanics* 45(4), 679–683.

Prakash, K. B., Zhou, S., Morgan, T. C., Hanley, D. F. & Nowinski, W. L. (2012), 'Segmentation and quantification of intra-ventricular/cerebral hemorrhage in ct scans by modified distance regularized level set evolution technique', *International journal of computer assisted radiology and surgery* 7(5), 785–798.

Puech, P. A., Boussel, L., Belfkih, S., Lemaitre, L., Douek, P. & Beuscart, R. (2007), 'Dicomworks: software for reviewing dicom studies and promoting low-cost teleradiology', *Journal of Digital Imaging* 20(2), 122–130.

Quekel, L. G., Kessels, A. G., Goei, R. & van Engelshoven, J. M. (1999), 'Miss rate of lung cancer on the chest radiograph in clinical practice', *CHEST Journal* 115(3), 720–724.

Qureshi, A. I., Tuhrim, S., Broderick, J. P., Batjer, H. H., Hondo, H. & Hanley, D. F. (2001), 'Spontaneous intracerebral hemorrhage', *New England Journal of Medicine* 344(19), 1450–1460.

Radiopaedia.org (2014), 'Wiki-based collaborative radiology resource'. [Online; accessed 18-July-2014].
URL: *http://www.radiopaedia.org/*

Ragan, L., Waczulikova, I., Guller, L., Bilicky, J., Benuska, J. et al. (2009), 'Cella media distance in human brain in relation to age and gender', *Biomed Pap Med Fac Univ Palacky Olomouc Czech Repub* 153(4), 307–313.

Ramana, K., JNTU, K., Reddy, L. P. & JNTU, H. (2009), 'A neural network based classification and diagnosis of brain hemorrhages', *Academy of Information and Management Sciences* 13(1), 52.

Rao, A., Ledig, C., Newcombe, V., Menon, D. & Rueckert, D. (2014), Contusion segmentation from subjects with traumatic brain injury: a random forest framework, *in* 'Biomedical Imaging (ISBI), 2014 IEEE 11th International Symposium on', IEEE, pp. 333–336.

Reitsma, J. B., Glas, A. S., Rutjes, A. W., Scholten, R. J., Bossuyt, P. M. & Zwinderman, A. H. (2005), 'Bivariate analysis of sensitivity and specificity produces informative summary measures in diagnostic reviews', *Journal of clinical epidemiology* 58(10), 982–990.

Richards, O. (1977), 'Effects of luminance and contrast on visual acuity, ages 16 to 90 years.', *American Journal of Optometry and Physiological Optics* 54(3), 178.

Richardson, W. S., Wilson, M. C. & Guyatt, G. (2008), 'The process of diagnosis', *Users' Guides to the Medical Literature: A Manual for Evidence-Based Clinical Practice, 2nd ed. New York, NY: McGraw-Hill* .

Rill, L. N., Huda, W. & Gkanatsios, N. A. (1999), 'View box luminance measurements and their effect on reader performance', *Academic radiology* 6(9), 521–529.

Robinson, P. (1997), 'Radiology's achilles' heel: error and variation in the interpretation of the röntgen image.', *British Journal of Radiology* 70(839), 1085–1098.

Rojas, R. (2013), *Neural networks: a systematic introduction*, Springer Science & Business Media.

Roos, J. E., Paik, D., Olsen, D., Liu, E. G., Chow, L. C., Leung, A. N., Mindelzun, R., Choudhury, K. R., Naidich, D. P., Napel, S. et al. (2010), 'Computer-aided detection (cad) of lung nodules in ct scans: radiologist performance and reading time with incremental cad assistance', *European radiology* 20(3), 549–557.

Rousson, M. & Paragios, N. (2002), Shape priors for level set representations, *in* 'Computer Vision—ECCV 2002', Springer, pp. 78–92.

Ruan, J., Khalil, T. & King, A. I. (1994), 'Dynamic response of the human head to impact by three-dimensional finite element analysis', *Journal of Biomechanical Engineering* 116(1), 44–50.

Saatman, Duhaime, Bullock, Maas, Valadka, Manley, Team, W. S. & Members, A. P. (2008), 'Classification of Traumatic Brain Injury for Targeted Therapies', *Journal of Neurotrauma* 25, 719–738.

Sapiro, G. (2006), *Geometric partial differential equations and image analysis*, Cambridge university press.

Saposnik, G., Baibergenova, A., Bayer, N. & Hachinski, V. (2007), 'Weekends: a dangerous time for having a stroke?', *Stroke* 38(4), 1211–1215.

Schetinin, V. & Schult, J. (2005), 'A neural-network technique to learn concepts from electroencephalograms', *Theory in Biosciences* 124(1), 41–53.

Schetinin, V. & Schult, J. (2006), 'Learning polynomial networks for classification of clinical electroencephalograms', *Soft Computing* 10(4), 397–403.

Schoonjans, F., Zalata, A., Depuydt, C. & Comhaire, F. (1995), 'Medcalc: a new computer program for medical statistics', *Computer methods and programs in biomedicine* 48(3), 257–262.

Schreiber, M. A., Aoki, N., Scott, B. G. & Beck, J. R. (2002), 'Determinants of mortality in patients with severe blunt head injury', *Archives of Surgery* 137(3), 285.

Shah, S. M. & Kelly, K. M. (2003), *Principles and practice of emergency neurology: Handbook for emergency physicians*, Cambridge University Press.

Shahangian, B. & Pourghassem, H. (2013), Automatic brain hemorrhage segmentation and classification in ct scan images, *in* 'Machine Vision and Image Processing (MVIP), 2013 8th Iranian Conference on', IEEE, pp. 467–471.

Sharma, N. & Aggarwal, L. M. (2010), 'Automated medical image segmentation techniques', *Journal of medical physics/Association of Medical Physicists of India* 35(1), 3.

Shattuck, D. W., Prasad, G., Mirza, M., Narr, K. L. & Toga, A. W. (2009), 'Online resource for validation of brain segmentation methods', *NeuroImage* 45(2), 431–439.

Shi, J. & Malik, J. (2000), 'Normalized cuts and image segmentation', *Pattern Analysis and Machine Intelligence, IEEE Transactions on* 22(8), 888–905.

Shi, Z. & He, L. (2010), Application of neural networks in medical image processing, *in* 'Proceedings of the Second International Symposium on Networking and Network Security', pp. 2–4.

Shiraishi, J., Li, Q., Appelbaum, D. & Doi, K. (2011), Computer-aided diagnosis and artificial intelligence in clinical imaging, *in* 'Seminars in Nuclear Medicine', Vol. 41, Elsevier, pp. 449–462.

Shneiderman, S. B. & Plaisant, C. (2005), 'Designing the user interface 4 th edition', *ed: Pearson Addison Wesley, USA* .

Sia, D. I., Martin, S., Wittert, G. & Casson, R. J. (2012), 'Age-related change in contrast sensitivity among australian male adults: Florey adult male ageing study', *Acta Ophthalmologica* .

Signorini, D. F., Andrews, P. J., Jones, P. A., Wardlaw, J. M. & Miller, J. D. (1999), 'Predicting survival using simple clinical variables: a case study in traumatic brain injury', *Journal of Neurology, Neurosurgery & Psychiatry* 66(1), 20–25.

Sinha, M., Kennedy, C. S., Ramundo, M. L. et al. (2001), 'Artificial neural network predicts ct scan abnormalities in pediatric patients with closed head injury', *Journal of Trauma and Acute Care Surgery* 50(2), 308–312.

Smirniotopoulos, J. G. (2012), 'Acute brain imaging - the 3 slice method'. Accessed: July, 11, 2014.
URL: *http://www.youtube.com/watch?v=0JJFkNkzuYg*

Sokolova, M., Japkowicz, N. & Szpakowicz, S. (2006), Beyond accuracy, f-score and roc: a family of discriminant measures for performance evaluation, *in* 'AI 2006: Advances in Artificial Intelligence', Springer, pp. 1015–1021.

Soltaninejad, M., Lambrou, T., Qureshi, A. N., Allinson, N. M. & Ye, X. (2014), A hybrid method for haemorrhage segmentation in trauma brain CT, *in* 'Medical Image Understanding and Analysis - MIUA 2014. 18th Annual Conference, Egham, UK, July 9-11, 2014. Proceedings.', pp. 99–104.

Ster, B., Dobnikar, A. et al. (1996), Neural networks in medical diagnosis: Comparison with other methods, *in* 'Proceedings of the International Conference EANN', Vol. 96, pp. 427–430.

Stevens, K. J., Griffiths, K. L., Rosenberg, J., Mahadevan, S., Zatz, L. M. & Leung, A. N. (2008), 'Discordance rates between preliminary and final radiology reports on cross-sectional imaging studies at a level 1 trauma center', *Academic radiology* 15(10), 1217–1226.

Steyerberg, E. W., Mushkudiani, N., Perel, P., Butcher, I., Lu, J., McHugh, G. S., Murray, G. D., Marmarou, A., Roberts, I., Habbema, J. D. F. et al. (2008), 'Predicting outcome after traumatic brain injury: development and international validation of prognostic scores based on admission characteristics', *PLoS medicine* 5(8), e165.

Suri, J. S., Setarehdan, S. K. & Singh, S. (2002), *Advanced algorithmic approaches to medical image segmentation: state-of-the-art applications in cardiology, neurology, mammography and pathology*, Springer.

Suzuki, K., Epstein, M. L., Kohlbrenner, R., Garg, S., Hori, M., Oto, A. & Baron, R. L. (2011), 'Quantitative radiology: automated ct liver volumetry compared with interactive volumetry and manual volumetry', *American Journal of Roentgenology* 197(4), W706–W712.

Tao, W., Jin, H. & Zhang, Y. (2007), 'Color image segmentation based on mean shift and normalized cuts', *Systems, Man, and Cybernetics, Part B: Cybernetics, IEEE Transactions on* 37(5), 1382–1389.

Thimm, G. & Fiesler, E. (1997), 'High-order and multilayer perceptron initialization', *Neural Networks, IEEE Transactions on* 8(2), 349–359.

Thompson, H. J., McCormick, W. C. & Kagan, S. H. (2006), 'Traumatic brain injury in older adults: epidemiology, outcomes, and future implications', *Journal of the American Geriatrics Society* 54(10), 1590–1595.

Timmons, S. D., Bee, T., Webb, S., Diaz-Arrastia, R. R. & Hesdorffer, D. (2011), 'Using the abbreviated injury severity and glasgow coma scale scores to predict 2-week mortality after traumatic brain injury', *The Journal of Trauma and Acute Care Surgery* 71(5), 1172–1178.

Tremeau, A. & Borel, N. (1997), 'A region growing and merging algorithm to color segmentation', *Pattern recognition* 30(7), 1191–1203.

Turaga, S. C., Murray, J. F., Jain, V., Roth, F., Helmstaedter, M., Briggman, K., Denk, W. & Seung, H. S. (2010), 'Convolutional networks can learn to generate affinity graphs for image segmentation', *Neural Computation* 22(2), 511–538.

University of Virginia (2014), 'Head ct technique'. [Online; accessed 18-July-2014]. **URL:** *https://www.med-ed.virginia.edu/courses/rad/headct/technique.html*

University of Wisconsin (2014), 'Ct technique'. [Online; accessed 18-July-2014]. **URL:** *https://sites.google.com/a/wisc.edu/neuroradiology/image-acquisition/computed-tomogra*

van Ginneken, B., Schaefer-Prokop, C. M. & Prokop, M. (2011), 'Computer-aided diagnosis: how to move from the laboratory to the clinic', *Radiology* 261(3), 719–732.

Vantaram, S. R. & Saber, E. (2012), 'Survey of contemporary trends in color image segmentation', *Journal of Electronic Imaging* 21(4), 040901–1.

Venu, N. & Anuradha, B. (2013), 'A novel multiple-kernel based fuzzy c-means algorithm with spatial information for medical image segmentation', *International Journal of Image Processing (IJIP)* 7(3), 286.

Vese, L. A. & Chan, T. F. (2002), 'A multiphase level set framework for image segmentation using the mumford and shah model', *International journal of computer vision* 50(3), 271–293.

Vespa, P. M. (2014), 'Imaging and decision-making in neurocritical care', *Neurologic clinics* 32(1), 211–224.

Vicente, S., Kolmogorov, V. & Rother, C. (2008), Graph cut based image segmentation with connectivity priors, *in* 'Computer Vision and Pattern Recognition, 2008. CVPR 2008. IEEE Conference on', IEEE, pp. 1–8.

Vrooman, H. A., Cocosco, C. A., van der Lijn, F., Stokking, R., Ikram, M. A., Vernooij, M. W., Breteler, M. M. & Niessen, W. J. (2007), 'Multi-spectral brain tissue segmentation using automatically trained k-nearest-neighbor classification', *Neuroimage* 37(1), 71–81.

Wang, L., Li, C., Sun, Q., Xia, D., Kao, C.-Y. et al. (2009), 'Active contours driven by local and global intensity fitting energy with application to brain mr image segmentation', *Computerized Medical Imaging and Graphics* 33(7), 520.

Wessels, L. F. & Barnard, E. (1992), 'Avoiding false local minima by proper initialization of connections', *Neural Networks, IEEE Transactions on* 3(6), 899–905.

Wilk, R., Kluczewska, E., Syc, B. & Bajor, G. (2011), 'Normative values for selected linear indices of the intracranial fluid spaces based on ct images of the head in children', *Polish Journal of Radiology* 76(3), 16.

Wolbarst, A. B. & Cook, G. (1999), *Looking Within: How X-ray, CT, MRI, Ultrasound, and Other Medical Images are Created and how They Help Physicians Save Lives*, University of California Press USA.

Yang, X., Tang, K. & Yao, X. (2009), The minimum redundancy–maximum relevance approach to building sparse support vector machines, *in* 'Intelligent Data Engineering and Automated Learning-IDEAL 2009', Springer, pp. 184–190.

Yegnanarayana, B. (2009), *Artificial neural networks*, PHI Learning Pvt. Ltd.

Yezzi Jr, A., Kichenassamy, S., Kumar, A., Olver, P. & Tannenbaum, A. (1997), 'A geometric snake model for segmentation of medical imagery', *Medical Imaging, IEEE Transactions on* 16(2), 199–209.

Yu, H. & Wilamowski, B. M. (2011), 'Levenberg-marquardt training', *Industrial Electronics Handbook* 5, 12–1.

Yuh, E., Cooper, S., Ferguson, A. & Manley, G. (2012), 'Quantitative ct improves outcome prediction in acute traumatic brain injury', *Journal of neurotrauma* 29(5), 735–746.

Zaki, W. M. D. W., Fauzi, M. F. A. & Besar, R. (2010), 'Retrieval of intracranial hemorrhages in computed tomography brain images using binary coherent vector', *Journal of Electronic Imaging* 19(4), 043021–043021.

Zanaty, E. (2012), 'Support vector machines (svms) versus multilayer perception (mlp) in data classification', *Egyptian Informatics Journal* 13(3), 177–183.

Zhang, Y., Chen, M., Hu, Q. & Huang, W. (2013), 'Detection and quantification of intracerebral and intraventricular hemorrhage from computed tomography images with adaptive thresholding and case-based reasoning', *International journal of computer assisted radiology and surgery* 8(6), 917–927.

Zhang, Y., Dong, Z., Wu, L. & Wang, S. (2011), 'A hybrid method for mri brain image classification', *Expert Systems with Applications* 38(8), 10049–10053.

Zhang, Y., Londos, E., Minthon, L., Wattmo, C., Liu, H., Aspelin, P. & Wahlund, L.-O. (2008), 'Usefulness of computed tomography linear measurements in diagnosing alzheimer's disease', *Acta Radiologica* 49(1), 91–97.

Zharkova, V. & Schetinin, V. (2005), 'Filament recognition in solar images with the neural network technique', *Solar Physics* 228(1-2), 137–148.

Zou, K. H., Warfield, S. K., Bharatha, A., Tempany, C., Kaus, M. R., Haker, S. J., Wells III, W. M., Jolesz, F. A. & Kikinis, R. (2004), 'Statistical validation of image segmentation quality based on a spatial overlap index: scientific reports', *Academic radiology* 11(2), 178–189.